Plasma Physics Reports, Vol. 28, No. 4, 2002, pp. 259–267. Translated from Fizika Plazmy, Vol. 28, No. 4, 2002, pp. 291–299.

MAGNETIC CONFINEMENT SYSTEMS

Analytic Examples of Force-Free Toroidal MHD Equilibria

A. A. Martynov and S. Yu. Medvedev

Keldysh Institute of Applied Mathematics, Russian Academy of Sciences, Miusskaya pl. 4, Moscow, 125047 Russia

e-mail: martynov@a5.kiam.ru, medvedev@a5.kiam.ru

Received October 30, 2001; in final form, November 22, 2001

Abstract—Analytically described toroidal (axisymmetric and three-dimensional) equilibrium magnetic field configurations with a "flat" current density, $\mathbf{j} = \lambda\mathbf{B}$ (λ = const), are proposed. Such configurations are superpositions of several force-free two-dimensional configurations with plane, axial, or helical coordinate symmetry. Each of them is generated by an exact partial solution to the corresponding Grad–Shafranov equation. A variety of toroidal configurations thus obtained allows one to model topological changes of magnetic surfaces, such as magnetic axis splitting (doublets) in axisymmetric equilibrium configurations and the appearance and interaction of magnetic islands and ergodic lines in three-dimensional configurations. © *2002 MAIK "Nauka/Interperiodica".*

1. GENERAL DESCRIPTION OF TWO-DIMENSIONAL FORCE-FREE CONFIGURATIONS

Two-dimensional equilibrium magnetic configurations with a corresponding coordinate symmetry (planar, axial, or helical) can be conveniently described using the following "poloidal" representation of the magnetic field,

$$\mathbf{B} = \nabla\psi \times \mathbf{b} + F\mathbf{b}, \tag{1}$$

with the known base vector fields $\mathbf{b}$ (see below), satisfying the relationships

$$\mathbf{b}\cdot\nabla\psi = 0, \quad \nabla\cdot\mathbf{b} = 0, \quad \mathbf{b}\times(\nabla\times\mathbf{b}) = 0, \tag{2}$$

and the scalar functions ψ and $F = F(\psi)$, proportional to the poloidal magnetic flux and electric current, respectively (see [1]). For the three above symmetries, periodic (closed in the axisymmetric case) streamlines of the base vectors $\mathbf{b}$ correspond to the natural topology of the contours through which the flux and current are calculated (here, we use cylindrical coordinates (r, ϕ, z)):

$$\mathbf{b} = \mathbf{b}_p = \nabla z, \quad \psi = \psi(r, \phi) \tag{3}$$

in case of planar symmetry;

$$\mathbf{b} = \mathbf{b}_a = \nabla\phi, \quad \psi = \psi(r, z) \tag{4}$$

in case of axial symmetry; and

$$\mathbf{b} = \mathbf{b}_h = (-n/k\nabla z + r^2\nabla\phi)/(n^2/k^2 + r^2), \quad \psi = \psi(r, \zeta), \quad \zeta = n\phi + kz \tag{5}$$

in case of helical symmetry.

Taking into account the base vector properties (2) and the current density definition $\mathbf{j} = \nabla\times\mathbf{B}$, it follows from the two-dimensional (2D) magnetic field representation (1) that, in all these cases, the function ψ satisfies the elliptic equation

$$\nabla\cdot(b^2\nabla\psi) = F\mathbf{b}\cdot(\nabla\times\mathbf{b}) - \mathbf{j}\cdot\mathbf{b}, \tag{6}$$

which is obtained by applying the operator $\nabla\cdot$ to the vector product of representation (1) with $\mathbf{b}$.

In the specific case of force-free equilibria, $\mathbf{j} = \lambda\mathbf{B}$, the coefficient $\lambda = \lambda(\psi)$ determines the relation between the current and magnetic flux: $F = \lambda\psi$ and $\mathbf{j}\cdot\mathbf{b} = \lambda^2 b^2\psi$. Therefore, all 2D force-free magnetic configurations can be described by the formula

$$\mathbf{B} = \nabla\psi\times\mathbf{b} + \lambda\psi\mathbf{b}, \tag{7}$$

where the function ψ satisfies the equation

$$\nabla\cdot(b^2\nabla\psi) = \lambda\psi(\mathbf{b}\cdot(\nabla\times\mathbf{b}) - \lambda b^2) \tag{8}$$

with one of the three versions of the base vector $\mathbf{b}$ [(3), (4), or (5)]. Equation (8) is a generalized Grad–Shafranov equation for force-free configurations under consideration.

We note that representation (7) and Eq. (8) are valid for any 2D force-free equilibrium configuration with an arbitrary function $\lambda(\psi)$; however, in this paper, we consider only the simplest case with λ = const, which allows the analytic generation and superposition of such magnetic configurations.

2. EXAMPLES OF 2D FORCE-FREE CONFIGURATIONS

In the case of a "flat" current profile, λ = const, partial analytic solutions for all three versions of Eq. (8)

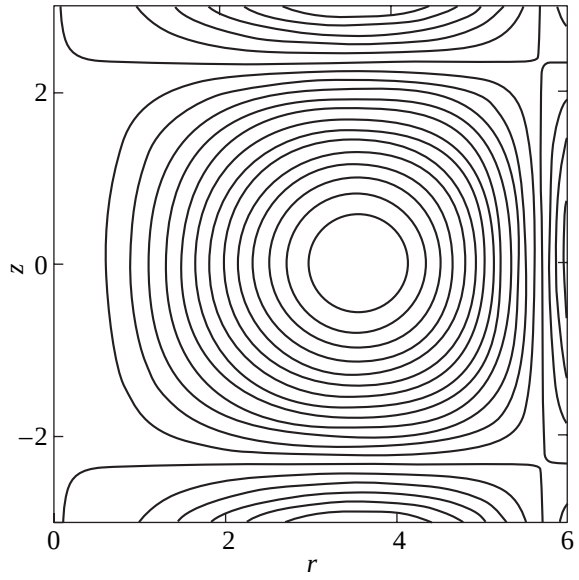

Fig. 1. Magnetic surfaces in the (r, z) plane for an axisymmetric equilibrium from family (4), (7), and (10) with the parameter values $\lambda = 0.95$, $\lambda_1 = \lambda_2 = \sqrt{0.5}\,\lambda$.

can be obtained. Here, we use some of them to examine the following specific examples:

$$\psi = \psi_p(y) = \cos(\lambda y) \tag{9}$$

in case of planar symmetry;

$$\psi = \psi_a(r, z) = rJ_1(\lambda_2 r)\cos(\lambda_1 z), \quad \lambda_1^2 + \lambda_2^2 = \lambda^2 \tag{10}$$

in case of axial symmetry; and

$$\psi = \psi_h(r, \zeta) = \left(\frac{1}{\sqrt{|k^2 - \lambda^2|}} rI_n'(t) + \frac{n\lambda}{k(k^2 - \lambda^2)} I_n(t)\right)\cos\zeta, \quad t = \sqrt{|k^2 - \lambda^2|}\, r \tag{11}$$

in case of helical symmetry, assuming that $k^2 > \lambda^2$. Here, J_1 is the first-order Bessel function and I_n is the nth-order modified Bessel function. The corresponding magnetic fields will be referred to as $\mathbf{B}_p$, $\mathbf{B}_a$, and $\mathbf{B}_h$, respectively.

Numerous other exact solutions can be generated using other (in particular, higher order) trigonometric and cylindrical functions.

Moreover, any superposition of symmetric magnetic fields of form (7) with the same value of the parameter λ is again an equilibrium force-free configuration. This makes it possible to generate essentially three-dimensional (3D) equilibrium magnetic configurations.

Analytic solutions for force-free fields were previously obtained by the variable separation method: in the 1950s, axially and helically symmetric fields [2–4] and, later, essentially 3D configurations [5], including those with a split magnetic axis and magnetic islands beyond the region of nested magnetic surfaces. One of the 2D force-free configurations with helical symmetry [4] was used to test the PIES 3D equilibrium code [6].

In this paper, the attention is focused on closed toroidal configurations as the most interesting from a practical standpoint. They are formed primarily by axisymmetric fields determined by flux function (10). Let us consider in more detail the corresponding system of magnetic surfaces, i.e., the isolines of function (10) on the (r, z) plane. This is a mirror symmetric system of rectangular cells having O-points (magnetic axes) in the equatorial plane $z = 0$, where $J_0(\lambda_2 r) = 0$. The elongation of the magnetic surfaces near the axes is the same and is determined by the ratio $E = |\lambda_2/\lambda_1|$. One such cell with circular magnetic surfaces in the vicinity of the magnetic axis ($\lambda_1 = \lambda_2$) is shown in Fig. 1.

Knowing the shape of the magnetic surfaces near the axes, we can exactly calculate the safety factor q using the following general expression relating its value at the magnetic axis q_{ax} to the derivative of the volume V enclosed by the surface:

$$q_{ax} = -\frac{F}{4\pi^2 r_{ax}^2}\frac{dV}{d\psi},$$

where all the values are taken at the magnetic axis.

For the flux function $\psi(r, z)$ belonging to family (10), we can easily calculate the derivative of the volume

$$\frac{dV}{d\psi} = -\frac{4\pi^2 r_{ax}^2}{\lambda_1\lambda_2\psi_{ax}},$$

which leads to the following expression for q_{ax}:

$$q_{ax} = \frac{\lambda}{r_{ax}\lambda_1\lambda_2} = \frac{\lambda}{\lambda_1 r_{0,i}}, \tag{12}$$

where $r_{0,i}$ is the ith zero of the Bessel function J_0.

In particular, for the cell shown in Fig. 1, we have $q_{ax} = \sqrt{2}/r_{0,1} = 0.5881$. To obtain the entire profile of the safety factor, we used the CAXE 2D equilibrium code [7]. As was expected, the flat current density profile corresponds to the q profile decreasing from the value q_{ax} at the magnetic axis to zero at the separatrix (see Fig. 2). Apparently, such a profile is typical of all the magnetic axes and all the values of the parameters λ_1 and λ_2.

Combining several functions from family (10), more complicated configurations can be generated. Let us show how a special combination of the two functions

$$\psi_a^{(j)} = rJ_1(\lambda_2^{(j)} r)\cos(\lambda_1^{(j)} z), \quad j = 1, 2 \tag{13}$$

(and, accordingly, the magnetic fields $\mathbf{B}_a^{(1)}$ and $\mathbf{B}_a^{(2)}$) transforms an O-point into an X-point, as a result of which a doublet configuration appears.

We chose the values of the parameters λ_1^j and λ_2^j such that the position of the first extremum (maximum) of the function $\psi_a^{(1)}$ coincides with the position of the second extremum (minimum) of the function $\psi_a^{(2)}$:

$$\lambda_2^{(1)} r_{ax} = r_{0,1}, \quad \lambda_2^{(2)} r_{ax} = r_{0,2}, \tag{14}$$

where $r_{0,1} = 2.4048$ and $r_{0,2} = 5.5201$ are the first two zeros of the Bessel function J_0.

The remaining freedom in the choice of λ_1^j and λ_2^j can be used to impose the additional relations

$$\lambda_1^{(1)} = \lambda_2^{(2)}, \quad \lambda_2^{(1)} = \lambda_1^{(2)}, \tag{15}$$

which are not of crucial importance, but are chosen here for the sake of convenience.

The above conditions are satisfied with the following parameter values:

$$\lambda_2^{(1)} = \lambda_1^{(2)} = (1 + (r_{0,2}/r_{0,1})^2)^{-1/2}\lambda = 0.3994\lambda,$$

$$\lambda_1^{(1)} = \lambda_2^{(2)} = (1 + (r_{0,1}/r_{0,2})^2)^{-1/2}\lambda = 0.9168\lambda.$$

Due to condition (15), the elongation of the magnetic surfaces is the same at all the magnetic axes: $E^{(2)} = 1/E^{(1)} = \lambda_2^{(2)}/\lambda_1^{(2)} = 2.295$; however, the surfaces are elongated in different directions (see Fig. 3): in the vertical direction for the function $\psi_a^{(2)}$ and in the horizontal direction for the function $\psi_a^{(1)}$.

In the case of the function $\psi_a^{(2)}$, formula (12) gives $q_{ax} = \lambda/(\lambda_1^{(2)} r_{0,1}) = 1.041$ for the first extremum and $q_{ax} = \lambda/(\lambda_1^{(2)} r_{0,2}) = 0.4536$ for the second extremum. It follows from conditions (14) that the latter value of q_{ax} also corresponds to the first extremum of the function $\psi_a^{(1)}$.

Let us now consider a field superposition corresponding to the linear combination

$$\psi^{(sum)} = w_1 \psi_a^{(1)}/\psi_{\max}^{(1)} - w_2 \psi_a^{(2)}/\psi_{\min}^{(2)}, \tag{16}$$

where $\psi_{\min}^{(2)} < 0$ and $\psi_{\max}^{(1)} > 0$ are, respectively, the values of the functions $\psi_a^{(2)}$ and $\psi_a^{(1)}$ at the point $(r_{ax}, 0)$.

By appropriately choosing the weight coefficients w_1 and w_2, we can provide the following properties of the function $\psi^{(sum)}$ (16) at this point:

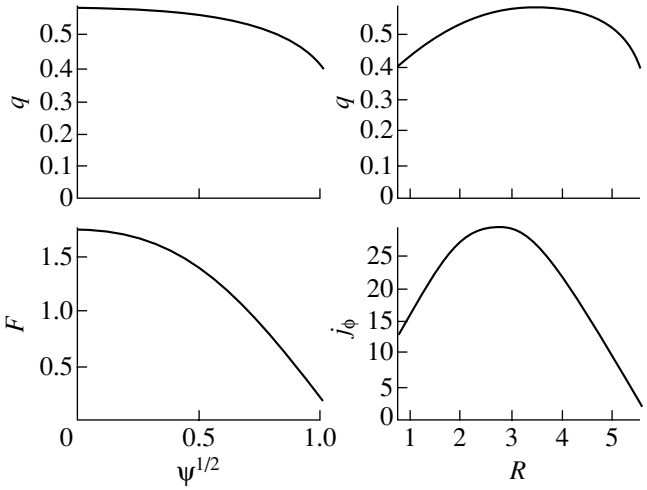

Fig. 2. Profiles of the plasma current and safety factor q for the configuration shown in Fig.1. The normalized poloidal flux ψ, changing from zero at the magnetic axis to unity at the boundary, is used here as a surface label.

(i) $\dfrac{\partial^2 \psi^{(sum)}}{\partial z^2} = 0$, which corresponds to the infinitely elongated vertical magnetic axis with $w_2/w_1 = (\lambda_1^{(1)}/\lambda_1^{(2)})^2 = (r_{0,2}/r_{0,1})^2 = 5.269$;

(ii) $\dfrac{\partial^2 \psi^{(sum)}}{\partial r^2} = 0$, which corresponds to the infinitely elongated horizontal magnetic axis with $w_2/w_1 = (\lambda_2^{(1)}/\lambda_2^{(2)})^2 = (r_{0,1}/r_{0,2})^2 = 0.1898$; and

(iii) $\dfrac{\partial^2 \psi^{(sum)}}{\partial r^2}\dfrac{\partial^2 \psi^{(sum)}}{\partial z^2} < 0$, which corresponds to an X-point (in place of an O-point) with $0.1898 < w_2/w_1 < 5.269$. In the latter case, the values of w_2/w_1 close to the left (right) boundary of the interval correspond to the vertical (horizontal) figure-eight separatrix surrounded by nested magnetic surfaces. Figure 4 shows examples for all these cases.[1]

3. 3D TOROIDAL CONFIGURATIONS AS SUPERPOSITIONS OF 2D ONES

As was noted above, any linear combination of magnetic fields (7) with the same value of the parameter λ is also a force-free equilibrium configuration. Moreover, the surfaces of the resulting 3D configuration remain closed (toroidal) in the vicinity of the magnetic axis if the axisymmetric field has sufficiently high weight in the superposition.

[1] All the axisymmetric configurations considered here are also mirror symmetric. By using another partial solution, asymmetric configurations can easily be generated (see, e.g., [8]).

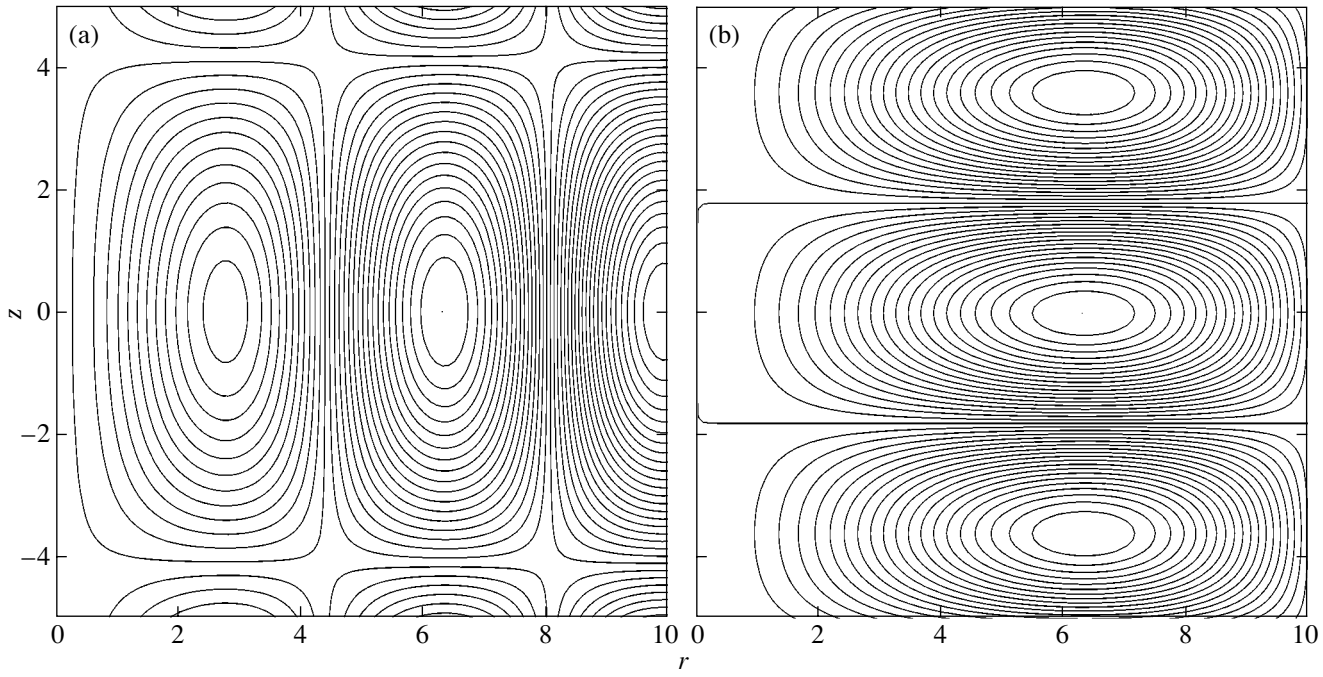

Fig. 3. Magnetic surfaces in the (r, z) plane for two axisymmetric configurations from family (4), (7), and (10) with vertical and horizontal elongations: the contour lines of the functions (a) $\psi_a^{(2)}$ and (b) $\psi_a^{(1)}$ with the parameter values $\lambda = 0.95$ and $\lambda_2^{(1)} = \lambda_1^{(2)} = 0.3994\lambda$ and $\lambda_1^{(1)} = \lambda_2^{(2)} = 0.9168\lambda$.

In general, such essentially 3D configurations cannot be described by scalar flux functions. They can be analyzed by using the numerical tracing of the magnetic field lines and the Poincaré mapping in several cross sections $\phi = \text{const}$. The results presented below were obtained with the use of a standard ordinary differential equation solver from the NAG library by tracing the magnetic field line over 400 turns in the toroidal angle.

Two examples of 3D toroidal force-free magnetic configurations were presented in [8]. One of them demonstrates a big magnetic island $m/n = 1/2$ appearing at the resonant surface $q = 0.5$ when an axisymmetric equilibrium configuration with circular surfaces (Fig. 1) is perturbed with a small helical field. A distinctive feature of the example is the presence of "good" magnetic surfaces, including the island separatrix: no evidence of the field line stochastization was found in the region under consideration. Another example in [8] shows the effect of 3D stochastization of an internal figure-eight axisymmetric separatrix of the doublet type. These and other examples presented below confirm the general expectation that the regions with a fast change of q (an external separatrix, a doublet separatrix, or a strongly elongated magnetic axis) are topologically unstable: small 3D perturbations make field lines stochastic, whereas, in low-shear regions, the magnetic surfaces can remain well shaped even in the presence of big islands.

Several new examples (Figs. 5–7) show various transformations of the magnetic surface topology for the same parent axisymmetric configuration (Fig. 3a) and different additional fields.

As was mentioned in the previous section, the vertically elongated configuration in Fig. 3a has a decreasing q profile with $q_{ax} = 1.041$. Hence, 3D effects manifest themselves, first of all, at the resonant surface $q = 1$.

Figure 5 shows a series of magnetic configurations, $\mathbf{B} = \mathbf{B}_a^{(2)} + w_h\mathbf{B}_h$, with a progressively increasing contribution (weight w_h) of the helical field $\mathbf{B}_h$. Here, the growing magnetic island $m/n = 1/1$ suppresses the main magnetic axis; finally, at sufficiently large values of w_h, the configuration with nested magnetic surfaces (Fig. 5c) appears again.

Another example is a superposition of an axisymmetric and a plane 2D field, $\mathbf{B} = \mathbf{B}_a^{(2)} + w_p\mathbf{B}_p$, which provokes an $m/n = 2/2$ island at the same resonant surface (Fig. 6).

Perturbing an axisymmetric field with a helical and a plane field, $\mathbf{B} = \mathbf{B}_a^{(2)} + w_h\mathbf{B}_h + w_p\mathbf{B}_p$, leads to the interaction of the islands (Fig. 7): inside the $m/n = 1/1$ island, a figure-eight separatrix (helical doublet)

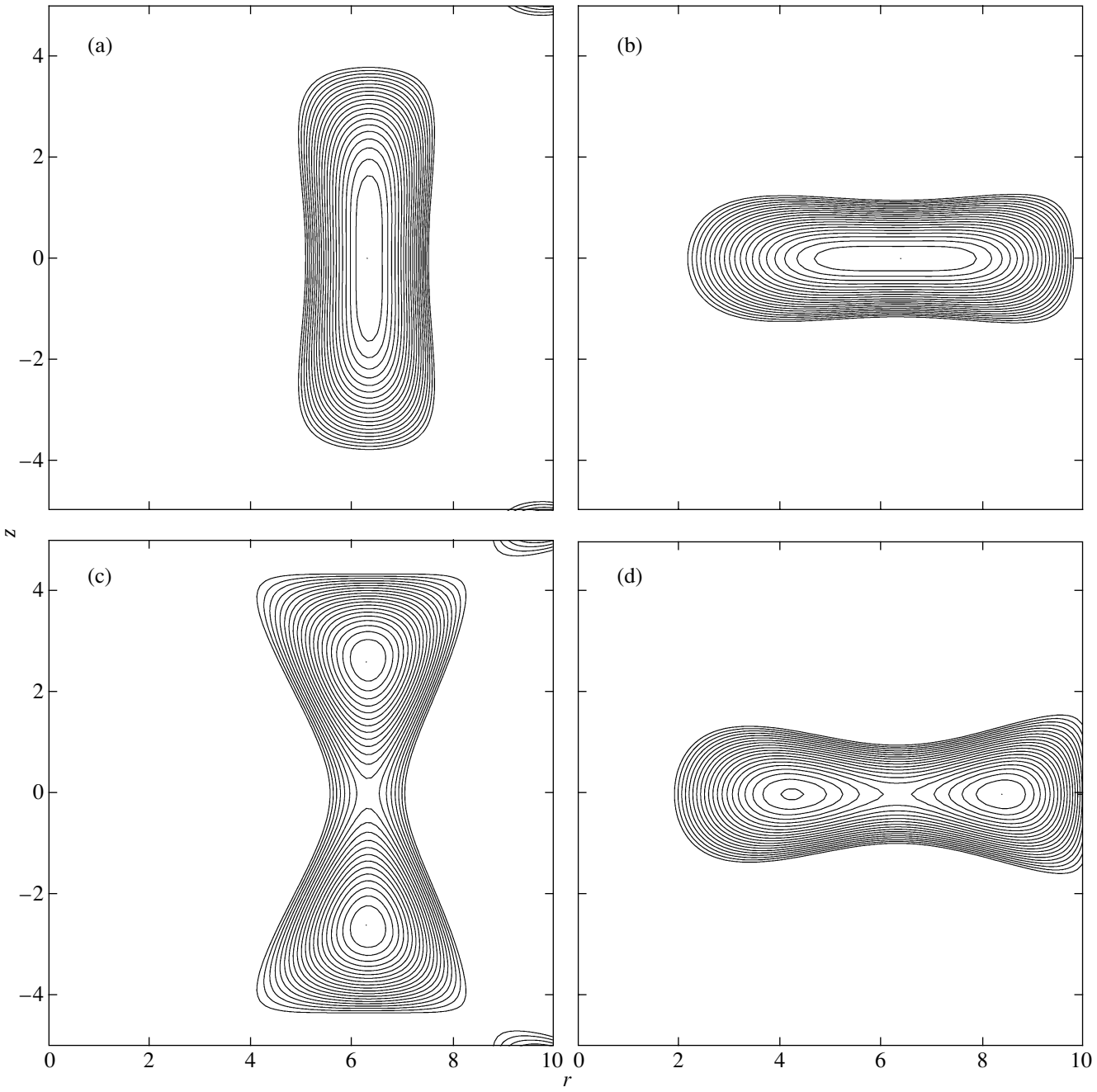

Fig. 4. Result of superposition $\psi^{(sum)}$ (16) of the two functions $\psi_a^{(1)}$ and $\psi_a^{(2)}$ for different values of weight coefficients: (a) an infinitely elongated vertical magnetic axis, $w_2/w_1 = 5.269$; (b) an infinitely elongated horizontal magnetic axis, $w_2/w_1 = 0.1898$; (c) a vertical doublet configuration, $w_2/w_1 = 2.02$; and (d) a horizontal doublet configuration, $w_2/w_1 = 0.32$.

appears in place of the island magnetic axis. At the same time, magnetic surfaces remain well shaped.

Figure 8 demonstrates the stochastization of the magnetic field near the magnetic axis with infinitely elongated surfaces. Here, the parent axisymmetric configuration corresponding to Fig. 4b is perturbed by a helical field, $\mathbf{B} = w_1\mathbf{B}_a^{(1)} + w_2\mathbf{B}_a^{(2)} + w_h\mathbf{B}_h$ with $w_1 = 1$ and $w_2 = 0.1898$. It is interesting to note the appearance of good nested magnetic surfaces inside the stochastic region.

In conclusion, we note that the family of force-free equilibrium configurations presented here contains a

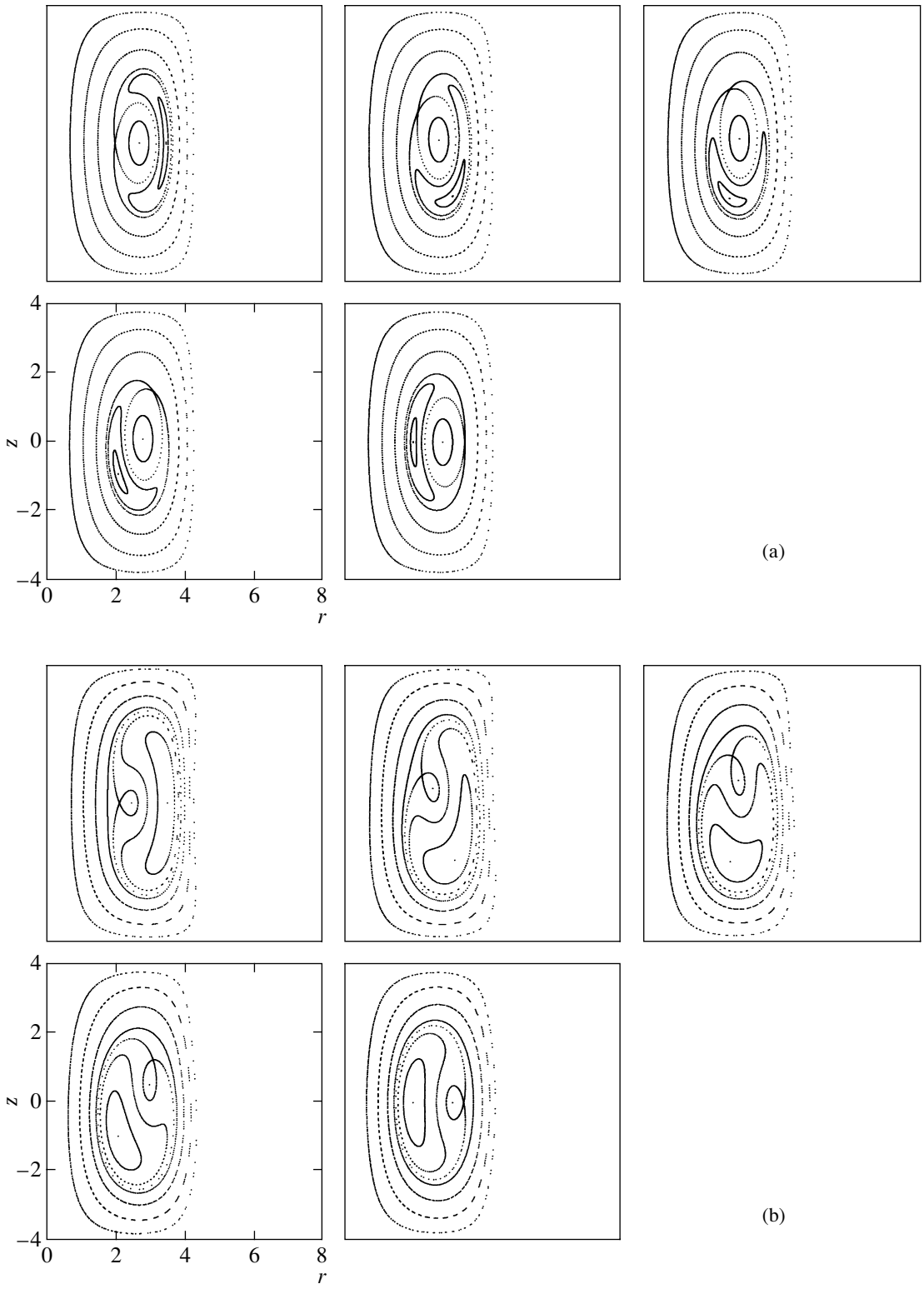

Fig. 5. Suppression of the main magnetic axis by a growing magnetic island $m/n = 1/1$: Poincaré maps for the 3D toroidal magnetic field $\mathbf{B} = \mathbf{B}_a^{(2)} + w_h\mathbf{B}_h$, generated by the superposition of an axisymmetric field (Fig. 3a) and a helical field corresponding to flux function (11) with the parameter values $\lambda = 0.95$, $n = 1$, and $k = -1$ for w_h = (a) 0.004, (b) 0.02, and (c) 0.04. Here and in the following figures, the toroidal cross sections $\phi = 0$, $\pi/4$, $\pi/2$, $3\pi/4$, and π are shown.

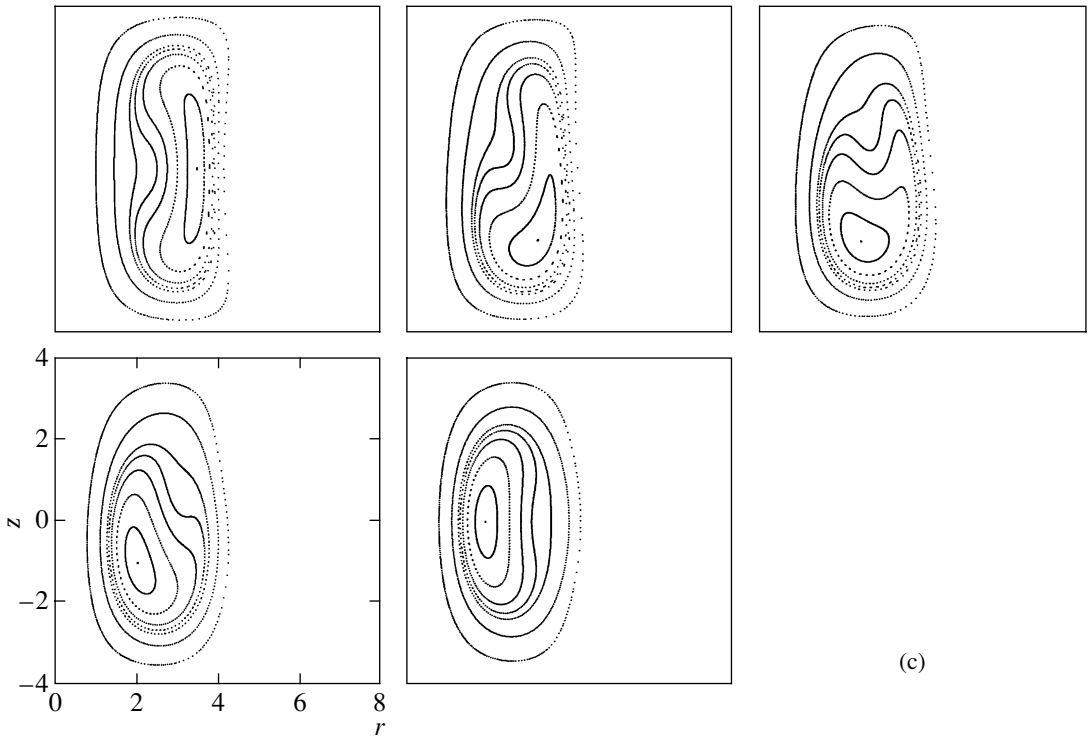

Fig. 5. (Contd.)

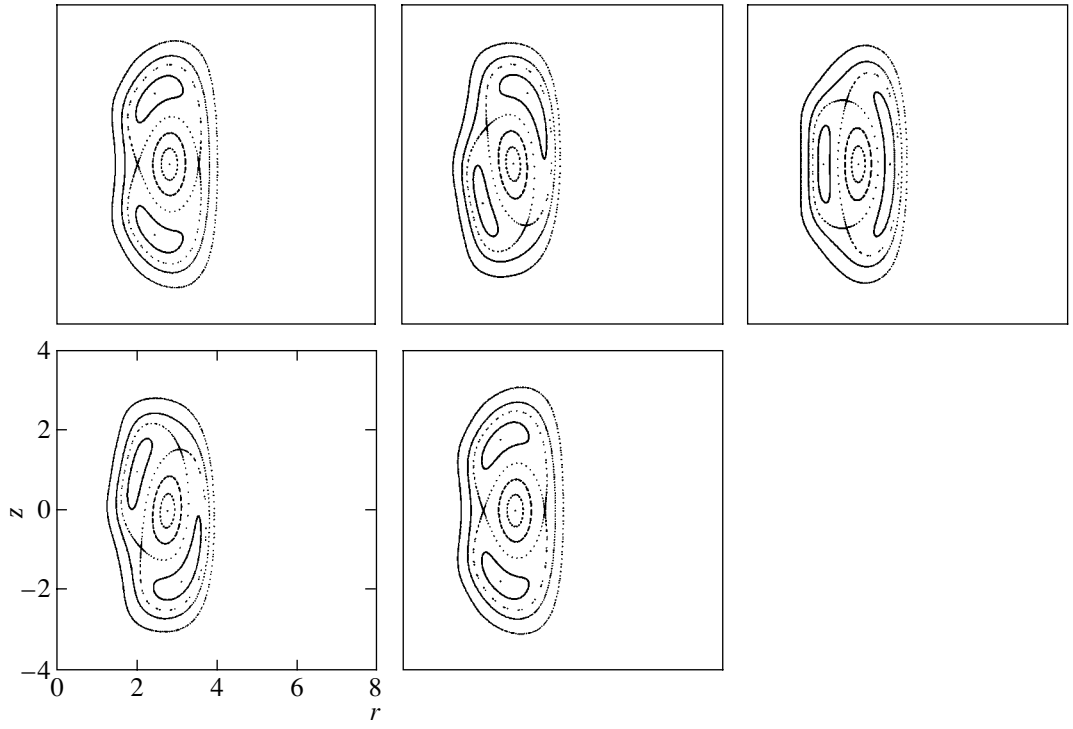

Fig. 6. Magnetic island $m/n = 2/2$: Poincaré maps for the 3D toroidal magnetic field $\mathbf{B} = \mathbf{B}_a^{(2)} + w_p\mathbf{B}_p$, generated by the superposition of an axisymmetric field (Fig. 3a) and a plane field corresponding to flux function (9) with the parameter values $\lambda = 0.95$ and $w_p = 0.02$.

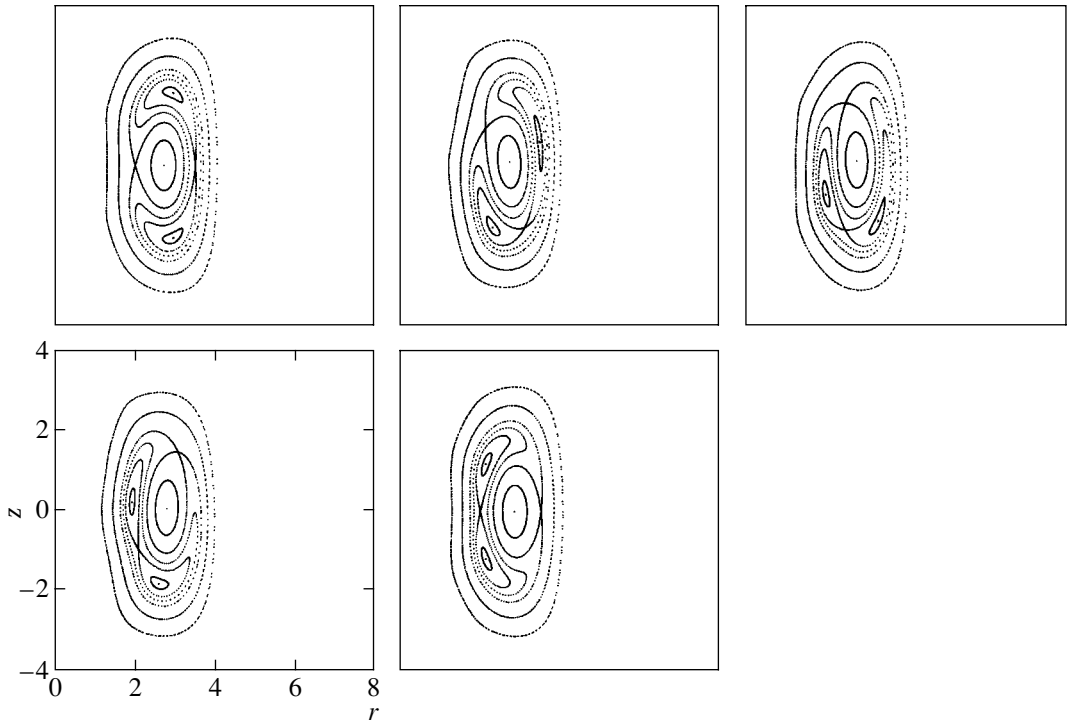

Fig. 7. Result of the interaction between two magnetic islands, $m/n = 1/1$ and $m/n = 2/2$: Poincaré maps for the 3D toroidal magnetic field $\mathbf{B} = \mathbf{B}_a^{(2)} + w_h\mathbf{B}_h + w_p\mathbf{B}_p$, generated by the superposition of an axisymmetric field (Fig. 3a), a helical field, and a plane field. The parameters of the additional fields are the same as in Figs. 5 and 6 with the weight coefficients $w_h = 0.004$ and $w_p = 0.01$.

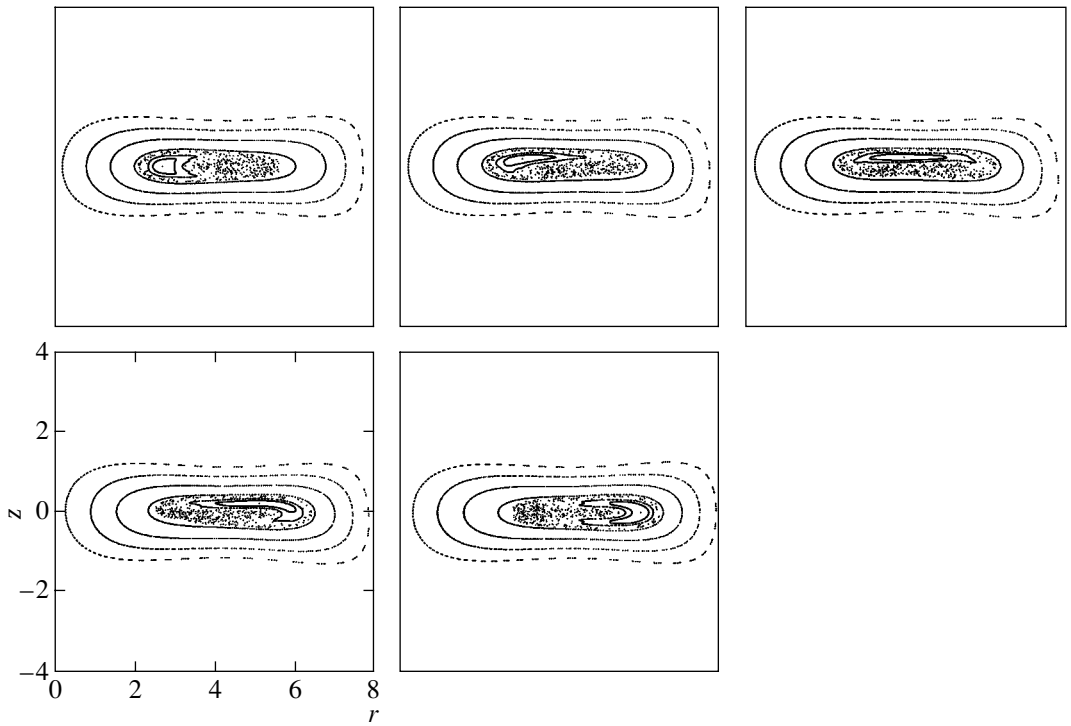

Fig. 8. Two regions with nested magnetic surfaces separated by a stochasticity zone: Poincaré maps of the 3D toroidal magnetic field $\mathbf{B} = w_1\mathbf{B}_a^{(1)} + w_2\mathbf{B}_a^{(2)} + w_h\mathbf{B}_h$ (with $w_1 = 1$, $w_2 = 0.1898$, and $w_h = 0.002$), generated by the superposition of two axisymmetric magnetic fields (Fig. 4b) and a helical one. The parameters of additional fields are the same as in Fig. 5.

wide range of different magnetic field topologies. They can be modeled and analyzed with relatively simple tools, which can help to understand the specific features of 3D MHD equilibrium configurations. They can also be used as a nontrivial test for equilibrium numerical codes.

ACKNOWLEDGMENTS

We are grateful to V.D. Shafranov and J. Nührenberg for discussions and valuable advice. This work was supported by the Centre de Recherches en Physique des Plasmas, Ecole Polytechnique Fédérale de Lausanne, and INTAS (grant no. 99-00592).

REFERENCES

1. R. Gruber, L. M. Degtyarev, W. A. Cooper, *et al.*, Fiz. Plazmy **22**, 204 (1996) [Plasma Phys. Rep. **22**, 186 (1996)].
2. R. Lüst and A. Schlüter, Z. Astrophys. **34**, 263 (1954).
3. S. Chandrasekhar, Proc. Natl. Acad. Sci. USA **42**, 1 (1956).
4. S. Chandrasekhar and P. C. Kendall, Astrophys. J. **126**, 457 (1957).
5. D. Lortz, W. Lotz, J. Nührenberg, *et al.*, Z. Naturforsch. A **36**, 144 (1981).
6. A. H. Reiman and H. S. Greenside, J. Comput. Phys. **87**, 349 (1990).
7. L. Degtyarev, A. Martynov, S. Medvedev, *et al.*, Comput. Phys. Commun. **103**, 10 (1997).
8. W. A. Cooper, R. Gruber, A. A. Martynov, *et al.*, in *Proceedings of the 26th EPS Conference on Controlled Fusion and Plasma Physics, Maastricht, 1999*, ECA, Vol. 23J, p. 869.

Translated by the authors

Plasma Physics Reports, Vol. 28, No. 4, 2002, pp. 268–273. Translated from Fizika Plazmy, Vol. 28, No. 4, 2002, pp. 300–306.

MAGNETIC CONFINEMENT SYSTEMS

Dynamics of Ion Heating in a Gas-Dynamic Trap during Neutral Beam Injection

A. A. Zuev, A. A. Ivanov, A. N. Karpushov, E. Yu. Kolesnikov, S. V. Murakhtin, and S. L. Strogalova

Budker Institute of Nuclear Physics, Siberian Division, Russian Academy of Sciences, pr. Akademika Lavrent'eva 11, Novosibirsk, 630090 Russia

Received October 15, 2001; in final form, November 8, 2001

Abstract—The dynamics of the ion temperature of the target plasma in a gas-dynamic trap during high-power neutral beam injection is measured by using the Rutherford scattering technique. A comparison of the experimental results with the results of simulations by a model based on the theory of pair Coulomb collisions indicates no significant anomalous losses from the ion plasma component.© *2002 MAIK "Nauka/Interperiodica".*

1. INTRODUCTION

The paper is devoted to investigating the dynamics of the ion and electron temperatures in a warm target plasma in a gas-dynamic trap (GDT) during high-power neutral beam injection (NBI).

The GDT device [1] (Fig. 1) is an axisymmetric magnetic mirror system with a mirror-to-mirror distance of 7 m and two end tanks (*2*, *5*) playing the role of MHD stabilizers. In one of these tanks, a plasma gun (*7*) designed for creating a relatively cold (T_e = 3–10 eV) and dense (up to 10^{14} cm^{-3}) plasma is installed. An NBI system consisting of six START injectors (*4*) is used to heat the target plasma and form the fast ion component. The injectors are divided into two groups and situated on the opposite sides of the central cell. The most important technical characteristics of the experimental setup and the plasma parameters are listed in Table 1.

Fast ions originated due to the trapping of the injected neutral beams are decelerated mainly in collisions with plasma electrons, thereby heating them to a temperature of about 100 eV. Then, the electron energy is transferred to the target plasma ions due to electron–ion collisions. Simultaneously, the plasma flows out of the trap through the end magnetic mirrors. The characteristic time of the longitudinal loss of the target plasma is determined by the ion and electron temperatures and changes significantly during the NBI pulse. Along with the longitudinal energy losses, there is a loss channel across the magnetic field. Under the GDT experimental conditions, the NBI duration is comparable to both the time of electron–ion energy exchange and the characteristic time of longitudinal energy losses. As a result, the electron temperature differs significantly from the ion temperature. A comparison of the theoretical predictions with the experimental results allows us to evaluate the possible contribution of instabilities to the target plasma heating and to correct the model of energy balance in the target plasma during the NBI pulse.

2. EXPERIMENTAL TECHNIQUE

2.1. The Choice of Experimental Conditions

The method used to determine the ion temperature is based on the injection of a monoenergetic beam of fast atoms and the subsequent measurement of the energy spectrum of the atoms scattered at a certain fixed angle.

It follows from the laws of energy and momentum conservation that the spectrum of the scattered atoms broadens and shifts with respect to the spectrum of the injected atoms. In elastic scattering, this shift is determined by the scattering angle and the mass ratio between injected atoms and plasma ions, as well as by the ion directed velocity, whereas the broadening is governed by the ion thermal motion [2, 3]. It was shown in [4] that, if the velocity of the injected atoms substantially exceeds the thermal velocity of the target plasma ions ($v_b \gg v_{T_i}$) and the scattering angle is sufficiently

Table 1. GDT parameters

Distance between the mirrors	7 m
Magnetic field in the midplane	Up to 0.22 T
Field in the mirrors	2.5–15 T
Injection energy	Up to 16 keV
Injection power	Up to 4.5 MW
NBI duration	≈1.2 ms
Injection angle	45°
Average fast ion energy	3–10 keV
Fast ion density	Up to 10^{13} cm^{-3}
Target plasma density	$(0.1–1.5) \times 10^{14}$ cm^{-3}

1063-780X/02/2804-0268$22.00

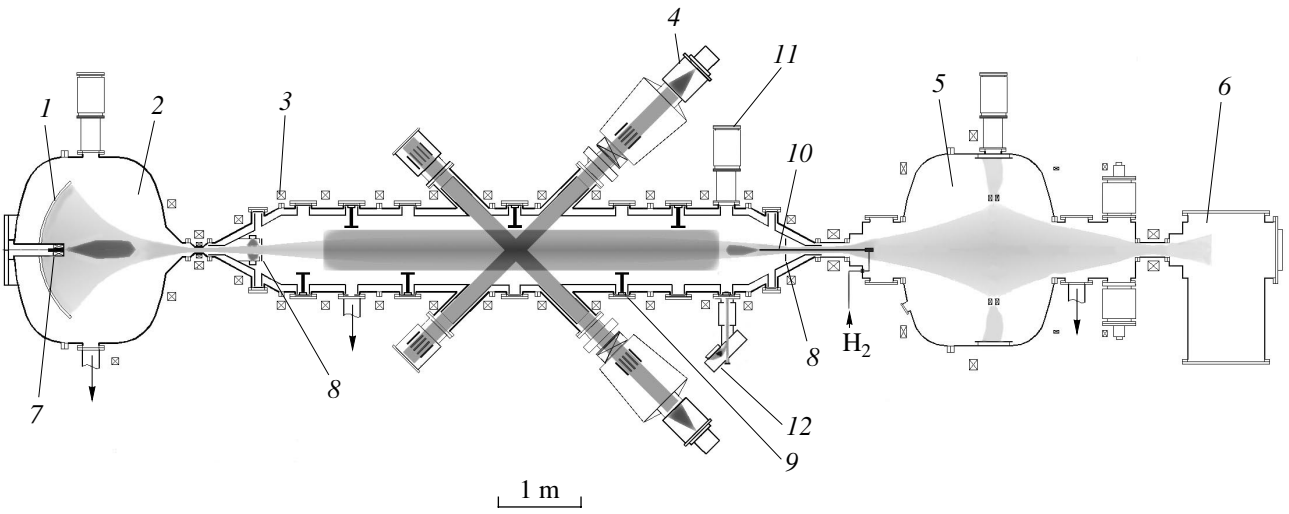

Fig. 1. Schematic of the GDT: (*1*) plasma receiver, (*2*) expander, (*3*) main magnetic coils, (*4*) START-3 atomic injector, (*5*) cusp, (*6*) end tank, (*7*) plasma gun, (*8*) limiters, (*9*) titanium evaporator, (*10*) facility for axial gas injection, (*11*) DINA-4 diagnostic injector, and (*12*) energy analyzer of scattered atoms.

small, the full width at half-maximum $\Delta E_b'$ of the energy spectrum of the scattered atoms is

$$\Delta E_b' = 4\vartheta\sqrt{E_b T_i \eta \ln 2}, \quad (1)$$

where E_b is the energy of the injected particle, T_i is the plasma ion temperature, $\eta = m_b/m_i$ is the incident-to-target particle mass ratio, and ϑ is the scattering angle in the laboratory frame. It is seen that $\Delta E_b'$ increases in proportion to the square root of T_i and is fairly high even at moderate temperatures. Under the GDT experimental conditions ($T_i \approx 50$ eV, the scattering angle $\vartheta = 5°$, and the injection energy of helium atoms $E_b = 9$ keV), the energy spectrum of width $\Delta E_b'$ should be ≈160 eV. The average energy of the scattered particles E_b' is lower than the injection energy E_b and depends on the scattering angle ϑ as

$$E_b' = E_b(1 - \eta \sin^2 \vartheta). \quad (2)$$

When choosing the scattering angle and the species and energy of the probing atoms, the following circumstances were taken into account:

(i) The scattering differential cross section increases with increasing charge number Z_b and decreasing injection energy and scattering angle (Fig. 2) as

$$\sigma(E_b, \vartheta) = \left(\frac{Z_b Z_i e^2}{E_b}\right)^2 \frac{(1+\eta)^2}{\sin^4\left(\frac{\chi}{2}\right)}, \quad (3)$$

where χ is the scattering angle in the center-of-mass frame. The scattering angles in the laboratory and the center-of-mass frames are related by $\chi = \vartheta + \arcsin(\eta \sin\vartheta)$.

(ii) The flux density of the injected particles increases with increasing injection energy ($j \sim E^{3/2}$) and decreasing particle mass.

(iii) The recording efficiency of scattered atoms sharply decreases when the injection energy falls below 1–2 keV and varies slightly in the energy range above 5–10 keV.

(iv) In the stripping chamber of the energy analyzer, the efficiency of ionization of hydrogen atoms is several times higher than that of helium atoms.

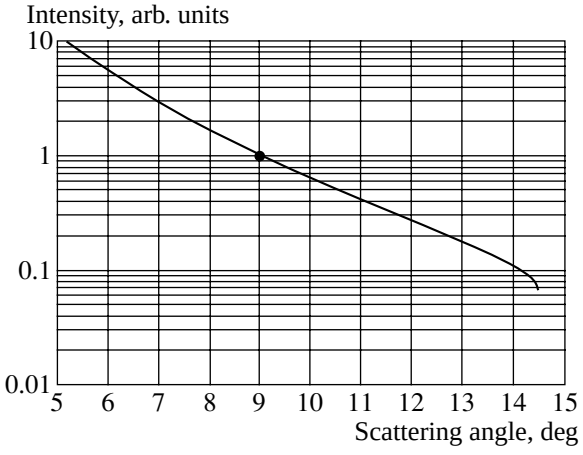

Fig. 2. Flux density of helium atoms scattered by a cold hydrogen target vs. observation angle in the laboratory frame.

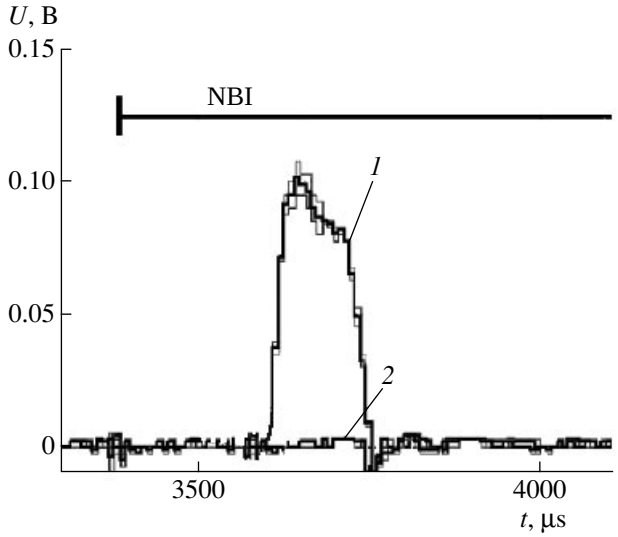

Fig. 3. Time evolution of the total flux of scattered helium atoms toward the energy analyzer: (*1*) scattered helium atoms and (*2*) background (charge-exchange neutrals and photons).

(v) At injection energies lower than 8 keV, the processes of elastic and inelastic scattering of the beam particles in the stripping chamber of the energy analyzer become of importance.

Under the GDT experimental conditions, a helium atomic beam is preferable for measuring the ion temperature of the target plasma by the Rutherford scattering technique. The minimum energy of the probing atoms is limited by a value of 8–9 keV, mainly because of the reduction in the attainable beam current density and a possible decrease in the useful signal due to the processes of elastic and inelastic scattering in the stripping chamber of the energy analyzer and the charge-exchange chamber of the diagnostic injector. On the other hand, the increase in the helium atom energy to higher than 10 keV seems to be inexpedient because of the decrease in the scattering cross section and the more rigid requirements for the angular divergence of the injected beam [see inequality (7)].

The presence of a significant flux of charge-exchange atoms emitted from the plasma is characteristic of the GDT experiments. These atoms are produced in the interaction of fast ions with the residual gas. Estimates show that, in the central cell, the flux of charge-exchange atoms can exceed the flux of scattered atoms by several orders of magnitude. To minimize the flux of charge-exchange atoms, the diagnostic complex was placed behind the fast-ion stopping point, in the region where the mirror ratio was $R = 3$, which made it possible to increase the signal-to-noise ratio by almost two orders of magnitude. A typical time behavior of the total current of the scattered atoms is shown in Fig. 3.

Since the flux density of scattered atoms is relatively low, the fluctuations of the recorded signal play an important role. To attain the required accuracy of the measurements of the target plasma ion temperature (±10%), the results were averaged over a series of shots with the same parameters.

The acceptable divergence of the injected beam and the acceptable spread in the atom energies can be found from the following requirement: the instrumental line width measured in experiments with a cold gas (e.g., hydrogen at room temperature) must be less than the expected experimental thermal broadening $\Delta E_b'$. It follows from formula (2) that the contribution of $\Delta_E E_b'$ to the instrumental line width is determined by the expression

$$\Delta_E E_b' \approx \frac{dE_b'}{dE_b}\Delta E_b = \Delta E_b, \tag{4}$$

whereas the contribution related to the angular spread is

$$\Delta_\vartheta E_b' \approx \frac{dE_b'}{d\vartheta}\Delta\vartheta = 2\eta E_b \vartheta \Delta\vartheta. \tag{5}$$

Comparing these expressions with the temperature broadening (1), we obtain

$$\Delta E_b < 4\vartheta\sqrt{\eta E_b T_i}; \tag{6}$$

$$\Delta\vartheta < 2\sqrt{\frac{T_i}{E_b\eta}}. \tag{7}$$

Thus, to measure the ion temperature starting from 20 eV with the use of a beam of helium atoms with an energy of 9 keV at a scattering angle of 5°, it is necessary that $\Delta E_b < 150$ eV and $\Delta\vartheta < 2°$. Thus, the requirements for the energy and angular spreads of the injected beam are not too stringent. It must however be taken into account that the maximum angular spread also depends on the angle specified by the collimation system of the energy analyzer (Fig. 4). To provide a sufficient flux of scattered atoms into the analyzer, this angle should not be too small (a value of 1°–1.5° can be considered a compromise).

2.2. Experimental Setup

An electrostatic energy analyzer and a DINA-4 diagnostic injector were used to measure the ion temperature. The electron temperature and the target plasma density in the GDT were measured by the Thomson scattering technique.

A schematic of the experiment on fast atom scattering is shown in Fig. 4. The DINA-4 diagnostic injector *1* was installed at the side flange of the GDT facility, in the region where the mirror ratio was $R = 3$. The energy and equivalent current density (on the facility axis) of the helium atomic beam were 9 keV and 25 mA/cm^2, respectively. The beam diameter was 5 cm, the total equivalent beam current was 1.5–2 A, the beam angular divergence was ±1° in the drawing plane and ±1.5° in

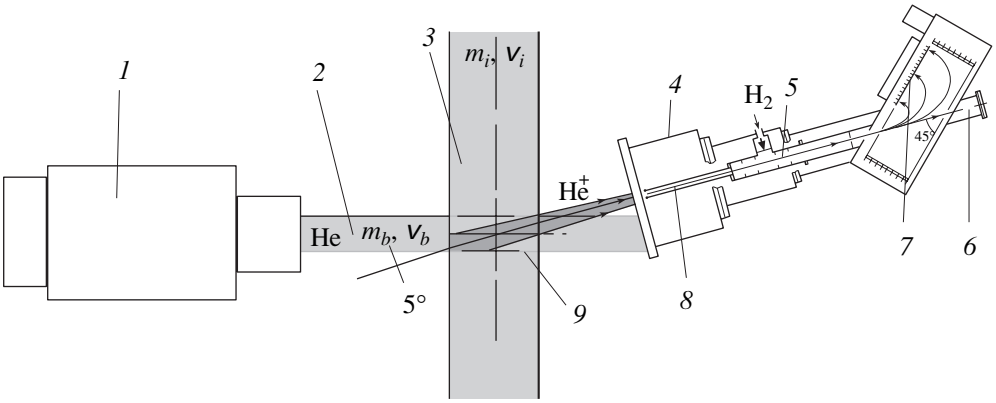

Fig. 4. Schematic of the diagnostic facility for measuring the ion temperature of the target plasma: (*1*) DINA-4 diagnostic injector, (*2*) helium atomic beam, (*3*) target plasma, (*4*) energy analyzer of scattered atoms, (*5*) stripping chamber, (*6*) system for trapping the light emitted from the plasma, (*7*) microchannel plate and receiving collectors of the 12-channel dc amplifier, (*8*) collimation system, and (*9*) volume under investigation.

the perpendicular direction, and the duration of the injection pulse was 150 μs. The beam passing through the target plasma was recorded with secondary emission detectors. A 45° electrostatic analyzer of neutral particles *4* equipped with a stripping gas target was used to detect and analyze the scattered atoms. The use of a detector based on a microchannel plate made it possible to reliably record the shape of the relatively narrow spectrum of scattered particles. A provision was made for the preliminary deceleration of the detected ions in the analyzer, which allowed us to greatly enhance the energy resolution. The resolution of the 12-channel analyzer was $\Delta E/E_b \approx 0.5\%$. The energy range (i.e., the ratio between the maximum and minimum energies measured simultaneously) attained $E_{max}/E_{min} \approx 2.5$. To increase the measurement accuracy, the analyzer was calibrated by measuring the relative sensitivity of the analyzer channels with the help of a low-current ion source.

The recording efficiency of the scattered atoms depends on the stripping efficiency in the analyzer gas target. To enhance the analyzer sensitivity, we used pulsed gas puffing into the stripping chamber *5* of the analyzer up to the pressure that enabled the maximum efficiency of ionization of the scattered atoms. To detect helium atoms, hydrogen puffing into the target proved to be the most efficient. The main technical characteristics of the diagnostic beam and the analyzer are listed in Table 2.

3. EXPERIMENTAL RESULTS AND NUMERICAL SIMULATIONS

The measured energy spectra of the scattered particles are shown in Fig. 5. Test experiments with scattering by argon (*1*), when both elastic and inelastic energy losses are negligible, made it possible to determine the initial energy and energy spectrum of the probing particles without changing the geometry of the experiment. The measurements of the spectrum of the atoms scattered by a cold plasma (*3*) allowed us to evaluate the minimum ion temperature that can be measured with the help of our diagnostic system. The broadening of the energy spectrum of the scattered atoms in a hot plasma (*2*) enables the determination of the ion temperature.

3.1. Brief Description of the Numerical Code

To determine the ion temperature, the spectra of the scattered atoms for different ion temperatures were calculated using the Rutherford Scattering Code (RSC) based on the Monte Carlo method. The results obtained were statistically averaged and compared with the measured energy spectrum of the atoms scattered in the

Table 2. Parameters of the diagnostic beam and analyzer

Injected particles	He
Helium atom energy	9 keV
Scattering angle	5°
Equivalent injection current	1.5–2 A
Current density (on the facility axis)	25 mA/cm^2
Injection duration	150 μs
Beam angular divergence:	
in the scattering plane	±1°
in the perpendicular plane	±1.5°
Spread in the beam atom energy	≈100 eV
Spatial resolution	$5 \times 5 \times 10$ cm^3
Number of recording channels	12
Energy resolution	≈0.5%
Temperature resolution	≈10 eV

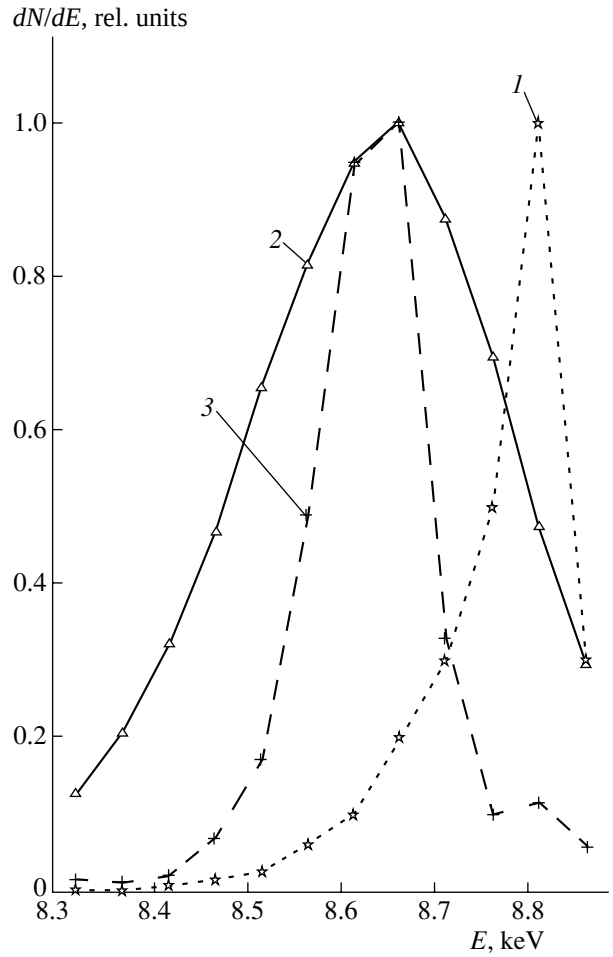

Fig. 5. Energy spectra of the scattered helium atoms for an injected particle energy of 8.8 keV: scattering (*1*) by argon (T = 0 eV), (*2*) hydrogen plasma with T_i = 66 eV, and (*3*) hydrogen plasma with T_i = 6 eV.

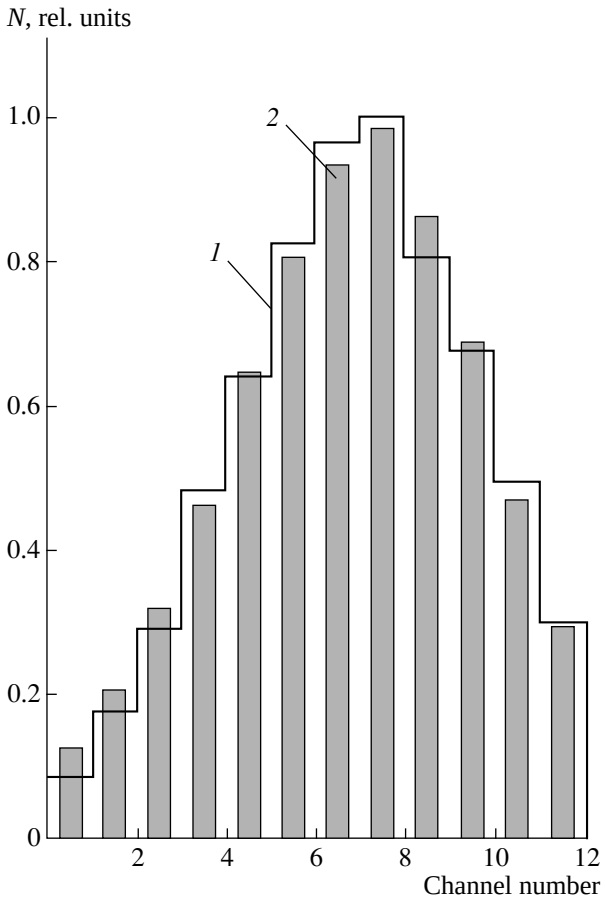

Fig. 6. Measured and computed distribution functions of the scattered atoms: (*1*) experiment and (*2*) calculations by Monte Carlo RSC code for T_i = 66 eV.

plasma. The initial data for calculating the ion temperature of the target plasma incorporate

(i) the energy spread and the angular divergence of the injected atomic beam,

(ii) the energy of the injected helium atoms,

(iii) the potentials of the capacitor plates in the energy analyzer (Fig. 4),

(iv) the radial profile of the plasma density, and

(v) the data on the actual geometry of the experiment.

The injection energy and the potentials at the capacitor plates were measured in the main shots. The data on the energy distribution function of the injected atoms were obtained by analyzing the spectra of the helium atoms scattered by argon. The beam angular divergence was estimated from the profile measured with a set of secondary emission detectors.

Figure 6 presents the energy spectrum of the scattered helium atoms calculated by the RSC code (*2*) for a scattering angle of 5° and an ion temperature of the target plasma of 66 eV. For comparison, the figure also presents the measured energy spectrum of the scattered helium atoms (*1*).

A model describing the heating of the target plasma in the GDT during NBI incorporates the following processes: the trapping of the neutral beams and the formation of the fast ion group, the loss of fast ions because of charge exchange with the residual gas and the neutral beams, the scattering by the plasma ions, the deceleration of the fast ions by the plasma electrons and the heating of the target plasma, the longitudinal confinement of the particles and energy, and transverse losses from the plasma. The Fast Integrated Transport Code (FITC) [5] was used to describe the target plasma heating and approximately calculate the fast ion parameters. In the calculations, the radial profiles of the target plasma density and the electron temperature measured by the Thomson scattering technique were used as the initial data. The electron temperature and density at the plasma periphery were measured with a triple probe.

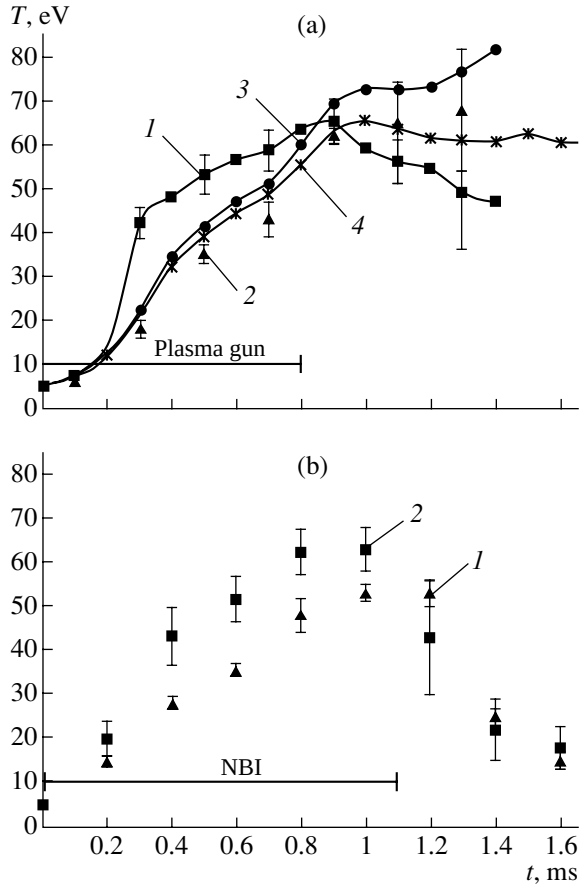

Fig. 7. Dynamics of the ion and electron temperatures during NBI (the instant $t = 0$ corresponds to the beginning of NBI) for two regimes (a) with the plasma gun: (*1*) T_e on the axis (measurements), (*2*) $\langle T_i \rangle$ (measurements), (*3*) T_i on the axis (calculations), and (*4*) $\langle T_i \rangle$ (calculations) and (b) with axial gas injection: (*1*) $\langle T_i \rangle$ (measurements) and (*2*) T_e on the axis (measurements).

3.2. Ion Temperature Measurements

Figure 7 shows the dynamics of the ion temperature of the target plasma measured by the Rutherford scattering technique for two characteristic GDT regimes.

Figure 7a presents the temperature behavior for the regime in which the plasma density in the GDT was sustained with the help of a plasma gun (Fig. 1, position *7*). In this regime, the plasma gun was switched off a short time before the end of the NBI pulse. The figure also shows the results of numerical simulations of the ion temperature relaxation with allowance for only collisional mechanism for the energy exchange between the electrons and ions of the target plasma and the energy losses along the magnetic field lines through the magnetic mirrors. In the simulations, the profiles of the density and electron temperature of the target plasma measured by the Thomson scattering technique were used. It is seen that, within the measurement error, the experimental data are in fair agreement with the results of numerical simulations. The ion temperature becomes noticeably higher than the electron temperature 900 μs after the beginning of NBI, which can also be seen in the calculated curves *3* and *4*. This is related to the high electron longitudinal thermal conductivity and the significant particle flux in phase space from the "decelerated" group of fast ions toward the target plasma. The decrease in the accuracy of ion temperature measurements at the end of the NBI pulse is related to the decrease in the target plasma density to $(1.5–4) \times 10^{13}$ cm^{-3}.

Figure 7b presents the temperature behavior for the regime in which the plasma density in the GDT during the operation of the heating injectors (Fig. 1, position *4*) was sustained by the paraxial injection of molecular hydrogen [6] (Fig. 1, position *10*). In this case, the gun produced an initial target plasma required to trap the atomic beams and was switched off a short time before the beginning of the NBI pulse. The target plasma density gradually increased during the NBI pulse to $(1.5–4) \times 10^{14}$ cm^{-3}. At such a high density, the electron and ion temperature were equalized ≈200 μs after switching off the heating injectors. This time is close to the calculated characteristic time of the energy exchange between the electrons and ions under the given experimental conditions.

4. CONCLUSION

The experimental data obtained make it possible to refine the model of the plasma energy balance during pulsed NBI. The data also indicate no significant anomalous energy losses from the ion plasma component in the GDT operation regimes studied.

REFERENCES

1. V. V. Mirnov, V. P. Nagornyĭ, and D. D. Ryutov, Preprint No. 84-40 (Institute of Nuclear Physics, Siberian Division, USSR Acad. Sci., Novosibirsk, 1984).
2. E. L. Berezovskiĭ, A. I. Kislyakov, S. Ya. Petrov, and G. V. Roslyakov, Fiz. Plazmy **6**, 1385 (1980) [Sov. J. Plasma Phys. **6**, 760 (1980)].
3. A. Russek, Phys. Rev. **120**, 1536 (1960).
4. V. G. Abramov, V. V. Afrosimov, I. P. Gladkovskiĭ, *et al.*, Zh. Tekh. Fiz. **41**, 1924 (1971) [Sov. Phys. Tech. Phys. **16**, 1520 (1972)].
5. A. V. Anikeev, A. N. Karpushov, K. Noak, and S. L. Strogalova, Preprint No. 2000-4 (Budker Institute of Nuclear Physics, Siberian Division, Russian Academy of Sciences, Novosibirsk, 2000).
6. P. A. Bagryansky, A. A. Lizunov, V. V. Maximov, *et al.*, in *Proceedings of 27th EPS Conference on Controlled Fusion and Plasma Physics, Budapest, 2000*, ECA, Vol. 24B, p. 318.

Translated by N. Ustinovskiĭ

Plasma Physics Reports, Vol. 28, No. 4, 2002, pp. 274–285. Translated from Fizika Plazmy, Vol. 28, No. 4, 2002, pp. 307–318.

PLASMA DIAGNOSTICS

Diagnostics of Plasma Oscillations by the Field of Surface Waves Guided by a Dielectric Waveguide

G. A. Markov* and I. V. Khazanov**

**Lobachevsky State University, Nizhni Novgorod, Russia*

***Institute of Applied Physics, Russian Academy of Sciences, ul. Ul'yanova 46, Nizhni Novgorod, 603600 Russia*

Received June 2, 2000; in final form, September 11, 2001

Abstract—The potentialities of the diagnostic method for determining the plasma parameters by recording the surface waves guided by a dielectric waveguide and scattered by plasma oscillations are discussed. The use of surface (slowed) waves makes it possible to improve both the sensitivity and spatial resolution of measurements. The scattering is the most intense near the waveguide cutoff, at which the dependence of the wave propagation constant on the plasma density is the steepest. It is shown experimentally that the method proposed makes it possible to determine the discharge plasma density and electron energy and to estimate the amplitude of the RF field of the plasma waves forming the discharge and the amplitude of plasma density oscillations in these waves. The data obtained from the measurements of the amplitudes of both high- and low-frequency plasma density oscillations by the proposed method agree satisfactorily with theoretical predictions. The experimental data on the plasma density are confirmed by other diagnostic measurements. The ways of reducing measurement errors are proposed. © *2002 MAIK "Nauka/Interperiodica".*

1. INTRODUCTION

It is well known (see, e.g., [1]) that wave diagnostics of plasmas with a comparatively low density in various medium-size devices encounter serious difficulties. This is true of both interferometric methods and the methods based on wave scattering by a plasma. Conventional interferometry requires that the following two main conditions be satisfied: first, the plasma should significantly affect the phase of the wave propagating through it (in order for the phase change to be recorded) and, second, the wavelength of the sounding wave should be smaller than the plasma size (in order for the geometrical-optics approximation to be applicable). It is easy to see that, for a finite-size low-density plasma, these two conditions are mutually contradictory. However, this contradiction can be resolved by slowing the wave in the plasma in one way or another, thereby shortening its wavelength and, accordingly, increasing the phase change. For this purpose, Katin and Markov [2] proposed to place thin dielectric plates in the plasma and to use the surface waves guided by them. Such plates may serve as a diagnostic tool for determining the phase change of the waves in plasmas; however, the field of applicability of this method is wider. Thus, in [2], it was proposed to determine the plasma density by using the plates as low-Q resonators for surface waves. The aim of this paper is to consider the ways of improving the accuracy of the measurements of the plasma density, taking into account the fact that the amplitude of the surface wave excited by a dipole antenna depends on the extent to which the wave is slowed.

One of the main difficulties of implementing the scattering diagnostic method in a low-density plasma is that the scattering effect is small. In [3, 4], it was proposed to enhance this effect by observing the scattering of the sounding wave in the vicinity of the hybrid resonance, where the wave field and wave vector both increase considerably.[1] Since the scattering occurs in a narrow resonance layer, the scale of the plasma oscillations by which the sounding waves are scattered is fairly short. Here, we consider another possible way of enhancing the scattering. Specifically, we propose to use not only the above method for slowing the sounding and scattered waves but also the fact that the propagation constant of the surface wave depends strongly on the plasma density near the cutoff of a dielectric waveguide (plate).[2] We tested the proposed method experimentally and obtained preliminary estimates for the plasma wave amplitudes, which are significantly above the thermal level, and for the oscillation amplitudes of the plasma density in such waves. The measurements were carried out in a device for studying the ionization self-channeling of fine-scale whistlers (oblique plasma waves in the frequency range between the electron and ion gyrofrequencies, $\omega_{Hi} < \omega < \omega_{He}$) by exciting specific RF discharges in the form of spatially localized plasma-waveguide channels [6]. The data

[1] It is also assumed that, during the scattering, the wave frequency changes only slightly (e.g., by an amount equal to the ion acoustic frequency), so that, in the scattering region, the hybrid resonance condition is also satisfied for the scattered wave. On the other hand, a strong increase in the wave field in this region can, in particular, give rise to additional plasma ionization (see, e.g., [5]).

[2] This fact actually indicates a stronger nonlinearity in this range of the plasma and plate parameters.

1063-780X/02/2804-0274$22.00 © 2002 MAIK "Nauka/Interperiodica"

obtained by applying this diagnostic method to measure the amplitudes of both high-frequency (at the frequency ω of the discharge-forming field) and low-frequency plasma density oscillations are compared with theoretical predictions. In the Appendix, the question is discussed of how to reduce the measurement errors in determining these parameters. The electron energy in the discharge is calculated from the measured data on low-frequency plasma density oscillations.

We also propose another, fairly exact, diagnostic method for determining the plasma density in such discharges in a magnetic field. This method is related to the condition for wave propagation in the channel, which implies that the wave frequency should be lower than the critical frequency corresponding to the maximum plasma density in the channel.

2. EXPERIMENTAL CONDITIONS AND MEASUREMENT RESULTS

The experiments were carried out with a glass discharge chamber 200 mm in diameter and 1800 mm in length in the presence of a longitudinal magnetic field $\mathbf{B}_0$. The discharge was excited in air at pressures in the range $p \le 10^{-3}$ torr by a symmetric dipole antenna consisting of three coaxial rings 60 mm in diameter located at the axis of the chamber near its end at a distance of 30 mm from each other. The end rings were connected to the outer conductor of the supply cable, and the central ring was connected to the inner conductor of the cable. The total length of the antenna for exciting plasma waves was l_u = 6 cm. An RF voltage (f = 200 MHz and U_0 = 50 V) was supplied to the antenna from a GST-2 oscillator. The plasma column formed as a result of the ionization self-channeling of plasma waves in the magnetic field $\mathbf{B}_0$ [6] originated from the dipole antenna and was stretched out over the entire length of the discharge chamber. A 160×160-mm diagnostic plate made of fiberglass plastic with the permittivity $\varepsilon = 4$ (the dielectric dissipation factor being $\tan\chi = 10^{-2}$) and thickness $2\delta = 2$ mm was placed in the longitudinal cross section of the plasma column in a position symmetric with respect to the column axis at a distance of 300 mm from the RF antenna. The diagnostic signal (f_D = 920 MHz) from a G4-160 oscillator propagated in the direction perpendicular to $\mathbf{B}_0$, along the dielectric waveguide and was fed to the input of an S4-27 spectrum analyzer. In a thin dielectric waveguide, the first (lowest order) even TM mode was excited by a T-shaped junction from the coaxial supply cable [2]. At the opposite end of the plate, a similar junction was used to record the signal, whose intensity was proportional to the wave field amplitude at this point. It should be noted that the intensity E_D^2 of the sounding signal that has passed through the dielectric waveguide increases by 25–30 dB after switching on the discharge and is maximum near the waveguide cut-off [2] at $B_0 \sim 330$ G, $p \le 10^{-3}$ torr, and $N_e \sim 3 \times 10^9$ cm^{-3}. We also point out a substantial spectral broadening of the signal transmitted through the plasma column of the discharge.

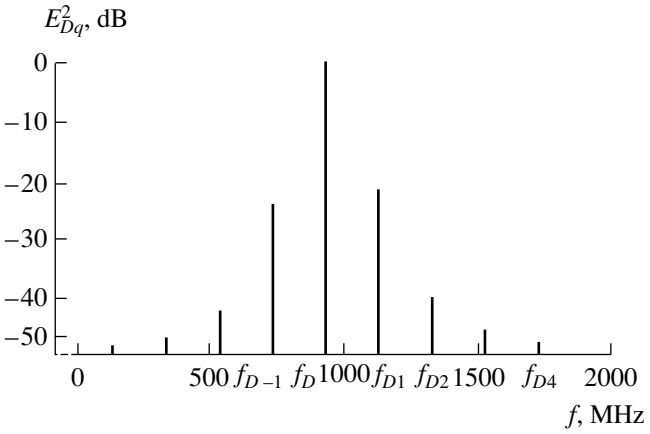

Fig. 1. Spectral content and relative intensities ($\sim E_{Dq}^2$) of the wave fields of a diagnostic signal scattered in the discharge by plasma density oscillations at the frequencies of the pump field (f = 200 MHz) and its satellites (qf) for $p = 10^{-3}$ torr, B_0 = 330 G, and U_0 = 50 V, the sounding frequency being f_D = 920 MHz. The nonlinear decibel scale on the vertical axis at high decibel levels is associated with the nonlinearity of the measurement channel of a C4-27 analyzer.

In Fig. 1, the squared amplitude of the wave fields of the sounding signal scattered by the plasma is plotted on the vertical axis on a logarithmic scale, and the frequency (in MHz) is plotted on the horizontal axis. In Fig. 1, we can see not only the signal at the sounding frequency f_D but also four modulation peaks, which provide evidence for the existence of plasma oscillations at the pump frequency (f = 200 MHz) and at its harmonics with frequencies $2f$, $3f$, and $4f$. It was found that these harmonics, as well as the main signal, are generated by the GST-2 oscillator itself and that their fields increase significantly in the presence of a plasma due to both their trapping in the produced plasma waveguide channel and the enhanced coupling of the antenna to the plasma under the actual discharge conditions. Figure 2 shows how the normalized (to the amplitude of the main signal at the frequency $\omega = 2\pi f$) amplitudes $E_{q\omega}$ of the harmonics observed during the discharge depend on the strength of the external magnetic field. The harmonics were measured by the above-described method in the absence of the diagnostic signal. It is seen that the curves showing the amplitudes of the first and second harmonics are generally similar in shape. The observed discrepancies are probably associated with different degrees of the antenna–plasma coupling at different frequencies. As the wave frequency increases and approaches the critical frequency above which the wave cannot propagate in the channel, this

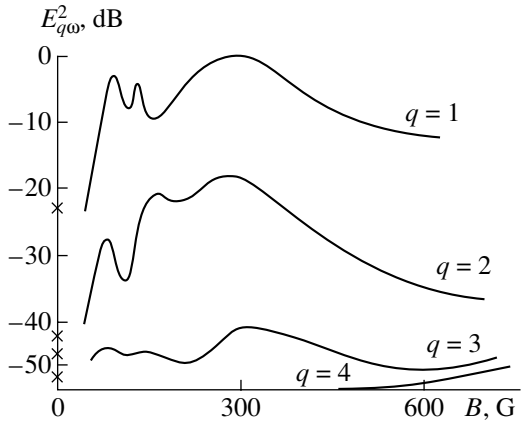

Fig. 2. Relative values of the squared amplitudes of the plasma density oscillations ($E^2_{q\omega}$) at the pump frequency and its satellites vs. the external magnetic field B_0 for $p = 10^{-3}$ torr and $U_0 = 50$ V.

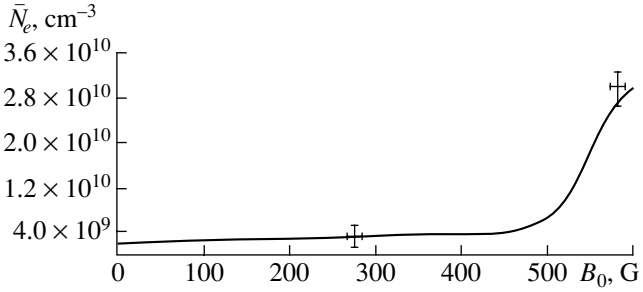

Fig. 3. Plasma density $\bar{N}_e$ (averaged over the cross section of the plasma column) vs. the external magnetic field B_0 at the distance $z = 400$ mm from the RF antenna for $p = 10^{-3}$ torr and $U_0 = 50$ V.

coupling reduces, as expected. On the other hand, according to our estimates, the amplitude of, e.g., the second harmonic of the pump wave, which is generated due to the nonlinear effects in a plasma, is about $E_{2\omega} \leq \frac{n_\omega}{N_e} E_\omega$ (where n_ω is the amplitude of the electron density oscillations in the wave and N_e is an unperturbed plasma density), which is insufficient to fit the experiment. According to Fig. 2, the harmonics are the most intense at about $B_0 \sim 300$ G; the amplitude of the second harmonic is about one order of magnitude smaller than the amplitude of the first harmonic; the amplitude of the third harmonic is about one order of magnitude smaller than the amplitude of the second harmonic; and, for the magnetic fields in the range $72 < B_0 < 450$ G, the amplitude of the fourth harmonic is two orders of magnitude smaller than the amplitude of the third harmonic. For $B_0 \leq 72$ G ($\omega_{He} \leq \omega$), the discharge structure changes: the discharge resembles a diffuse ellipsoid rather than a plasma waveguide channel localized at the chamber axis. At $B_0 \leq 50$ G and $p \leq 10^{-3}$ torr, the discharge comes to an end because the amplitude of the RF field produced by our pump oscillator is insufficient to maintain the discharge, in which case the relative amplitudes of the harmonics change substantially. In Fig. 2, these relative amplitudes are indicated by the asterisks at the vertical axis. The data in Fig. 2 imply that, in contrast to the first three harmonics, the fourth harmonic is not guided by the plasma column of the discharge at $B_0 < 450$ G. This indicates that the plasma density in the column is below the critical density for the frequency $4f = 800$ MHz because, for $B_0 \geq 300$ G, we have $\omega_{He} > 4\omega = 2\pi \times 4f$, so that, at $N_e > N_{e\,\mathrm{cr}}(4f)$, fine-scale plasma waves at the frequency of the fourth harmonic can propagate in the plasma column [7]. Figure 3 shows the measured dependence of the plasma density N_e averaged over the cross section of the plasma column on the external magnetic field B_0 under the same discharge conditions [2]. On the other hand, the probe measurements show that the plasma density distribution along the dielectric waveguide is fairly well described by a power law $N_e(x) \approx N_0/[1 + (x/d)^3]$, where the scale $d = 2.7$ cm is approximately equal to the radius of the bright discharge region in the chamber. This power law yields the following relationship between the averaged and maximum plasma densities:

$$\bar{N}_e = \frac{2}{L}\int_0^{L/2} \frac{N_0 dx}{1 + (x/d)^3} \approx 0.5 N_0, \qquad (1)$$

where $L = 14$ cm is the length of the dielectric waveguide (the distance between T-shaped junctions).

Based on both relationship (1) between $\bar{N}_e$ and N_0 and the data from Fig. 3, we can explain the sharp growth of the fourth harmonic in the range $B_0 > 450$ G in Fig. 2 as being due to the fact that, as the magnetic field in this range increases, the central plasma region in which the plasma density is above the critical density progressively expands, so that the antenna is increasingly well coupled to the plasma column at the frequency of the fourth harmonic. The averaged plasma density $\bar{N}_e \sim N_0/2 \sim 4 \times 10^9$ cm^{-3} at the critical point ($B_0 \sim 450$ G), at which the wave at this frequency can still propagate in the channel, corresponds to the density determined by the curve $\bar{N}_e(B_0)$ in Fig. 3. In the range $B_0 \geq 600$ G, in which the averaged density $\bar{N}_e$ is a factor of 3 higher than the critical density for the fourth harmonic, the amplitude of the fourth harmonic is only several times smaller than the amplitude of the third harmonic. Note that the signals scattered at the harmonics of the pump wave were the most intense at $B_0 \sim 300$ G, and the spectral widths of these signals

were determined by the line widths of the corresponding harmonics. The relationship between the amplitudes of the transmitted diagnostic signal and its satellites, which are generated as a result of the scattering of the sounding wave by plasma density oscillations, depends on the magnitude B_0 of the external magnetic field. As an example, Fig. 4 shows the field amplitudes of both the main diagnostic signal at the frequency f_D = 920 MHz (upper curve) and its first satellite at the frequency f_{D1} = 1120 MHz (lower curve) as functions of B_0. It is important that the observed amplitudes vary in antiphase over the entire range of B_0 values, except for the subrange ΔB_0 from 290 to 340 G. Calculations of the dispersion curves [2] show that, in the range ΔB_0 = 290–340 G, the slowing-down factor of the sounding wave is maximum and even a slight change in B_0 produces a substantial change in the transmission coefficient for the signal. Because of the spatial magnetic-field variations, the fine structure of the maxima and minima in the transmitted signals $E_D(B_0)$ and $E_{D1}(B_0)$ in the range ΔB_0 is smoothed into a broad peak. For this reason, under our experimental conditions, it is impossible to establish whether or not the changes in $E_D(B_0)$ and $E_{D1}(B_0)$ correlate in the range of B_0 values from 290 to 340 G.

The spectral lines of the scattered signals are rather complicated in shape. As an example, we show in Fig. 5 the spectral line of the signal scattered by the plasma at the frequency f_D for B_0 = 330 G and $p = 10^{-3}$ torr. The curve is seen to have modulation peaks separated by frequency intervals $\Delta f_D \approx 10^5$ Hz. The amplitude of the peaks decreases sharply as the external magnetic field either decreases or increases from the value B_0 = 330 G. Under the same discharge conditions, analogous peaks (but less pronounced and of smaller amplitude) were observed in the spectral line of the pump signal scattered by the plasma at the frequency f. These experimental findings provide evidence for the existence of oscillations of the discharge plasma density at low frequencies $f_S \sim 10^5$ Hz. The scattering of both the plasma waves forming the discharge and the diagnostic signal with its satellites gives rise to the modulation peaks in the spectral lines of the scattered pump signal (at the frequency f) and its harmonics (at the frequencies qf) and the scattered diagnostic signals (at the frequencies f_D and f_{Dq}). Below, we will show that these low-frequency (at frequencies f_S) oscillations can be excited by a pump signal whose spectral width exceeds f_S.

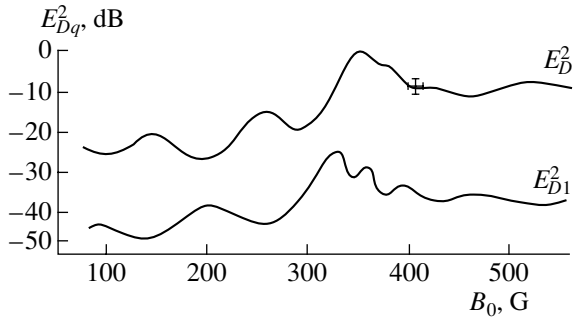

Fig. 4. Relative variations in the intensities of the main diagnostic signal scattered by the plasma, $\sim E_D^2$ (f_D = 920 MHz), and its first satellite, $\sim E_{D1}^2$ (f_{D1} = 1120 MHz), vs. the external magnetic field B_0 for $p = 10^{-3}$ torr and U_0 = 50 V.

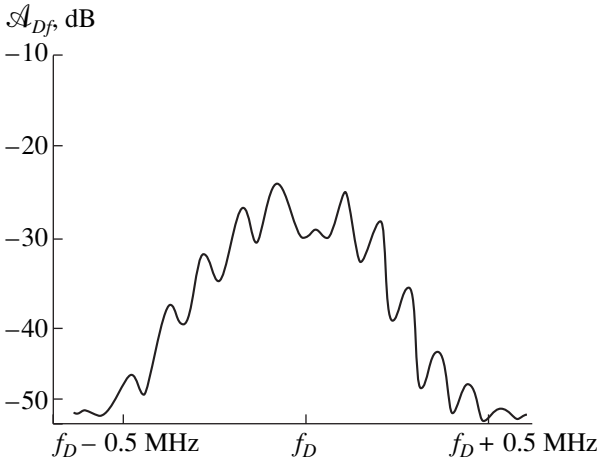

Fig. 5. Spectral structure of the main diagnostic signal scattered by the plasma (the spectral density of the signal intensity is $\sim \mathcal{A}_{Df}$) for B_0 = 330 G, U_0 = 50 V, and $p = 10^{-3}$ torr.

3. DISCUSSION OF THE EXPERIMENTAL RESULTS

The dependence of the amplitude of the diagnostic signal recorded at the output of a dielectric waveguide (resonator) on the plasma parameters can be determined through the following approximate expression for the transmission coefficient:

$$T \sim \cos\left(\int_{-L/2}^{L/2} h\,dx\right), \qquad (2)$$

where the propagation constant $h(\bar{N}_e, B_0)$ of a diagnostic wave along a dielectric waveguide is determined from the solution of the corresponding dispersion relations [2]. The plasma density oscillations in the waves forming the discharge change the value of h. In the cross section of the plasma column, these oscillations, as well as the field of the plasma waves forming a cylindrical waveguide channel [6], possess the structure of a standing wave whose amplitude decreases in the radial

direction. Since this amplitude is small, we can expand the propagation constant h in a series and keep only the first two terms in the expansion:

$$h \sim h(\bar{N}_{e0}) + \frac{\partial h}{\partial \bar{N}_e} n_{q\omega}(x)\cos(q\omega t)\cos(k_{\perp q}x) + \ldots,$$
$$q = 1, 2, \ldots,$$

where $k_{\perp q}$ is the transverse (with respect to $\mathbf{B}_0$) component of the wave vector of plasma waves and the dependence of the quantities on the z-coordinate along the channel is ignored, for simplicity. Substituting the expression for h into expansion (2), we obtain the time-varying (modulation) terms in the transmission coefficient:

$$T \sim \cos(h_0 L) - \sin(h_0 L)\frac{\partial h}{\partial \bar{N}_e}\cos(q\omega t) \times \int_{-L/2}^{L/2} n_{q\omega}(x)\cos(k_{\perp q}x)dx \sim T_0 - 2T_q\cos(q\omega t), \quad (3)$$

where $T_0 \equiv \cos(h_0 L)$ and $h_0 \equiv h(\bar{N}_{e0})$. From expression (3), we can see that, as the phase change $h_0 L$ in the plasma varies, the amplitudes of the modulation terms, which describe the scattered signal, vary in antiphase with the amplitude of the main diagnostic signal (T_0). This is confirmed by the experimental data illustrated in Fig. 4. Other conditions being equal, the ratio of the transmission coefficient of the satellite (T_q), shifted by the frequency of the plasma oscillations ($q\omega$), to that of the main signal (T_0) at the sounding frequency is maximal in the magnetic field range in which the dependence of the wave propagation constant h on the plasma density is the steepest, i.e., at $B_0 \sim 300$ G. The value of the corresponding derivative $\frac{\partial h}{\partial \bar{N}_e}$ can be estimated from Figs. 3 and 4. In fact, as may be seen in Fig. 3, the change in the magnetic field strongly affects the plasma density in the discharge; moreover, for magnetic fields up to $B_0 \approx 400$ G, the plasma density increases linearly by 2×10^9 cm^{-3}. As a result, the phase change $h_0 L$ of the diagnostic signal also varies. When it varies by $\pi/2$, this can correspond, in particular, to the transition from the maximum value of E_D to the minimum value, and vice versa (Fig. 4). With this point in mind, we can readily find that $\frac{\partial h}{\partial \bar{N}_e} \sim \frac{\pi}{2 \times 14 \times 2 \times 10^8} \approx 5 \times 10^{-10}$ cm^2 for $\bar{N}_e \sim 3 \times 10^9$ cm^{-3}. We should note that, by virtue of the specific properties of the antenna, namely, its symmetry about the chamber (channel) axis ($x = 0$) and the fact that all the points of any of the exciting rings have almost identical potentials, the radial component of the electric field of the plasma waves vanishes at the axis, $\mathcal{E}_\perp(x = 0) = 0$. On the other hand, under our experimental conditions, the amplitude of this electric field component at $x \sim d/2$ is several times greater than the amplitude of the longitudinal electric field component and, as was mentioned above, it decreases in the radial direction. Consequently, the equation $\nabla \cdot \mathcal{E} = -4\pi e(N_e - N_{e0})$ implies that the amplitude of the wave of the perturbed plasma density has an extremum (maximum or minimum) at the chamber axis, in which case we can estimate the integral in expression (3) as $\frac{\pi}{k_{\perp q}} n_{q\omega}(0)$. In particular, at the carrier frequency ω and for $B_0 \approx 300$ G ($\bar{N}_e \approx 3 \times 10^9$ cm^{-3}), the component $k_{\perp 1}$ can easily be determined from the dispersion relation for the oblique waves, $\omega \sim \bar{\omega}_{pe}\frac{k_\parallel}{\sqrt{k_{\perp 1}^2 + k_\parallel^2}}$ (where $\bar{\omega}_{pe}$ is the electron plasma frequency corresponding to $\bar{N}_e$), in which it is reasonable to treat the quantity $2\pi/k_\parallel$ as the distance l_u between the end rings of the antenna, which are held at the same potential. Therefore, we have $k_{\perp 1} \sim 2.5$ cm^{-1}. In expression (3), we also set $\tan(h_0 L) \sim 1$, which corresponds to $B_0 \approx 275$ G (Fig. 4) and, accordingly, to $T_1/T_0 \approx -25$ dB. As a result, we arrive at the estimate

$$n_\omega(0) \sim \frac{2T_1}{T_0}\left(\frac{\partial h}{\partial \bar{N}_e}\right)^{-1}\frac{k_{\perp 1}}{\pi} \sim 2 \times 10^8 \text{ см}^{-3}. \quad (4)$$

We can compare this approximate value with the following estimate, which follows from Maxwell's equations for the potential wave:

$$k_1 E_\omega \approx k_{\perp 1} E_{\omega\parallel}\frac{k_{\perp 1}}{k_\parallel} \approx -4\pi e n_\omega, \quad (5)$$

where $E_{\omega\parallel} \sim 2\frac{U_0}{l_u/2}$ is the amplitude of the electric field component along the chamber axis, $2U_0 \approx 100$ V is the voltage difference between the central and end rings of the antenna (the coefficient 2 accounts for the onset of the antinode of the voltage as the wave excited by the GST-2 generator is reflected from the open end of the coaxial supply cable), and $l_u \approx 6$ cm. Inserting these values into formula (5), we obtain $n_\omega \sim 10^8$ cm^{-3}.

The strong dependence of the slowing-down factors $\gamma \equiv h/k_D$ of the waves guided by the dielectric waveguide on the plasma density makes it possible to substantially improve the sensitivity of the proposed diagnostic method based on the recording of the sounding wave fields scattered by plasma density oscillations. Thus, under the experimental conditions, when the power carried by the surface wave was ≤ 10 mW and the external magnetic field was $B_0 > 450$ G, the method was able to record a significant increase in the amplitude of the signal scattered by the plasma oscillations at the fourth harmonic of the pump wave. This result allowed us to determine the averaged plasma density in

the discharge, $\bar{N}_e$ (450 G) ~ $N_{e\mathrm{cr}}(4f)/2 \sim 4 \times 10^9$ cm^{-3}, and to calibrate the curve $\bar{N}_e(B_0)$ in Fig. 3. In our method, the accuracy of measurements of the plasma density is governed by the frequency difference between the harmonics and increases with the harmonic number, $\Delta N_e/N_e \sim 1/q$. For $q \geq 3$, our method provides more accurate measurements as compared to probe measurements.

The sharp dispersion of the slowing-down factor $\gamma(\bar{N}_e)$ near the cutoff of the waveguide (plate) also makes it possible to resolve the modulation peaks associated with the scattering of the sounding wave by low-frequency oscillations of the plasma density. Since the frequency f_S of these oscillations is several times lower than the line width of the signal from the pump oscillator, they can be excited in the nonlinear interactions between the spectral components of the pump signal. In accordance with the estimates that will be made below, this excitation mechanism is more probable than the drift instability mechanism (discussed, e.g., in relation to experiments with narrow tubes [5]).[3] The reasons for this are twofold. On the one hand, in our experiments, the plasma density gradient was relatively small—it was actually near the threshold for the onset of the drift instability, $\frac{\rho_e}{d} > \left(\frac{m}{M}\right)^{1/2}$, where the electron distribution function is assumed to be Maxwellian, ρ_e is the electron gyroradius, m is the electron mass, M is the ion mass, and $\left(\frac{m}{M}\right)^{1/2} \approx \frac{1}{150}$ [7]. On the other hand, under our experimental conditions, the plasma diffusion from the discharge occurred mainly in the longitudinal direction, so that the intensity of the low-frequency plasma density oscillations changed moderately along the chamber, in contrast to the drift instability mechanism, which implies an exponential change.

To obtain estimates, we can represent the structure of the pump field at the first harmonic in the form[4]

$$\mathscr{E}_{\omega\perp} \sim \sin(k_{\perp 1}x)\cos\left(\frac{\pi x}{4d}\right)\cos(\omega t - k_\parallel z) \tag{6}$$
$$= \frac{1}{2}\left[\sin\left(k_{\perp 1} - \frac{\pi}{4d}\right)x + \sin\left(k_{\perp 1} + \frac{\pi}{4d}\right)x\right]\cos(\omega t - k_\parallel z),$$

where the frequency ω varies insignificantly within the above spectral line. We can easily see that the nonlinearity in the averaged ponderomotive force of the high-frequency field gives rise to the beat term with the wavenumber $\kappa = \pi/2d$, which is equal to the difference of the wavenumbers in the arguments of the sines in representation (6). If these wavenumbers refer to the spectral components with the frequency difference $2\pi f_S \approx \kappa v_S$ (where $v_S = \sqrt{T_e/M}$ is the ion acoustic speed and T_e is the electron temperature), then the above component of the ponderomotive force can efficiently generate ion acoustic waves in a plasma under the conditions $T_e \gg T_i$ and $\kappa\rho_i \ll 1$ (where T_i is the ion temperature and ρ_i is the ion gyroradius) [7], which are consistent with our experimental conditions.

The amplitude of the excited ion acoustic waves can be estimated in the same way as was done for the plasma waves. In this way, we can use a formula analogous to expression (4) in which we now must set $\tan(h_0 L) \neq 1$. The reason is that the waves are scattered by low-frequency plasma density oscillations at the path of the diagnostic signal (Fig. 5). Consequently, it is clear that the larger the quantity $\tan(h_0 L)$, the more distinguishable are these scattered waves against the background of the diagnostic signal. In turn, it is seen from Fig. 4 that $\tan(h_0 L) \sim 3$ at $B_0 \approx 300$ G. As a result, making the replacement $\frac{k_{\perp 1}}{\pi} \longrightarrow \frac{\kappa}{\pi}\frac{1}{\tan(h_0 L)}$ and putting $T_1/T_0 \sim 1$ (Fig. 5) in expression (4), we obtain

$$n_S \sim 3 \times 10^8 \text{ cm}^{-3}. \tag{7}$$

Note also that the multipeak character of the spectral line in Fig. 5 can be explained using a formula analogous to expression (3) and in which account is taken of not only the first term but also higher order terms in the expansion of the sine of the perturbed argument, $\sin(\int_{-L/2}^{L/2}(h - h_0)dx$, in a Taylor series. Clearly, this corresponds to taking into account cascade scattering processes. The scattering at the harmonics of the frequency f_S seems less probable, because the above condition for the existence of ion acoustic waves in a magnetized plasma, $q\kappa\rho_i \ll 1$ ($q = 2, 3, \ldots$), does not hold for them.

Now, let us determine whether the above amplitudes of the pump fields are sufficient to excite ion acoustic waves with the required intensities. To do this, we must take into account the following two circumstances: on the one hand, the GST-2 oscillator operates in a continuous mode and, on the other hand, the line width of the signal from this oscillator is several times greater than the frequency of the excited low-frequency oscillations (see the above discussion). As a consequence, the characteristic time over which the phase of the emitted radiation deflects from being regular is shorter than the period of the ion acoustic oscillations, so that their excitation is incoherent and, moreover, the waves themselves are excited "within the emission line." In order to analyze this fairly complicated process, we turn to the well-known models of plasma turbulence [8, 9],

[3] Note that, in [5], the frequency of the excited low-frequency oscillations was significantly higher than the line width of the pump signal.

[4] Here, we take into account the fact that, in the radial direction, the field of the oblique plasma waves is nonzero up to the radius $x \approx 2d$, at which we have $N_e(2d) \approx N_{e\mathrm{cr}}(f)$ in accordance with the radial plasma density profile (1).

according to which the excited ion acoustic waves in the assumed decay interaction are described by the equation

$$v_{Sz}\frac{\partial \mathcal{B}_{\mathbf{\kappa}}}{\partial z} = \int w_{\kappa}(\mathbf{k}_1, \mathbf{k}_1 - \mathbf{\kappa}) \cdot \frac{d\mathbf{k}_1}{(2\pi)^6}\{\mathcal{A}_{\mathbf{k}_1}\mathcal{A}_{\mathbf{k}_1 - \mathbf{\kappa}} - \mathcal{A}_{\mathbf{k}_1 - \mathbf{\kappa}}\mathcal{B}_{\mathbf{\kappa}} + \mathcal{A}_{\mathbf{k}_1}\mathcal{B}_{\mathbf{\kappa}}\}\pi\delta(\Delta\Omega). \quad (8)$$

Here, v_{Sz} is the projection of the velocity of ion acoustic waves onto the z-axis; $\mathcal{A}_{\mathbf{k}_1}$ and $\mathcal{B}_{\mathbf{\kappa}}$ are the spectral densities of the number of plasmons of the oblique Langmuir waves and ion acoustic waves, respectively; $w_{\kappa}(\mathbf{k}_1, \mathbf{k}_1 - \mathbf{\kappa})$ is the probability for an oblique Langmuir plasmon with the wave vector $\mathbf{k}_1$ to emit an ion acoustic plasmon with the wave number $\mathbf{\kappa}$; and $\delta(\Delta\Omega)$ is the delta function of the frequency mismatch $\Delta\Omega = \kappa v_S - \omega(\mathbf{k}_1) + \omega(\mathbf{k}_1 - \mathbf{\kappa})$.

Note that all spectral components of the pump signal contribute to the generation of ion acoustic waves, and the integration in Eq. (8) is carried out over the entire spectrum of the pump wave. The first term in parentheses in Eq. (8) is the main term for the following two reasons. On the one hand, the s-plasmons ($\mathcal{B}_{\mathbf{\kappa}}$) originate over the entire path along the z direction and are absent in the initial stage, in contrast to the l-plasmons ($\mathcal{A}_{\mathbf{k}_1}$). On the other hand (and more importantly), after integration, the second and third terms in parentheses cancel each other, in which case each of the high-frequency components of the emission line generates s-plasmons when it decays and absorbs them when it grows, thereby increasing the number of higher frequency l-plasmons. As a result, using Eq. (8), we arrive at the following estimate for the generation of s-plasmons:

$$v_{Sz}\frac{\partial \mathcal{B}_{\mathbf{\kappa}}}{\partial z} \sim w_{\kappa}\overline{\mathcal{A}}_{\mathbf{k}_1}\frac{W_1}{(2\pi)^3\hbar\omega}\frac{\pi}{\delta\Omega}, \quad (9)$$

where $\overline{\mathcal{A}}_{\mathbf{k}_1}$ is the averaged spectral density of the number of plasmons in the packet, $W_1 = \int\frac{\hbar\omega\mathcal{A}_{\mathbf{k}_1}d\mathbf{k}_1}{(2\pi)^3}$ is the energy density of the pump wave, and $\delta\Omega$ is the averaged frequency mismatch of the interacting waves ($\delta\Omega$ is on the order of the emission line width, i.e., about ω_S).[5] We multiply relationship (9) by the phase volume occupied by the s-plasmons (because of the cylindrical geometry of the problem, this volume is about k_1/κ times smaller than that occupied by the l-plasmons) and obtain

$$\frac{n_S}{N_e} \sim \left(\frac{\kappa}{k_1}\frac{\omega_{pe}^2}{\omega_{He}^2}\frac{\omega_{pe}}{\omega}\frac{\kappa z}{2}\right)^{1/2}\frac{W_1}{N_e T_e} \sim \frac{1}{15}. \quad (10)$$

In deriving this estimate, we used the well-known relationship between the energy of an ion acoustic wave and the plasma density perturbation in it, $\frac{W_S}{N_e T_e} = \frac{1}{2}\left(\frac{n_S}{N_e}\right)^2$, and took into account the fact that the distance from the entrance to the chamber (from the antenna) to the center of the plate is $z = z_0 \sim 40$ cm. Then, from estimate (10), we obtain[6]

$$n_S \sim 2 \times 10^8 \text{ cm}^{-3}. \quad (11)$$

The excitation of ion acoustic waves influences the spectrum of the pump signal (Fig. 6). This influence is described by an equation analogous to Eq. (8). For the case of energy transfer down to the spectrum (from higher to lower frequencies), it has the following form:

$$v_{\omega z}\frac{\partial \mathcal{A}_{\mathbf{k}_1}}{\partial z} = \int w_{\kappa}(\mathbf{k}_1 + \mathbf{\kappa}, \mathbf{k}_1) \times \frac{d\mathbf{\kappa}}{(2\pi)^6}\{\mathcal{A}_{\mathbf{k}_1 + \mathbf{\kappa}}\mathcal{A}_{\mathbf{k}_1} - \mathcal{A}_{\mathbf{k}_1}\mathcal{B}_{\mathbf{\kappa}} + \mathcal{A}_{\mathbf{k}_1 + \mathbf{\kappa}}\mathcal{B}_{\mathbf{\kappa}}\}\pi\delta(\Delta\Omega), \quad (12)$$

where $v_{\omega z} \sim \frac{\omega_{pe}}{k_1}$ is the component of the group velocity of the plasma waves along the channel and the remaining notations are similar to those used in Eq. (8). However, in contrast to the processes described by Eq. (8), Eq. (12) implies that each of the components of the emission line interacts not with the entire spectrum but rather with the components whose frequencies differ from its frequency by an amount ω_S, with allowance for the width of the low-frequency spectral line and the above-mentioned broadening of the resonance. Consequently, after integration, the second and third terms in

[5] Note that the spatial spectrum of the pump signal in a plasma is more rich than the temporal spectrum and that the frequency of each emission line corresponds to a finite set of wave vectors $\mathbf{k}_1$ arising, e.g., due to the inhomogeneity of the formed waveguide. However, the effect of this factor, which increases the number of triplets of the waves that do not satisfy the exact synchronism conditions, is somewhat balanced by the effect of the correlation broadening of the resonance itself ($\Delta\mathbf{k} = 0$, $\Delta\Omega = 0$) because of the nonlinearity arising in a sufficiently strong field ($W_1/N_e T_e \sim 4 \times 10^{-2}$) [9]. This circumstance was taken into account in deriving expression (9) from Eq. (8).

[6] Note that estimates (10) and (11) were derived for a forward-propagating wave, i.e., for an ion acoustic wave whose propagation direction along the magnetic field coincides with the direction of the plasma ambipolar diffusion. Under the steady-state discharge conditions of our experiments, it is a simple matter to estimate that the ambipolar diffusion rate is about the sound speed. On the other hand, we have $v_{Sz} = v_S\frac{\kappa_z}{\kappa} \sim v_S\frac{k_\parallel}{k_1}$. Therefore, the backward-propagating wave, traveling in the direction opposite to that of the diffusion flux, is generated more efficiently, because the plasma density perturbations in it escape from the interaction region much slower than the perturbations in the forward-propagating wave. As a result, the density perturbations n_S associated with the backward-propagating wave may exceed those in formulas (10) and (11) by several times or more.

parentheses in Eq. (12) do not cancel each other out. In addition, according to the above estimates, the spectral density of the low-frequency plasmons is much higher than that of the high-frequency plasmons, although the energy of high-frequency plasmons is much higher than the energy of low-frequency plasmons. In this case, the main terms in parentheses in Eq. (12) are the second and third terms. As a result, the deformation of the high-frequency spectrum is the most pronounced in the part of the line over which the line shape depends most strongly on the frequency. So, we can set $\mathcal{A}_{\mathbf{k}_1+\boldsymbol{\kappa}} \gg \mathcal{A}_{\mathbf{k}_1}$ in Eq. (12) and take into account relationships (10) to obtain

$$\frac{\mathcal{A}_{\mathbf{k}_1}}{\mathcal{A}_{\mathbf{k}_1+\boldsymbol{\kappa}}} \sim \frac{1}{20}\frac{\omega_{pe}^2}{\omega_{He}^2}\frac{\omega}{\omega_{pe}}\frac{\omega}{\omega_S}\left(\frac{n_S}{N_e}\right)^2 k_1 z. \qquad (13)$$

Setting $n_S \sim 10^8$ cm^{-3} at the plate ($z = z_0$) gives $\mathcal{A}_{\mathbf{k}_1}/\mathcal{A}_{\mathbf{k}_1+\boldsymbol{\kappa}} \sim 1$, which indicates the spectrum broadening. This broadening increases as the path length along the z-direction increases. However, the increase is relatively insignificant (Fig. 6), because, on the one hand, the ion acoustic perturbations (10) grow at a moderate rate and, on the other hand, the damping of plasma waves, which was neglected up to this point, comes into play on long paths ($z_1 \approx 100$ cm). Under our experimental conditions, the plasma wave energy is damped over a distance of length $\Lambda_{\mathrm{damp}W} \sim \dfrac{v_{\omega z}}{\nu_{em}} \sim 100$ cm $\sim z_1$ (where $\nu_{em} \sim 10^7$ s^{-1} is the electron–molecule collision frequency in the discharge plasma). The damping reduces nonlinear effects.

Finally, we note that the experimental profiles in the figures are seen to be asymmetric, indicating the asymmetry of the spectrum of waves propagating in the plasma. On the other hand, an equation that is similar to Eq. (12) and describes the transfer of the ion acoustic energy from lower to higher frequencies leads to the same estimate (13). In principle, it follows from these equations that energy transfer toward the red part of the spectrum is more intense (because of the presence of the terms $\mathcal{A}_{\mathbf{k}_1+\boldsymbol{\kappa}}\mathcal{A}_{\mathbf{k}_1}$ in braces). However, under our experimental conditions, these terms are insufficiently large to fit the observed asymmetry. Presumably, agreement with the experiment can be achieved through a more correct description of the relevant nonlinear processes, without assuming the plasma turbulence to be weak, because, as was already mentioned, our experiments were carried out with fairly strong fields. Thus, the nonlinear scale length on which the ion acoustic fields increase along the chamber axis is about their longitudinal wavelength. The development of such a description is a fairly complicated task and goes beyond the scope of this study.

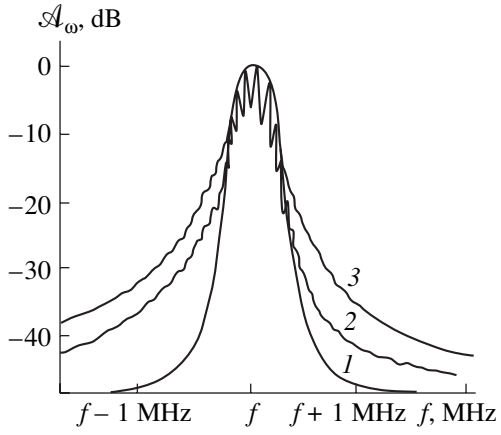

Fig. 6. Shape of the spectral line of the discharge-forming pump field from a T-shaped junction between the coaxial supply cable and the dielectric plate (the spectral density of the diagnostic signal intensity is $\sim\mathcal{A}_\omega$) for $B_0 = 330$ G, $U_0 = 50$ V, and $p = 10^{-3}$ torr. Curves *1* and *2* (the signal is attenuated by 20 dB) refer to the cases without and with the discharge, respectively. Curve *3* (the signal is attenuated by 15 dB) was measured under the same conditions as curve *2* by an electric probe at a distance of $z \sim 1$ m from the RF antenna.

Note that the above parameters of the excited ion acoustic waves permit us to determine the electron temperature:

$$T_e = Mv_S^2 = M\frac{\omega_S^2}{\kappa^2} \approx 20 \text{ eV}, \qquad (14)$$

where M is the mass of a nitrogen atom. This temperature value is confirmed by direct measurements of the retardation curves of the electron flux toward the electrostatic energy analyzer of charged particles. For the discharge parameters under consideration, these measurements were carried out by Markov *et al.* [6].

The results obtained show that dielectric waveguides and resonators are promising for the wave diagnostics of gas-discharge plasmas.

ACKNOWLEDGMENTS

This work was supported by the programs “Leading Scientific Schools” (project no. 00-15-96772) and “Universities of Russia” (project no. 992852), the Russian Foundation for Basic Research (project no. 01-02-16949), and the Ministry of Education of the Russian Federation (project no. E00-3.5-227).

APPENDIX

Possible Ways of Extending the Range of Applicability of the Proposed Diagnostic Method

In the case of a significant slowing-down, which is the most interesting for our study, the dispersion prop-

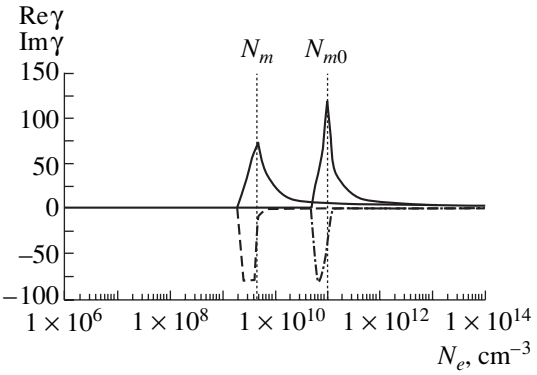

Fig. 7. Real part (solid curves) and imaginary part (dashed and dot-and-dash curves) of the slowing-down factor γ for the forward-propagating (Re$h > 0$) and backward-propagating (Re$h < 0$) surface waves vs. the plasma density N_e for $\omega_D = 5.78 \times 10^9$ s^{-1}, $\omega_{He} = 5.27 \times 10^9$ s^{-1} ($B_0 = 300$ G), $\delta =$ 0.1 cm, $\nu_{em} = 5 \times 10^6$ s^{-1}, and; $\gamma = \begin{cases} h/k_D, & \mathrm{Re}\, h > 0 \\ -h/k_D, & \mathrm{Re}\, h < 0 \end{cases}$, N_m and N_{m0} are the plasma densities at which the real part Reγ reaches the maximum values for the forward- and backward-propagating waves, respectively).

erties of the waves traveling along a dielectric waveguide can be determined analytically. These properties can be found from the following set of characteristic equations, which were investigated numerically in [2]:

$$\begin{cases} \alpha\varepsilon_1 - h\delta\varepsilon_2 = \beta\dfrac{\varepsilon_1^2 - \varepsilon_2^2}{\varepsilon}\tan\beta \\ \beta^2 + h^2\delta^2 = k_D^2\delta^2\varepsilon \\ h^2\delta^2 - \alpha^2 = k_D^2\delta^2\dfrac{\varepsilon_1^2 - \varepsilon_2^2}{\varepsilon_1}. \end{cases} \tag{A.1}$$

Here, h is the longitudinal wavenumber and α and β are the external and internal dimensionless transverse wavenumbers, respectively, in terms of which the components of the wave field are expressed. Thus, the H_z-component of the magnetic field of a symmetric TM mode has the form

$$H_z = \begin{cases} H_m \cos\left(\beta\dfrac{y}{\delta}\right)\exp(-ihx), & |y| \le \delta \\ H_m \cos\beta \exp\left(-\alpha\left(\dfrac{|y|}{\delta} - 1\right)\right)\exp(-ihx), & |y| \ge \delta. \end{cases} \tag{A.2}$$

The unit vectors of the coordinate system with which we are working here form a right-hand triad: the z-axis is directed along the external magnetic field $\mathbf{B}_0$ and the y-axis is perpendicular to the plate. We are considering waves propagating transverse to $\mathbf{B}_0$. The quantities ε_1 and ε_2 in Eqs. (A.1) are the elements of the dielectric tensor of the plasma surrounding the plate [10]:

$$\varepsilon_1 = 1 - \frac{\omega_{pe}^2(\omega_D - i\nu_{em})}{\omega_D[(\omega_D - i\nu_{em})^2 - \omega_{He}^2]}, \qquad \varepsilon_2 = \frac{-\omega_{pe}^2\omega_{He}}{\omega_D[(\omega_D - i\nu_{em})^2 - \omega_{He}^2]}. \tag{A.3}$$

Setting $h^2 \gg k_D^2\varepsilon$, $k_D^2(\varepsilon_1^2 - \varepsilon_2^2)/\varepsilon_1$ in the last two of the characteristic equations (A.1), we obtain $\beta \approx \pm ih\delta$ and $\alpha \approx h\delta$ (the latter value will be used in further analysis).[7] We substitute these expressions into the first equation in system (A.1) and obtain the following equation for h:

$$1 \approx \left[\frac{1}{4} - \frac{\omega_{pe}^2}{4\omega_D(\omega_D - \omega_{He})}\right]\frac{e^{-h\delta} - e^{h\delta}}{e^{-h\delta} + e^{h\delta}}, \tag{A.4}$$

where we set $|\omega_D - \omega_{He}| \gg \nu_{em}$ and, in accordance with the above analysis, $\varepsilon = 4$. It is easy to see that, if $\omega_D > \omega_{He}$, this equation has positive solutions, $h > 0$. The existence of such solutions imposes the following restriction on the factor in the square brackets:

$$\frac{1}{4} - \frac{\omega_{pe}^2}{4\omega_D(\omega_D - \omega_{He})} \le -1. \tag{A.5}$$

For $h\delta \ll 1$, the solution to Eq. (A.4) has the form

$$h\delta \approx \frac{4\omega_D(\omega_D - \omega_{He})}{\omega_{pe}^2}. \tag{A.6}$$

This brief analysis is confirmed by the results from solving Eqs. (A.1) on a computer (see, e.g., Fig. 7). We can see that, at plasma densities for which condition (A.5) fails to hold, the imaginary part Imγ of solutions with a large real part Reγ is large, indicating strong wave damping or, in fact, the cutoff of the waveguide. On the other hand, at minimum possible plasma densities, which satisfy condition (A.5), or, equivalently, near the peaks of the curves in Fig. 7, the slowing-down factor is actually smaller than that predicted by numerical simulations. The reason for this is the following: the wave that is slowed down very strongly turns out to be tightly bound to the plate ($\alpha \approx h\delta$, see the above analysis), in the immediate vicinity of which the plasma density decreases sharply to almost zero. The thickness of the transition layer between the plasma and the plate is about several Debye radii $r_{de} = (T_e/m\omega_{pe}^2)^{1/2}$. Consequently, our analysis is valid if the layer thickness is much smaller than the size h^{-1} of the region occupied by the surface wave [see expression (A.2)]. Thus, under our experimental conditions, we have $r_{de} \sim 0.5$ mm,

[7] We must also keep in mind the condition $h > 0$, which follows from the definition of surface waves.

$k_D^{-1} = 5$ cm, and $h^{-1} = 0.5$ cm for $\gamma = 10$. We also mention an interesting property of such waveguide systems surrounded by the plasma. Since the first equation in system (A.1) comprises an odd power of h, the waves in such waveguides are nonreciprocal [11]. A similar analysis of system (A.1) and the results of numerical integration (Fig. 7) show that, in the region of comparatively low plasma densities, the backward-propagating surface wave is slowed to a much lesser extent than the forward-propagating wave.

The wave characteristics described allow us to propose the following diagnostic technique for measuring the plasma density. The technique is based on the use of an oscillator that excites a diagnostic wave, whose frequency ω_D can be continuously tuned over a comparatively broad range. First, this frequency should be chosen to be markedly higher than ω_{He}. Then, it is necessary to continuously reduce the difference $\omega_D - \omega_{He}$. It is readily seen that, as this difference decreases, the curve in Fig. 7 passes from the left to the right, first, through the region where inequality (A.5) fails to hold and, then, through the region where this inequality holds. It is the transition point ω_D^* between these regions that is determined by condition (A.5). At this point, the surface wave is slowed to the greatest extent (which corresponds to the peak in the curve in Fig. 7). However, we recall that, under actual experimental conditions, this peak is appreciably smoothed out and is lower. Nevertheless, the ω_D value at which the measured intensity of the diagnostic wave sharply increases corresponds to the above transition point ω_D^*. Hence, the plasma density can be determined with acceptable accuracy. In an inhomogeneous plasma (as in our experiments), the path of the diagnostic wave at the frequency ω_D^* (from the emitting antenna at the entrance of the waveguide to the receiver, through the central higher-density plasma) is entirely within the transparency region of the plate in view of the wave characteristics described above.[8] Moreover, it is easy to see that, due to the above-mentioned smoothing of the peak of the slowing-down factor, this factor remains essentially unchanged along the entire path of the diagnostic wave.[9] Then, by displacing the emitting and receiving dipoles along the plate, while keeping them symmetric with respect to the chamber axis, it is possible to measure the radial plasma density profile. For this purpose, the plate with fixed dipoles can also be raised and descended parallel to itself, while keeping it perpendicular to the vertical longitudinal cross section of the chamber and symmetric with respect to this cross section.

The above analysis implies clearly that, for the proposed method to be implemented, it is important that the external magnetic field $\mathbf{B}_0$ be uniform. Consequently, in order to improve the measurement accuracy, the diagnostic plate should be placed in the region enclosed by the magnetic coils, where the magnetic field is fairly uniform. Another important factor is the form of an antenna emitting a surface wave. Our experiments were carried out with the simplest antenna, namely, a dipole whose length was equal to the plate thickness and which was oriented perpendicular to the plate. However, such a dipole can emit not only the modes that are the subject of our discussion but also other types of modes. For the modes under consideration to dominate the emission spectrum of the dipole, the dipole itself should be sufficiently uniform in the direction transverse to the plate (along $\mathbf{B}_0$). The dipole can be made sufficiently uniform by equipping it with two mutually parallel conductors (filaments), which should be attached to its ends, should be oriented along $\mathbf{B}_0$, and whose length should be equal to the transverse size of the plate.

The accuracy of the method proposed here for determining the amplitudes of the discharge-forming plasma waves by recording the diagnostic signal scattered by them can be improved in an analogous (but a more complicated) way. However, since the longitudinal component of the wave vector of the plasma waves in our experiments was $k_\parallel \approx 1$ cm^{-1}, system (A.1) is insufficient to characterize the scattering process, because it describes only the transverse propagation of the waves. Of course, this question requires a separate consideration, but here we put forward certain ideas that may, in our opinion, provide the basis for the improvement of the method. Thus, we propose to strongly slow down the first satellite of the scattered diagnostic wave with the frequency ω_D (e.g., the blue satellite). The frequency $\omega_{D1} = \omega_D + \omega$ of the satellite slowed down to the desired extent should be determined from the corresponding equations in a way analogous to the derivation of formula (A.6). For convenience, in further calculations, the wavenumber of the satellite in an inhomogeneous plasma should satisfy (at least, in the region where the diagnostic signal is scattered) the condition of the geometrical-optics approximation: $h_{D1}d \gg 1$. The radial plasma density profile is calculated by the method described above. In particular, if the slowing-down factor is set equal to $\gamma = 10$ at the radius $x = 2d$ under the conditions corresponding to the radial plasma density profile (1), then the possible decrease in the slowing-down factor in the direction in which the plasma density gradually increases (toward $x = 0$) can be compensated to a significant extent by a continuous

[8] Here, by ω_D^*, we mean the frequency corresponding to the plasma density in the region of a dipole antenna.

[9] A strong wave slowing-down makes it possible to use a plate with a smaller transverse size (along $\mathbf{B}_0$). On the other hand, since the backward-propagating surface wave is slowed down to a much lesser extent than the forward-propagating wave (see the above discussion), such a plate reduces the resonator effect that manifests itself in the segment of a dielectric waveguide (plate).

reduction in the plate thickness δ [see, e.g., solution (A.6)].[10]

The frequency ω_D of the diagnostic wave is determined from the frequency ω_{D1}. Let us assume that the diagnostic wave propagates in the direction perpendicular to $\mathbf{B}_0$. Taking into account the fact that, at a comparatively low plasma density, this wave is strongly slowed down in a narrow frequency range around the frequency ω_{He} [see Eq. (A.5)], we can expect that the frequency ω_D will lie outside this range and that the wave will be slowed down only slightly.[11] In this case, as in the geometrical-optics approximation, the structure of the diagnostic wave in the plasma can also be determined analytically.

In order to derive an expression for the nonlinear current exciting the satellite wave at the frequency ω_{D1}, it is necessary to know not only the field at the sounding frequency ω_D but also the field of the plasma waves. In a channel with the known profile $N_e(x)$, the field structure of the plasma waves can be calculated analytically. Thus, for the radial plasma density profile (1), the field structure in the region $|x| \le d$ can easily be described in the geometrical-optics approximation because the condition $k_{\perp 1} d \gg 1$ is satisfied in this region.

The experimental conditions should ensure the scattering of the diagnostic wave when it propagates in the plate segment between the reflection points of oblique plasma waves. The generation of the satellite wave at the frequency ω_{D1} should be described in a weakly nonlinear approximation, using shortened equations and assuming that the wave field at the frequency ω_D and the plasma wave fields are both prescribed. A dipole antenna that emits radiation at the frequency ω_D should be located outside the discharge plasma region, closer to the chamber wall, and the frequency itself should be chosen in such a way that the slowing-down factor for the satellite at the frequency ω_{D1} in the region of reflection of the plasma waves is equal to $\gamma \approx 10$. In order to enhance the scattering effect, it is desirable to achieve (if possible) the spatial synchronization of the interacting waves, especially in the central discharge region, where the amplitudes of the plasma waves are maximum. In fact, this indicates that the condition $h_{D1}(x) \approx k_{\perp 1}(x)$ should be satisfied along the entire plate, because $h_D \ll h_{D1}$ (see the above analysis); in other words, the plate thickness should be appropriately shaped in the x direction.[12]

An antenna receiving the scattered wave should be located in such a way that it and the emitting antenna are symmetric with respect to the chamber axis. The receiving antenna should be designed so as to record the scattered wave with the above-described transverse or longitudinal (in the z direction) structure as efficiently as possible.[13] Let the power recorded by the receiving antenna at the frequency ω_{D1} be equal to $\Pi_a = \eta P_{D1}$, where P_{D1} is the wave power at the exit from the generation region and the coefficient η needs to be determined. In order to find this coefficient, we choose the emitting antenna to be the same as the receiving antenna and place them in a symmetric position with respect to each other. Let a voltage at the frequency ω_{D1} be supplied to the emitting antenna. In this case, we can expect that the power Π_r from the emitting antenna will be related to the power of the surface wave in the generation region (recall that, in this region, the surface wave is described in the geometrical-optics approximation) in a similar way: $P_{D1} = \eta \Pi_r$. As a result, we obtain[14]

$$\eta = \sqrt{\frac{\Pi_a}{\Pi_r}}. \qquad \text{(A.7)}$$

Finally, we note that, in order for the above considerations to be valid, the possible resonator effect of the plate should be destroyed by slightly varying the sounding frequency ω_D.

REFERENCES

1. V. E. Golant, in *Handbook of Plasma Physics*, Vol. 2: *Basic Plasma Physics*, Ed. by A. A. Galeev and R. N. Sudan (Énergoatomizdat, Moscow, 1984; North-Holland, Amsterdam, 1984).
2. I. V. Katin and G. A. Markov, Izv. Vyssh. Uchebn. Zaved., Radiofiz. **42**, 2154 (1999) [Radiophys. Quantum Electron. **42**, 191 (1999)].
3. A. D. Piliya, Zh. Tekh. Fiz. **36**, 2195 (1966) [Sov. Phys. Tech. Phys. **11**, 1639 (1967)]; E. Z. Gusakov and

[10] Note that the plasma density gradient in the higher density region corresponding to the upper part of the profile $N_e(x)$ is smaller than that at the periphery; consequently, in this region, the slowing-down factor can be set somewhat smaller.

[11] In particular, for waves with the frequencies ω_D and ω_{D1} traveling in the direction transverse to the external magnetic field, the wavenumber h of a weakly slowed diagnostic wave can easily be found from the basic equations (A.1). Setting $h \sim k_D$ in these equations and taking into account the fact that the frequency difference entering the dielectric tensor elements ε_1 and ε_2 is $\omega_{He} - \omega_D \approx \omega$, we can see that the right-hand side of the first equation (A.1) in system (A.1) can be neglected, in which case we obtain $\alpha = h\delta\varepsilon_2/\varepsilon_1$. We substitute this relationship into the third equation to find $h \approx k_D\sqrt{\varepsilon_1}$, which agrees with the results of numerical integration of system (A.1) on a computer. Thus, for the parameter values typical of our experiments ($N_e = 3 \times 10^9$ cm^{-3}), we have $\sqrt{\varepsilon_1} \approx 1.3$.

[12] At the discharge center, where the transverse component $k_{\perp 1}$ of the wave vector is larger, the h_{D1} value can also be larger because the thickness of the transition layer decreases as the plasma density increases (see above).

[13] In particular, across a plate with appropriate dimensions, the scattered wave is likely to be a standing wave.

[14] It is expected that, as the discharge is switched on, both the emitted and received powers should increase considerably because of the excitation of a surface wave. If this increase is insufficiently large, both of the antennas should be somewhat displaced away from the chamber wall toward the chamber axis.

A. D. Piliya, Pis'ma Zh. Tekh. Fiz. **18**, 63 (1992) [Sov. Tech. Phys. Lett. **18**, 325 (1992)].

4. V. I. Arkhipenko, V. N. Budnikov, E. Z. Gusakov, *et al.*, Pis'ma Zh. Éksp. Teor. Fiz. **59**, 393 (1994) [JETP Lett. **59**, 420 (1994)]; E. Z. Gusakov, N. M. Kaganskaya, M. Kremer, *et al.*, Pis'ma Zh. Tekh. Fiz. **24** (20), 43 (1998) [Tech. Phys. Lett. **24**, 806 (1998)].
5. V. S. Bazhanov, G. A. Markov, and I. V. Khazanov, Izv. Vyssh. Uchebn. Zaved., Radiofiz. **24**, 519 (1981).
6. G. A. Markov, V. A. Mironov, A. M. Sergeev, and I. A. Sokolova, Zh. Éksp. Teor. Fiz. **80**, 2264 (1981) [Sov. Phys. JETP **53**, 1183 (1981)]; G. A. Markov, Zh. Éksp. Teor. Fiz. **113**, 1989 (1998) [JETP **86**, 703 (1998)].
7. A. B. Mikhailovskii, *Theory of Plasma Instabilities* (Atomizdat, Moscow, 1971; Consultants Bureau, New York, 1974).
8. V. N. Tsytovich, *Nonlinear Effects in Plasmas* (Nauka, Moscow, 1967; Plenum, New York, 1970).
9. V. N. Tsytovich, *Theory of Turbulent Plasma* (Atomizdat, Moscow, 1971; Plenum, New York, 1974).
10. V. L. Ginzburg, *The Propagation of Electromagnetic Waves in Plasmas* (Fizmatgiz, Moscow, 1967; Pergamon, Oxford, 1970).
11. A. N. Kondratenko and V. M. Kuklin, *Principles of Plasma Electronics* (Énergoatomizdat, Moscow, 1988).

Translated by G. Shepekina

Plasma Physics Reports, Vol. 28, No. 4, 2002, pp. 286–295. Translated from Fizika Plazmy, Vol. 28, No. 4, 2002, pp. 319–328.

PLASMA DYNAMICS

Numerical Modeling of the Dynamics of a Slow Z-Pinch

A. S. Kingsep*, V. E. Karpov, A. I. Lobanov**, Y. Maron***, A. A. Starobinets***, and V. I. Fisher*****

**Russian Research Centre Kurchatov Institute, pl. Kurchatova 1, Moscow, 123182 Russia*

***Moscow Institute of Physics and Technology, Institutskiĭ proezd 9, Dolgoprudnyĭ, Moscow oblast, 141700 Russia*

****Weizmann Institute of Sciences, Rehovot, Israel*

Received May 24, 2001; in final form, November 22, 2001

Abstract—A study is made of the method for numerical modeling of pulsed plasma systems by simultaneously solving two-temperature MHD equations and the equations of ionization kinetics. As an example, the method is applied to simulate a relatively slow moderate-density Z-pinch, whose dynamics is well studied experimentally. A specially devised two-dimensional computer code makes use of a promising technique of parallel modeling. *© 2002 MAIK "Nauka/Interperiodica".*

1. INTRODUCTION

In this paper, we present the results of numerical experiments aimed at modeling the dynamics of a moderate-density Z-pinch on characteristic time scales of about 600–700 ns [1–3]. The computer code devised for simulations is based on the hydrodynamic model developed in [4] and on the kinetic model describing the dynamics of ionization states [1]. In the experiments of [1–3], the pinch was created with the help of a ring nozzle with an electromagnetic valve in CO_2, which served as the standard working gas. Since our numerical experiments were based on one-fluid MHD theory, we considered a purely carbon gas jet. The main objective of our simulations was not only to reproduce the experimental results in detail but, even more importantly, to prove the feasibility of our combined method and to test numerical techniques. The reason is that the most informative methods for investigating pulsed plasmas (regardless of the way in which they are produced) are provided by spectroscopy and the most convenient objects in testing spectroscopic methods are Z-pinches, which ensure a sufficiently high radiation intensity and high reproducibility of results at a relatively low cost of experiments.

2. MATHEMATICAL MODEL AND BRIEF DESCRIPTION OF THE NUMERICAL METHOD

The MHD part of the combined method assumes the solution of the following one-dimensional model equations of motion for a two-temperature one-fluid plasma in a magnetic field in dimensionless form:

$$\frac{d\rho}{dt} + \rho\frac{1}{r}\frac{\partial(rv_r)}{\partial r} = 0,$$

$$\frac{dv_r}{dt} = -\frac{1}{\rho}\left(\frac{\partial}{\partial r}\left(P + \frac{B^2}{8\pi}\right)\right) - \frac{B^2}{4\pi\rho r},$$

$$\frac{\rho}{A}\frac{d}{dt}(z_{\text{eff}}\varepsilon_e + J(z_{\text{eff}})) = -P_e\frac{1}{r}\frac{\partial(rv_r)}{\partial r} + \frac{1}{r}\left(\kappa_e r\frac{\partial T_e}{\partial r}\right) + \frac{\nu}{4\pi}\left(\frac{1}{r}\frac{\partial rB}{\partial r}\right)^2 - Q_r + Q_{ei},$$

$$\frac{\rho}{A}\frac{d\varepsilon_i}{dt} = -P_i\frac{1}{r}\frac{\partial(rv_r)}{\partial r} + \frac{1}{r}\frac{\partial}{\partial R}\left(\kappa_i r\frac{\partial T_i}{\partial r}\right) - Q_{ei},$$

$$\frac{dB}{dt} = -B\frac{1}{r}\frac{\partial(rv_r)}{\partial r} - \frac{\partial}{\partial r}\left(\frac{1}{r}\frac{\partial rB}{\partial r}\right), \quad (1)$$

where Q_r is the radiative (bremsstrahlung) loss power and Q_{ei} is the power of collisional energy exchange between electrons and ions. The subscripts e and i refer to electrons and ions, respectively. Most of the notation is standard: P without the subscript is the total pressure (i.e., the sum of the partial pressures of plasma electrons and ions), and the function $J(z_{\text{eff}})$ accounts for energy losses from ionization. The equations were nondimensionalized with respect to the following main scales: the time scale is $[t] = 10^{-7}$ s, the length scale is $[r] = 1$ cm, the mass density scale is $[\rho] = 10^{-3}$ g/cm^3, and the temperature (energy) scale is $[T] = 1$ keV. The plasma is described by the ideal gas equations of state:

$$P_e = 9.68\frac{\rho T_e z_{\text{eff}}}{A}, \quad \varepsilon_e = 14.4T_e,$$
$$P_e = 9.68\frac{\rho T_i}{A}, \quad \varepsilon_i = 14.4T_i. \quad (2)$$

Here and below, A is the number of nucleons in a nucleus (the atomic weight). The model equations are written in dimensionless form. The power of collisional

energy exchange between electrons and ions is

$$Q_{ei} = 8.48 \times 10^{-1} \frac{\rho^2 z_{\text{eff}}^3}{A^3} \frac{T_i - T_e}{T_e^{3/2}}, \quad (3)$$

and the radiative loss power is

$$Q_r = 0.174 A^{-2} z_{\text{eff}}^2 \rho^2 T_e^{0.5}. \quad (4)$$

The electron and ion thermal diffusivities are chosen to be

$$\kappa_e = 2.21 \times 10^{-2} T_e^{2.5} z_{\text{eff}}^{-1}, \qquad \kappa_i = 6.6 \times 10^{-4} T_i^{2.5} z_{\text{eff}}^{-4} A^{-0.5}, \quad (5)$$

and the magnetic viscosity has the form

$$\nu = 2.59 \times 10^{-5} z_{\text{eff}} T_e^{-1.5}, \quad (6)$$

where z_{eff} is the effective ion charge number in the plasma. Our earlier studies showed that plasma magnetization at $\omega_{Be} \ll \omega_{pe}$ (or equivalently $B^2 \ll nmc^2$) has no significant effect on the macroscopic pinch dynamics. That is why we assumed that the plasma is unmagnetized, the more so because we were primarily interested in proving the feasibility of our combined method.

At the outer pinch boundary, we imposed the conditions corresponding to those at the boundary between a plasma and vacuum. In this case, the azimuthal magnetic field at the boundary is related to the total current in the external electric circuit by the familiar dimensionless relationship

$$B = \frac{0.2 I(t)}{R},$$

where I is the current in the external circuit and R is the instantaneous radius of the corresponding point in the Z-pinch corona.

The above set of MHD equations was solved by the method of separation of the scales of the physical processes. In the first stage of calculations, the code takes into account the plasma motion and solves inviscid MHD equations without allowance for dissipative effects. The difference scheme is constructed using Lagrangian mass coordinates and provides the second-order approximation in the spatial variables. In order to reduce the oscillations that appear in calculating discontinuous solutions (such as shock waves and contact and tangential discontinuities), the pressure term is supplemented with an artificial viscosity term. The simulations were carried out with a combination of linear and quadratic viscosity coefficients [5]. The explicit, completely conservative difference schemes that were implemented computationally in the code are analogous to those described in [5]. The code also imposes restrictions on the minimum size of cells of the difference mesh. When the spatial dimension of one of the cells becomes smaller than the minimum allowable dimension, all of the quantities (specifically, not only the "traditional" parameters such as the plasma temperature, momentum, and mass but also the mean ion charge in the cell and radiative losses) are conservatively recalculated for a new mesh. Since an algorithm for such recalculation is fairly obvious, we do not describe it here. The numerical methods used in computations are quite similar to those applied in earlier papers [4, 6]. In the next stages of calculations, the code solves the equations for the electron and ion thermal diffusivities and the magnetic-field diffusion equation by the flux sweep methods [7]. In the final stage, the code takes into account the energy exchange between electrons and ions and also radiative losses. The sets of ordinary differential equations (ODEs) that are precisely determined in this stage of separation of the scales of the physical processes are solved by the method of trapezoids.

In each Lagrangian cell in each hydrodynamic time step (or several steps), the code integrates (on the intrinsic kinetic time scale) a set of 200–300 ODEs determining the population of the quantum states of plasma atoms and ions. All of the seven charge states of carbon atoms are taken into account. For the first six charge states, systematic account is taken of the lowest 20–40 terms for electron configurations with one or two excited electrons. The higher terms are modeled by Rydberg levels with the statistical weights taking into account all of the terms of the residual atomic core [8]. For each charge state, the Rydberg levels are used to model all higher-lying levels, up to the instantaneous effective boundary of the continuum; in turn, this boundary is usually calculated in the ion sphere approximation (and, more rarely, in the Debye–Hückel approximation) [9]. The effective decrease in statistical weights for higher-lying levels as the boundary energy of the continuum decreases [10] is neglected because of the contradictions between the approaches to estimating this effect quantitatively (see, e.g., [11, 12]). The model used in our simulations assumes that, as the energy of a discrete level becomes higher than the boundary energy of the continuum, all of the electrons occupying this level remain unbound. An increase in the ionization potential above its previous value (e.g., during plasma expansion) is accompanied by the reproduction (or appearance) of the higher lying discrete quantum states, whose population is calculated from the Saha–Boltzmann relationships, which are valid for all discrete levels adjacent to the boundary of the continuum [9, 13].

The set of kinetic equations describes the populations of all quantum states incorporated into the model and expresses each of the populations in terms of the instantaneous populations of the remaining quantum states and the probabilities for all possible quantum transitions. Under the thermodynamic conditions prevailing in small Z-pinches (in the case at hand, the plasma line density is up to 50 mkg/cm), the most probable transitions are spontaneous radiative transitions and transitions induced by free electrons. Transitions

induced by the radiation field and ion impact are neglected because they are far less probable. The model incorporates the following one-electron processes: one-electron ionization (in the case at hand, the ejection of an electron from the outermost shell and from the nearest *nl* subshell, including ionization to the excited states [14, 15]) and transitions within the same charge state (collisional excitation and deexcitation as well as spontaneous radiative transitions).

For carbon, the data on the Grotrian diagrams for an atom and ions, the energies of the bonded states, the oscillatory forces, and the ionization potentials in vacuum are available in the NIST Atomic Database (http://physics.nist.gov/). In the computer code, the probabilities of all collision processes are expressed in terms of their cross sections for an arbitrary distribution function. In this paper, we present the results that were obtained only for a Maxwellian distribution function.

The cross sections for one-electron ionization are described by the semi-empirical formula [16], which is a refined version of the Lotz formula (see, e.g., [17]). Numerous comparisons with the results of quantum mechanical calculations showed that, to within 20%, the semi-empirical formula [16] yields the same ionization cross sections as the disturbed wave (DW) method, including the cross sections for ionizations from and to the excited states. The cross sections for the reverse processes (three-body recombination) are expressed through the ionization cross sections in accordance with the principle of detailed balance [18, 19], which is a consequence of the quantum mechanical reciprocity theorem [20]. The cross sections for multielectron ionization is calculated from the formula obtained in [21]. The cross sections for radiative recombination are described by the Milne formula [18, 19], which relates them to the associated photoionization cross sections, described, in turn, by the Kramers formula. It is well known that, for many-electron ions, the Kramers formula also provides a satisfactory degree of accuracy [9]. The dielectronic recombination is described in accordance with the monograph by Griem [9]. The cross sections for all of the excitation processes are calculated by L.A. Vainshtein's ATOM software program [22, 23], written on the basis of the Coulomb–Born method with allowance for exchange and renormalization. The excitation cross sections are included into the corresponding database and are then used to calculate the excitation probabilities. The cross sections for the reverse processes are expressed in terms of the excitation cross sections through the Klein–Rossealand formula [18, 19], which reflects the principle of detailed balance.

Previously, the model described here (or, more precisely, the corresponding model for a zero-dimensional Z-pinch) was tested by simulating different scenarios for plasma ionization. The software program devised for integrating the set of ODEs numerically is based on the Gear method [24] and includes the corresponding program module from the NAG library, which is widely used in computations. According to the present-day classification, the Gear method belongs to a class of the so-called "multivalued" methods. Given that the step of numerical integration is constant, the family of these methods is equivalent to the backward differentiation formulas [25–27]. The implicit backward differentiation formulas provide a high degree of approximation by the use of the results calculated at several preceding time steps, in which case, however, in several initial time steps, the set of ODEs should be integrated by some other numerical method. In contrast to these formulas, the Gear method starts to integrate the equations immediately from the first time step and has a variable order of approximation (convergence). At several initial time steps, it may have a somewhat lower order of convergence [25]. These intrinsic properties of the Gear method constitute its advantage in investigating the zero-dimensional model, because they make it possible to obtain solutions for different scenarios of the ionization of Z-pinch plasmas, including those at the limits of applicability of the physical model [21]. However, computer programs making allowance for ionization that were described in [21] are somewhat difficult to combine directly with the above MHD module of the code. In this context, the main advantage of the Gear method (namely, an algorithm for automatic choice of the time step, guaranteeing the desired accuracy) becomes unnecessary because the equations of ionization kinetics are integrated on a too short time scale and, accordingly, the mean degree of approximation decreases. On the other hand, the number of references to the subroutine integrating the set of kinetic equations is large.

In order to increase the mean order of convergence of the Gear method and to successfully carry out integration over the above initial time steps, the subroutine integrating the set of kinetic equations was called up after a fixed number of time steps. Note that, during the calculation of the processes occurring in a plasma, the time intervals after which the subroutine integrating the set of quantum mechanical equations was called up became progressively shorter. Simultaneously, the ionization processes being modeled became more rapid, thereby shortening the time integration step and, as a consequence, the time intervals after which the subroutine integrating the set of kinetic equations was called up.

The above features of the one-dimensional numerical method did not allow us to implement the two-dimensional method on sufficiently fine difference meshes, because a decrease in the spatial cell size leads to a proportional decrease in the time step and, consequently, worsens the approximation achievable in the calculation of ionization processes. Using implicit schemes does not improve the situation. The reason is that it is necessary to satisfy not only the Courant condition [28, 29] but also the following condition, which is important for a correct description of the physical

processes incorporated into the model: in each time step, the perturbations in the pinch should propagate through no more than one Lagrangian cell. These restrictions could be overcome by using implicit schemes, but then the model of ionization processes would be incorrect. Nevertheless, the results obtained in our numerical experiments are of interest from the physical standpoint.

3. NUMERICAL RESULTS FROM THE ONE-DIMENSIONAL MODEL

We simulated a Z-pinch in a carbon plasma. The line pinch density was in the range from 0.006 to 0.01 mg/cm, and the initial pinch radius was 2.6 cm. These values are close to the experimental data of [1–3]. We did not solved the electric-circuit equation but instead interpolated the experimental dependence of the total current in the circuit [1–3]. This dependence is well approximated by a straight line corresponding to a current rise time of 610 ns and a peak current of 300 kA. Because of the large amount of calculations, we succeeded in tracing all stages of the Z-pinch evolution on a mesh consisting of only 30 cells. A typical scenario for the pinch evolution can be described as follows. Initially (during a time interval of about 200 ns), the plasma is essentially at rest. The plasma of the liner is slightly heated only in the nascent corona (a low-density current-carrying plasma region), and this process is accompanied by a small increase in the effective ion charge number. In the remaining liner regions, the initial ion charge number (0.9) is somewhat different from its equilibrium value at these densities and temperatures, so that the effective ion charge number also increases only slightly (up to 0.93) and the plasma electron temperature decreases from 2 to 1.6–1.8 eV. At about 200 ns after the switching-on of the current, the liner starts moving, in which case the plasma is largely concentrated near the outer pinch boundary and the corona practically disappears; i.e., the “snowplow” effect is observed.

Figure 1 illustrates the time evolution of the radial profiles of the plasma mass density in the pinch. The profiles shown in Fig. 1a were obtained at 0, 150, 225, and 300 ns in the initial stage, during which the liner

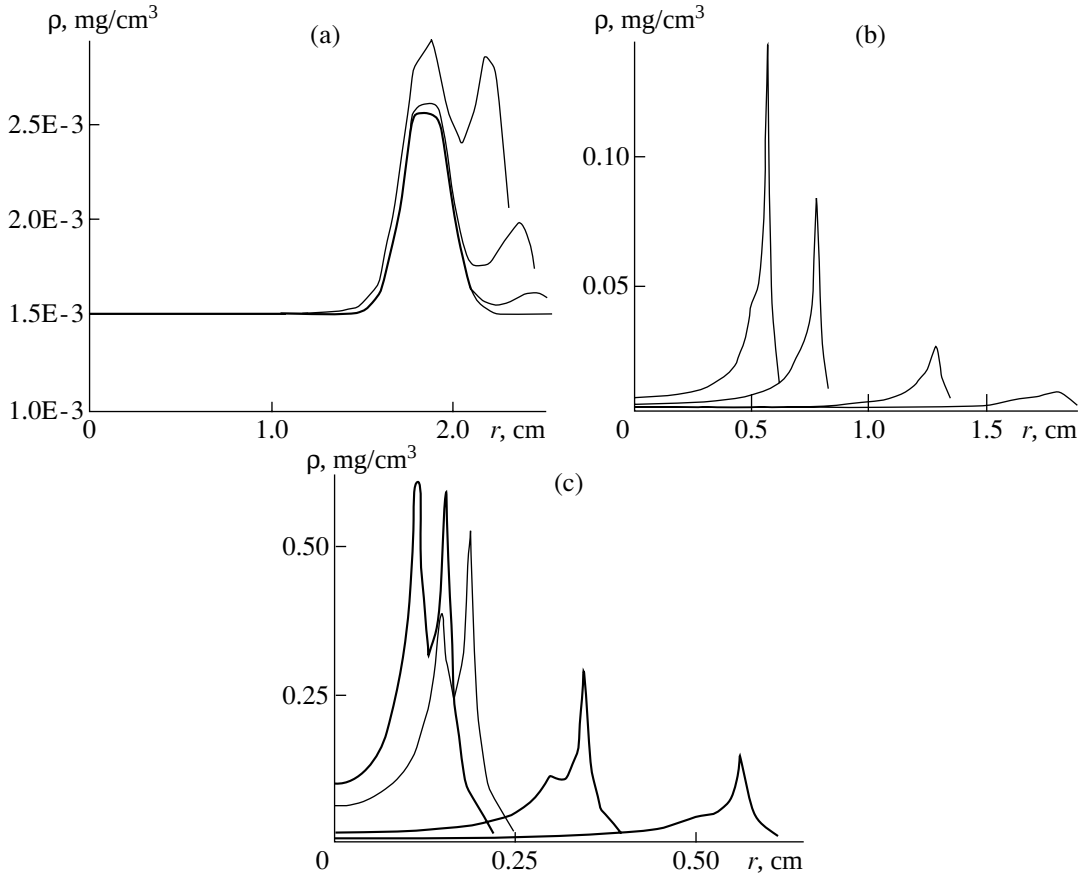

Fig. 1. Radial profiles of the plasma mass density obtained in the plasma compression stage and in the initial stage of plasma expansion. The profiles in Fig. 1a were calculated at 0, 150, 225, and 300 ns. The profiles in Fig. 1b were calculated at 420, 510, 570, and 590 ns. The profiles in Fig. 1c were calculated near the time of maximum compression, i.e., at 610, 630, and 655 ns (from right to left). The profile calculated at the time when the plasma starts expanding (690 ns) is shown by a light curve.

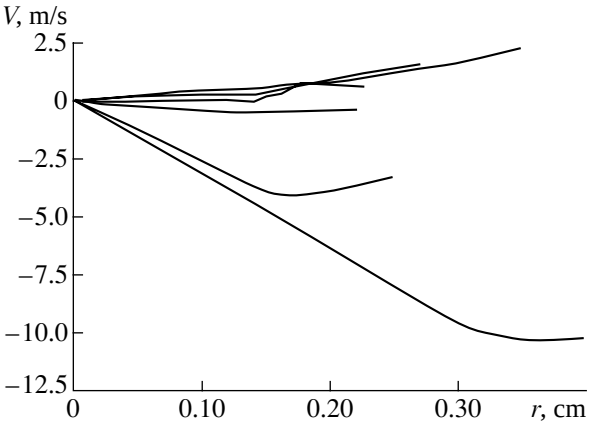

Fig. 2. Radial profiles of the plasma velocity calculated at 610, 630, 655, 690, 730, and 770 ns (from top to bottom).

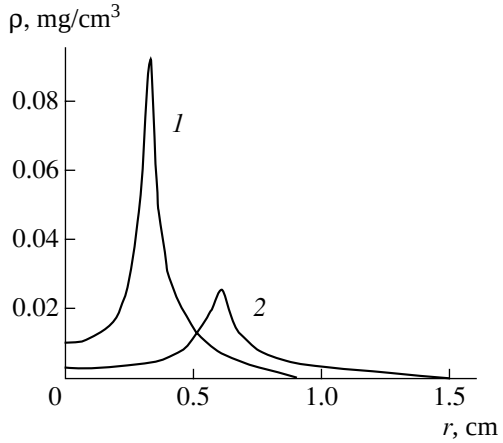

Fig. 3. Radial profiles of the plasma mass density obtained in the stage of plasma expansion (at 970 and 1170 ns).

plasma is at rest. At later times (up to about 550 ns), the plasma is compressed in essentially the same manner. The plasma mass is mostly accumulated in the snowplow region. The profiles shown in Fig. 1b were obtained at 420, 510, 570, and 590 ns. We can see that, after 550 ns, a shock wave forms ahead of the snowplow region.

Figure 1c shows the radial profiles of the plasma mass density calculated at 610, 630, 655, and 690 ns, i.e., over the time interval from the instant at which the current in the external electric circuit is switched on (610 ns) to the instant at which the plasma starts to expand (690 ns). The profile corresponding to the latter instant is shown by a light curve. We can clearly see the reflection of a shock wave from the pinch axis and the formation of an entropic layer [7], in which the plasma temperature is elevated and the plasma density is depressed. Such entropic effects are an undesirable feature of the numerical methods used to solve the MHD equations. The entropic layer is present throughout all subsequent stages of calculations and, as will be shown below, decreases the reliability of the results obtained in the stage of plasma expansion.

At the time of maximum compression, all the liner plasma essentially comes to a stop. Figure 2 shows the radial profiles of the plasma velocity calculated at 610, 630, 655, 690, 730, and 770 ns. We can see that, at 650 ns, the plasma is practically at rest, and, at 690 ns, it expands with a certain positive velocity. A discontinuity in the plasma velocity is associated with the reflection of the shock wave from the outer boundary of the liner. The representative radial profiles of the plasma mass density in the expansion stage (at 970 and 1170 ns) are shown in Fig. 3. The plasma velocity is uniform along the pinch radius, the maximum velocity at 1170 ns is about 3 cm/ms, and the radius of the entropic layer, which is present as before, is now about 5–6 mm.

Figure 4 illustrates the time evolution of the radial profiles of the electron and ion temperatures. The profiles were calculated at 610, 630, 655, and 690 ns. It is notable that the ion temperature in the entropic layer increases considerably (from 1300 to 4000 eV). The possible causes of this phenomenon will be discussed below. The ion temperature values behind the shock wave seem to be quite realistic (from 300 to 800 eV). This is also true for the electron temperature values in the main plasma (from 50 to 80 eV) and in the corona (from 100 to 350 eV).

Note that, at these times, the plasma is ionized almost completely, except in the maximum density region, in which the mean ion charge number is about five. The dynamics of the mean ion charge number in the plasma at earlier times (at 420, 510, 570, and 590 ns) is illustrated in Fig. 5. The ion charge in the corona increases because, at such electron temperatures, the magnetic field does not penetrate into the plasma, but rather is completely concentrated in the skin layer. Under these conditions, the Joule heating of the plasma in the skin layer plays an important role: in particular, it increases the mean ion charge. Initially, an increase in the mean ion charge ahead of the skin layer is associated with the effects of electron heat conduction, and later, with the combined action of electron heat conduction and the heating by a propagating shock wave.

Unfortunately, a completely developed shock wave affects the course of calculations: it slightly decreases the reliability of the results computed in the stage of plasma expansion.

We now address the question of the temperature increase immediately before the focusing of the shock wave at the pinch axis. This increase can only be explained as being due to the formation of one more (weaker) shock wave, which was focused at the axis at an earlier time and was not captured numerically because the time intervals after which the calculated

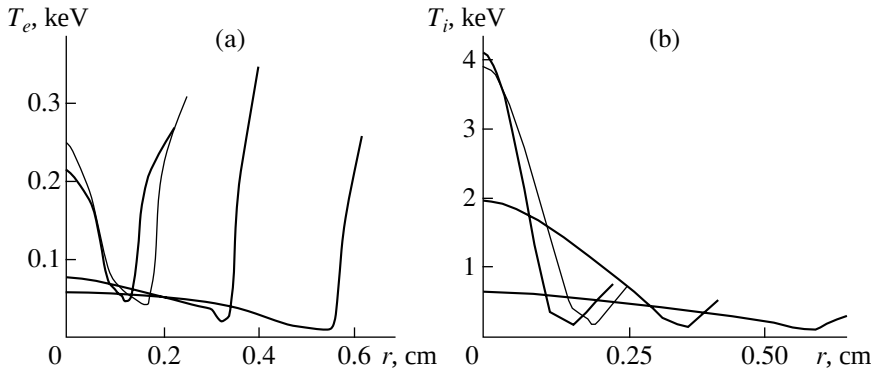

Fig. 4. Dynamics of the (a) electron and (b) ion temperatures. The radial profiles were calculated at 610, 630, and 655 ns. The profiles calculated at the time when the plasma starts expanding (690 ns) are shown by the light curves.

results were read into computer memory were too large. Such a wave does indeed exist and was captured in the simulations of a pinch with a line density of 0.01 mg/cm and with small values of the artificial viscosity coefficients on the difference mesh.

Because of the larger mass of the pinch, it was compressed on a somewhat longer time scale (about 695 ns). Figure 6 shows the radial profiles of the effective ion charge number, plasma mass density, and electron and ion temperatures calculated at 670 and 690 ns.

In the case of a liner with a line density of 0.01 mg/cm, the time 690 ns coincides not only with the time at which a weaker shock wave starts to form but also with the time at which the previous shock wave is reflected from the axis. On the calculated profiles, one can see the nascent entropic layer and oscillations stemming from the small artificial viscosity used in the simulation of the liner under consideration. The oscillations are most pronounced in the radial profile of the electron temperature. The oscillations of the effective ion charge number result from those of the electron temperature.

Another interesting effect revealed in simulations is that the electron temperature and effective ion charge number oscillate in a fixed Lagrangian cell. Such small-amplitude periodic variations in the electron temperature in a fixed cell were observed between 300 and 500 ns in essentially all of the calculation versions. Unexpectedly, this effect was also captured by two-dimensional modeling.

4. RESULTS OF TWO-DIMENSIONAL SIMULATIONS

Here, we describe the results of modeling of a pinch with a line density of 0.006 mg/cm, an initial radius of 2.6 cm, and a length of 2 cm. The pinch was initiated in a carbon gas between two electrodes, which were assumed to be "cold" (in simulations, their temperature was set equal to zero) and impenetrable by the plasma. The corresponding boundary conditions for Eqs. (1)–(5) were chosen to be analogous to those used in [4].

Up to 500 ns, a two-dimensional pinch evolves in the same manner as a one-dimensional pinch, the only difference being that the plasma temperature near the cold electrodes is slightly depressed. The discrepancy between the evolutions becomes significant on longer time scales. The depressed temperature of the electrode plasmas (Fig. 7) gives rise to a slight longitudinal (in the z-direction) plasma inhomogeneity, which is enhanced by oscillations of the plasma temperature and of the effective ion charge number. As a result, two inward-directed plasma jets form at a distance of about 0.3 cm from each of the electrodes. The jets are distinctly seen in the ion pressure distribution in Fig. 8 and in the projections of the isolines of the plasma mass density in Fig. 9.

Figures 7–9 show the distributions calculated at 630 ns, at which time, two jets reach the symmetry axis

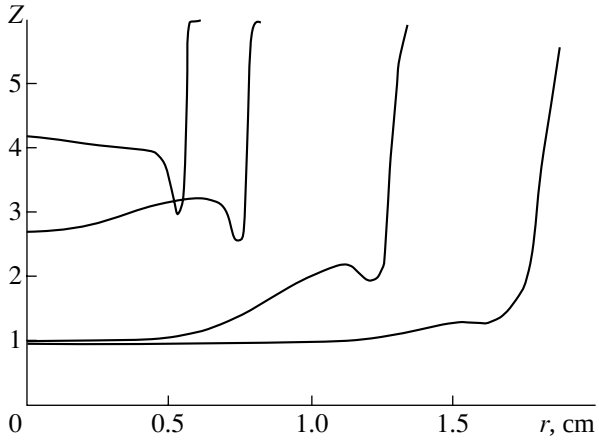

Fig. 5. Radial profiles of the mean ion charge calculated in the liner compression stage (at 420, 510, 570, and 590 ns).

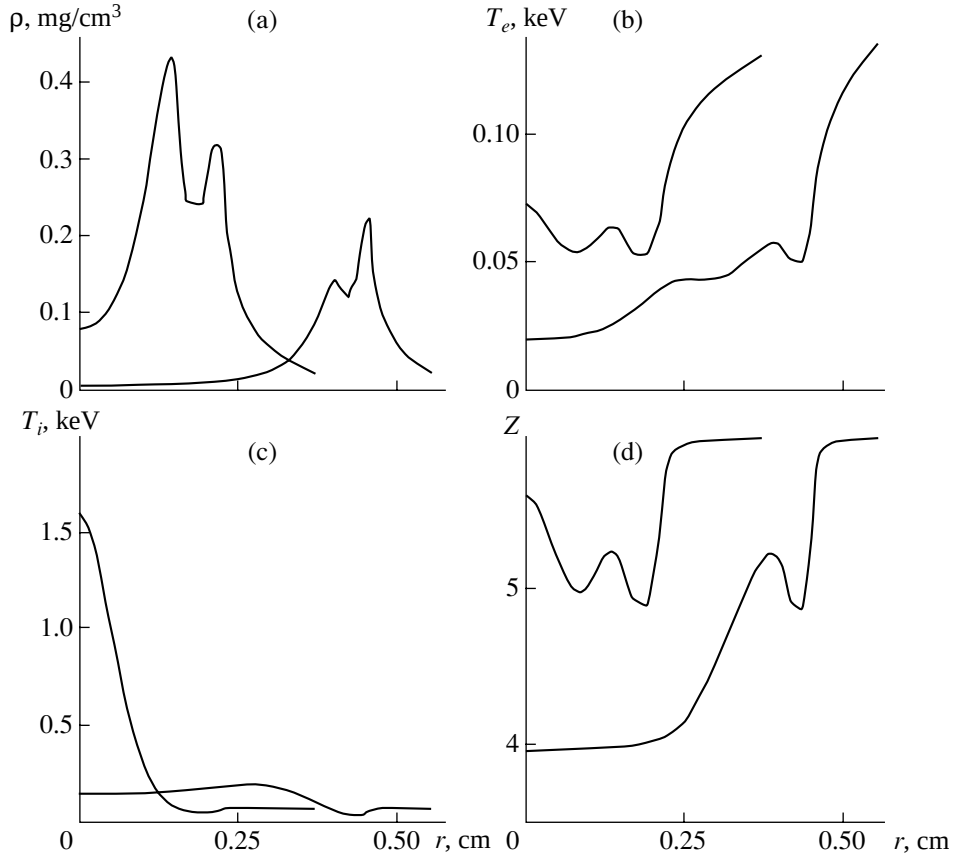

Fig. 6. Reflection of a shock wave from the axis and formation of a subsequent shock wave during the evolution of a pinch with a line density of 0.01 mg/cm. The radial profiles of the (a) plasma mass density, (b) electron and (c) ion temperatures, and (d) mean ion charge number were calculated at 670 and 690 ns. At 670 ns, the position of the shock front (at about 1 mm) is most clearly seen in the electron temperature profile. The entropic layer is seen to develop at 690 ns.

(Fig. 8) and the third jet forms in the main pinch just between the electrodes. This jet is seen in both the ion pressure (Fig. 8) and plasma mass density (Fig. 9) distributions. It appears in the region of elevated electron temperature.

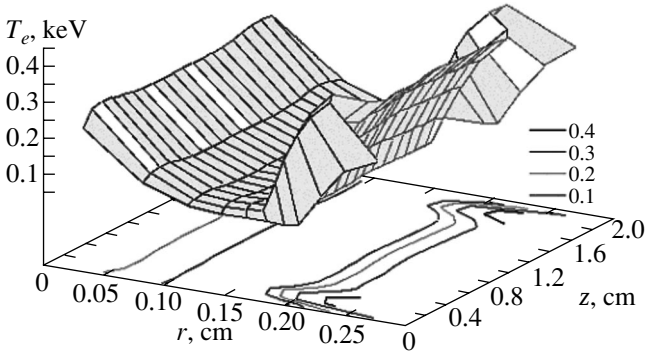

Fig. 7. Electron temperature distribution in two-dimensional modeling.

After the jet reaches the pinch axis, the electron and ion temperatures in the axial region increase. The calculated results show that the ion temperature increases to a significant extent, specifically up to 6–7 keV, which is high in comparison with the ion temperature in the "cold" regions (4 keV). However, such a significant increase is only associated with the entropic effects. In the electron temperature distribution, similar hot points appear somewhat later. They are associated with the energy exchange between very hot ions and comparatively cold electrons and are less pronounced than those in the ion temperature distribution. The presence of hot points at the pinch axis can be established primarily from the calculated ion pressure distribution, because the ion pressure is least sensitive to the entropic effects.

Unfortunately, we failed to obtain the two-dimensional picture of plasma motion on time scales longer than 670 ns.

On time scales of up to 500 ns, the perturbations of the outer pinch boundary were found to result only in slight deviations from the evolution of a one-dimensional pinch.

5. USE OF THE CLUSTER OF PERSONAL COMPUTERS FOR TWO-DIMENSIONAL SIMULATIONS

Estimates show that, with present-day single-processor personal computers (PCs), numerical integration of two-dimensional problems on fine meshes (containing from 60×134 to 100×204 Lagrangian cells) usually takes from a week to a month of computer time. Because of this, it is desirable to exploit parallel computers. Since most computer time (up to 90%) is expended on simulating the kinetic (quantum mechanical) part of the problem, it is expedient to parallel only kinetic calculations, whereas the hydrodynamic processes and magnetic field diffusion can be simulated, as before, on a single-processor PC.

Even with the semiautomatic estimation of the run time of the program (™BERT77, the trademark of Paralogic Inc., http://www.plogic.com), it was not possible to estimate the total time required to execute it, because the cycles in the program are organized so that it terminates only when the prescribed accuracy is achieved. In order to estimate the actual efficiency of using a parallel computer, we carried out some test measurements in solving the kinetic part of the problem on the above difference mesh under the Linux operating system on a PC with a Celeron-366 microprocessor. On average, this part took 27 min of computer time. The fact that the kinetic part can be calculated for each Lagrangian cell independently opens great possibilities for using parallel computers. In order to distribute the kinetic calculations almost equally between 12 processors in a PC cluster, the difference mesh was divided into 12 equal components in the radial direction. The choice of the direction was dictated by the fact that the main perturbations (shock waves) propagate from the periphery of the plasma toward its center, so that, with such a division of the plasma region, the processors handle an approximately equal number of Lagrangian cells adjacent to the shock front.

The execution of the remaining part of the program requires that the amount of information exchanged between the PCs be 280 KB, which takes less than one second.

Estimates showed that, on a PC cluster organized in this way, calculating the kinetic part of the problem takes about 2.5 minutes. With allowance for the time required to execute all of the moduli of the program, the cluster completes the problem 10.8 times faster than does a single-processor PC.

Let us consider some of the results from two-dimensional simulations on a PC cluster. The results again refer to a pinch with a line density of 0.006 mg/cm, an initial radius of 2.6 cm, and a length of 2 cm, but now the simulations were carried out on a finer mesh. The pinch was initiated in a carbon gas between two electrodes, which were assumed to be "cold" (in simulations, their temperature was set equal to zero) and impenetrable by the plasma. In order to describe the

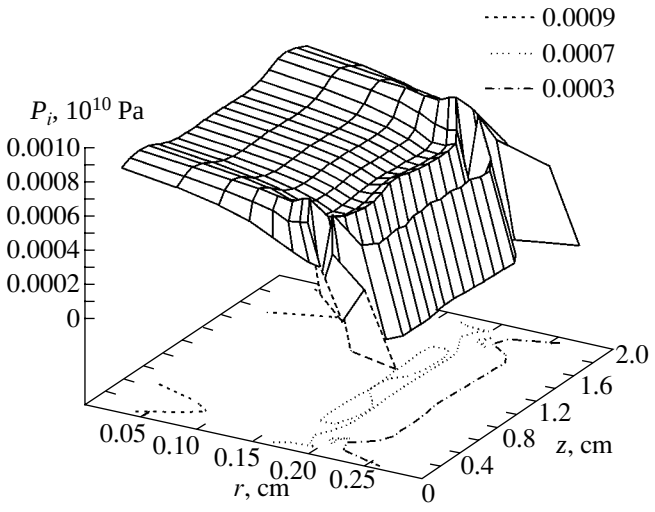

Fig. 8. Ion pressure distribution and the initial stage of the formation of hot points at the axis in two-dimensional modeling.

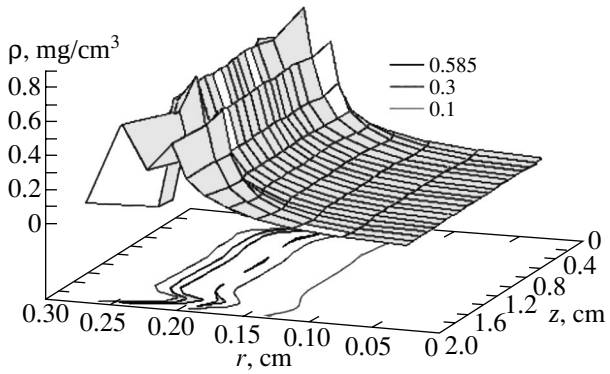

Fig. 9. Distribution of the mass density of a plasma compressed to one-tenth of its initial volume.

effects of the Rayleigh–Taylor instability, the conditions imposed at the right boundary of the plasma region specified a small sinusoidal perturbation with an amplitude of 0.25 to 5% of the initial pinch radius. The problem was solved on meshes containing from 60×134 to 100×206 Lagrangian cells, and the corresponding calculations on a 12-PC cluster took from 24 to 48 h.

In order to illustrate the effects revealed in simulations, we present the electron and ion temperature distributions calculated for a pinch whose right boundary was perturbed sinusoidally at an amplitude of about 2.5% of the initial pinch radius. The temperature distributions obtained from two-dimensional simulations on a fine mesh are shown graphically in Fig. 10, in which only each fourth point obtained in every direction is plotted. We can see that the compression proceeds in

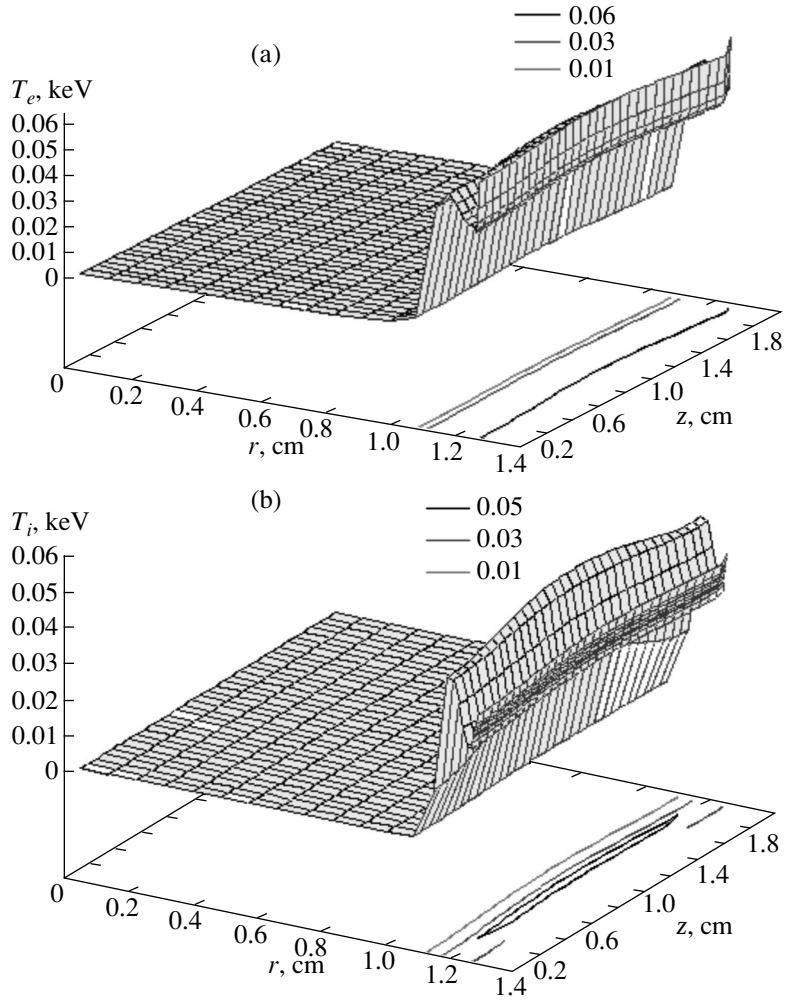

Fig. 10. Electron and ion temperature distributions calculated on a fine (60×134) mesh on a PC cluster at 450 ns (only some of the calculated points are plotted). Small-scale structures are seen to appear near the cooled electrode.

essentially the same way as in the above one-dimensional case. On such time scales, the Rayleigh–Taylor instability does not affect the compression of the liner. Nonetheless, small-scale structures are seen to appear near the electrodes (Fig. 10). The PC cluster was capable of handling the problem on time scales of about 500–510 ns. On longer time scales, the simulations were terminated because of the rapid deformation of the Lagrangian mesh near the cooled electrode.

6. CONCLUSIONS

An analysis of the results of our one- and two-dimensional simulations show that we can speak of the formation of a high-density plasma layer and its subsequent transformation into a shock wave. Although our numerical experiments provide indirect evidence for such behavior of an imploding plasma, they cannot give detailed information about the underlying mechanisms that cause it. It is also of interest to point out the role of the supersonic propagation of the ionization front: presumably, it is this factor that is responsible for the destruction of a shock wave.

Note that our main results were obtained on fairly rough meshes, containing from 17×17 to 27×47 Lagrangian cells. On a mesh with 30 cells, one-dimensional calculations of all the stages of the process (compression, pinching, and plasma expansion) on time scales of about 1200 ns require 60–80 h of computer time on a PC with a Celeron-433 microprocessor; moreover, about 90% of this time is expended on simulating the kinetic (quantum mechanical) part of the problem. Even with very rough meshes, two-dimensional simulations of the pinch evolution up to the stage of maximum compression require at least 100 h. The progress toward the development of the models combining hydrodynamic and quantum mechanical approaches is expected to be made through increased use of parallel computers. That this way is promising is evidenced, in particular, by the results of our work.

ACKNOWLEDGMENTS

This work was supported in part by the Israeli Academy of Sciences and Arts, INTAS (grant no. 97-0021), and the Russian Foundation for Basic Research (project no. 01-01-00401).

REFERENCES

1. M. E. Foord, Y. Maron, G. Davara, *et al.*, Phys. Rev. Lett. **72**, 3827 (1994).
2. M. E. Foord, Y. Maron, G. Davara, *et al.*, Phys. Rev. Lett. **73**, 1190 (1994).
3. G. Davara, L. Gregorian, E. Kroupp, and Y. Maron, Phys. Plasmas **5**, 1068 (1998).
4. Yu. G. Kalinin, A. S. Kingsep, V. I. Kosarev, and A. I. Lobanov, Mat. Model. **12** (11), 47 (2000).
5. A. A. Samarskiĭ and Yu. P. Popov, *Difference Methods for Solving Gas Dynamics Problems* (Nauka, Moscow, 1992, 3rd ed.).
6. A. S. Kingsep, V. I. Kosarev, A. I. Lobanov, and A. A. Sevast'yanov, Fiz. Plazmy **23**, 953 (1997) [Plasma Phys. Rep. **23**, 879 (1997)].
7. R. P. Fedorenko, *Introduction to the Computer Physics* (MFTI, Moscow, 1994).
8. L. M. Biberman, B. S. Vorob'ev, and I. T. Yakubov, *Kinetics of Nonequilibrium Low-Temperature Plasmas* (Nauka, Moscow, 1982; Consultants Bureau, New York, 1987).
9. H. R. Griem, *Principles of Plasma Spectroscopy* (Cambridge Univ. Press, Cambridge, 1997).
10. V. E. Fortov and I. T. Iakubov, *Physics of Nonideal Plasma* (Inst. Khim. Fiz., Chernogolovka, 1984; Hemisphere, New York, 1990).
11. R. M. More, Adv. At. Mol. Phys. **21**, 305 (1985).
12. D. G. Hummer and D. Michalas, Astrophys. J. **331**, 794 (1988).
13. H. R. Griem, *Plasma Spectroscopy* (McGraw-Hill, New York, 1964; Atomizdat, Moscow, 1969).
14. D. H. Sampson, Phys. Rev. A **34**, 986 (1986).
15. M. E. Foord and E. Nardi, J. Appl. Phys. **68**, 5028 (1990).
16. V. A. Bernshtam, Yu. V. Ralchenko, and Y. Maron, J. Phys. B **33**, 5025 (2000).
17. S. M. Younger and T. D. Mark, in *Electron Impact Ionization*, Ed. by T. D. Mark and G. H. Dunn (Springer-Verlag, New York, 1985).
18. I. I. Sobelman, L. A. Vainshtein, and E. A. Yukov, *Excitation of Atoms and Broadening of Spectral Lines* (Springer-Verlag, Berlin, 1995).
19. J. Oxenius, *Kinetic Theory of Particles and Photons* (Springer-Verlag, Berlin, 1986).
20. L. D. Landau and E. M. Lifshitz, *Quantum Mechanics: Non-Relativistic Theory* (Nauka, Moscow, 1989; Pergamon, New York, 1977).
21. V. I. Fisher, Yu. V. Ralchenko, A. A. Goldgrish, *et al.*, J. Phys. B **28**, 3027 (1995).
22. V. P. Shevelko and L. A. Vainshtein, *Atomic Physics for Hot Plasmas* (Inst. of Physics Press, Bristol, 1993).
23. V. I. Fisher, Yu. V. Ralchenko, V. A. Bernshtam, *et al.*, Phys. Rev. A **55**, 329 (1997).
24. D. Kahaner, C. Moler, and S. Nash, *Numerical Methods and Software* (Prentice-Hall, Englewood Cliffs, 1989; Mir, Moscow, 1998).
25. E. Hairer, S. Norsett, and G. Wanner, *Solving Ordinary Differential Equations*, Vol. 1: *Nonstiff Problems* (Springer-Verlag, Berlin, 1987; Mir, Moscow, 1990).
26. E. Hairer and G. Wanner, *Solving Ordinary Differential Equations*, Vol. 2: *Stiff and Differential-Algebraic Problems* (Springer-Verlag, Berlin, 1996; Mir, Moscow, 1999).
27. A. Nordsieck, Math. Comput. **16**, 22 (1962).
28. S. K. Godunov and V. S. Ryaben'kiĭ, *Difference Schemes* (Nauka, Moscow, 1977).
29. D. A. Anderson, J. C. Tannehill, and R. H. Pletcher, *Computational Fluid Mechanics and Heat Transfer* (Hemisphere, New York, 1984; Mir, Moscow, 1990), Vols. 1, 2.

Translated by O. Khadin

Plasma Physics Reports, Vol. 28, No. 4, 2002, pp. 296–302. Translated from Fizika Plazmy, Vol. 28, No. 4, 2002, pp. 329–336.

PLASMA DYNAMICS

Dynamics of an Al Wire Corona of a Megaampere Z-pinch

P. Kubeš*, J. Kravárik*, O. Renner, E. Krouský**, Yu. L. Bakshaev***, P. I. Blinov***, A. S. Chernenko***, E. M. Gordeev***, S. A. Dan'ko***, V. D. Korolev***, and A. Yu. Shashkov*****

**Czech Technical University, Technická 2, 166 27 Prague 6, Czech Republic*

***Institute of Physics, Na Slovance 2, 182 21 Prague 8, Czech Republic*

****Russian Research Centre Kurchatov Institute, pl. Kurchatova 1, Moscow, 123182 Russia*

Received October 4, 2001

Abstract—It is shown that the development of instabilities in a Z-pinch plasma formed by loading a relatively thick Al wire (an initial diameter of 120 μm and a maximum discharge current of 2–3 MA) is slowed down due to the high plasma density in the wire corona. A cylindrically symmetric, regular, and stable corona surrounding the wire contains a helical formation with a dense, cold, and magnetized plasma. X-ray pulses with a photon energy of several keV and an FWHM duration of 10–20 ns are generated by a few imploded neck structures in the pinch phase of the corona evolution (70–100 ns after the current onset). The main part of X radiation emitted by individual bright spots in the photon energy range 1.5–2.4 keV (up to 40 J at a peak power of 4 GW) consists of the continuum and the bound–bound transition radiation from H- and He-like Al ions. A possible scenario for the axial magnetic field evolution during an X-ray pulse is outlined. © *2002 MAIK "Nauka/Interperiodica".*

1. INTRODUCTION

Z-pinches, which are the most intense sources of X radiation, offer a large variety of applications [1]. Currently, the main subject of Z-pinch investigations is the suppression of instabilities and the optimization of the X-ray yield. Liners [2–4] and fibers [5] are often used as discharge loads. Recently, the diagnostic characteristics of a plasma corona formed on a wire load at a current of several megaamperes were reported [6–8]. Most of the radiation is emitted in the thermal energy range from 10 to 200 eV in the phase of maximum compression. Only a few percent of the overall emission corresponds to unstable and randomly located hot spots emitting in the kiloelectronvolt energy range. A systematic investigation of the stable corona generated by using thicker fibers in small Z-pinch devices and, in particular, its intense nonthermal emission have recently been reported [9–12]. Strong emission in the wavelength range 17–25 nm accompanying the explosion of a carbon fiber with a diameter of 6–20 μm was observed at a discharge current of 20 kA [9, 10]. Loading a graphite rod with a diameter of 2 mm resulted in the creation of a relatively stable corona with a helical or toroidal surface [11], which emitted in the wavelength range 14–21 nm. The soft X-ray and VUV spectra of the corona produced in the same device with carbon fibers 20 and 100 μm in diameter [12] indicated that 60% of the energy was emitted in the nonthermal range 17–35 nm; the recombinative character of the emitted lines was pointed out.

A fairly large diameter of the wires used in those experiments seems to be a stabilizing factor. Presumably, the fiber material in the central region near the axis remains in solid state and the corona plasma is confined by the high magnetic field. High-energy photons are mainly emitted from the helical and ringlike structures. In this paper, we present analogous diagnostic results on the corona generated with thicker wires (up to 120 μm) by using an S-300 megaampere Z-pinch generator (4 MA, 70 ns) developed at the Russian Research Centre Kurchatov Institute, Moscow.

2. EXPERIMENTAL TECHNIQUE AND DIAGNOSTIC SETUP

A powerful pulsed S-300 machine [13] is intended for investigating the compression of a liner or fiber corona and the development of bright X-ray sources. The eight-module generator (see Fig. 1) consists of a capacitor energy storage system; two water pulse-forming stages; and a vacuum chamber, containing an energy concentrator based on magnetically insulated transmission lines (MITL). The output forming stage, transmission lines, and the vacuum chamber are placed in a common water tank 4 m in diameter. The current flowing through the wire attains 3 MA, and the current rise time is 100 ns.

The complex information on the pinch behavior was obtained with a set of diagnostics (Fig. 2):

(i) visible photography with a streak camera observing the plasma in the radial direction with a slit aligned either parallel to the wire axis or perpendicular to it (in the latter case, a region located at a distance of 4 mm from the anode and cathode faces was observed) and

1063-780X/02/2804-0296$22.00 © 2002 MAIK "Nauka/Interperiodica"

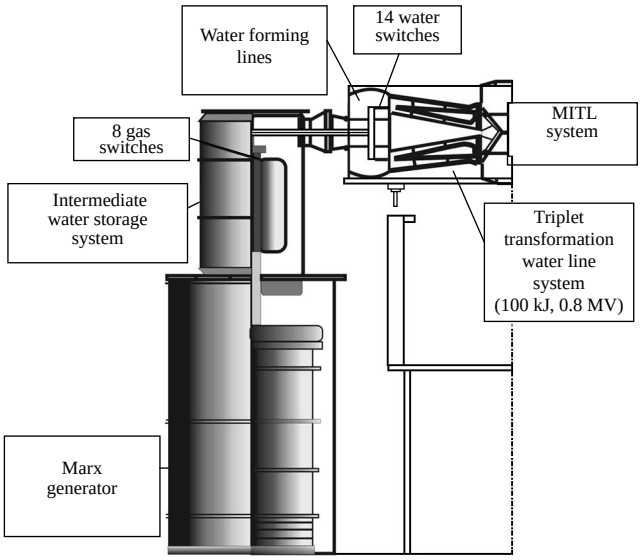

Fig. 1. Schematic of the S-300 Z-pinch generator. The vertical axis of the installation is indicated on the right-hand side of the figure.

three frame image converters (FICs) grabbing plasma images in the radial direction with an exposure time of 3 ns with an interval between frames of 10–15 ns;

(ii) VUV and soft X-ray FIC photography with an exposure time of 3 ns;

(iii) detection of X-ray emission with two beryllium-filtered semiconductor PIN diodes observing plasma from both radial and axial directions with a temporal resolution of 3–4 ns;

(iv) convex mica crystal X-ray spectrometer with one-dimensional spatial resolution, absolutely calibrated in a photon energy range of 1–10 keV;

(v) pinhole camera (100-μm diameter pinhole filtered with mylar and Al foils) located in the radial position; and

(vi) two- or three-frame shadow and schlieren diagnostics based on the second harmonics emission of a YAD : Nd laser (a wavelength of 532 nm and pulse duration of 10 ns) and observing the plasma in the radial direction.

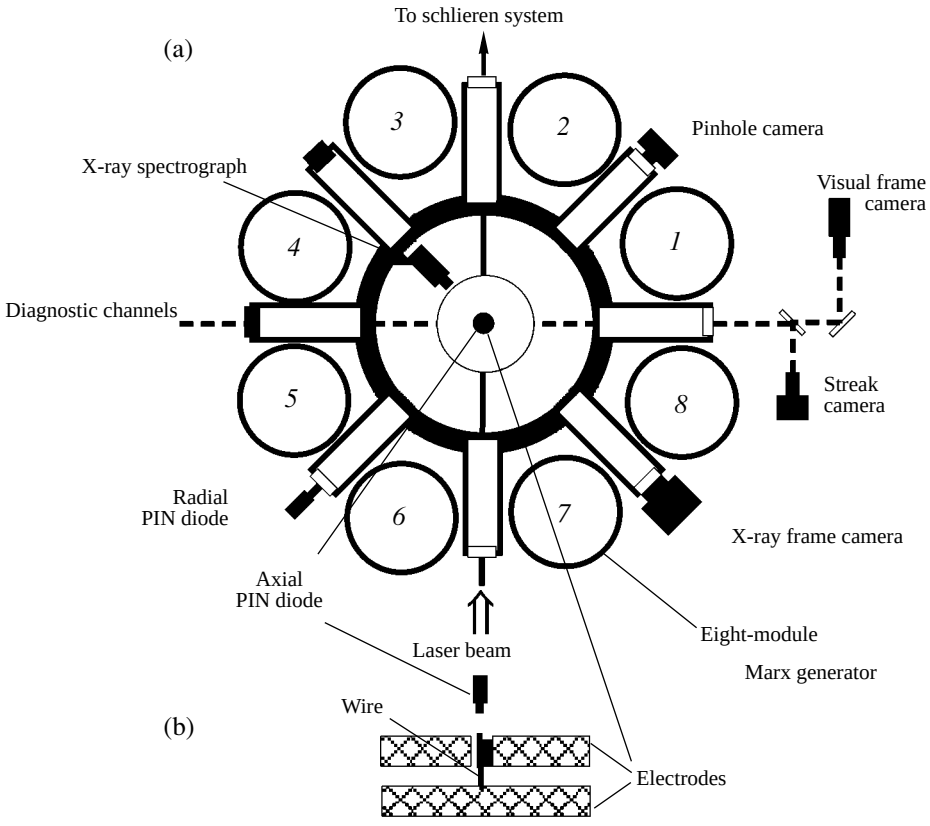

Fig. 2. Spatial configuration of the diagnostics: (a) axial and (b) radial views.

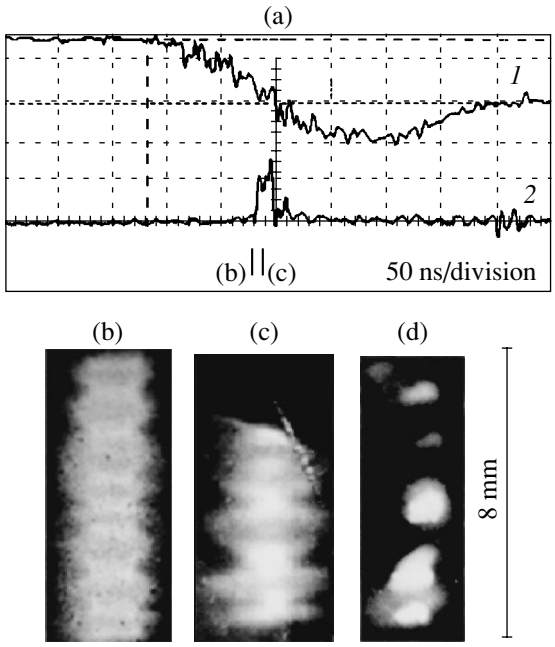

Fig. 3. Shot no. 193: (a) oscilloscope records of (*1*) the current and (*2*) X-ray signal from a PIN diode filtered with a beryllium foil, (b, c) X-ray frame images, and (d) a pinhole image filtered with a 10-μm Al foil and 10-μm mylar foil. One can see the spatial correlation between the regular necks (b), imploding necks (c), and bright spots (d) and the temporal correlation between the imploding necks (c) and the X-ray pulse (a). Marks on the bottom of plot (a) indicate the instants corresponding to frame images (b) and (c).

3. EXPERIMENTAL RESULTS

In the experiments, Al wires with a diameter of 120 μm and length of 8 mm were used as loads. To demonstrate the complexity of the diagnostics used to explore the pinch plasma, Figs. 3–5 show the temporally and spatially resolved data taken at three different shots. The data presented in these records are of key importance for understanding the evolution and properties of the corona and X-ray bursts. Their detailed interpretation is given in Section 4.

The absolutely calibrated PIN diodes were filtered with beryllium foils 100–300 μm thick. During each discharge, they detected one to three short X-ray bursts with a FWHM duration of ~10–20 ns. The bursts were emitted randomly 70–100 ns after the current onset. Typical examples of oscillograph records are shown in Figs. 3a, 4a, and 5a; trace *1* characterizes the discharge current (1.3 MA/division) and traces *2* and *3* correspond to the axial and radial PIN diode signals, respectively. At the bottom, the instants of the relevant diagnostic records are marked. The sensitivity range of the X-ray frame cameras corresponded to the photon energy range 0.02–10 keV. The records exposed before an X-ray burst display a regular sausage structure containing five to eight brighter ringlike constrictions (necks) with a diameter of 1.8–2 mm and darker crests with a diameter of 2–3.5 mm, in which the plasma expands in the radial direction (Figs. 3b, 4d, 5b).

These radially symmetric regular structures are stable over several nanoseconds. Photographs exposed during the X-ray bursts display the increase in the neck brightness and the implosion of one to five necks to a diameter smaller than 1 mm with a velocity of 2×10^6 cm/s and the explosion of the crests to a diameter of 6–10 mm with a velocity of (5–10) × 106 cm/s (Figs. 3b, 3c, 5b, 5c).

A similar plasma behavior was observed with the use of the schlieren diagnostics. Two records shown in Figs. 4b and 4c were exposed with a time interval of 50 ns. The images were recorded by using the refraction of a probing diagnostic laser beam in the outer plasma layers, where the electron density gradient is fairly high.

Schlieren images recorded before an X-ray burst clearly display four to five necks with a diameter of about 2 mm and a crest with a diameter of 2.5 mm (Fig. 4b). Schlieren images recorded during an X-ray burst (Fig. 4c) show that some necks implode to lower than 1 mm and the crests expand to 6–10 mm. The corona contour indicates that the instability is symmetric along the axis. The positions of the imploded necks in the schlieren images correlate well with those in the X-ray frame images recorded before the plasma corona starts to expand (Fig. 4c, 4d). After the X-ray burst, the corona shape becomes irregular.

The pinhole camera records were protected from visible light by using an aluminized mylar film 12 μm thick or a combination of a 12-μm mylar film and 10-μm aluminum film (X-ray emission with a photon energy lower than 1 keV was cut off). The filtered images indicate that the keV radiation is emitted from oblong spots with characteristic dimensions of ~1 mm. These spots corresponds to the imploded necks visualized by schlieren and X-ray frame diagnostics (Fig. 3d).

The velocity of the corona expansion (10^6 cm/s) was estimated from the visible streak camera images (Fig. 5f) observed perpendicularly to the wire axis. This velocity is constant to about 300 ns after the current onset, i.e., up to the end of the corona expansion (which probably corresponds to the time of the complete wire evaporation). In the course of the neck evolution, the diameter of the intense plasma region decreases to 1 mm over 60–100 ns after the current onset. The appearance of these compressed regions correlates in time with the X-ray signal from the PIN diode (Fig. 5a, trace *2*). After the end of the soft X-ray pulse, these regions rapidly expand (with a velocity of 10^7 cm/s) to a diameter of 5–6 mm; then, they continue to expand with a velocity of 10^6 cm/s up to the instant of corona explosion.

Streak camera images obtained with a longitudinally orientated slit recorded emission pulses from sev-

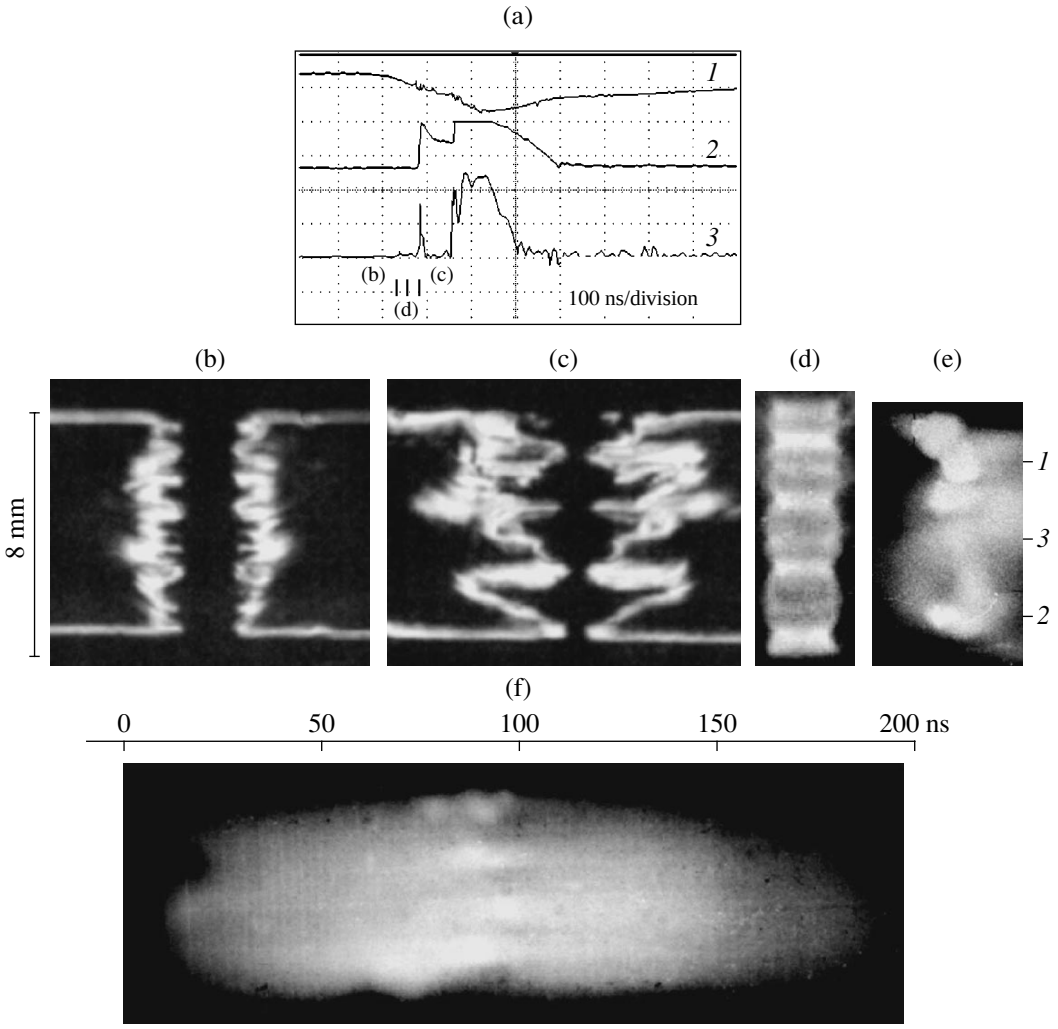

Fig. 4. Shot no. 152: (a) oscilloscope records of (*1*) the current and (*2, 3*) X-ray signals, (b, c) schlieren photographs, (d) X-ray frame images, (e) a pinhole image filtered with a 10-μm aluminized mylar film, and (f) a visible streak image taken with a slit parallel to the wire. One can see the spatial correlation between the necks (c, d) and bright spots (e, f) and the temporal correlation between the imploding necks (c), bright spots (f), and the X-ray pulse (a). Marks on the bottom of plot (a) indicate the instants corresponding to (b, c) the schlieren photographs and (d) X-ray frame image.

eral spots ~1 mm in diameter with a characteristic duration of 10 ns. Repeated emission from the same spot was also observed (Fig. 4f).

Visible frame camera images recorded before an X-ray pulse showed the formation of a helical structure on the corona surface with a diameter of 1 mm and a lifetime of several nanoseconds (Fig. 5d).

The time-integrated X-ray spectrum was recorded with the average spectral resolution $\lambda/\Delta\lambda = 200$. A rather coarse spatial resolution of 500 μm was provided along the discharge column. The theoretically calculated energy-dependent characteristics of the spectrograph with a convex mica crystal and the transmission coefficients of filters and protective foils were used to convert the blackening of a Kodak DEF X-ray film to the absolutely calibrated emission spectra. The intensity of line emission corresponding to the bound–bound transitions of H- and He-like Al ions was higher than that of the bremsstrahlung and recombination continuum. As an example, Fig. 6 shows the spectra corresponding to Fig. 4e (necks *1*, *2*, and *3*). The character of the spectrum depends strongly on the parameters of the emitting plasma object.

A comparison of the measured spectra with spectra computed with the RATION diagnostic code [14] allowed us to estimate the electron temperature T_e and the electron density n_e in the imploded necks. A detailed analysis shows that at least two characteristic sets of plasma parameters can be associated with the first spectrum in Fig. 6. The intensity distribution in the $\Delta n = 1$ spectral lines (where n is the principal quantum number) of H- and He-like ions can be satisfactorily

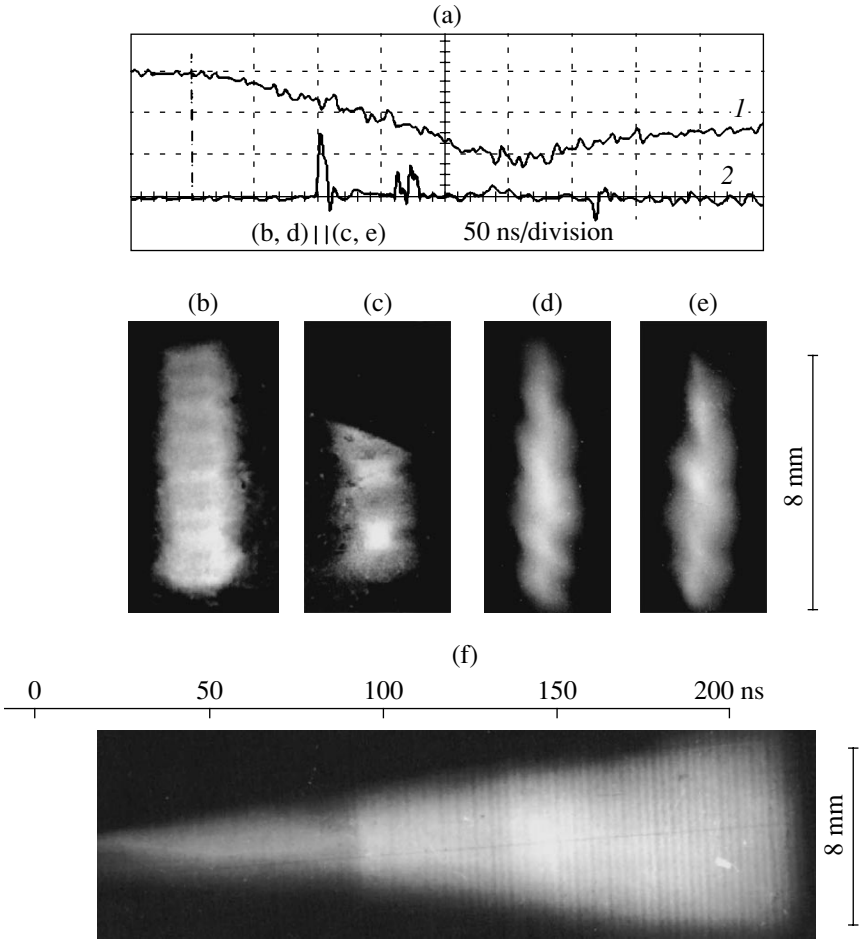

Fig. 5. Shot no. 192: (a) oscilloscope records of (*1*) the current (1.3 MA/div) and (*2*) X-ray signal, (b, c) X-ray frame images, (d, e) visible frame images, and (f) a visible streak camera image taken with a slit oriented perpendicularly to the wire. One can see the spatial correlation between the helical tubes (d, e) and X-ray frame images (b, c) and the temporal correlation between the imploding necks (c) and the X-ray pulse (a). Marks on the bottom of plot (a) indicate the instants corresponding to (b, c) the X-ray frame images and (d, e) visible frame images.

approximated with $T_e = 250$ eV and $n_e = 3 \times 10^{21}$ cm^{-3}, whereas the relative intensities of the $\Delta n = 2$ spectral lines correspond to higher temperature and density ($T_e = 550$ eV and $n_e = 2 \times 10^{22}$ cm^{-3}). This fact can be attributed to the overlap of emission from two stages of the neck implosion. In contrast, the spectra of X-ray emission from the other spots are satisfactorily described by a single set of plasma parameters. The absolute spectral intensity determined from the spectrograph gathering power provides information on the radiance of different bright spots. For the above spectrum, the integral emission energy in the spectral ranges 1500–1670, 1670–1780, and 1780–2400 eV is 20, 3, and 16 J, respectively.

4. DISCUSSION AND CONCLUSIONS

The results obtained with optical and X-ray diagnostics allow us to suggest the following scenario of the plasma evolution. After the current onset, a stable corona with an average expansion velocity of 10^6 cm/s is formed around the wire. As is seen in schlieren and X-ray frame images, the corona surface is characterized by the large plasma density gradient and emits in the soft X-ray and VUV regions. Typically, the corona undergoes the $m = 0$ (sausage) instability with a wavelength of about 1 mm, which results in the formation of narrow necks and broader crests. About 50–100 ns after the current onset, the characteristic diameter of this structure amounts to 2 mm. The surface temperature is estimated as a few tens of electronvolts, and the plasma density inside the structure is higher than 10^{19} cm^{-3}.

At currents of 0.7–1 MA, X-ray pulses with a photon energy of above 1 keV were observed 100 ns after the current onset. The FWHM duration of these pulses was 10–20 ns, and the total energy was ~40 J. The main part of this radiation was identified as the continuum and *K*-shell emission of H- and He-like Al ions. The

pulses correlate in time with the abrupt change of the coronal surface shape. Ringlike necks implode with a velocity of 2×10^6 m/s, and their diameter decreases to 1 mm over several nanoseconds. Simultaneously, the crests interleaving the compressed plasma necks expand with a velocity of about ~10^7 cm/s. The positions of the imploded necks correspond to bright spots emitting in the kiloelectronvolt photon energy range. The spot positions were determined from time-integrated pinhole photographs and spatially resolved *K*-shell spectra of Al emission. The bright spot parameters determined from spectroscopic measurements (an electron temperature of 200–500 eV and a density of 10^{21}–10^{22} cm^{-3}) indicate the high degree of plasma compression—up to 10^{11} Pa. This value is consistent with the magnetic pressure induced by the 1-MA current flowing through the corona with a radius of 0.5 mm. After the X-ray pulse, the regular corona surface and internal helical formations disintegrate and vanish.

Spectroscopic measurements indicate that the dense plasma of the wire corona can be an efficient source of soft X radiation and, thus, can be used to produce inverse population in recombination lasing schemes [15].

Images taken with a frame camera in the visible spectral region indicate that, inside the corona, a 1.5-turn helical surface with a radius of ~1 mm and length of 8 mm is formed (Figs. 5d, 5e). The helicity direction seems to be random: it can be either clockwise or counter-clockwise. The helical structures can induce axial and azimuthal electric currents and magnetic fields. The plasma in these structures is magnetized, dense, and relatively cold. The magnetic field is ~10^6 G, the electron and ion densities are estimated as 10^{21} cm^{-3}, and the temperature amounts to several electronvolts.

The dynamics of the helical formations can be roughly estimated from the pressure ratio between the azimuthal and axial magnetic field components, B_φ and B_z. We consider a simple model for the current distribution in the helical formations, which fill a thin cylindrical layer with a diameter of $2r \approx 1$ mm. The current in this layer flows along the helical magnetic field lines directed at an angle α with respect to the *z*-axis. According to Fig. 5d, the length of the 1.5-turn structure is 8 mm and $\alpha \approx 30°$. Then, the azimuthal and axial currents are

$$I_\varphi = I\sin\alpha, \quad (1)$$

$$I_z = I\cos\alpha, \quad (2)$$

respectively. Both the current components are depicted in Fig. 7.

The azimuthal and axial magnetic field components can be estimated by the formulas

$$B_\varphi = \frac{\mu I\cos\alpha}{2\pi r}, \quad B_z = \frac{\mu I\sin\alpha}{2r}.$$

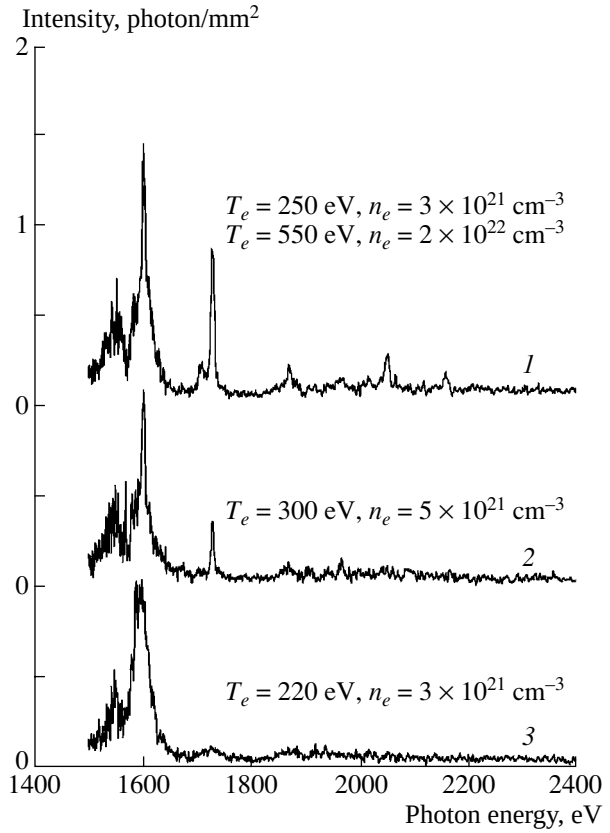

Fig. 6. Spatially resolved X-ray spectra demonstrating the variation in the effective parameters of individual imploding necks at positions *1*, *2*, and *3* (Fig. 4, shot no. 152). The emission of the Al He_α line and accompanying satellites is always dominant; the appearance and relative intensities of the other spectral lines depend strongly on the temperature and density of the emitting plasma formations.

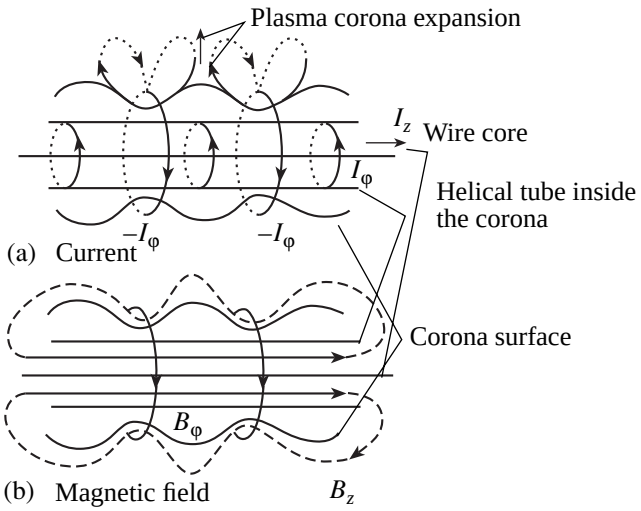

Fig. 7. Tentative picture of the (a) current and (b) magnetic field distribution in the wire plasma corona.

The ratio between the imploding and expanding pressures can be written as

$$\frac{B_\varphi^2}{B_z^2} = \frac{\cos^2\alpha}{\pi^2\sin^2\alpha} \approx 0.3.$$

These estimates imply the dominating role of the helical structure expansion. The existence of relative stable helical structures is provided by an addition compression of the outer corona layers. The outer corona layer recorded with an X-ray frame camera is shown in Figs. 3b, 4d, and 5b. In this cylindrically symmetric layer, the ringlike necks probably result in additional compression. Assuming that, in these necks, the induced azimuthal current ($-I_\varphi$ in Fig. 7) is directed oppositely to the azimuthal current flowing along the helical structure, the total axial magnetic field inside the ringlike neck is zero. In the expansion stage of the helical structure, the magnetic field pressure tends to zero during the diffusion and penetration of the magnetic fields induced by the oppositely directed currents I_φ and $-I_\varphi$. This process enables the pinching of the rings (see Figs. 3c, 4d, and 5c) and the emission of high-energy photons.

The reason for the generation of current loops with oppositely directed currents is not quite clear. Probably, they can be formed by radial plasma streams flowing out of the corona.

It seems that the main part of the current $I \approx 1$ MA flows through the internal helical tube. According to formula (1), for a helical structure 8 mm long, the azimuthal component of the current is $I_\varphi \approx 0.8$ MA. Then, the oppositely directed current I_φ in each of the five or six rings is 150 kA. The maximum value of the azimuthal component of the internal magnetic field induced by the helical current is $B_\varphi \approx 10^6$ G, whereas the mean value of the axial magnetic field can be estimated as $B_z \approx 4 \times 10^6$ G.

The generation of radiation with a photon energy on the order of several kiloelectronvolts can be ascribed to electric fields induced by the variations in the helical magnetic fields. These fields are strong enough to accelerate electrons up to energies required for the ionization of the *K*-shell of Al ions. The induced voltage *U* can be estimated as

$$U = \frac{\Delta B}{\Delta t}\pi r^2 \approx \frac{100}{10^{-8}}\pi(5\times 10^{-3})^2 \approx 8 \text{ kV}.$$

To resume, the diagnostic data obtained in these experiments demonstrate the important role of the axial magnetic field in the evolution of the Z-pinch plasma formed by loading thick Al wires. The investigated radiative characteristics of the corona stabilized by a dense wire plasma can be used in developing various Z-pinch applications.

ACKNOWLEDGMENTS

This study was supported by grants from the Ministry of Education, Youth, and Sports of the Czech Republic under contract nos. LA 055, LA00A100, LN00A100, and J04/98:212300017.

REFERENCES

1. G. Yonas, Sci. Am. **279** (2), 22 (1998).
2. T. W. L. Sanford, R. B. Spielman, G. O. Allshouse, *et al.*, IEEE Trans. Plasma Sci. **26**, 1086 (1998).
3. A. Alexandrov, A. Branitskii, G. Volkov, *et al.*, in *Proceedings of the 1st International Conference on Inertial Fusion Science and Application, Bordeaux, 1999*, p. 19.
4. A. S. Chernenko, P. I. Blinov, S. A. Dan'ko, *et al.*, Czech. J. Phys. **50**, 91 (2000).
5. L. E. Aranchuk, S. L. Bogolyubskii, G. S. Volkov, *et al.*, Fiz. Plazmy **12**, 1324 (1986) [Sov. J. Plasma Phys. **12**, 765 (1986)].
6. R. Alliaga-Rossel, S. V. Lebedev, P. Chittenden, *et al.*, IEEE Trans. Plasma Sci. **12**, 765 (1998).
7. F. N. Beg, A. E. Dangor, P. Lee, *et al.*, Plasma Phys. Controlled Fusion **39**, 1 (1997).
8. J. P. Chittenden, S. V. Lebedev, A. L. Bell, *et al.*, Phys. Rev. Lett. **83**, 100 (1999).
9. P. Kubeš and J. Kravárik, AIP Conf. Proc. **409**, 449 (1997).
10. J. Kravárik and P. Kubeš, AIP Conf. Proc. **409**, 503 (1997).
11. P. Kubeš, J. Kravarik, L. Aschke, *et al.*, in *Proceedings of the 14th International Symposium on Plasma Chemistry, Prague*, Ed. by M. Hrabovský *et al.* (Inst. Plasma Phys. Acad. Sci. Czech Rep., Prague, 1999), Vol. II, p. 979.
12. P. Kubeš, J. Kravárik, L. Karpinski, *et al.*, in *Proceedings of the International Congress on Plasma Physics and 25th EPS Conference on Controlled Fusion and Plasma Physics, Prague*, Ed. by P. Pavlo *et al.* (Inst. Plasma Phys. Acad. Sci. Czech Rep., Prague, 1997), p. 998.
13. A. S. Chernenko, Yu. M. Gorbulin, Yu. G. Kalinin, *et al.*, in *Proceedings of the International Conference on High-Power Particle Beams, Prague, 1996*, Eb. by K. Jungwirth and J. Ullschmied (Inst. Plasma Phys. Acad. Sci. Czech Rep., Prague, 1996), Vol. 1, p. 154.
14. R. W. Lee, B. L. Whitten, and R. E. Stout, J. Quant. Spectrosc. Radiat. Transfer. **32**, 91 (1984).
15. R. C. Elton, *X-ray Lasers* (Academic, Boston, 1990), p. 146.

Translated by the authors

Plasma Physics Reports, Vol. 28, No. 4, 2002, pp. 303–311. Translated from Fizika Plazmy, Vol. 28, No. 4, 2002, pp. 337–345.

RADIATION IN PLASMA

Polarization Mechanism for Bremsstrahlung and Radiative Recombination in a Plasma with Heavy Ions

V. A. Astapenko*, L. A. Bureyeva, and V. S. Lisitsa*****

**Moscow Institute of Physics and Technology, Institutskiĭ proezd 9, Dolgoprudnyĭ, Moscow oblast, 141700 Russia*
***Scientific Council on Spectroscopy, Russian Academy of Sciences, Moscow, 117942 Russia*
****Russian Research Centre Kurchatov Institute, pl. Kurchatova 1, Moscow, 123182 Russia*

Received October 4, 2001

Abstract—The role of the polarization mechanism in bremsstrahlung and radiative recombination in a plasma with heavy ions is investigated. A study is made of a hot plasma with the electron temperature T_e = 0.5 keV, containing Fe, Mo, W, and U ions, a relatively cold plasma with a temperature of 0.1–10 eV, and a storage-ring plasma with relatively low-energy electrons. The spectral characteristics, as well as the total cross sections and rate constants for electron–ion recombination, are calculated with allowance for real ionization equilibrium in a plasma. The calculations are carried out using the quasiclassical approximation for electron scattering and the statistical model for the ions, which provides a universal description of the spectra of various chemical elements over a wide temperature range. It is shown that the polarization mechanism contributes to both the effective radiation intensity and the total radiative recombination rate. The temperature range is found where the polarization recombination of electrons in collisions with FeIII ions plays an important role, which indicates the collective behavior of the electron core of an iron ion in this temperature range. Taking into account polarization effects increases the calculated total continuum intensity. As a consequence, the effective plasma charge Z_{eff} determined from this intensity without allowance for polarization effects turns out to be overestimated. © *2002 MAIK "Nauka/Interperiodica".*

1. INTRODUCTION

Numerous theoretical investigations of the polarization radiation (PR) carried out over the past decade [1] were based on calculating the parameters of the most elementary radiation event and dealt primarily with free–free transitions in the interaction with neutral atoms. At the same time, the actual plasma ion composition was not taken into account when studying the role of the polarization mechanism in the radiation observed and in the recombination of a plasma with heavy ions. The present study bridges this gap.

In what follows, we will calculate the contribution of the PR to the total intensity of radiation from a plasma containing multicharged ions of heavy elements. As was already noted, this contribution depends on the plasma ion composition, which is determined by the plasma temperature and the atomic number of the element under consideration. In fact, we consider a hot plasma with intermediate and heavy elements, such as Fe, Mo, W, and U. Note that the investigation of the polarization mechanisms at a fixed ion charge is important for describing plasmas in storage rings, in which the energy of the relative motion of the electrons and ions is very low. In this case, the PR is accompanied by electron–ion recombination. Hence, we are interested in calculating the radiation intensity in free–free and free–bound transitions of quasiclassical electrons scattered by the electron core of an ion. It is well known (see, e.g., [1]) that, in this case, radiation can be generated through two different mechanisms: the conventional (static) mechanism and the polarization mechanism. The "static" radiation (SR) is produced by the acceleration of an incident electron (IE) in the static field of the target atom (ion) [2]. The PR is associated with the electron core of an ion and arises from the dynamic polarization of the core under the action of the electric field of an IE. In [3], the spectral intensity of the PR from fast electrons in a partially ionized plasma was calculated by the standard methods of perturbation theory and by describing the IE motion in the Born approximation. The same issue was also investigated by the method of the dynamic form factor of the plasma components (see [1], Section 4), which makes it possible to systematically take into account the scattering of the equivalent electric field of an IE into a real photon by the fluctuations of the plasma charge. The PR from thermal electrons scattered by the Debye sphere of an ion in a low-temperature plasma was considered by one of us in [5].

Earlier, the SR spectra of moderate energy electrons typical of plasmas were calculated by the consistent quantum-mechanical approach [6] and by various approximate methods [4, 7–11]. In [10, 11], it was shown that the predictions of the quasiclassical approximation and the methods of the so-called Kramers electrodynamics [12], in particular, the rotational approximation (RA) [10], agree well with the results of detailed quantum-mechanical calculations [6]. The RA

1063-780X/02/2804-0303$22.00 © 2002 MAIK "Nauka/Interperiodica"

can easily be generalized to the case of PR [13]; it is only necessary that the polarizability of the electron core of a target ion be estimated using the model of the local plasma frequency [14]. In this model, all of the emissive parameters of the target ion are functionals of the density $n(r)$ of its electron core, thereby providing the possibility of a universal (applicable to all atomic numbers Z) description of the PR on the basis of the Thomas–Fermi statistical profiles [15] for the density $n(r)$. An important point here is that this approach is also capable of incorporating the effects that are associated with the penetration of an IE into the electron core of a target ion and, thus, play an important role in both the static and polarization mechanisms. In our paper [16], we applied this approach to obtain a universal expression that describes the effective radiation from quasiclassical electrons in collisions with neutral atoms with the Thomas–Fermi potential and generalizes the corresponding result obtained by Kogan and Kukushkin [10] to the case of PR. Applying these results to a plasma requires that they be generalized to atomic ions in a way analogous to the generalization done for the static mechanism by Ivanov *et al.* [11]. In this way, the dipole (with respect to the interaction of an IE with the electron core) approximation, which was applied by two of us [17] to analyze the phenomenon in question, should be generalized to include the effects of the penetration of a recombining electron into the electron core.

2. METHOD OF CALCULATION

The method of calculation of the effective radiation and radiative recombination of an electron scattered by the electron core of an ion is based on the Thomas–Fermi model distribution of the electron density in the electron core [18] (here and below, we use the atomic system of units):

$$n(r, q, Z) = Z^2 f(x = r/r_{TF}, q),$$
$$f(x, q) = \frac{32}{9\pi^2}\left(\frac{\chi(x, q)}{x}\right)^{3/2}, \quad (1)$$

where $r_{TF} = b/Z^{1/3}$ is the Thomas–Fermi radius, Z is the atomic number, Z_i is the ion charge number, $b = \left(\frac{9\pi^2}{128}\right)^{1/3} \simeq 0.8853$, $q = Z_i/Z$ is the degree of ionization, and $\chi(x, q)$ is the Thomas–Fermi function for an ion with a given q value. It is convenient to calculate the function $\chi(x, q)$ from the following expression, which was derived by Sommerfeld and was refined in [15]:

$$\chi(x, q) = \chi_0(x)\left[1 - \left(\frac{1 + z(x)}{1 + z_0(q)}\right)^{\lambda_1/\lambda_2}\right],$$
$$z(x) = \left(\frac{x}{\sqrt[3]{144}}\right)^{\lambda_2}, \quad z_0(q) = \left(\frac{x_0(q)}{\sqrt[3]{144}}\right)^{\lambda_2}, \quad (2)$$

where $x_0(q)$ is the reduced radius of an ion, $\chi_0(x)$ is the Thomas–Fermi function for a neutral atom, $\lambda_1 = (7 + \sqrt{73})/2$, and $\lambda_2 = (-7 + \sqrt{73})/2$. The reduced radius of the ion is approximated well by the following formula in the Thomas–Fermi–Dirac model [19]:

$$x_0(q) = 2.96\left(\frac{1 - q}{q}\right)^{2/3}, \quad 0.2 < q \le 1. \quad (3)$$

Approximation (3) is sufficient for the description of a high-temperature plasma with the electron temperature $T > 500$ eV. For a plasma with a lower temperature and, accordingly, with a lower degree of ionization, the parameter $x_0(q)$ can be found by solving the transcendental equation $q = -xd\chi/dx$ [15], in which the function $\chi(x, q)$ is given by formula (2).

In the approximation at hand, the electron–ion interaction potential has the form

$$U(r = xr_{TF}) = \frac{Z^{4/3}}{b}\left\{\theta(x_0 - x)\left[\frac{\chi(x, q)}{x} + \frac{q}{x_0}\right] + \theta(x - x_0)\frac{q}{x}\right\}, \quad (4)$$

where $\theta(x)$ is the Heaviside step function.

In the high-frequency (Kramers) spectral range $\omega > \omega^*$ (where $\omega^* = v/r^*$, v is the initial velocity of the IE, and r^* is the minimum distance to which the IE approaches the nucleus of the ion), the effective spectral intensity of the SR can be calculated in the RA [10, 12], which implies that, at these frequencies, the IE radiates most strongly when it moves at a minimum distance from the scattering center. Consequently, each point of the trajectory of the IE is assigned a "rotational" frequency $\omega_{rot}(r)$ defined by the relationship

$$\omega_{rot}(r, E) = \frac{\sqrt{2(E + |U(r)|)}}{r}, \quad (5)$$

where E is the initial energy of the IE, and it is assumed that the frequency ω at which the IE radiates is equal to the rotational frequency. The RA yields the following expression for the effective spectral intensity of the SR [7, 10, 12]:

$$\left(\frac{d\kappa}{d\omega}\right)^{rot}_{st} = \frac{8\pi\sqrt{3}}{3c^3\sqrt{2E}}\int_0^\infty (Z_{eff}(r))^2\sqrt{1 + \frac{|U(r)|}{E}}\,\delta(\omega - \omega_{rot}(r))r^{-2}dr, \quad (6)$$

where $Z_{eff}(r) = r^2|dU/dr|$ is the effective charge of the target ion at a given point and c is the speed of light.

The most simple way to generalize the RA to include the PR is to replace the effective charge Z_{eff} of the target ion in formula (6) by the frequency-dependent effective charge $N_{pol}(r, \omega)$ of the electron core.

This charge determines the PR intensity at a given frequency ω and, in the model of the local electron density, it can be represented as [13, 16]

$$N_{\rm pol}(r, \omega) = \omega^2 \left| \int_0^r \beta(r', \omega) 4\pi r'^2 dr' \right|, \quad (7)$$

where $\beta(r, \omega)$ is the spatial density of the dynamic polarizability of the target ion. In a statistical description of the electron core of a target ion, a physically correct expression for this quantity is provided by the Brandt–Lundqvist model [14, 16]:

$$\beta(r, \omega) = \frac{\omega_{pe}^2(r, q)/4\pi}{\omega_{pe}^2(r, q) - \omega^2 - i0}, \quad (8)$$

where $\omega_{pe}^2(r, q) = 4\pi n(r, q)$ is the local electron plasma frequency, in which the density $n(r, q)$ is to be calculated from the Thomas–Fermi–Sommerfeld model expressions (1)–(3). The variable upper limit of integration in formula (7), namely, the instantaneous distance from the IE to the nucleus, describes the effects associated with the penetration of an IE into the electron core. Note that the effective polarization charge depends also on the degree of ionization (through the electron density $n(r, q)$) in such a way that it decreases as the degree of ionization (the parameter q) increases.

Hence, in the RA, we arrive at the following expression for the effective spectral intensity of the PR, which is completely analogous to expression (6) for the SR:

$$\left(\frac{d\kappa}{d\omega}\right)_{\rm pol}^{\rm rot} = \frac{8\pi\sqrt{3}}{3c^3\sqrt{2E}} \times \int_0^\infty (N_{\rm pol}(r, \omega))^2 \sqrt{1 + \frac{|U(r)|}{E}} \delta(\omega - \omega_{\rm rot}(r)) r^{-2} dr. \quad (9)$$

An important point here is that, as was shown in [16], formula (9) can be extended over the entire spectral range of the emitted photons, because the PR is weakly sensitive to the trajectory of the IE. In contrast, extending formula (6) for the SR to the low-frequency range is a fairly difficult problem, which is solved in different ways for a neutral atom and for a target ion. It turned out that, for a neutral atom, it is sufficient to linearly interpolate formula (6) to the transport limit [10]. However, this interpolation is inapplicable to an ion, because the transport cross section for electron scattering in the Coulomb field diverges as the energy of the IE approaches zero. In this limit, we will use the formula obtained by matching the corresponding formulas in the high- and low-frequency ranges, as was done in [11]. The corresponding Gaunt factor for the SR has the form

$$g_{\rm st} = \frac{\sqrt{6}}{\pi} q^{\mu(\varepsilon)} \ln\left\{ \exp\left[\frac{\pi \max(q^2, g_{\rm st}^a(\nu, \varepsilon))}{\sqrt{6} q^{\mu(\varepsilon)}} \right] + \left[\frac{4\varepsilon^{3/2}}{1.78\sqrt{\frac{b^3}{2}}\nu q} \right]^{\frac{q^{2-\mu(\varepsilon)}}{\sqrt{2}}} \right\}, \quad (10)$$

where $\nu = \omega/Z$ and $\varepsilon = Eb/Z^{4/3}$ are the reduced frequency and reduced energy, $\mu(\varepsilon) = (1 - \ln\sqrt{\varepsilon})/2$, and $g_{\rm st}^a(\nu, \varepsilon)$ is the Gaunt factor for the SR from an electron scattered by a neutral atom with the Thomas–Fermi potential. A comparison between the spectral cross sections for bremsstrahlung obtained from the interpolation formula (10) and from systematic quantum-mechanical calculations [6] shows that formula (10) provides a good degree of accuracy (usually, about 10%).

Notably, in the RA, the spectral intensities of the bremsstrahlung and recombination radiation gradually approach one another at the high-frequency boundary of the spectrum, $\omega^h = E + I(Z_i, Z)$, where $I(Z_i, Z)$ is the ionization potential of the target ion.

3. RADIATION FROM QUASICLASSICAL ELECTRONS IN COLLISIONS WITH MANY-ELECTRON IONS

We start by considering both mechanisms for the effective radiation, without applying the procedure of averaging over the temperature. It is of interest to estimate the contribution of the PR from low-energy IEs (such that $E \ll I(Z_i, Z)$) in the interaction with multicharged ions, in which case the recombination radiation is dominant. This situation is, in particular, typical of experiments on storage rings [20]. The ionization potential $I(Z_i, Z)$ of an ion, which determines the high-frequency boundary of the spectrum emitted in the case at hand, can be described by the analytic fit obtained in [4]:

$$I(Z_i, Z)\ [\text{eV}] = \frac{3(1 + Z_i)^{4/3}}{1 - 0.96\left(\frac{1 + Z_i}{Z}\right)^{0.257}}. \quad (11)$$

The effective spectral intensities of the PR and SR calculated from formulas (9) and (6) with the Gaunt factor (10) are shown in Fig. 1. The calculations were

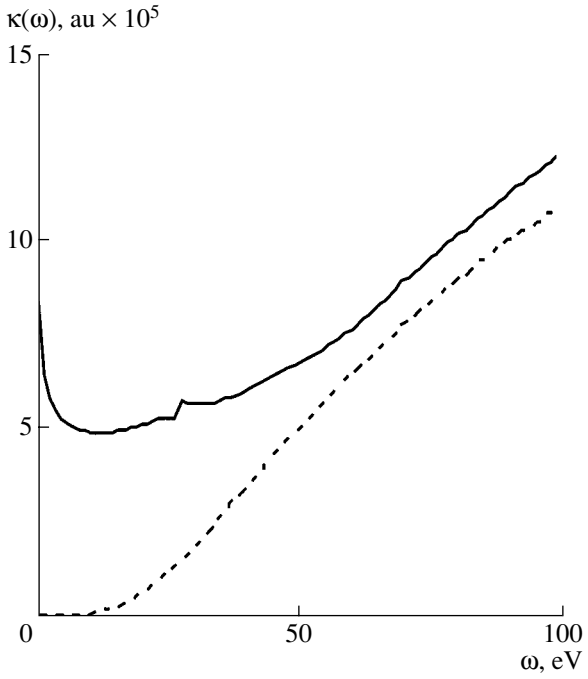

Fig. 1. Effective spectral intensities of the PR (dashed curve) and SR (solid curve) in the scattering of a quasiclassical electron with an energy equal to 1 au by a Fe^{4+} ion.

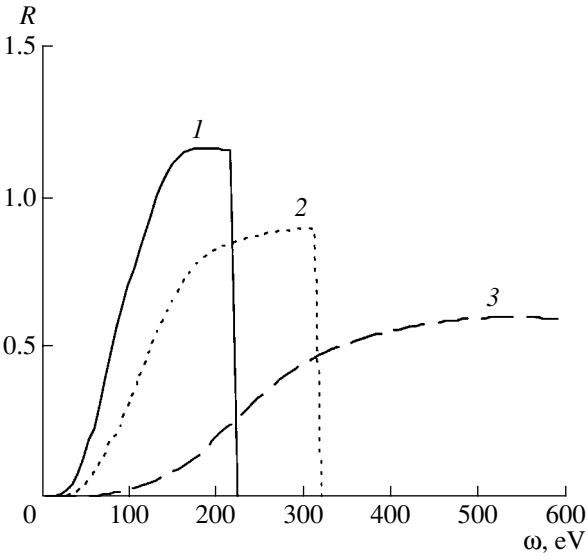

Fig. 2. Spectral *R* factor for the recombination radiation emitted by electrons with an energy equal to 0.1 au in the scattering by uranium ions ($Z = 92$) with different degrees of ionization: Z_i = (*1*) 12, (*2*) 15, and (*3*) 28.

carried out using the statistical model expressions (1)–(4), (7), and (8) for an iron ion with a charge number of four and for an IE with the energy equal to one atomic unit. We can see that the contribution from the PR increases with increasing radiation frequency and becomes comparable to that from the SR in the frequency range $\omega > 50$ eV. Since the initial energy of the IE is relatively low, its penetration into the electron core of the target ion does not substantially lower the PR intensity in the high-frequency limit, in which case, however, the SR intensity somewhat increases. In the frequency range $\omega < E = 1$ au, the IE generates only PR, while, at higher frequencies, only recombination radiation is emitted. Of course, as the energy of the IE decreases, the short-wavelength boundary of the emitted radiation is displaced toward the lower frequencies. The shapes of the spectra and the relationship between the effective spectral intensities remain essentially the same.

We define the spectral *R* factor as the ratio of the contribution from the PR to the contribution from conventional SR:

$$R(\omega, q) = \frac{d\kappa_{\text{pol}}(\omega, q)}{d\kappa_{\text{st}}(\omega, q)}. \qquad (12)$$

Here, we introduce the explicit dependence of all the quantities on the degree of ionization of the target atom. This is an important point in which our analysis differs radically from that of the radiation generated in collisions of electrons with neutral atoms.

The frequency dependence of the *R* factor for the recombination radiation emitted by monoenergetic ($E = 0.1$ au) slow electrons in collisions with uranium ions with different degrees of ionization is illustrated in Fig. 2. Among the chemical elements under consideration, we chose uranium ($Z = 92$) atoms because they have the largest electron core. Of course, the *R* factor is maximum for the lowest degree of ionization (in the case at hand, $Z_i = 12$), when the polarization charge (7) is relatively large. In this case, the contribution from the polarization mechanism to the recombination radiation at sufficiently high frequencies exceeds that from the static mechanism. For the parameter values of Fig. 2, the *R* factor is seen to be maximum at a certain optimum frequency. At higher frequencies, the relative contribution of PR to the total radiation intensity decreases because of the effects associated with the penetration of an IE into the electron core of the target ion (and, accordingly, with the accompanying decrease in the polarization charge N_{pol}). The larger the ion charge, the higher the optimum frequency. In this case, the *R* factor decreases and the short-wavelength boundary of the emitted radiation is displaced toward the higher frequencies.

Now, we calculate the spectral intensities of the SR and PR in a high-temperature plasma in coronal equilibrium. We approximate the temperature dependence of the mean degree of ionization of ions with a given atomic number by the expression

$$\bar{q}(T, Z) = \frac{26}{Z}\sqrt{\frac{0.0272T\ [\text{au}]}{1 + 0.015T\ [\text{au}](26/Z)^2}}. \qquad (13)$$

This formula, which is a slightly modified version of the corresponding formula from [21], provides the reproducibility of the data presented in [22] with an accuracy of 5–10% (by solving the set of coronal equilibrium equations). Formula (13) makes it possible to easily calculate the SR, PR, and recombination radiation intensities (per one electron–ion collision event) as functions of the plasma temperature:

$$k(\omega, T, Z) = \frac{2\sqrt{2}}{\pi} T^{-3/2} \times \int\limits_{E_{\min}(\omega, T)}^{\infty} \frac{d\kappa}{d\omega}(\omega, E, \bar{q}(T, Z), Z) \exp\left(-\frac{E}{T}\right) E dE, \quad (14)$$

where the lower integration limit is determined by the obvious equality

$$E_{\min}(\omega, T, Z) = \max\{0, \omega - I(Z\bar{q}(T, Z), Z)\}. \quad (15)$$

The R factor, which describes the ratio of the temperature-averaged PR and SR intensities, can be written in a form analogous to definition (12):

$$\bar{R}_T(\omega, T, Z) = \frac{k_{\text{pol}}(\omega, T, Z)}{k_{\text{st}}(\omega, T, Z)}. \quad (16)$$

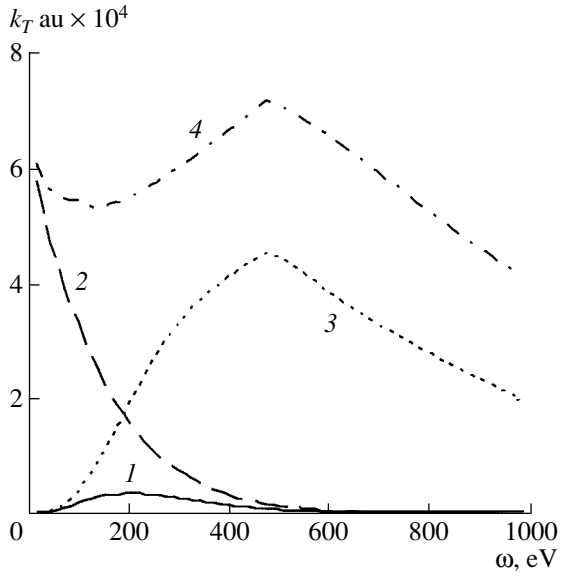

Fig. 3. Radiation spectra from plasma electrons scattered by tungsten ions (Z = 74): (*1*) PR spectrum, (*2*) SR spectrum, (*3*) total PR spectrum, and (*4*) total SR spectrum. The spectra are averaged over the coronal equilibrium state of a plasma with the electron temperature T = 500 eV.

Figure 3 displays the PR and SR spectra calculated from formula (14) with (the total spectra) and without allowance for recombination. The calculations were carried out for the scattering of plasma electrons with a temperature of 500 eV by tungsten ions (Z = 74) whose degree of ionization was determined from expression (13). The bremsstrahlung intensity was calculated from formula (14) by using the radiation frequency as the lower integration limit. For the above plasma temperature and ion atomic number, we have $\bar{q} = 0.244$ and $\bar{I}$ = 473 eV. It can be seen in the figure that the total PR and SR spectra are peaked and have breaks just at the frequency $\omega = \bar{I}$, reflecting the well-known threshold nature of the frequency spectrum of the recombination radiation, which is the dominant process in the situation at hand. In the frequency range $\omega < I$, the recombination radiation is emitted by electrons as they undergo transitions to states with lower bonding energies (with larger principal quantum numbers). In the approximation used here, the energy states of the bound electrons of the target ion are modeled by a continuous electron energy distribution. The relative contributions from the polarization mechanism to the bremsstrahlung and total radiation intensities (the R factor) are practically the same. The corresponding frequency dependence of the R factor is represented by curve *4*. It is seen that the R factor increases according to a power law at low frequencies, reaches its maximum $\bar{R}_T^{\max}$ (T = 500 eV, W) ≈ 0.6 at a frequency approximately equal to the electron temperature (in energy units), and decreases monotonically in the high-frequency range (because of the effects associated with the penetration of an IE into the electron core of the target ion). These results show that the PR plays an important role in the case under discussion, although, for the above parameters, the mean charge of the target ions is fairly large, $\bar{Z}_i$ = 18.

The frequency dependence of the R factor averaged over the coronal equilibrium state of a plasma with the electron temperature T = 500 eV in the case of electron scattering by the ions of different chemical elements (Fe, Mo, and W) is illustrated in Fig. 4. One can see that, at the given electron temperature, the contribution of PR increases with increasing atomic number—from 0.1 for iron (at the peak of the frequency dependence) to 0.6 for tungsten. The reason for this is the decrease in the temperature-averaged degree of ionization of the target ion as the atomic number increases. This results in an increase in the effective core charge, which governs the PR. We should point out that the mean charge of iron ions (equal to 16.3) differs insignificantly from that of tungsten ions (equal to 18). The R factor for iron ions peaks at a somewhat higher frequency than that for tungsten ions. As the plasma electron temperature increases, the contribution of PR to the total radiation intensity decreases because of the increase in the mean degree of ionization of the target ions, in which case the optimum frequency also increases. Thus, for T = 1000 eV and for tungsten ions (in which case $\bar{q}_T = 0.34$ and, accordingly, $\bar{Z}_i$ = 25), our calculations give $\bar{R}_T^{\max} \approx 0.43$ and $\omega_{\max} \approx 900$ eV.

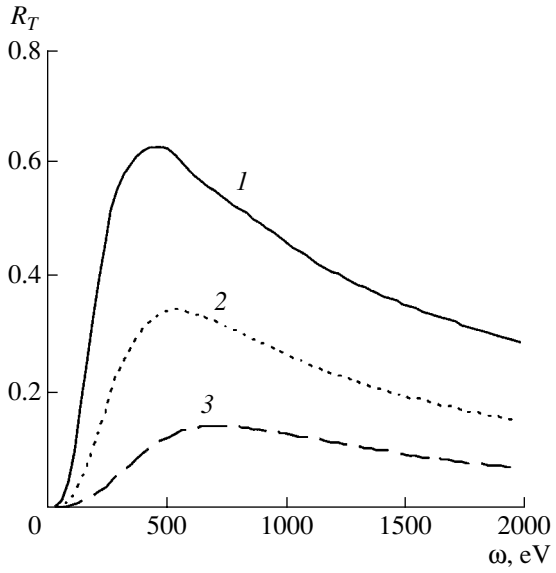

Fig. 4. *R* factor averaged over the coronal equilibrium state of a plasma with an electron temperature of 500 eV for (*1*) W, (*2*) Mo, and (*3*) Fe target ions.

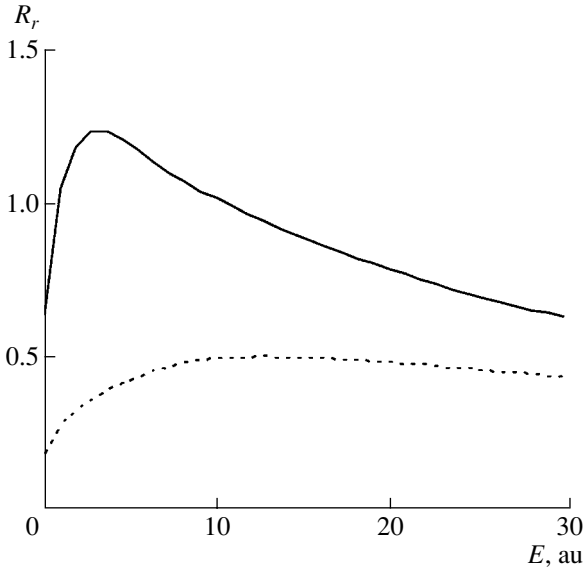

Fig. 5. *R* factor for the recombination radiation vs. the initial energy of an IE scattered by uranium ions with the degrees of ionization $q = 0.1$ (solid curve) and $q = 0.3$ (dashed curve).

The analysis of the role of PR by means of the approach developed here shows that the polarization mechanism can also contribute substantially to the total intensity of radiation from a plasma with light atoms, provided that the plasma electron temperature is sufficiently low. Thus, for carbon ions in a plasma with $T = 10$ eV ($\bar{q}_T = 0.32$), the maximum averaged *R* factor is approximately equal to 0.46. In this case, the optimum frequency at which the polarization effects are most pronounced is about $\omega_{max} \approx 80$ eV, which is higher than the optimum frequency $\omega_{max} \approx T$ for heavy elements. Of course, for light elements, our statistical model is only a rough approximation.

4. CONTRIBUTION FROM THE POLARIZATION MECHANISM TO THE CROSS SECTION AND RATE OF RADIATIVE RECOMBINATION

In our approach, the cross section for the radiative recombination of an electron with the initial energy *E* is related to the effective spectral radiation intensity by

$$\sigma_r(E, q, Z) = \int_E^{E+I} \frac{d\kappa}{d\omega}\frac{d\omega}{\omega}. \quad (17)$$

Formula (17), which was derived with allowance for the relationship $\kappa = \omega\sigma$ between the effective spectral intensity and the cross section for radiative recombination, describes both the SR and PR if the quantity $d\kappa/d\omega$ is assumed to mean the corresponding effective spectral intensity.

It should be kept in mind that the classical approach used here, of course, does not take into account virtual excitations of the electron core of the target ions. Consequently, the accuracy of the approach depends on the contribution from the discrete spectrum to the polarizability of the electron core of the target ion: the smaller the contribution, the more accurate the approach will be. Since the role of the discrete spectrum is insignificant for atoms (or ions) with closed electron shells [23], our approach is best suited for describing this type of target. Otherwise, the approach, as a rule, allows only lower estimates for the contribution from polarization effects to the processes under consideration.

The effects of the polarization of the electron core on radiative recombination can also be characterized by the *R* factor in a form similar to definition (12):

$$R_r(E) = \frac{d\sigma_r^{pol}(E)}{d\sigma_r^{st}(E)}. \quad (18)$$

Figure 5 shows how the contribution from the polarization processes to the cross section for the recombination of electrons and uranium atoms with different degrees of ionization *q* depends on the initial energy of the IE. These results are of interest for interpreting experimental data from storage rings [20], in which both the degree of ionization of the target ions and the energy of an electron beam can be fixed. The larger the degree of ionization *q*, the lesser the role played by the polarization of the electron core of the target ion in the recombination process (as in the case of the spectral *R* factor in Fig. 2).

The radiative recombination rate averaged over the coronal equilibrium state is also an important parame-

ter characterizing recombination processes in a plasma. In terms of the radiative recombination cross section, this rate is expressed as

$$\alpha_r(T, Z) = 2\sqrt{\frac{2T}{\pi}}\int_0^\infty \sigma_r(xT, \bar{q}(T, Z), Z)e^{-x}x\,dx. \quad (19)$$

Here, we used the mean degree of ionization (13), which depends on the electron temperature and ion atomic number.

In particular, in the Kramers approximation, we can use formula (17) to obtain the following expression for the contribution from the static mechanism to the radiative recombination rate:

$$\alpha_r^{(\mathrm{Kr})}(T, I) = \left(\frac{2}{3}\right)^{3/2}\frac{8\sqrt{\pi}}{c^3}\frac{1}{\sqrt{T}}\int_0^\infty Z_{\mathrm{eff}}^2(x)e^{-x}\ln\left(1 + \frac{I}{xT}\right)dx, \quad (20)$$

where $Z_{\mathrm{eff}}(x)$ is the effective ion charge, which depends generally on the initial IE energy. At sufficiently low electron temperatures (when an electron recombining with an ion penetrates into the electron core for a small distance), the effective ion charge can be set equal to the total ion charge and thus can be factored out of the integral sign on the right-hand side of expression (20).

Figure 6 illustrates the results of our calculations of the contributions from the polarization and static channels to the rate of the radiative recombination of quasiclassical electrons with uranium ions. We can see that the polarization and static mechanisms lead to different temperature dependences of the degree of ionization. The radiative recombination rate associated with the static mechanism increases monotonically with temperature, whereas the recombination rate associated with the polarization mechanism is maximum at a certain optimum temperature (in the case at hand, about 100 eV). When interpreting the dependences calculated from formula (19), it should be kept in mind that the mean degree of ionization of the target ions also increases with temperature. This leads to an increase in the effective ion charge, on the one hand, and to an increase in the characteristic frequency of recombination radiation, on the other. The first effect raises the rate of the static radiative recombination and lowers the rate of the polarization radiative recombination; in contrast, the second effect raises the rate of the polarization radiative recombination. As a result, the temperature dependence of the rate of the polarization radiative recombination has a maximum, at which the polarization mechanism for the chemical element at hand dominates over the static mechanism.

The results of our calculations show that there exists a fairly wide parameter range in which the polarization radiative recombination of electrons with multicharged ions is comparable in importance with or even dominates over the static recombination. At the same time, it

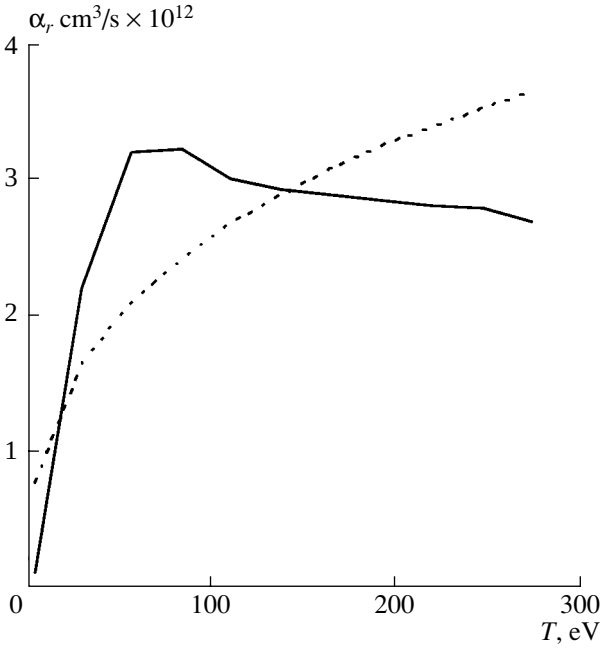

Fig. 6. Contributions from the polarization (solid curve) and static (dashed curve) channels to the rate of the radiative recombination of an electron and a uranium ion with a temperature-dependent degree of ionization.

is necessary to keep in mind that the IE energies corresponding to this parameter range are relatively high: they are comparable with the excitation energy of the electron shells of the target ions. In this case, the main contribution to recombination comes, as a rule, from dielectronic recombination. Consequently, the contribution from the polarization mechanism can be important only at intermediate energies between the low-energy range, in which radiative recombination is dominated by the static mechanism, and high-energy range, in which dielectronic recombination is dominant. This is well illustrated by the recombination of electrons with FeIII ions, which is of interest from an astrophysical standpoint. The recombination of these iron ions was calculated in detail by Nahar [24] in the framework of the so-called "Iron Project." The computations carried out in [24] by using the R-matrix method with allowance for 83 states of FeIII ions turned out to be very laborious (the number of ion states taken into account in simulations was restricted because of the limited computer time on a Cray computer), and the results obtained were found to be sensitive to the choice of the target ion states. It should be noted that those calculations were carried out for the recombination radiation from the entire "incident electron–recombining ion" system, without singling out the contributions from the static, polarization, and dielectronic recombination mechanisms to the total radiation intensity. A comparison between the computational results of [24] and the results on radiative and dielectronic recombinations in Fig. 7 shows that there exists a fairly wide tem-

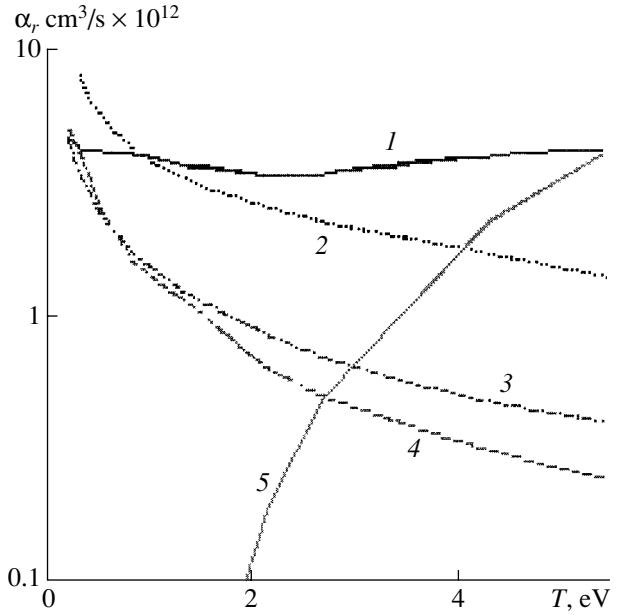

Fig. 7. Temperature dependence of the recombination rate of Fe^{2+} ions: (*1*) the total recombination rate calculated in [24] with allowance for 83 states of FeIII ions, (*2*) the total radiative recombination rate calculated in the present paper without allowance for interference, (*3*) the radiative recombination rate calculated from formula (20) in the Kramers approximation, (*4*) the static radiative recombination rate calculated in [25], and (*5*) the dielectronic recombination rate calculated in [26].

perature range (from 0.2 to 2 eV) in which the calculated recombination rate is several times (up to five times) higher than the total rate of the static recombination and the dielectronic recombination. The comparison also shows a marked discrepancy with the results of previous calculations of dielectronic recombination [26]; this discrepancy stems from the difference in the chosen states of the target ion. It is also of interest to compare the results of the detailed computations of [24] with the results from the classical approach developed here. For this purpose, we also show in Fig. 7 the results obtained by averaging formulas (17) and (18) over the Maxwellian electron velocity distribution function under the assumption of constructive interference of the SR and PR (the constructive interference was modeled by summing the intensities of these types of radiation). We can see that the agreement between our results and the results of [24] is fairly good, especially if we take into account the fact that the statistical ion model used here takes no account of the specific features of the electron structure of FeIII ions. Such a close agreement indicates that, from a physical standpoint, our approach to describing the polarization channel as an independent mechanism for radiation and recombination may be judged adequate. Moreover, since the approach is based on the model of the local plasma frequency and the results obtained agree with the results of more exact calculations, we can speak with a relatively high degree of confidence about the collective behavior of the electron core of an ion in these processes. It is also of interest to note that a comparison between the curves describing the static radiative recombination permits us to conclude that, in calculations over the temperature range under consideration, the Kramers approximation provides a high degree of accuracy.

5. CONCLUSION

Using the model of the local plasma frequency, we have developed a unified method for calculating the intensity of radiation from quasiclassical electrons and the rate of their radiative recombination in the scattering by partially ionized ions with allowance for the contribution from the polarization mechanism and the effects associated with the penetration of IEs into the electron cores of the target ions. We have described the electron cores using the Thomas–Fermi–Sommerfeld model, which provides a universal means for taking into account the dependence of the electron density distribution on the degree of ionization. PR from the IEs has been considered by using one of the methods of the Kramers electrodynamics, namely, the RA, which was successfully applied in previous studies to describe SR [10, 11].

The approach developed here has been applied to analyze how PR affects both the averaged (over the coronal equilibrium state of the plasma) and unaveraged radiation spectra and the radiative recombination rate depending on the parameters of the problem. It has been shown that the contribution of PR can be comparable with or even larger than the contribution of the conventional SR (including the case of multicharged ions), provided that the number of bound electrons in an ion at a given plasma electron temperature is sufficiently large.

We have calculated the spectrum of the recombination radiation of low-energy IEs scattered by the ions with a given degree of ionization. The resulting spectrum is of interest for experiments with storage rings [19]. For the particular case of uranium ions, we have established that PR dominates over SR in the range $Z_i \le 12$.

We have shown that, at a given electron temperature, the role of polarization effects in the radiation process increases with the atomic number of the target ions. The reason for this is the increase in the effective bound polarization charge. The higher the plasma electron temperature, the higher the degree of ionization and the lower the relative PR intensity.

We have found that PR also plays an important role for light elements (carbon, oxygen, etc.) in a plasma with a sufficiently low electron temperature.

The contribution from the polarization channel to the cross section and to the rate of radiative recombination has been analyzed for both fixed and temperature-dependent degrees of ionization of the target ions with allowance for the effects associated with the penetra-

tion of IEs into the electron cores. It is shown that, in certain energy and temperature ranges, the contribution from the polarization channel can exceed the contribution from the static channel, provided that the plasma contains sufficiently heavy ions.

We have determined the electron temperature range in which the polarization mechanism for the recombination of a FeIII ion plays an important role along with the well-known radiative and dielectronic recombination mechanisms. This allows us to draw the conclusion about the collective behavior of the electron core of an iron ion in this temperature range.

The results of our investigations may prove to be useful, in particular, for improving plasma diagnostic methods. In fact, taking into account polarization effects changes the relationship used to determine the effective charge Z_{eff} of the plasma ions, namely, the relationship between the intensity of the experimentally recorded continuum and the mean ion charge. This relationship, which is traditionally calculated in the static approximation, should be supplemented with the correction factor $1 + R$. As a result, the actual mean ion charge turns out to be smaller than that calculated in the static approximation.

ACKNOWLEDGMENTS

We are grateful to V.I. Gervids, V.I. Kogan, and A.B. Kukushkin for fruitful discussions of the quasiclassical methods for calculating static bremsstrahlung. This work was supported in part by the Russian Foundation for Basic Research (project no. 01-02-16305) and the Ministry of Science of the Russian Federation (under the program "Fundamental Spectroscopy").

REFERENCES

1. *Polarization Bremsstrahlung from Particles and Atoms*, Ed. by V. N. Tsytovich and I. M. Oĭringel' (Nauka, Moscow, 1987).
2. L. D. Landau and E. M. Lifshitz, *The Classical Theory of Fields* (Nauka, Moscow, 1974; Pergamon, Oxford, 1975).
3. V. A. Astapenko, V. M. Buĭmistrov, Yu. A. Krotov, and V. N. Tsytovich, Fiz. Plazmy **15**, 202 (1989) [Sov. J. Plasma Phys. **15**, 116 (1989)].
4. V. D. Kirillov, B. A. Trubnikov, and S. A. Trushin, Fiz. Plazmy **1**, 218 (1975) [Sov. J. Plasma Phys. **1**, 117 (1975)].
5. V. A. Astapenko, Fiz. Plazmy **27**, 503 (2001) [Plasma Phys. Rep. **27**, 474 (2001)].
6. C. M. Lee, R. H. Pratt, and H. K. Tseng, Phys. Rev. A **16**, 2169 (1977).
7. V. I. Gervids and V. I. Kogan, Pis'ma Zh. Éksp. Teor. Fiz. **22**, 308 (1975) [JETP Lett. **22**, 142 (1975)].
8. V. P. Zhdanov and M. I. Chibisov, Zh. Tekh. Fiz. **47**, 1804 (1977) [Sov. Phys. Tech. Phys. **22**, 1045 (1977)].
9. V. P. Zhdanov, Fiz. Plazmy **4**, 128 (1978) [Sov. J. Plasma Phys. **4**, 71 (1978)].
10. V. I. Kogan and A. B. Kukushkin, Zh. Éksp. Teor. Fiz. **87**, 1164 (1984) [Sov. Phys. JETP **60**, 665 (1984)].
11. V. V. Ivanov, V. I. Kogan, and A. B. Kukushkin, Fiz. Plazmy **15**, 1531 (1989) [Sov. J. Plasma Phys. **15**, 892 (1989)].
12. V. I. Kogan, A. B. Kukushkin, and V. S. Lisitsa, Phys. Rep. **213**, 1 (1992).
13. V. A. Astapenko, L. A. Bureyeva, and V. S. Lisitsa, Phys. Scr. T **T86**, 62 (2000).
14. W. Brandt and S. Lundqvist, Phys. Rev. **139**, A612 (1965).
15. P. Gombas, *Die statistische Theorie des Atoms und ihre Anwendungen* (Springer-Verlag, Vienna, 1949; Inostrannaya Literatura, Moscow, 1951).
16. V. A. Astapenko, L. A. Bureeva, and V. S. Lisitsa, Zh. Éksp. Teor. Fiz. **121** (1), 19 (2002) [JETP **94**, 12 (2002)].
17. L. A. Bureyeva and V. S. Lisitsa, J. Phys. B **31**, 1477 (1998).
18. L. D. Landau and E. M. Lifshitz, *Quantum Mechanics: Non-Relativistic Theory* (Nauka, Moscow, 1974; Pergamon, New York, 1977).
19. A. D. Ulantsev and V. P. Shevel'ko, Opt. Spektrosk. **65**, 1003 (1988) [Opt. Spectrosc. **65**, 590 (1988)].
20. M. Mueller, Nucl. Instrum. Methods Phys. Res. B **99**, 58 (1995).
21. K. Dick and H. Pepin, J. Appl. Phys. **44**, 3284 (1973).
22. D. E. Post and R. V. Jensen, At. Data Nucl. Data Tables **20**, 397 (1977).
23. M. Ya. Amus'ya, N. A. Cherepkov, and S. G. Shapiro, Zh. Éksp. Teor. Fiz. **63**, 889 (1972) [Sov. Phys. JETP **36**, 468 (1972)].
24. S. N. Nahar, Phys. Rev. A **55**, 1980 (1997).
25. D. T. Woods, J. M. Shull, and C. L. Sarazin, Astrophys. J. **249**, 399 (1981).
26. M. Arnaud and J. Raymond, Astrophys. J. **398**, 394 (1992).

Translated by O. Khadin

Plasma Physics Reports, Vol. 28, No. 4, 2002, pp. 312–326. Translated from Fizika Plazmy, Vol. 28, No. 4, 2002, pp. 346–359.

NONLINEAR PHENOMENA

Current Filaments in Plasmas

B. A. Trubnikov

Russian Research Centre Kurchatov Institute, pl. Kurchatova 1, Moscow, 123182 Russia

Received June 25, 2001; in final form, November 27, 2001

Abstract—Possible configurations of current filaments in Z-pinch and tokamak plasmas are analyzed. A thin current-carrying beam injected in a plasma should be surrounded by a halo of countercurrents, in which case the resulting configuration may resemble a tubular structure. A.B. Kukushkin and V.A. Rantsev-Kartinov pointed out the existence of specific plasma structures of the squirrel-cage type and interpreted them as "wild cables of solid-state nanotubes." It is shown that these structures can also be attributed to the fundamental mode of the conventional magnetic filamentation in the form of a "hexagonal parquet." Also, a study is made of the phenomena governing the pattern of plasma structures, namely, tearing filamentation, two types of longitudinal beam bunching, and self-organization of the filaments. *© 2002 MAIK "Nauka/Interperiodica".*

1. INTRODUCTION. OBSERVATIONS OF PLASMA FILAMENTS

Thin filaments that are stretched both along and across the direction of the current and resemble lightning channels are often seen in the photographs of high-temperature discharge plasmas in Z-pinches and tokamaks. In some experiments, the formation of individual current filaments was artificially stimulated by shaping the electrodes in a special way. Thus, some experiments of N.V. Filippov and his colleagues were carried out with a planar circular anode with a finely serrated edge, generating a set of current filaments, which merge into one during subsequent compression of the pinch. Similar current filaments were observed in the experiments of [1, 2], as well as in many experiments with pinches, e.g., in [3, 4], where the discharges were initiated in a discharge tube with the hexagonal cross section, which stimulated the formation of six current filaments.

The role of another mechanism for forming filaments may be played by various filamentation and bunching instabilities of the beams of accelerated electrons or ions. The phenomenon of filamentation and bunching of the plasma discharges under different conditions has been studied experimentally for many years. Thus, the well-studied phenomenon of stratification of a low-temperature plasma is governed by the ionization of gas atoms by electrons accelerated in an external electric field and by the recombination of gas atoms with these electrons.

This paper is aimed at a theoretical analysis of current filaments in fully ionized, high-temperature plasmas of Z-pinches, plasma foci, and tokamaks, in which case the filamentation processes are not, as a rule, associated with ionization and recombination phenomena. It should be noted that typical filaments are very thin and thus cannot be treated in the linear approximation, because linear equations yield only sinusoidal perturbation profiles. The development of perturbations with very nonsinusoidal, strongly peaked profiles can be described only by solutions to the nonlinear equations. A solid basis for a description of regimes with strongly peaked perturbation profiles is provided by the so-called quasi-gaseous equations, the general theory of which was developed in a book by Zhdanov and Trubnikov [5], where about 50 examples of different instabilities are described and solutions to the corresponding equations are presented. In what follows, only four of these instabilities will be recounted here and will be compared with the results of particular observations of the beams and plasma filaments. Formally, quasi-gaseous equations lead to perturbation profiles, which collapse completely on finite time scales. However, these equations actually assume that the plasma is quasineutral and that the quasineutrality condition fails to hold when the profiles become peaked at spatial scales of about the Debye length, which thus determines the maximum possible degree of peakedness of the profiles.

The theory of the acceleration of ion beams in Z-pinches and plasma foci was originally developed in my paper [6], in which, among other things, the disruption of current sheets of different configurations was considered (see Figs. 4–8 in [6]) and it was shown that the current disruption gives rise to an increasing electric field, which accelerates the particles. In subsequent papers [7–10], it was shown that the peripheral plasma that always surrounds the main pinch prevents the current compression into an ultrathin filament in which thermonuclear conditions are achievable. (It is for this reason that "direct" plasma ignition in traditional pinches is impossible, so that, at present, the most high-power pinches are regarded as possible sources of X radiation, which, in principle, can be used to compress fusion targets.) In discharges in deuterium, the observed neutrons are produced by the generated beams of D^+ ions accelerated to energies of several MeV,

1063-780X/02/2804-0312$22.00

in which case the beams may split into individual microbeams.

The trace of an ion beam extracted from a hole in the cathode of a plasma focus is shown in Fig. 1 from [11]. As may be seen, the beam splits into many individual microbeams, which produce their own images on the plate. Experiments aimed at revealing the number of such microbeams for a relativistic electron beam (REB) are reported in [12], and, for Z-pinches, this number was estimated theoretically in [13].

The results of theoretical calculations of the beam filamentation are shown in Fig. 2 from [14], which is very similar to Fig. 1. It is clear that the plasma in current-carrying filaments is hotter than the surrounding plasma. In positives, the filaments can be seen either brighter or darker than the surrounding background. The filaments are brighter in a plasma with a low degree of ionization, in which case they emit radiation in the form of recombination spectral lines in the visible range (as is the case with a lightning). However, when the plasma temperature is sufficiently high ($T \sim 10^2$–10^3 eV), the recombination processes are suppressed and the filaments are darker than the surrounding medium.

In contrast to Z-pinches, the tokamak plasma is more quiescent, but it can also generate beams of accelerated electrons and ions, because the operating conditions of tokamaks with Joule heating are close to those of betatrons with a continuous acceleration of runaway electrons. The runaways are generated when the main induction electric field is stronger than the so-called Dreicer critical field $E_{cr} \approx |e|/D^2$, where $D = \sqrt{T/4\pi ne^2}$ is the Debye length. At $T = 1$ keV and $n = 10^{13}$ cm^{-3}, we have $D \sim 10^{-2}$ cm and $E_{cr} \sim 0.01$ V/cm, so that the Dreicer criterion fails to hold for $n \geq 10^{13}$ cm^{-3}. However, even when the Dreicer criterion is not satisfied, some electrons from the tail of the Maxwellian distribution function will run away, forming accelerated beams, which may also tend to split into filaments. Filamentation phenomena can also take place when the current is carried by the majority of electrons rather than by the beam. For certain aspects of filamentation, it does not matter whether the current is driven by the beam or is associated with the relative motion of the majority of electrons against the background of majority ions.

Figure 3 from paper [15] by Kukushkin and Rantsev-Kartinov (KRK) shows a unique case of a cable (in their original terminology) in the form of a dark "squirrel cage" in the TM-2 tokamak. KRK called analogous plasma formations "tubular structures." They anticipated that these are "solid-state carbon nanotubes" (!) but ignored the fact that, at typical tokamak plasma temperatures of $T \sim 100$ eV ~ 1 million degrees, any nanotubes should instantly evaporate. As will be shown below, the particular structures observed by KRK might be explained in terms of the familiar filamentation and bunching mechanisms. (Notably, they obtain the figures by the method of contrasting the photographs on a computer. However, some physicists doubt the efficiency of this method and even the very existence of tubular structures; see, e.g., a comment by Strelkov [15].)

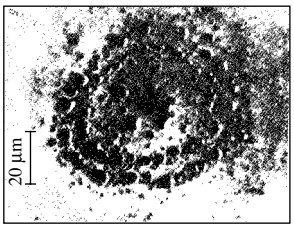

Fig. 1. Trace of a microbeam (borrowed from [11]).

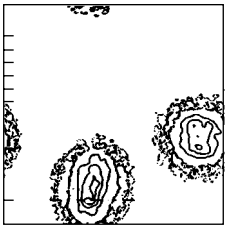

Fig. 2. Calculated beam trace (borrowed from [14]).

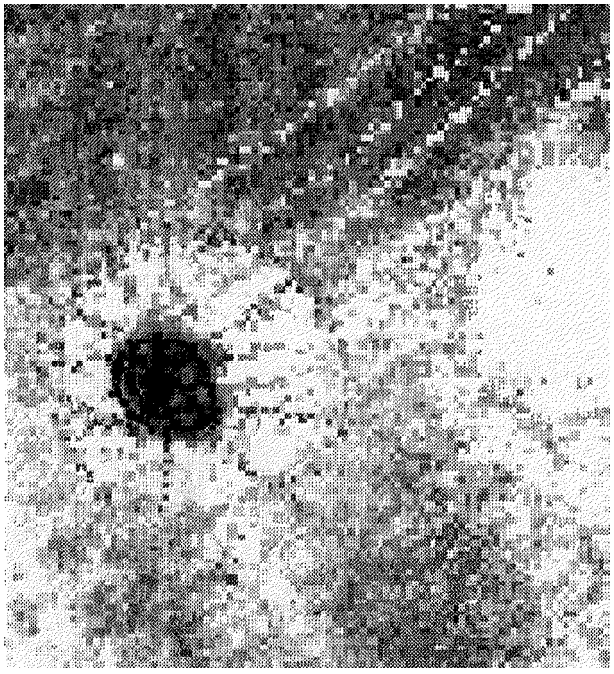

Fig. 3. Example of the cable observed by KRK (borrowed from [15]).

2. NONLINEAR FILAMENTATION EQUATIONS

A beam of accelerated particles can be split into filaments by several types of instabilities, e.g., by thermal instability or thermal–ionizational instability, which develop on the Coulomb collision time scale. However, in what follows, we restrict ourselves to considering several dissipationless instabilities, which grow on shorter time scales. In the long-wavelength approximation, most of them are described by the so-called quasigaseous equations in the standard form [5, 7–10]:

$$\frac{\partial}{\partial t}\rho_* + \nabla\cdot(\rho_*\mathbf{v}) = 0, \quad \frac{\partial}{\partial t}\mathbf{v} + (\mathbf{v}\cdot\nabla)\mathbf{v} = mc_0^2\nabla\rho_*^{1/m}, \tag{1}$$

where $\rho_* = n/n_0$ is the electron density normalized to the unperturbed density, m is the azimuthal number, and c_0 = const. In the linear approximation, in which $\rho_* = 1 + \rho^{(1)}$ and $\rho^{(1)} \ll 1$, these equations describe standing perturbations $\rho^{(1)} \sim \exp(\gamma t)\sin(kx)$ with the growth rate $\gamma = kc_0$. However, Eqs. (1) also admit solutions in nonlinear cases.

We start by considering the magnetic filamentation instability, which is associated with the appearance of a magnetic field perpendicular to the propagation direction of the beam. In principle, this well-studied filamentation mechanism has been known for many years, but it is nontrivial and can manifest itself in several ways. First, it is expedient to discuss this mechanism for the simple case of beams of accelerated particles in a plasma with no magnetic field present. In this case, of particular importance is the following equation describing the screening of the current by electrons:

$$\mathbf{E} = -\frac{4\pi}{\omega_0^2}\frac{\partial}{\partial t}\mathbf{j}_{ext}, \tag{2}$$

where $\mathbf{j}_{ext} = -|e|n\mathbf{v}_0$ is the external beam current. This equation implies that an increase in the current produces the electric field pointing in the direction opposite to the current, and vice versa, a decrease in the current produces the field pointing in the direction of the current.

If the beam is no longer fed with new particles, it should be gradually damped. This process can be described by supplementing Eq. (2) with Ohm's law $\mathbf{E} = \rho\mathbf{j}$, where $\rho = m_e/\tau ne^2$ is the Spitzer electrical resistivity of the plasma. We thus arrive at the equations

$$\frac{\partial}{\partial t}j = -\frac{\omega_0^2}{4\pi}E = -\frac{1}{\tau}j, \quad j(t) = j(0)\exp(-t/\tau), \tag{3}$$

where $\tau = 1/nv_T\sigma_C$ is the time scale on which the beam is damped by Coulomb collisions. Under the conditions prevailing in tokamaks, the plasma density is about $n \sim 10^{13}$ cm^{-3}, the plasma temperature is about $T \sim 1$ keV, the electron thermal velocity is about $v_T = \sqrt{T/m_e} \sim 10^9$ cm/s, and the cross section for Coulomb collisions is about $\sigma_C = \Lambda(e^2/T)^2 \sim 2\times 10^{-19}$ cm^2, so that we have $\tau \sim 0.5$ ms (note that the duration of one stroke in lightning, which may consist of 10 to 40 strokes, is shorter by a factor of 10 to 100). For tokamaks and Z-pinches, we consider faster filamentation processes, neglecting the damping of filaments.

Equation (2) is derived from Maxwell's equations with allowance for the permittivity operator:

$$\nabla\times\mathbf{B} = \frac{4\pi}{c}\mathbf{j}_{ext} + \frac{\partial}{c\partial t}(\varepsilon_\perp\mathbf{E}), \quad \nabla\times\mathbf{E} = -\frac{\partial}{c\partial t}\mathbf{B}, \tag{4}$$

where $\varepsilon_\perp = 1 - (\omega_0/\omega)^2$, $\omega_0^2 = 4\pi Ne^2/m_e$, and N is the density of the plasma electrons. For $\omega \ll \omega_0$, we can neglect unity in the expression for $\varepsilon_\perp$. Then, we differentiate with respect to t, make the replacement $(\partial/\partial t)^2 = -\omega^2$, and take into account the second equation to obtain the screening equation in the form

$$\Delta\mathbf{E} - \left(\frac{\omega_0}{c}\right)^2\mathbf{E} = \frac{4\pi}{c^2}\frac{\partial}{\partial t}\mathbf{j}_{ext}. \tag{5}$$

According to this equation, the electric field $\mathbf{E}$ is screened on the skin depth $\delta = c/\omega_0$. For a tokamak plasma density of $N \sim 10^{14}$ cm^{-3}, we have $\omega_0 \sim 5\times 10^{11}$ s^{-1} and $\delta \sim 1$ mm. In what follows, we restrict ourselves to considering larger-scale structures, so that we neglect the term $\Delta\mathbf{E}$ and thus arrive at formula (2).

3. MAGNETIC FILAMENTATION INSTABILITY OF A BEAM

In this case, the second of the Maxwell equations determines the transverse components of the magnetic field $\mathbf{B} = (mc/Ne^2)\nabla\times\mathbf{j}_{ext}$. If the beam propagates along the z-axis, these components are equal to

$$\mathbf{B}_x = -(m_e c v_0/N|e|)\frac{\partial}{\partial y}n, \qquad \mathbf{B}_y = (m_e c v_0/N|e|)\frac{\partial}{\partial x}n, \tag{6}$$

and the equation of transverse motion of the beam electrons takes the form

$$\dot{\mathbf{v}}_\perp = \frac{\partial}{\partial t}\mathbf{v}_\perp + v_0\frac{\partial}{\partial z}\mathbf{v}_\perp + (\mathbf{v}_\perp\cdot\nabla)\mathbf{v}_\perp = -\frac{|e|}{m_e c}[\mathbf{v}\times\mathbf{B}]_\perp = c_0^2\nabla_\perp\rho_*. \tag{7}$$

Here, $\rho_* = n/n_0$ is the reduced density of the beam electrons (with n_0 = const being their unperturbed density) and $c_0^2 = (n_0/N)v_0^2$. Equation (7) should be supple-

mented with the continuity equation, which can be written as

$$\frac{\partial}{\partial t}\rho_* + v_0\frac{\partial}{\partial z}\rho_* + \nabla\cdot(\rho_*\mathbf{v}_\perp) = 0. \quad (8)$$

Finally, we transform to the reference frame moving uniformly with the beam velocity $v_z = v_0$ and introduce the operator $(\ldots)'_\tau = (\ldots)'_t + v_0(\ldots)'_z$ in order to write the above two equations in the form

$$\frac{\partial}{\partial\tau}\rho_* + \nabla\cdot(\rho_*\mathbf{v}_\perp) = 0,$$
$$\frac{\partial}{\partial\tau}\mathbf{v}_\perp + (\mathbf{v}_\perp\cdot\nabla)\mathbf{v}_\perp = c_0^2\nabla_\perp\rho_*. \quad (9)$$

These equations were used in a number of papers to solve the problems of beam filamentation (see [14, 16, 17]). Equations (9) are represented in the standard form of the "quasi-Chaplygin" dynamic equations for unstable media; a comprehensive theory of these equations is given in monographs [5, 9, 10]. They describe the growing perturbations of the type of water droplets on the ceiling (or inverted shallow water layer).

If the perturbations depend only on the x coordinate and the time τ, then we can derive the relevant exact nonlinear "spontaneous" solution, which is expressed in terms of the complete elliptic integrals and describes the splitting of an initially homogeneous beam into planar layers. Two-dimensional numerical calculations carried out by Lee and Lampe [14] yielded the picture reproduced in Fig. 2, in which an individual spot is very similar to the experimental picture from Fig. 1. If the structures shown in these two figures were continued along the z-axis, they also would be similar to the squirrel-cage structure observed by KRK (Fig. 3). Clearly, the specific structure in Fig. 2 originates from the initial (seed) perturbations. However, below, we try to *analytically* model the development of the slowest two-dimensional intrinsic perturbation mode.

Assuming that the initial (at $\tau = -\infty$) beam density is uniform (n_0 = const), we consider the ideal case, in which the entire (x, y) plane is covered by a perturbation "parquet." In this case, the fastest growing modes are those in the form of hexagonal cells similar to Benar cells. Setting $\mathbf{v}_\perp = \nabla\varphi(\tau, x, y)$, we obtain from the last equation the Bernoulli integral $\varphi'_\tau + (1/2)(\nabla\varphi)^2 = c_0^2(\rho_* - 1)$, so that Eqs. (9) reduce to the following equation for the velocity potential:

$$\varphi''_{\tau\tau} + c_0^2\Delta\varphi = A_2 + A_3, \quad A_2 = -\varphi'_\tau\Delta\varphi - [(\nabla\varphi)^2]'_\tau,$$
$$A_3 = -((1/2)\nabla\cdot[(\nabla\varphi)^2\nabla\varphi].) \quad (10)$$

It is of interest to note that this nonlinear equation is formally similar in structure to the equation describing parametric waves on the water surface in a vessel with a vibrating bottom (see [18]). Small-amplitude waves on the water surface are organized into a hexagonal parquet, larger-amplitude waves form square parquet, and waves with even larger amplitudes are one-dimensional, so that we can speak of the phase transitions in the lattice of parametric waves on a water surface.

4. PARTICULAR SOLUTIONS TO THE FILAMENTATION EQUATIONS

In the case under consideration, the perturbations grow exponentially, so that, in the linear approximation, the structure that is first to occur is that composed of hexagonal beams:

$$\varphi = T(\tau)R(x, y),$$
$$R = C_1 + C_2 + C_3 = \sum C_j, \quad C_j = \cos(\mathbf{r}\cdot\mathbf{k}_j), \quad (11)$$

where the vectors $\mathbf{k}_j$ lie in the same plane, the angle between them being 120°, so that we have $|\mathbf{k}|_j = k$ and $\mathbf{k}_1 + \mathbf{k}_2 + \mathbf{k}_3 = 0$. For such a cellular structure, we obtain $\Delta R = -k^2R$; in the first approximation, this gives $T = a\exp(\gamma\tau)$ and $\gamma = kc_0$. The pattern of the contour lines $R(x, y) = C_* = \text{const} < 3$ (or, in explicit form, $y = (2/\sqrt{3})\arccos[(C_* - x)/2\cos(x/2)]$) is depicted in Fig. 4, and the three-dimensional relief of the function $R = R(x, y)$ is displayed in Fig. 5. The two-dimensional

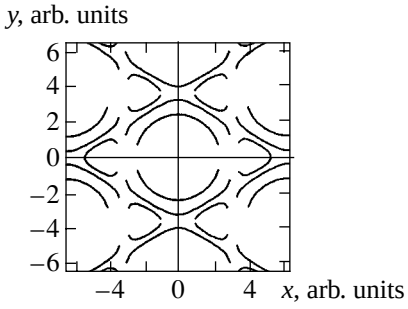

Fig. 4. Hexagonal parquet.

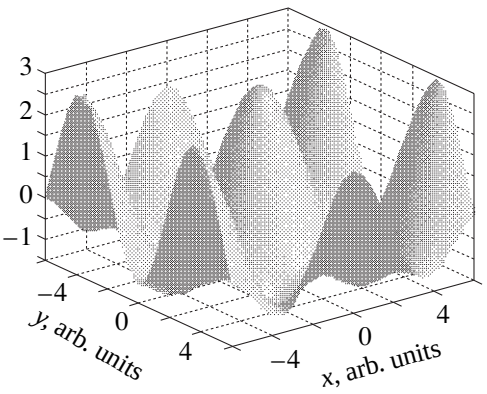

Fig. 5. Function $R(x, y)$.

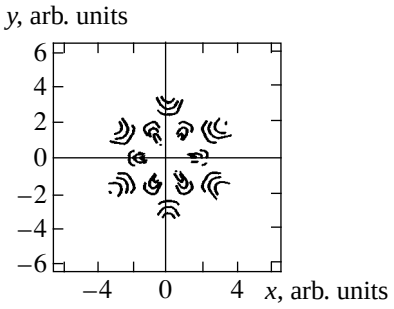

Fig. 6. Bessel wheel.

equations can be solved only numerically (cf. Fig. 2). However, we will not present here the relevant solution, because it is clear that the nonlinear solution leads to peakier profiles in comparison with the simple linear cosinusoidal profiles. Since the filaments in the photograph are very thin, the nonlinear approach is more adequate for describing them. Another difference between the linear and nonlinear approximations is that nonlinear equations describe a collapse on a finite time scale rather than the exponential growth of the linear perturbations. Also, the simplest nonlinear solutions can correspond to solitary local perturbations.

Another linear solution in polar coordinates (ϑ, r) is that expressed through the Bessel function, $R_n = \cos(n\vartheta)J_n(kr)$, with the asymptotic $J_n \sim r^{-1/2}\cos[kr - (\pi/2)n - (\pi/4)]$. For $n = 6$, this solution is close to a hexagonal parquet. The related pattern of contour lines $R_6 = \text{const}$, which will be referred to as the "Bessel wheel" for brevity, is presented in Fig. 6. An essentially similar family of current filaments of the squirrel-cage type, continued along the z-axis, is shown in Fig. 3, which is borrowed from a paper by KRK [15]. The nonlinear terms in Eq. (9) give rise to additional filaments. Thus, the hexagonal parquet (11) is imposed on the square parquet described by the quadratic term $R^{(2)} = \cos[(\mathbf{k}_1 - \mathbf{k}_2)\cdot\mathbf{r}] + \cos[(\mathbf{k}_1 - \mathbf{k}_3)\cdot\mathbf{r}] + \cos[(\mathbf{k}_2 - \mathbf{k}_3)\cdot\mathbf{r}]$, so that the resulting structure is similar to the experimentally obtained structure shown in Fig. 1.

In some cases, the structures that are treated by KRK as solid-state nanotubes may actually be current sheets, which can also be described by Eq. (9). For such current sheets with $\varphi = \varphi(\tau, x)$, this equation becomes

$$\frac{\partial^2}{\partial\tau^2}\varphi + c_0^2\varphi'' = -\varphi''\frac{\partial}{\partial\tau}\varphi - \frac{\partial}{\partial\tau}[(\varphi')^2] - \frac{1}{2}[(\varphi')^3]', \quad (12)$$

where the prime denotes the partial derivative with respect to x. Although the nonlinear equation (12) is fairly complicated, it admits an exact solution, which can be derived in the following way. We introduce the notation

$$\varphi' = v, \quad \dot\varphi = c_0^2(\rho_* - 1) - \frac{1}{2}v^2, \quad (13)$$

and again obtain two quasilinear equations:

$$\dot\rho_* + (\rho_* v)' = 0, \quad \dot v + vv' = c_0^2\rho_*'. \quad (14)$$

Switching to the inverse functions $t = T(\rho_*, v)$ and $x = X(\rho_*, v)$, we arrive at the linear equations, whose exact solutions are presented in monographs [5, 9, 10].

It is also useful to consider the two-dimensional case with allowance for the pressure in the compressed plasma filaments. To do this, we supplement the right-hand side of the second of Eqs. (14) with the conventional term $\delta = -\rho^{-1}\nabla p$ with the pressure described by the Poisson's adiabat, $p = p_0(\rho/\rho_0)^\gamma$. The simplest case is that with the model adiabatic index $\gamma = 2$, for which we have $\delta = -c_s^2\nabla\rho_*$, where $c_s^2 = 2p_0/\rho_0$ is the squared speed of sound in the beam plasma. Then, Eqs. (14) can be written in the standard form

$$\dot\rho_* + \nabla\cdot(\rho_*\mathbf{v}) = 0, \quad \dot{\mathbf{v}} + (\mathbf{v}\cdot\nabla)\mathbf{v} = c_{\text{eff}}^2\nabla\rho_*, \quad (15)$$

where $c_{\text{eff}}^2 = c_0^2 - c_s^2$. Hence, for $c_{\text{eff}}^2 > 0$, we deal with unstable standing perturbations, and, for $c_{\text{eff}}^2 < 0$, Eqs. (15) admit solutions describing the waves running with the velocity c_{eff} across the propagation direction of the beam.

To conclude this section, we explain the mechanism for generating ion beams in Z-pinches, in which the bulk of the plasma is compressed toward the axis (until a singularity arises at the axis), whereas a certain fraction of the plasma always remains in the peripheral regions. We can assume that, by the time at which the current in the main plasma column reaches its maximum value $I_{\max}$, the peripheral plasma turns out to be magnetized by the main magnetic field $B_0 = 2I_{\max}/cr = \text{const}/r$ of the pinch. In the limit $m_e \longrightarrow 0$, the dispersion relation for a radially propagating extraordinary wave has the form $\omega^2 = k^2c^2 + (\omega_{0e}^2/\omega_{Be})^2$. For low frequencies ω, we can make the replacement $k^2 \longrightarrow -\Delta$ in order to see that this dispersion relation is equivalent to the following equation describing the magnetic screening of a cylindrical pinch:

$$\Delta A = \frac{\partial}{r\partial r}\left(r\frac{\partial}{\partial r}A\right) = (\omega_{0e}^2/c\omega_{Be})^2 A = C_* r^2 A, \quad (16)$$

where $A = A_z$ is the vector magnetic potential of the wave and $C_* = (2\pi Nec/I_{\max})^2 = \text{const}$ (the density of the peripheral plasma is also assumed to be constant, $N = \text{const}$). Setting $C_* = 4/R_0^4$ (where $R_0 = \sqrt{I_{\max}/\pi N|e|c}$ is the radius at which the current is screened by the magnetic field) and introducing the new argument $x = (r/R_0)^2$ yields the solution $A = aK_0(x)$, where K_0 is the modified Bessel function of the second kind, which, at

small arguments, is approximately equal to $K_0 \approx \ln(2/x)$.

In the model developed here, the main pinch is assumed to be an infinitely thin conductor with the current $I = I_{max} + I_1(t)$. In the limit $r \longrightarrow 0$, the correction $I_1(t)$ gives the wave magnetic field $B_1 = 2I_1/cr = -A_r'$, which allows us to find the wave amplitude, $a = a(t) = I_1(t)/c$, and the wave electric field

$$E = E_z(t, r) = -\frac{\partial}{c\partial t}A = -K_0(x)\frac{d}{c^2 dt}I_1(t). \quad (17)$$

Since $K_0(x) > 0$, we can see that a decrease in the main pinch current generates the induction electric field in the peripheral regions, which is directed along the current, as is the case described by formula (2). At the "singularity" time, when the main pinch current in a deuterium pinch breaks, this field accelerates beams of deuterium ions and produces nonthermonuclear neutrons. Simultaneously, the beams can be split into thinner filaments by the above-described mechanism.

In essence, it is this filamentation mechanism that hinders the ignition of fusion targets by the beams of ions and relativistic electrons: attempts to focus the beams give rise to their filamentation. The situation with laser beams in plasmas is essentially the same: the laser beam self-focusing, described by the familiar nonlinear Schrödinger equation, actually leads to defocusing in a way that is analogous to the above filamentation of particle beams.

5. FILAMENTATION BY TEARING INSTABILITY

Along with the magnetic filamentation, thin current-carrying layers can also be subjected to the tearing filamentation. A simple example of the tearing filamentation mechanism was described by Bulanov and Sasorov [17] (see also [5]). Let us briefly discuss this example.

We consider a thin plasma layer of thickness $L(t, x)$ and assume that the current in the layer flows in the z direction. The layer is located near the plane $y = 0$. The plasma density in the layer is $n(t, x) = n_e = n_i$ and the volume current density is $j_z = |e|n(v_{iz} - v_{ez})$, so that the current per unit width of the layer is equal to $i_1 = j_z L = cB_0/2\pi = \text{const}$, where $\pm B_0$ is the magnetic field on the outside of the layer.

For long-wavelength perturbations (with $\lambda \gg L$) propagating with the velocity $v_x = v(t, x)$, the conservation law for the number of particles in the cross section of the layer, nL, has the form

$$\frac{\partial}{\partial t}\rho_* + \frac{\partial}{\partial x}\rho_* v = 0, \quad \rho_* = \frac{nL}{n_0 L_0} \quad (18)$$

and yields the first of the quasi-gaseous equations. In the second quasi-gaseous equation, we neglect the plasma motion in the x direction and set $v_{ze} \gg v_{Te}$. We thus arrive at the equations

$$\frac{\partial}{\partial t}v + v\frac{\partial}{\partial x}v = -\frac{1}{m_i nc}j_z B_y, \quad B_y = -\frac{\partial}{\partial x}A, \quad (19)$$

where $A = A_z^{(1)}(t, x)$ is the correction to the unperturbed vector potential. Then, we take into account the conservation laws for the generalized electron and ion momenta and their consequences

$$\frac{\partial}{\partial x}\left(m_i v_{zi} + \frac{e}{c}A\right) = 0, \quad \frac{\partial}{\partial x}\left(m_e v_{ze} - \frac{e}{c}A\right) = 0, \quad (20)$$

which yield the following expression for the magnetic field component transverse to the layer:

$$B_y = -\frac{\partial A}{\partial x} = \frac{c}{\mu e}\frac{\partial}{\partial x}(v_{zi} - v_{ze}), \qquad \mu = \frac{m_e m_i}{m_e + m_i}. \quad (21)$$

With all these results in mind, we rewrite the second of Eqs. (19) in the final form:

$$\frac{\partial}{\partial t}v + v\frac{\partial}{\partial x}v = -\frac{m_e}{2m_i}\frac{\partial}{\partial x}(v_{zi} - v_{ze})^2 = -\frac{1}{2}c_0^2\frac{\partial}{\partial x}\rho_*^{-2}, \quad (22)$$

where $c_0 = 2c_A(\delta/L_0)$, $c_A = B_0/\sqrt{4\pi n_0 m_i}$ is the Alfvén speed, and $\delta = c/\omega_0$ is the skin depth. The nonlinear equations (18) and (22) have the structure of the quasi-gaseous equations (1) with the azimuthal number $m = -1/2$ and admit the simplest nonlinear spontaneous solution

$$\rho_* = \frac{-\sinh T}{\cosh T - \cos X}, \quad v = c_0\frac{\sin X}{\sinh T}, \quad (23)$$

where $T = \gamma t < 0$, $X = kx$, and $\gamma = kc_0$. For $t \longrightarrow -\infty$, we deal with an unperturbed state with $\rho_* = 1$. However, as time elapses, the perturbations grow with the rate $\gamma = 2\pi c_0/\lambda_0$, where λ_0 is the wavelength of the seed perturbations. At the critical time $t = 0$, the layer splits into individual filaments, as in the case observed in Z-pinches and plasma foci.

6. CURRENTS TRANSVERSE TO THE MAGNETIC FIELD

Here, we consider the injection of a current-carrying beam into the plasma in the direction perpendicular to the uniform magnetic field $B_y = B_0 = \text{const}$. We start by analyzing an infinitely thin conductor with the current J that is directed along the z-axis and passes through the point ($x = a = J/cB_0 > 0$, $y = 0$). In the plane $y = 0$, this current creates the magnetic field $B_y^{(1)} = 2J/cx$. At the line ($x = -a$, $y = 0$), the total magnetic field is zero. If a second conductor with the opposite current $J_z = -J$ were

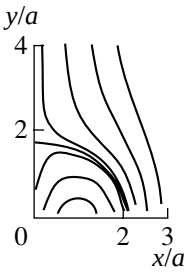

Fig. 7. Two currents in a magnetic field.

placed at this line, then, on the one hand, it would experience no Ampére force and, on the other, it would cancel the external magnetic field at the position of the first conductor. We thus can conclude that the dipole system of these two oppositely directed currents should be in equilibrium, in which case the vector potential $A = A_z$ of the total magnetic field and the magnetic field lines are described by the equations

$$A = B_0[a(\ln(r_+^2/r_-^2) - x)] = \text{const}, \qquad Y = \pm\sqrt{2X\coth\xi - 1 - X^2}, \tag{24}$$

where $r_\pm^2 = y^2 + (x \pm a)^2$, $X = x/a$, $Y = y/a$, and $\xi = X/2 +$ const. The pattern of the magnetic field lines in the first quadrant in the (x, y) plane is shown in Fig. 7.

Instead of infinitely thin currents, we now consider an analogous equilibrium dipole MHD configuration with distributed currents. We assume that the currents $j = j_z$ flow inside a cylinder of radius $r = a$ and that there are no currents on the outside of the cylinder. In this situation, the external magnetic field is equal to $\mathbf{B}^e = \nabla\psi$ (where $\Delta\psi = 0$, as is the case in vacuum), so that, in cylindrical coordinates, the scalar magnetic potential in terms of the field components has the form

$$\psi(r, \varphi) = \left(B_0 r + \frac{\alpha}{r}\right)\sin\varphi, \qquad B_r = \left(B_0 - \frac{\alpha}{r^2}\right)\sin\varphi, \quad B_\varphi = \left(B_0 + \frac{\alpha}{r^2}\right)\cos\varphi, \tag{25}$$

where α is a constant. At infinity, this scalar potential corresponds to a uniform magnetic field $B_y = B_0 =$ const. At the cylinder surface $r = a$, we impose the condition $B_r = 0$, so that we have $\alpha = a^2 B_0$. Hence, at the cylinder surface, the only nonzero magnetic field component is the component $B_\varphi = 2B_0\cos\varphi$, which produces the magnetic pressure $P_m = B_\varphi^2/8\pi = P_{\max}\cos^2\varphi$, where $P_{\max} = B_0^2/2\pi$. If the cylinder is surrounded by a plasma at a uniform pressure $p_0 =$ const, then the total pressure at its surface is equal to $P_\Sigma = p_0 + P_{\max}\cos^2\varphi$. Let us consider the pressure inside the cylinder ($r < a$).

Because of the currents $j = j_z$ flowing inside the cylinder, the magnetic field is determined by the vector potential $A = A_z$, so that we arrive at the MHD equations

$$\Delta A = -\frac{4\pi}{c}j, \quad B_x = A_y', \quad B_y = -A_x', \qquad p_x' = \frac{j}{c}A_x', \quad p_y' = \frac{j}{c}A_y', \tag{26}$$

which imply that $p = p(A)$ is an arbitrary function and that the current density is equal to $j = cdp/dA$. Setting $p(A) = p_0 + |\beta|A^2$ gives the current density $j = 2c|\beta|A$ and yields the following Bessel equation for the vector potential:

$$A_{rr}'' + \frac{1}{r}A_r' + \frac{1}{r^2}A_{\varphi\varphi}'' + k^2 A = 0, \tag{27}$$

where $k = \sqrt{8\pi|\beta|}$. The solution in terms of the first-order Bessel function gives the components of the vector potential and magnetic field:

$$A = A_0 J\cos\varphi, \quad B_r = -\frac{A_0}{r}J\sin\varphi, \qquad B_\varphi = -A_0 k J'\cos\varphi, \tag{28}$$

where $J = J_1 = J_1(\rho)$ and $\rho = kr$. This solution also satisfies all of the required conditions under which the configuration is in equilibrium.

Specifically, at the cylinder surface $r = a$, the component B_r of the internal magnetic field vanishes if $J_1(ka) = 0$, where $ka = \xi_1 = 3.8317$ is the first zero of the Bessel function J_1, which is approximately equal to $J_1(\rho) \approx (\rho/2)[1 - (\rho/3.8317)^2]$ across the region $0 < \rho < 3.8317$. In this case, we have $A = 0$ at the cylinder surface, at which the pressure of the plasma inside the cylinder is accordingly equal to $p_{A=0} = p_0$ and thus coincides with the plasma pressure on the outside of the cylinder.

The magnetic field component $B_\varphi = B_a\cos\varphi$, where $B_a = -A_0 kJ'(ka)$, produces the magnetic pressure $P_m = (B_a^2/8\pi)\cos^2\varphi$, so that the complete equilibrium of a configuration with a dipole current-carrying cylindrical beam, which moves apart the lines of the external magnetic field, will be achieved when $B_a = 2B_0$. The tabulated values of the Bessel functions give $J'(\xi_1) = -0.4028$, which enables us to determine the amplitude $A_0 = 1.3aB_0$ and, thereby, the current density $j = j_0 J_1(kr)\cos\varphi$, where $j_0 = 1.5(cB_0/a)$. In such a configuration, the current flowing through the right half of the cylinder is about $I_+ \approx 0.8caB_0$, and the same current flows through the left part but in the opposite direction. If the current I_+ and the field B_0 are specified, we can determine the equilibrium radius a of the cylinder. Thus, in order for the dipole current $I_+ = -I_- = 10$ A to be in equilibrium with the tokamak magnetic field $B_0 =$ 10 kG, it should flow across the field B_0 and inside the

region with a diameter of about $2a \sim 3$ mm. The filaments of roughly the same diameter were observed by KRK.

For brevity, we will refer to this configuration as a plasma bicylinder. It can be shown that, on the outside of the cylinder, the so-called "stability integral" $J = \int dl/B$ decreases with increasing distance from the cylinder surface (this result was obtained in collaboration with V.P. Vlasov). Consequently, it might be expected that such a bicylinder will be stable at least against the sausage instability. Inside the bicylinder, snakelike perturbations should be unstable; however, we can anticipate that the time scale on which the bicylinder forms is too short for them to develop. For comparison, recall that, for an ordinary Z-pinch, in which current I is distributed uniformly over the cross section of radius a, the integral $J = \int dl/B$ inside the pinch is constant, $J_i = \pi a^2 c/I = \text{const}$, while, on the outside, it increases with increasing distance from the cylinder surface according to the law $J_e = J_i(r/a)^2$, thereby leading to instability.

Figure 8 shows the pattern of the magnetic field lines inside the bicylinder, where the magnetic potential is expressed in terms of the first Bessel function $J_1 = (kr/2)\prod_{i=1}^{\infty}[1 - (kr/R_i)^2]$ (where $R_i = 3.83, 7.02, 10.17, \ldots$ are the zeros of the function). However, to a high accuracy, we can keep only the first factor, corresponding to the first zero, and set $J_1 \sim \rho(1 - \rho^2)$, where $\rho = kr/R_1$, in which case the potentials inside and outside the cylinder are described by the approximate formulas

$$A_{int} = \rho(1 - \rho^2)\cos\varphi, \quad A_{ext} = \rho(1 - \rho^{-2})\cos\varphi. \quad (29)$$

Accordingly, the equations for the magnetic field lines in these regions have the form

$$\begin{aligned} Y_{int} &= \pm\sqrt{1 - (C_i/X) - X^2}, \\ Y_{ext} &= \pm\sqrt{[1 - (C_e/X)]^{-1} - X^2}, \end{aligned} \quad (30)$$

where $C_{i,e}$ are constants. These magnetic field lines are shown in Fig. 8, illustrating the configuration (for brevity, called the current bicylinder) that is very similar to the configuration in Fig. 7. Recall that Figs. 7 and 8 present the patterns of the field lines only in the first quadrant ($x > 0$, $y > 0$). The overall pattern of the magnetic field lines is symmetric about the origin of the coordinates (see Fig. 16). Now, we proceed to an analysis of longitudinal beam bunching.

7. TWO TYPES OF THE BUNCHING INSTABILITY

The photographs of plasma focus discharges of the Mather type, taken from the end of the device, often show double filamentary structures in the form of current-aligned filaments and a set of rings perpendicular to them. The appearance of filaments can be attributed to current filamentation by the mechanisms considered above, while the formation of rings is, presumably, a consequence of the synchronous longitudinal bunching of the parallel beams, which was also studied earlier in many papers. Let us briefly describe two possible bunching mechanisms.

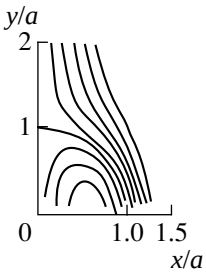

Fig. 8. Current bicylinder.

The first is the so-called Buneman instability, which involves both electrons and ions. In the linear approximation, it was studied by Buneman [19]; however, we describe it here in the nonlinear approximation. We denote the density, velocity, charge, and mass of the electrons by n_e, v_e, $q_e = -|e|$, and m_e, respectively; the same parameters of the ions, by n_i, v_i, $q_i = Z_i|e|$, and m_i; and the longitudinal electric field, by E. For the five functions n_e, n_i, v_e, v_i, and E, we have the following five one-dimensional nonlinear equations:

$$\begin{aligned} n_e &= Z_i n_i, \quad \frac{\partial}{\partial t}n_\alpha + \frac{\partial}{\partial x}n_\alpha v_\alpha = 0, \\ &\frac{\partial}{\partial t}v_\alpha + v_\alpha\frac{\partial}{\partial x}v_\alpha = \frac{q_\alpha}{m_\alpha}E, \end{aligned} \quad (31)$$

where $\alpha = e, i$. Here, the pressure is neglected, the initial velocity v_{0e} of the electron is assumed to be higher than their thermal velocity, and the ions at the initial instant (at $t \longrightarrow -\infty$) are assumed to be immobile. These equations can be easily solved in the linear approximation. However, in [5, 9, 20], it was shown that, in the nonlinear approximation, they also admit an exact solution. In order to obtain this solution without making any additional assumptions, it is sufficient to introduce the effective density $\rho = n_e/n_{0e} = n_i/n_{0i}$ and effective velocity $v = (Z_i m_e v_e + m_i v_i)/(Z_i m_e + m_i)$, with which Eqs. (31) is reduced to the two quasi-Chaplygin equations

$$\begin{aligned} &\frac{\partial}{\partial t}\rho + \frac{\partial}{\partial x}\rho v = 0, \\ &\frac{\partial}{\partial t}v + v\frac{\partial}{\partial x}v = mc_0^2\frac{\partial}{\partial x}\rho^{1/m}, \end{aligned} \quad (32)$$

where $c_0 = v_{0e}\sqrt{Z_i m_e/m_i}$ and the azimuthal number is equal to $m = -1/2$, as is the case with tearing instability.

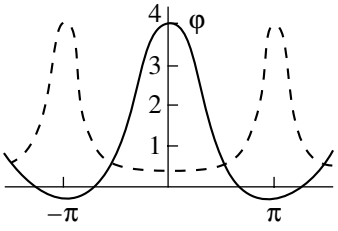

Fig. 9. Beam bunching.

For this reason, the simplest spontaneous solution is analogous to solution (23):

$$\rho = \frac{-\sinh T}{\cosh T - \cos X}, \quad v = c_0 \frac{\sin X}{\sinh T}, \tag{33}$$

where $T = \gamma t < 0$, $X = kx$, and $\gamma = kc_0$. For $t \longrightarrow -\infty$, we deal with an unperturbed state with $\rho = 1$. However, as time progresses, the seed perturbations grow at the rate $\gamma = 2\pi c_0/\lambda_0$ (where λ_0 is the wavelength of the seed perturbations) and, at the critical time $t = 0$, the plasma breaks into pancakelike bunches, as is the case shown in Fig. 9. In Z-pinches, this may results in the disruption of the conduction current.

The role of the second mechanism can be played by the bunching of an electron beam propagating through the main plasma. In contrast to the Buneman instability, we assume here that the ions are immobile and that their density is constant, $N_i = \text{const}$. We denote the electron densities of the beam and of the main plasma by n_b and n_e, respectively, and the corresponding electron velocities, by v_b and v_e in order to write the initial equations in the form

$$\frac{\partial}{\partial t} n_\alpha + \frac{\partial}{\partial x} n_\alpha v_\alpha = 0, \quad \frac{\partial}{\partial t} v_\alpha + v_\alpha \frac{\partial}{\partial t} v_\alpha = \frac{q_e}{m_e} E. \tag{34}$$

From these equations, we obtain the quasineutrality condition and the current conservation law

$$\begin{aligned} n_b + n_e &= N_i = \text{const}, \\ n_b v_b + n_e v_e &= n_b^0 v_b^0 = \text{const}, \end{aligned} \tag{35}$$

where n_b^0 and v_b^0 are the initial (at $t \longrightarrow -\infty$) density and velocity of the beam. An approximate solution to Eqs. (34) is presented in [21]. However, in [5, 9, 10], it was shown that, without making any additional assumptions, they can also be reduced to two quasi-Chaplygin equations with the azimuthal number $m = 1$ and the parameter $c_0 = v_b^0 \sqrt{n_b^0/N_i}$, which determines the linear growth rate $\gamma = kc_0$.

In order to convince ourselves of this, we must carry out the following nontrivial transformations. First, we introduce two new functions, $u = v_b - v_e$ and $\xi = (n_e - n_b)/N_i$, and the constant mean electron velocity $V_0 = (n_b v_b + n_e v_e)/N_i$. Then, we pass over to the reference frame moving with the velocity V_0 and introduce the operator $(\ldots)'_{t^*} = (\ldots)'_t + V_0(\ldots)'_x$ in order to rewrite Eqs. (34) as

$$\frac{\partial}{\partial t^*}\xi = \frac{\partial}{2\partial x}[(1-\xi^2)u], \quad \frac{\partial}{\partial t^*}u = -\frac{\partial}{2\partial x}(\xi u^2). \tag{36}$$

These equations cannot be reduced to the standard quasi-Chaplygin equations. However, introducing a new pair of functions, $\rho = (u/u_0)^2(1 - \xi^2)/(1 - \xi_0^2)$ and $v = u\xi - u_0\xi_0$, and the new operator $(\ldots)'_\tau + (V_0 + u_0\xi_0)(\ldots)'_x$ puts Eqs. (36) in the standard quasi-Chaplygin form

$$\frac{\partial}{\partial \tau}\rho + \frac{\partial}{\partial x}(\rho v) = 0, \quad \frac{\partial}{\partial \tau} v + v\frac{\partial}{\partial x} v = c_0^2 \frac{\partial}{\partial x}\rho \tag{37}$$

with the parameter $c_0^2 = (1 - \xi_0^2)u_0^2/4 > 0$ and the azimuthal number $m = 1$ (which differs from $m = 1/2$ in the case of Buneman instability). The growing nonlinear parametric spontaneous solutions (which originate from indefinitely small seed perturbations at $t \longrightarrow -\infty$) are expressed in terms of elliptic integrals and also describe the bunching process that breaks the beam into pancakelike bunches of the Buneman type.

Hence, the beam filamentation may result in a set of longitudinal parallel filaments and synchronous beam bunching may give rise to bright ring structures perpendicular to the current direction. Presumably, it is this effect that is observed in plasma focus discharges.

It is expedient to compare the growth rates $\gamma^{(i)} = 2\pi c_0^{(i)}/\lambda$ of the above three instabilities, assuming, for definiteness, that their wavelengths λ are the same. In this case, the instabilities differ only in the value of the parameter determining the growth rate:

(i) for the magnetic filamentation instability, we have $c_0^{(1)} = v_0 \sqrt{n_0/N_i}$;

(ii) for the Buneman instability, we have $c_0^{(2)} = v_0\sqrt{Z_i m_e/m_i}$; and

(iii) for the electron bunching instability, we have $c_0^{(3)} = v_0\sqrt{n_b^0/N_i}$.

The growth rates of the instabilities will be close to each other for beams with densities such that n $n_b/N_i \sim m_e/m_i \sim 5 \times 10^{-4}$. In plasma foci, fast (accelerated) electrons generate X-ray photons with energies of about 100–200 keV, so that their velocities can be regarded as being weakly relativistic: $v_0 \sim 10^{10}$ cm/s and $c_0 \sim 10^8$ cm/s. We thus can see that the perturbations grow on nanosecond time scales.

8. CONCLUSION

The main features of the behavior of beams in plasmas can finally be summarized as follows:

(i) Thin current filaments that are sometimes observed in Z-pinch and tokamak plasmas should be analyzed theoretically not by simple linear equations, but rather by a more adequate set of nonlinear equations capable of describing operating modes with nonsinusoidal, strongly peaked plasma density profiles.

(ii) It is clear that a beam can be injected into a plasma only when a halo of Foucault currents that screen the magnetic self-field of the beam and are directed opposite to it is immediately generated around the beam path (this is generally true for any thin current channel in a plasma). In this case, the screening radius is about $\delta \sim c/\omega_0$ (in tokamaks, the electron density is $n_e \sim 10^{13}$ cm^{-3}, so that we have $\delta \sim 1$ mm) and, in photographs, such a configuration may resemble a tubular structure.

(iii) In certain cases, the currents that are opposite to the main current (countercurrents) can presumably attract each other, thus evolving into a spiral wound around the central current channel, whose magnetic field helps them to group together into a spiral. However, it is extremely difficult to calculate such a configuration theoretically.

(iv) If there is a magnetic field B_0 frozen in the plasma, a beam can be injected both along and across this field, moving apart the field lines and simultaneously splitting into thinner filaments (see also Appendices 1, 2).

(v) A beam of initially finite length and the countercurrents that it itself excites may stop moving as a single entity after the beam has passed a certain distance in a plasma. However, the beam current may be short-circuited by the countercurrents at the beam ends and thus can continue to circulate for a certain time, but now in closed current circuits (loops) of the form of paper clips. Presumably, configurations of the squirrel-cage type, which might have been observed sometimes by KRK in several tokamaks, form precisely in this way.

In conclusion, it may be worthwhile to say a few words about the papers by KRK that were devoted to the problem under consideration here, namely, current filaments (or, in KRK's terminology, solid-state cables).

Since 1993, they have written about 50 papers on this subject, but most of them were reported at conferences as poster papers, so that only papers [15, 22–25] are listed here as references. These five papers have much in common (which is already clear from their titles), but in none of them do the authors mention that there is an alternative (and generally accepted!) interpretation, according to which the structures that they observed are explained as current filaments. They consider these structures as rigid solid-state nanotubes, which may be present not only in Z-pinch and tokamak plasmas but also in plasmas of space objects (see [22, 23]).

The abstract of their recent paper [15] may be cited as an example.

"Evidence is obtained for the existence of straight tubular structures in a tokamak plasma that are similar to long-lived filaments observed previously in Z-pinches. A hypothesis is advanced to explain these structures as wild cables formed as a result of the channeling of electromagnetic energy. The energy is supplied from an external electric circuit and propagates as high-frequency electromagnetic waves toward the plasma core along hypothetical microsolid (carbon) skeletons that are assembled during electric breakdown and are protected by the waves from the violent action of the surrounding high-temperature plasma."

Let us discuss this hypothesis. In pinch and tokamak plasmas, in which the plasma temperature may be as high as several keV, any solid objects (like pellets) rapidly evaporate. Since the plasma density in tokamaks is approximately a million times lower than the air density under normal conditions (Loschmidt's number) and the plasma temperature is approximately a million times higher than the room temperature, the pressure of the plasma that should be pushed away from the cables is about the atmospheric pressure. Assuming that this plasma pressure is even ten times lower, we obtain from the equality $p_{atm}/10 = E^2/8\pi$ the required electric field strength $E \sim 1$ MV/cm. The question then arises: what is the mechanism for generating such an enormous high-frequency field?

Here are some other quotations from [15].

"An analysis of the phenomenology of filamentary structures allowed us to hypothesize that the observed rigidity of such structures can be provided only by quantum mechanisms because it cannot be explained in terms of the known structuring mechanisms in systems of classical charged particles. Going beyond the scope of classical electrodynamics is also motivated by the following (equally important) considerations. In [22, 23], topologically equivalent structures were observed to occur over an immensely wide ranges of spatial scales: from those consisting of individual filaments several micrometers in diameter in laboratory discharge plasmas to those arising on galactic (and even larger) scales… . This equivalence gave rise to the idea of the possible existence of a universal block on a quantum spatial scale that is similar to one or another of the observed characteristic structures… . A carbon nanotube was chosen to be a candidate for such an elementary block of the filamentary structure."

No comments will be given to the ideas of KRK about galaxies composed of carbon nanotubes.

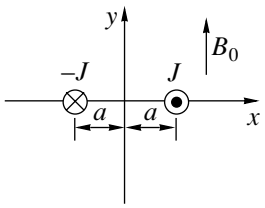

Fig. 10. Two currents in a magnetic field.

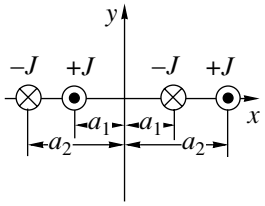

Fig. 11. Four currents in a magnetic field.

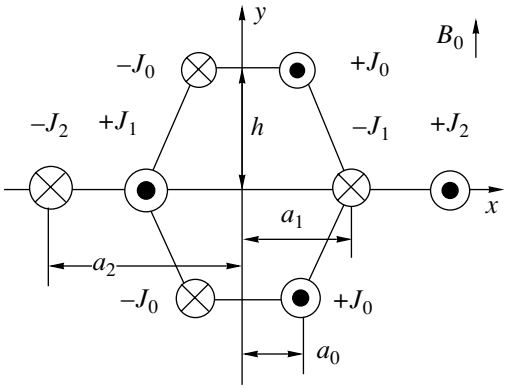

Fig. 12. Eight currents in a magnetic field.

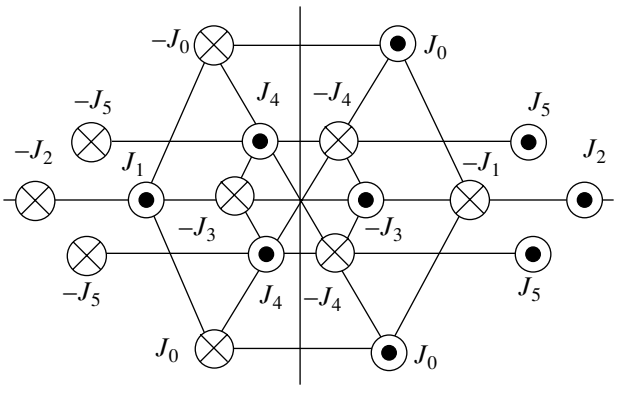

Fig. 13. Eighteen currents in a magnetic field.

It seems that KRK merely observed some specific filamentary structures on the photographs of plasma bunches. However, they were wrong in interpreting such structures as solid-state cables, because they ignored the generally accepted explanation of such structures as current filaments.

Appendices 1 and 2 present examples of possible equilibrium configurations of pairwise countercurrents perpendicular to the main magnetic field. Although most of these configurations are unstable, they may occur on short time scales. Presumably, it is these configurations that were observed by KRK and were reported in their papers.

ACKNOWLEDGMENTS

I am grateful to V.I. Il'gisonis and V.V. Arsenin for useful remarks. This work was supported in part by the Council on the Grants of the President of the Russian Federation and the Council of the Federal Program "Government Support of the Leading Scientific Schools," project no. 00-15-96526.

APPENDIX 1

Equilibrium Configurations of Conductors in a Magnetic Field

The most interesting objects observed by KRK are likely those of the squirrel-cage type, which, however, can be explained as a system of close filaments interacting by means of magnetic forces. In Section 4, it was shown that, in the linear approximation, these filaments in the absence of the main magnetic field are described by the formula $\rho = A\exp(\gamma t)J_n(kr)\cos n\varphi$, containing the Bessel function, so that they also can be referred to as Bessel wheels. However, according to KRK's observations, they are oriented predominantly perpendicular to the main magnetic field. Let us consider a simplified model of such structures in the approximation of infinitely thin filaments in free space.

As an example, Figs. 10–13 show four model configurations that consist of pairs of conductors with oppositely directed currents in vacuum, are oriented along the *z*-axis, and are perpendicular to the external uniform magnetic field $B_0 = B_y$. All dimensions and the directions of the currents are indicated. In order for these configurations to be equilibrium, the total magnetic field (the field of the currents plus the external field) should vanish at the intersection points of the conductors with the (x, y) plane. The relative dimensions and the relationships between the currents were determined precisely from these equilibrium conditions.

Let us examine these examples in more detail. The first model configuration, which is equilibrium for $a_0 = J_0/cB_0$, was analyzed above and the relevant patterns of the magnetic field lines are shown in Figs. 7 and 16. It is clear that, in the idealized case of infinitely thin conductors, all these configurations, although equilibrium, are unstable against the merging of the nearest unidirectional currents. The stability of a configuration in which the regions enclosed by the separatrices of the

currents are filled with plasma (as is the case with a plasma bicylinder considered in Section 6) requires a separate analysis.

In the second model configuration, which is formed by four conductors that are all positioned at $y = 0$, the magnetic field coefficient B_x vanishes at $y = 0$, so that we need to determine only the component B_y at the positions x_i of the conductors. The conditions $B_y(x_i) = 0$ yield two relationships

$$\alpha = \frac{J_2}{J_1} = f(p) = p\frac{3+p^2}{3p^2+1}, \qquad \beta = \frac{ca_1B_0}{J_1} = g(p) = \frac{4pf(p)}{p^2-1} - 1, \tag{A1.1}$$

where $p = a_2/a_1 > 1$. If the field B_0, the first current J_1, and the first dimension a_1 (and, accordingly, the parameter β) are all specified, it is expedient to introduce the parameter $\gamma = (3 + \beta)/2$. Further, by inverting the second of formulas (A.1.1), we find the argument $p^2 = (2 + \gamma + \sqrt{7 + 2\gamma^2})/(3\gamma - 5)$ and then determine the second dimension $a_2 = a_1p$ and the second current $J_2 = J_1f(p)$.

As for the third example illustrated in Fig. 12, we can readily see that, because of the symmetry of the configuration, the upper and lower pairs of the currents do not affect the middle four currents because the magnetic field of the four currents J_0 vanishes at $y = 0$. Consequently, the two stability conditions for the middle currents can be taken from the previous example. Further, by virtue of the symmetry of the configuration, it is sufficient to take into account the reverse effect of the middle currents only on one of the four currents J_0. Let us choose the case with $a_1 = 2a_0$ and $h = \sqrt{3}\,a_0$, in which the six currents are at the vertices of a regular hexagon but $J_1 \neq J_0$. Then, at the upper right point, the total magnetic field has the components

$$B_x = \frac{1}{4\sqrt{3}ca_0}\left(4J_1 - J_0 - \frac{12p}{1+p^2+p^4}J_2\right), \qquad B_y = B_0 + \frac{1}{ca_0}\left(J_1 - \frac{5}{4}J_0 - p\frac{2p^2+1}{1+p^2+p^4}J_2\right), \tag{A1.2}$$

where $p = a_2/a_1 = a_2/2a_0$. The necessary equilibrium conditions $B_x = B_y = 0$, $J_2 = J_1f(p)$, and $ca_1B_0 = J_1g(p)$ give the relationships

$$\frac{J_0}{J_1} = \frac{3x+1}{3x-2} = 4 - \frac{12x(3+x)}{(1+x+z^2)(3x+1)}, \tag{A1.3}$$

where $x = p^2$. We thus arrive at the fourth-order equation for x and obtain the values $x = p^2 = 2.1283$, $p = a_2/a_1 = 1.4588$, and $J_0/J_1 = 1.684$, which ensure the equilibrium of the system of eight currents shown in Fig. 12.

Finally, Fig. 13 shows a possible equilibrium system of 18 currents, which is very similar to the squirrel-cage structure observed by KRK (see Fig. 3). Note that, in Fig. 13, there are three repulsing countercurrents around each of the inner currents. However, the five negative currents from the left (as well as the five positive currents from the right) are unidirectional, thereby adjusting the pattern of the magnetic field lines to that of the lines of the external magnetic field.

KRK noted that, in discharge plasmas observed, the beams were several centimeters in length, so that the oppositely directed currents at the beam ends could be short-circuited to each other, forming structures similar to wheel spokes (see also Appendix 2).

APPENDIX 2

Self-Organization of Filaments in a Magnetic Field

An individual charged particle in a magnetic field moves along a Larmor orbit: the gyration of the electrons is that of a right-handed screw and, accordingly, the gyration of the ions is that of a left-handed screw. If the particles form a continuous thin beam with a sufficiently high current J, their behavior has a number of interesting features, which are associated with the fact that the current filament does not experience magnetic forces in the following two cases: when the current flows along a magnetic field line or when the magnetic field along the filament equals zero.

(i) In order to give better insight into these features, we consider an imaginary experiment illustrated schematically in Fig. 14.

Let two formless loops of flexible conductors be laid out on the table and let the ends of the conductors be fixed (Fig. 14). Also, let the magnetic field $B_y = B_0$ be directed upward and, accordingly, be perpendicular to the table's surface. After switching on a battery producing a direct current, the loops start to interact with the magnetic field, which thus drives them into motion (it is assumed that there is no friction between the loops and the table surface). The right loop, in which the direction of the current with respect to the magnetic

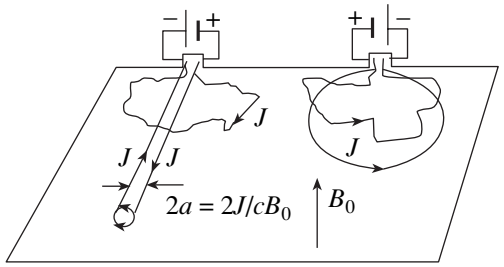

Fig. 14. Behavior of current loops in a magnetic field.

Fig. 15. Filaments at the plasma periphery in the T-6 tokamak (borrowed from [15]).

field is that of a right-handed screw, will form a circle whose radius will increase without bound provided that the loop is perfectly elastic.

In turn, in the interaction with the field B_0, the left loop, in which the current flows in the direction opposite to that in the right loop, will form two parallel lines, which will approach one another until the repulsing forces produced by the oppositely directed currents in them come into play. We can easily see that the parallel lines stop moving when the total magnetic field along them vanishes, i.e., when the distance between them becomes equal to $2a = 2J/cB_0$.

(ii) Then, we consider the behavior of the bridge between the ends of the lines. At first glance, it appears that the interaction of the current J flowing in the bridge with the magnetic field B_0 should push the bridge toward the battery while simultaneously trying to crease it. Instead, the bridge indeed moves away from the battery. In order to convince ourselves of this, note that, along the line z = const that crosses the two parallel conductors and is far from the bridge, the total magnetic field is equal to $B_y = B_0[1 - 4a^2/(a^2 - x^2)]$. We can see that, in the region between the conductors, the total field is negative; in particular, just between the conductors (at $x = 0$), we have $B_y = -3B_0 < 0$. In turn, the negative magnetic field pushes the bridge outward from the battery, thereby elongating the two parallel conductors. Figuratively speaking, the elongating conductors "germinate" in the direction perpendicular to the magnetic field.

Such germinated double filaments presumably form in tokamak plasmas. In particular, the photographs presented in the papers by KRK sometimes show pairs of close filaments perpendicular to the magnetic field, which are interpreted by KRK as nanotubes. Figure 15 shows one such photograph from [15]. The two filaments in Fig. 15 are most likely not nanotubes but rather the pair of countercurrents just described. However, it should be noted that the above configuration of two infinitely thin filamentary conductors is unstable against vertical displacements along the field B_0 (provided that the gravity force is negligible in comparison with the magnetic forces). Of course, the stability of a configuration in which two semi-cylinders formed by the separatrix are filled with plasma (see Fig. 8) requires a separate analysis.

(iii) Let us consider in more detail the equilibrium configuration of a pair of semi-infinite countercurrents. Using the Biot–Savart law, we can calculate the magnetic field of an arbitrarily thin, semi-infinite straight conductor in which the current J flows along the z-axis from $z = -\infty$ to $z = 0$. In cylindrical coordinates (r, φ, z), we obtain

$$B_\varphi = \frac{J}{cr}\left(1 - \frac{z}{\sqrt{r^2 + z^2}}\right). \qquad \text{(A2.1)}$$

At $z = -\infty$, this field, as is expected, is equal to $B_\varphi = 2J/cr$; however, at $z = 0$, it turns out to be two times weaker. Consequently, under equilibrium conditions in the external magnetic field $B_0 = B_y$, the distance between the ends (at $z = 0$) of two semi-infinite straight conductors with oppositely directed currents $\pm J_z$ should be equal to $2a_{new} = J/cB_0$, which is two times shorter than the distance between two infinite ($-\infty \le z \le +\infty$) conductors in equilibrium.

If we introduce the dimensionless variables $Z = z/a$ and $X = x/a$, where $a = J/cB_0$, then, from the above formula, we can readily find the equilibrium positions of two semi-infinite conductors that are in equilibrium with one another in an external magnetic field and the distance between which becomes progressively smaller toward their ends:

$$Z = (1 - 2|X|)\sqrt{|X|/(1 - |X|)}, \qquad \text{(A2.2)}$$

where $|x|$ is the absolute value of x. In the photograph in Fig. 15, the right two filaments are distinctly seen to approach one another up to the points at which they terminate.

(iv) Moreover, the current in the bridge presumably tends to bifurcate (branch) in two directions and to flow along the two semicircles shown in Fig. 16. This possible structure is evidenced by the pattern of the magnetic field lines in the end cross section. If, for simplicity, we assume that the pattern is the same as that for two arbitrarily thin, infinite conductors with countercurrents $\pm J$ separated by the two times smaller distance $2a_{new} = J/cB_0$, then the magnetic field lines A = const are described by the simple formula

$$Y = \frac{y}{a_{new}} = \pm\sqrt{4X\coth(A+2X) - 1 - 4X^2}. \quad \text{(A2.3)}$$

The pattern of these field lines is shown in Fig. 16, where the separatrix is indicated by dots.

The tubular structures in the photographs presented by KRK are such that the possible current path may be as follows. First, the current $+J$ flows from infinity ($z = -\infty$) to the point $x = +a_{new}$. Second, the current flows to the right toward the nearer (right) equatorial point of the common circular separatrix. Third, at this point, the current bifurcates into two equal currents $J/2$, which flow along the upper and lower semicircles (i.e., along the separatrix of the magnetic field lines) toward the left equatorial point of the separatrix, where they merge into one current. And finally, the current flows to the right toward the end $x = -a_{new}$, from where it flows to $z = -\infty$.

It is clear that, for straight-line parts of finite length, the separatrix in the form of two semicircles should form at the remote end of the structure, as is the case with the left tubular structure in Fig. 15. On the whole, such a structure may resemble a squirrel cage with wheel-like ends and two bridges between then. Presumably, it is these structures that were revealed by KRK in tokamak plasmas and were mistakenly interpreted by them as solid-state nanotubes.

It seems likely that, in tokamak plasmas, such structures may result from short-term local fluctuations of the main longitudinal magnetic field: the fluctuations give rise to closed current loops that are perpendicular to the main field and evolve into pairs of countercurrents in the way described above. Another possible mechanism for the onset of squirrel-cage structures that have bridges and are oriented perpendicular to the magnetic field may be associated with the local potential difference that arises between neighboring magnetic surfaces, especially in the vicinities of rational surfaces with integer q values. At a certain time, the differential rotation of a plasma along the magnetic surfaces in the poloidal direction may result in the close opposition of two local spotlike regions with different potentials, as is the case with two capacitor plates. In turn, the potential difference can generate a local cross-field particle beam, which splits into individual filamentary bridges and thereafter forms wheel-like ends.

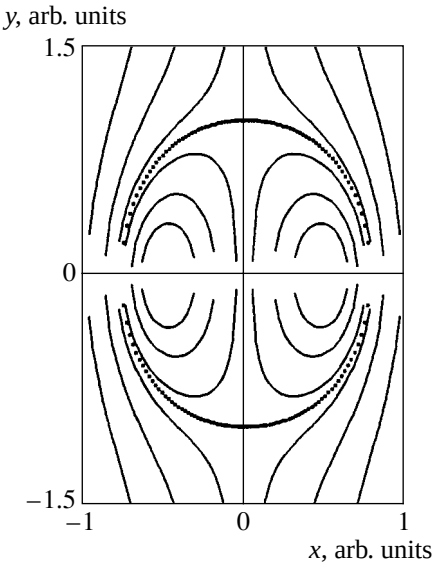

Fig. 16. Magnetic field lines of two oppositely directed currents in an external magnetic field.

To the best of my knowledge, it is unknown what the role is of such structures in the global heat transport in tokamak plasmas.

REFERENCES

1. R. G. Salukvadze, E. Yu. Khautiev, A. A. Batenyuk, *et al.*, in *Proceedings of the 14th European Conference on Controlled Fusion and Plasma Physics, Madrid, 1987*, ECA, Vol. 11D, Part 2, p. 530.
2. E. Yu. Khautiev, V. I. Krauz, V. V. Vikhrev, and V. M. Fadeev, in *Proceedings of the XXIV International Conference on Phenomena in Ionized Gases, Warsaw, 1999*, Vol. 5, p. 89.
3. N. N. Komarov, I. F. Kvarzhava, and V. M. Fadeev, Nucl. Fusion **5**, 192 (1965).
4. V. M. Fadeev, I. F. Kvarzhava, and N. N. Komarov, Nucl. Fusion **5**, 202 (1965).
5. S. K. Zhdanov and B. A. Trubnikov, *Quasi-Gaseous Unstable Media* (Nauka, Moscow, 1991).
6. B. A. Trubnikov, *Plasma Physics and Problems of Controlled Nuclear Fusion* (Akad. Nauk SSSR, Moscow, 1958), Vol. 4, p. 87.
7. B. A. Trubnikov, Pis'ma Zh. Éksp. Teor. Fiz. **42**, 317 (1985) [JETP Lett. **42**, 389 (1985)].
8. B. A. Trubnikov, Fiz. Plazmy **12**, 468 (1986) [Sov. J. Plasma Phys. **12**, 271 (1986)].
9. B. A. Trubnikov, S. K. Zhdanov, and S. M. Zverev, *Hydrodynamics of Unstable Media* (CRC Press, Boca Raton, 1996).
10. B. A. Trubnikov, *Theory of Plasma* (Énergoatomizdat, Moscow, 1996), p. 418.
11. V. Nardi, W. H. Bostick, J. Feugeas, and W. Prior, Phys. Rev. A **22**, 2211 (1980).
12. Z. Segalov, Y. Goren, Y. Carmel, *et al.*, Appl. Phys. Lett. **36**, 812 (1980).

13. B. É. Meĭerovich, *High-Current Channel* (Fima, Moscow, 1999).

14. R. Lee and M. Lampe, Phys. Rev. Lett. **31**, 1390 (1973).

15. A. B. Kukushkin and V. A. Rantsev-Kartinov, Vopr. At. Nauki Tekh., Ser. Termoyad. Sint., No. 2, 69 (2000) (see also references cited therein and two comments on this paper: a negative comment by V. S. Strelkov and a positive one by V.I. Kogan).

16. A. A. Rukhadze, L. S. Bogdankevich, S. E. Rosinskiĭ, and V. G. Rukhlin, *Physics of High-Current Relativistic Electron Beams* (Atomizdat, Moscow, 1980).

17. S. V. Bulanov and P. V. Sasorov, Fiz. Plazmy **4**, 746 (1978) [Sov. J. Plasma Phys. **4**, 418 (1978)].

18. B. V. Levin and B. A. Trubnikov, Pis'ma Zh. Éksp. Teor. Fiz. **44**, 311 (1986) [JETP Lett. **44**, 399 (1986)].

19. O. Buneman, in *Plasma Physics* (McGraw-Hill, New York, 1961), p. 202.

20. S. K. Zhdanov and B. A. Trubnikov, Zh. Éksp. Teor. Fiz. **94** (2), 104 (1988) [Sov. Phys. JETP **67**, 1575 (1988)].

21. S. V. Bulanov and P. V. Sasorov, Zh. Éksp. Teor. Fiz. **86**, 479 (1984) [Sov. Phys. JETP **59**, 279 (1984)].

22. A. B. Kukushkin and V. A. Rantsev-Kartinov, Laser Part. Beams **16**, 445 (1998).

23. A. B. Kukushkin and V. A. Rantsev-Kartinov, Rev. Sci. Instrum. **70**, 1387 (1999).

24. A. B. Kukushkin and V. A. Rantsev-Kartinov, Rev. Sci. Instrum. **70**, 1421 (1999).

25. A. B. Kukushkin and V. A. Rantsev-Kartinov, Rev. Sci. Instrum. **70**, 1392 (1999).

Translated by G. Shepekina

Plasma Physics Reports, Vol. 28, No. 4, 2002, pp. 327–334. Translated from Fizika Plazmy, Vol. 28, No. 4, 2002, pp. 360–367.

SPACE PLASMA

Calculation of the Electric Field in Space Plasma near a Conducting Sphere Injecting an Electron Beam

E. K. Kolesnikov

Smirnov Research Institute of Mathematics and Mechanics, St. Petersburg State University, St. Petersburg, 198904 Russia

Received February 27, 2001; in final form, October 1, 2001

Abstract—The problem is considered of determining the electric field induced in the vicinity of a conducting spherical body that is at rest in a collisionless plasma and at the surface of which there is a prescribed sink of negative charge. The problem is solved for the general relativistic case under the assumption that the electron velocity in the neutralizing current is comparable with the speed of light. An integrodifferential equation is derived that describes the radial behavior of the electric field potential in the vicinity of the injector. A simplified method for determining the potential in the perturbed region is developed. The method implies that the problems of the potentials in a space charge region of radius R^* (with a prescribed boundary potential φ^*) adjacent to the body and in the outer region $r > R^*$ are solved separately and then the solutions obtained are matched at the boundary between these regions. © *2002 MAIK "Nauka/Interperiodica".*

1. INTRODUCTION

It is well known that one of the problems arising in active space experiments on the injection of charged particle beams, as well as in the development of various special-purpose particle-beam space systems, is that of neutralizing the electric charge induced in a space vehicle (SV) during the operation of an onboard charged-particle accelerator. In ionospheric regions in which the ambient plasma density is relatively high, the neutralizing plasma current to the conducting surface of the SV is, as a rule, sufficient to prevent strong electrostatic charging of the injector [1, 2]. However, in experiments on the injection of charged particle beams from high-altitude SVs in a very tenuous plasma of the outer region of the plasmasphere or in the plasma sheet, as well as in particle-beam space systems intended for exploitation near celestial bodies having no atmosphere [3, 4], the operation of the onboard charged-particle accelerator can be accompanied by the generation of a strong electric field in the vicinity of the injector. In turn, the electric fields so generated can strongly affect the beam dynamics, so that, in some cases, it becomes impossible to inject beams from the SV. Under such conditions, special measures must be taken to prevent electrostatic charging of the injector and thus to keep it electrically neutral. These measures include, in particular, the use of "screen" neutralizing systems that enlarge the area of the SV surface collecting the neutralizing plasma current. The role of such a screen may be played, e.g., by a large-area inflatable sheet made of a thin metallized film and connected electrically to the SV injecting a charged particle beam [3].

The subject of the present paper is the problem of determining the electric field induced in the vicinity of a conducting spherical body that is at rest in a collisionless plasma and at the surface of which there is a prescribed sink of negative charge. Solving this problem provides a theoretical basis for calculating the required parameters of a spherical screen system for neutralizing the SV during the operation of an onboard electron-beam injector. In contrast to previous studies in this direction (see, e.g., [5]), the problem of the electric field in the vicinity of a spherical injecting body is treated in the general relativistic case (i.e., under the assumption that the electron velocity in the neutralizing plasma current is comparable with the speed of light). Consequently, the method developed here for solving the above problem can be used to calculate the parameters of the screen neutralizing system of a SV equipped with an onboard accelerator of relativistic electrons.

2. FORMULATION OF THE PROBLEM

We consider a spherical conducting body of a given radius R_0 from the surface of which the negative electric charge is removed at a specified constant rate, which is determined by the current J_b of an electron beam injected under actual space conditions. We assume that the body is at rest in the surrounding (background) plasma and that the plasma itself is collisionless. These assumptions correspond to the conditions

$$L_{e,i} \gg R^*, \tag{1}$$

$$V \ll \left(\frac{8kT_{e,i}}{\pi m_{e,i}}\right)^{1/2}, \tag{2}$$

where $L_{e,i}$ are the mean free paths of the plasma electrons and ions, R^* is the characteristic radius of the per-

1063-780X/02/2804-0327$22.00 © 2002 MAIK "Nauka/Interperiodica"

turbed region (see below), T_e and T_i are the electron and ion plasma temperatures, and V is the injector velocity with respect to the plasma. We treat the problem in a steady-state formulation with allowance for the numerical results of [6], which show that oscillations produced in a collisionless plasma at the beginning of injection are damped with time and the plasma parameters in the perturbed region relax to their steady-state values. We neglect the possible effect of turbulent plasma heating by the beam (due to the onset of the beam instability) at large distances from the injector, because, according to the results of experimental investigations of the collective interaction of an electron beam with a plasma (see, e.g., [7]), this effect is actually observed only when the energy and angular spreads of the beam electrons satisfy fairly strong restrictions.

Under the above assumptions, the electric field in the vicinity of the injecting body can be found by simultaneously solving the set of time-independent Vlasov kinetic equations for the distribution functions $F_{e,i}(\mathbf{r}, \mathbf{p})$ of the plasma electrons and ions in phase space $(\mathbf{r}, \mathbf{p})$:

$$\mathbf{v}_{e,i} \cdot \nabla_{\mathbf{r}} F_{e,i} - q_{e,i} \nabla_{\mathbf{r}} \varphi \cdot \nabla_{\mathbf{p}} F_{e,i} = 0, \quad (3)$$

where $\mathbf{v}_{e,i} = \mathbf{p}/\gamma_{e,i} m_{e,i}$ and $q_{e,i} = \mp e$, and Poisson's equation for the potential φ of the self-consistent electric field,

$$\nabla^2 \varphi = -4\pi e(n_i - n_e), \quad (4)$$

where

$$n_i = \int F_i(\mathbf{r}, \mathbf{p}) d\mathbf{p}, \quad n_e = \int F_e(\mathbf{r}, \mathbf{p}) d\mathbf{p}$$

are the ion and electron plasma densities.

Equations (3) and (4) should be solved under the corresponding boundary conditions for the distribution functions and the potential at the body surface and at infinity:

$$F_{e,i}(\mathbf{r}, \mathbf{p}) \longrightarrow F^{\infty}_{e,i}(p), \quad (5)$$

where $F^{\infty}_{e,i} = n_p^0 (2\pi m_{e,i} k T_{e,i})^{-3/2} \exp(-p^2/2 m_{e,i} k T_{e,i})$,

$$F_{e,i}(\mathbf{r}, \mathbf{p})\Big|_{\substack{r = R_0 \\ (\mathbf{p}, \mathbf{r}) > 0}} \equiv 0, \quad (6)$$

$$\varphi|_{r = R_0} = \text{const}, \quad (7)$$

$$\varphi \xrightarrow[r \to \infty]{} 0, \quad (8)$$

$$4\pi R_0^2 \sum_{e,i} q_{e,i} \int \left| v^r_{e,i} \right| F_{e,i}(\mathbf{r}, \mathbf{p})|_{r = R_0} d\mathbf{p} = J_b. \quad (9)$$

Boundary conditions (5)–(9) have the following physical meaning: condition (5) corresponds to the assumption that an unperturbed plasma is equilibrium, condition (6) indicates that the vehicle surface is perfectly absorbing for plasma particles, conditions (7) and (8) follow from the assumption that the injector material is conducting and there are no external electric fields, and condition (9) reflects the balance between the beam current J_b and the neutralizing plasma current.

Note that, unlike in the problem solved in the earlier paper [8], the electric potential at the body surface is not specified in advance, but is determined in solving the problem as formulated.

Now, we turn to Eqs. (3). Taking into account the equations of motion $\dot{\mathbf{p}} = -q_{e,i} \nabla \varphi$ and $\dot{\mathbf{r}} = \mathbf{v}_{e,i}$, we can readily see that Eqs. (3) are equivalent to the conservation laws for the distribution functions F_e and F_i along the electron and ion trajectories, respectively.

Then, using the boundary conditions (5) and (6), we obtain the distribution functions $F_{e,i}$ at an arbitrary point $\mathbf{r}$ in the vicinity of the body:

$$F_{e,i}(\mathbf{r}, \mathbf{p})\big|_{r > R_0} = \begin{cases} F^{\infty}_{e,i}[p^{\infty}_{e,i}(\mathbf{r}, \mathbf{p})], & \mathbf{p} \in G_{e,i}(\mathbf{r}) \\ 0, & \mathbf{p} \in Q_{e,i}(\mathbf{r}) \end{cases}. \quad (10)$$

Here, $Q_{e,i}(\mathbf{r})$ is the momentum space region of finite trajectories and trajectories coming to an observation point $\mathbf{r}$ from the surface of a spherical body, $G_{e,i} = CQ_{e,i}(\mathbf{r})$ is the complement of the region $Q_{e,i}(\mathbf{r})$ in momentum space, and $p^{\infty}_{e,i}$ is the momentum at infinity of a particle having momentum $\mathbf{p}$ at the point $\mathbf{r}$.

Taking into account distribution functions (10), we arrive at the following integral expressions for the electron and ion plasma densities at the point $\mathbf{r}$:

$$n_{e,i}(\mathbf{r}) = \int\limits_{G_{e,i}} F^{\infty}_{e,i}[p^{\infty}_{e,i}(\mathbf{p}, \mathbf{r})] d\mathbf{p}, \quad (11)$$

where $d\mathbf{p} = dp_r dp_\vartheta dp_\varphi$ is the momentum space volume element and p_r, p_ϑ, and p_φ are the projections of the momentum vector onto the unit vectors $\mathbf{i}_r$, $\mathbf{i}_\vartheta$, and $\mathbf{i}_\varphi$ of the spherical coordinate system. We pass over to the new variables p_θ, ψ, and p'_r, which are related to the projections p_r, p_ϑ, and p_φ by the relationships (see Fig. 1)

$$p_\theta^2 = p_\varphi^2 + p_\vartheta^2, \quad p'_r = p_r,$$

$$p_\theta \cos\psi = p_\varphi, \quad p_\theta \sin\psi = p_\vartheta.$$

In the new variables p_θ, ψ, and p'_r integrals (11) become

$$n_{e,i}(r) = \int\limits_{G_{e,i}} F^{\infty}_{e,i}[p^{\infty}_{e,i}(r, p_\theta, \psi, p'_r)] p_\theta dp_\theta d\psi dp'_r. \quad (12)$$

We introduce the variables ε and M^2, which have the meaning of the total particle energy and the squared

particle momentum, respectively. The variable p_θ can be expressed in terms of the variable M as

$$p_\theta = M/r. \tag{13}$$

The relationship of the variable $p_r = m\gamma v_r$ to ε and M can be obtained using the energy integral

$$m_{e,i}c^2(\gamma - 1) + q_{e,i}\varphi(r) = \varepsilon$$

and the formulas

$$\gamma = \left(1 - \frac{v_r^2 + v_\theta^2}{c^2}\right)^{-1/2}, \quad M = m_{e,i}\gamma r v_\theta.$$

After some simple manipulations, we find

$$p_r = m_{e,i}c\sqrt{\left[\frac{\varepsilon - q_{e,i}\varphi(r)}{m_{e,i}c^2} + 1\right]^2 - 1 - \frac{M^2}{m_{e,i}^2c^2r^2}}. \tag{14}$$

We transform integrals (12) to the variables ε, ψ, and M^2:

$$n_{e,i}(r) = \int\limits_{\tilde{G}_{e,i}} F_{e,i}^{\infty}[p^{\infty}(\varepsilon)]\, p_\theta(M^2, r)\left|\frac{D(p_\theta, \psi, p_r)}{D(\varepsilon, \psi, M^2)}\right| d\varepsilon d\psi dM^2, \tag{15}$$

where the region $\tilde{G}_{e,i}(r)$ in the space of the variables ε, ψ, and M^2 corresponds to the region $G_{e,i}(r)$ in momentum space and $D(p_\theta, \psi, p_r)/D(\varepsilon, \psi, M^2)$ is the Jacobian of the transformation $(\varepsilon, \psi, M^2) \longrightarrow (p_\theta, \psi, p_r)$. We calculate the Jacobian and take into account formula (13). As a result, the p_θ-dependent part of the integrand in expression (15) simplifies to

$$p_\theta(M^2, r)\left|\frac{D(p_\theta, \psi, p_r)}{D(\varepsilon, \psi, M^2)}\right| = \frac{1}{2r^2c}\left\{1 - \frac{1}{\left[\frac{\varepsilon - q_{e,i}\varphi(r)}{m_{e,i}c^2} + 1\right]^2} - \frac{M^2}{m_{e,i}^2c^2r^2\left[\frac{\varepsilon - q_{e,i}\varphi(r)}{m_{e,i}c^2} + 1\right]^2}\right\}^{-1/2}. \tag{16}$$

Generally, the particle momentum at infinity is related to the total energy by

$$p_{e,i}^{\infty} = \frac{1}{c}\sqrt{\varepsilon(\varepsilon + 2m_{e,i}c^2)}. \tag{17}$$

However, since the total energy of the plasma particles satisfies the condition $\varepsilon \ll m_{e,i}c^2$ by virtue of the assumed classical nature of the plasma at infinity, relationship (17) reduces to

$$p_{e,i}^{\infty} \approx \sqrt{2m_{e,i}\varepsilon}. \tag{18}$$

Substituting relationship (18) into expression (5) for the unperturbed distribution functions $F_{e,i}^{\infty}$ yields

$$F_{e,i}^{\infty}[p^{\infty}(\varepsilon)] = n_p^0(2\pi m_{e,i}kT_{e,i})^{-3/2}\exp(-\varepsilon/kT_{e,i}). \tag{19}$$

We take into account expressions (16) and (19) and perform integration over ψ in expression (15) to obtain

$$\frac{dN_{e,i}}{dV(\mathbf{r})} = n_{e,i}(\mathbf{r}) = \int\int\limits_{\Gamma_{e,i}(\mathbf{r})} \Phi_{e,i}(\mathbf{r}, \varepsilon, M^2)\, d\varepsilon dM^2, \tag{20}$$

where $dV(\mathbf{r})$ is the coordinate space volume element containing surface of radius $\mathbf{r}$ and

$$\Phi_{e,i}(r, \varepsilon, M^2) = \frac{n_p^0}{r^2\sqrt{8\pi c^2k^3T_{e,i}^3m_{e,i}^3}} \times \frac{e^{-\frac{\varepsilon}{kT_{e,i}}}}{\sqrt{1 - \frac{1}{\left[\frac{\varepsilon - q_{e,i}\varphi}{m_{e,i}c^2} + 1\right]^2} - \frac{M^2}{m_{e,i}^2c^2r^2\left[\frac{\varepsilon - q_{e,i}\varphi}{m_{e,i}c^2} + 1\right]^2}}}. \tag{21}$$

In expression (20), the region $\Gamma_{e,i}$ in the space of the variables ε and M^2 corresponds to the trajectories that come to the observation surface from infinity. Note that, according to this expression, the mathematical expectation of the number of particles in the volume element $dV(\mathbf{r})d\varepsilon dM^2$ in the space of the variables $\mathbf{r}$, ε, and M^2 has the form

$$dN_{e,i} = \Phi_{e,i}(r, \varepsilon, M)dV(\mathbf{r})d\varepsilon dM^2. \tag{22}$$

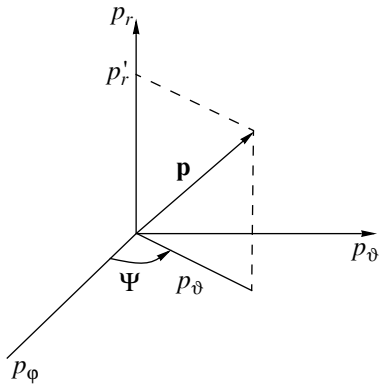

Fig. 1. Relationship between the old variables (p_r, p_ϑ, p_φ) and the new variables (p_θ, ψ, and p_r').

Consequently, the functions Φ_e and Φ_i have the meaning of the distribution functions of the plasma electrons and ions in the space of the variables $\mathbf{r}$, ε, and M^2.

Now, we turn to Poisson's equation (4). Inserting expression (20) into its right-hand side, we can rewrite it as

$$\frac{1}{r^2}\frac{d}{dr}\left(r^2\frac{d\varphi}{dr}\right) = -\frac{4\pi n_p^0}{r^2}\sum_{e,i}\frac{q_{e,i}}{8\pi c^2 k^3 T_{e,i}^3 m_{e,i}^3} \times \iint\limits_{\Gamma_{e,i}} \frac{e^{-\frac{\varepsilon}{kT_{e,i}}} d\varepsilon dM^2}{\sqrt{1-\frac{1}{\left[\frac{\varepsilon - q_{e,i}\varphi}{m_{e,i}c^2}+1\right]^2} - \frac{M^2}{m_{e,i}^2 c^2 r^2\left[\frac{\varepsilon - q_{e,i}\varphi}{m_{e,i}c^2}+1\right]^2}}}. \quad (23)$$

Hence, in the general case, the electric potential in the perturbed region should satisfy the integrodifferential equation (23).

3. STRUCTURE OF THE PERTURBED REGION AND EQUATION FOR THE ELECTRIC POTENTIAL IN THE SPACE CHARGE REGION

Before passing to the development of the procedure for solving Eq. (23), note that, under actual space conditions, the case of practical interest is that in which the body is charged to the surface potential φ_0 satisfying the condition

$$|q_{e,i}\varphi_0| \gg kT_{e,i}. \quad (24)$$

We restrict ourselves to constructing solutions to Eq. (23) in the class of monotonic potentials. In other words, we assume that the function $\varphi(r)$ decreases monotonically as r increases. We also assume that the plasma is isothermal; i.e., the electron and ion temperatures are the same, $T_e = T_i \equiv T$.

We define the space charge region as the region $R_0 \le r \le R^*$, which is adjacent to the body and in which the potential decreases from the surface value φ_0 to a certain fixed value φ^* satisfying the conditions

$$\frac{e\varphi^*}{kT} \gg 1, \quad (25)$$

$$\frac{e\varphi^*}{m_{e,i}c^2} \ll 1. \quad (26)$$

We assume that the radius R^* is large enough to satisfy the inequality

$$\frac{R^*}{D} \gg 1, \quad (27)$$

where $D = (kT/4\pi n_p^0 e^2)^{1/2}$ is the Debye radius in an unperturbed plasma. Note that the radius R^* corresponding to the chosen value φ^* is not known *a priori* and should be determined when solving the problem.

First, we consider the question of the radial behavior of the electric potential in the outer region $r \ge R^*$. By virtue of condition (25), there are essentially no ions at the distance R^* from the center of the sphere. At the same time, the plasma electrons move in nearly the radial direction, so that, under the additional restriction (34) on the radius R^* (see below), the majority of plasma electrons reach the body surface, where they are absorbed. In this case, the electric field in the region $r \ge R^*$ is equivalent to the electric field of an absorbing spherical body with the radius R^* satisfying condition (27) and with the surface potential φ^* satisfying conditions (25) and (26).

This problem was solved by Al'pert *et al.* in [5]. They showed, in particular, that, under the necessary condition

$$\frac{R^*}{D} \gg 0.78\left(\frac{e\varphi^*}{kT}\right)^{3/4}, \quad (28)$$

the perturbed plasma region $r \ge R^*$ consists of a double layer of thickness

$$\delta \sim \frac{\varphi^*}{E(R^*)} \quad (29)$$

adjacent to a sphere of radius $r = R^*$ and a quasineutral plasma region. They also developed the iterative method for calculating the radial behavior of the electric potential in the perturbed region. In relationship (29), the electric field strength $E(R^*)$ at the inner boundary of the double layer has the form

$$E(R^*) = 4.57\sqrt{n_p^0 kT}\sqrt[4]{|e\varphi^*|kT}. \quad (30)$$

In accordance with the results of [5], the total current of the plasma electrons that arrive at a sphere of radius R^* is described by the expression

$$I^+ = I_0^+\lambda(\varphi^*). \quad (31)$$

Here, $I_0^+ = (8\pi kT/m_e)^{1/2} n_p^0 R^{*2}$ and the function $\lambda(\varphi^*)$ is represented in integral form:

$$\lambda(\varphi^*) = 1 + \tilde{\varphi}_\infty + 2\int_1^\infty \xi\left[1 - \exp\left(\tilde{\varphi} + \frac{\xi}{2}\frac{d\tilde{\varphi}}{d\xi}\right)\right]d\xi, \quad (32)$$

where $\tilde{\varphi} = e|\varphi|/kT$ and $\xi = (r - R^*)/D$. In [5], the values of the function $\lambda(\varphi^*)$ were calculated by taking the integral in expression (32) for the function $\tilde{\varphi}$ and its derivative $d\tilde{\varphi}/d\xi$ corresponding to the solution to the problem of the radial behavior of the electric potential on the outside of an absorbing sphere of radius R^* with the boundary value $\varphi = \varphi^*$. The tabulated data on the

function $\lambda(\varphi^*)$ [5] show that it asymptotically approaches the value 1.47 as φ^* increases.

Now, we consider the equation for the electric potential in the region $r < R^*$. Let us show that, in this region, the basic equation (23) can be significantly simplified. First, note that, since there are essentially no plasma ions in the region $r < R^*$, we can neglect the ion contribution to the space charge density on the right-hand side of Eq. (23). By virtue of the condition $\varepsilon \ll m_{i,e}c^2$ on the total energy of the plasma particles, we can omit the terms on the order of $\varepsilon/m_e c^2$ in the expression for the electron distribution function $\Phi_e(r, \varepsilon, M^2)$. Finally, taking into account the fact that the angular momentum of the plasma electrons is equal in order of magnitude to $\sim R^* \sqrt{m_e kT}$, we can readily show that, if the electric potential in the region $r < R^*$ satisfies the conditions

$$e\varphi(r) \gg \begin{cases} \dfrac{R^*}{r}\left(\dfrac{kT}{m_e c^2}\right)^{1/2} m_e c^2 & \text{for} \quad \varphi(r) \gtrsim m_e c^2/e \\ \left(\dfrac{R^*}{r}\right)^2 kT & \text{for} \quad \varphi(r) \ll m_e c^2/e, \end{cases} \tag{33}$$

then the terms with M^2 in expression (21) for $\Phi_e(r, \varepsilon, M^2)$ can also be discarded. In fact, conditions (33) indicate the onset of the single-velocity radial motion of plasma electrons in the region $r < R^*$. From conditions (33), we find the following necessary conditions, which should be satisfied by the potential φ_0 and radius R^* in order for the single-velocity radial motion to occur in the region $r < R^*$:

$$e\varphi_0 \gg \begin{cases} \dfrac{R^*}{r}\left(\dfrac{kT}{m_e c^2}\right)^{1/2} m_e c^2 & \text{for} \quad \varphi_0 \gtrsim m_e c^2/e \\ \left(\dfrac{R^*}{R_0}\right)^2 kT & \text{for} \quad \varphi_0 \ll m_e c^2/e. \end{cases} \tag{34}$$

Under conditions (33), the current (31) of the plasma electrons that reach a sphere with the radius $r = R^*$ is equal to the current of the plasma electrons that are absorbed by the body. Then, we substitute formula (31) into condition (9) for the current balance at the body surface to obtain the following equation for the radius R^*:

$$J_b/e(8\pi kT/m_e)^{1/2} n_p^0 R^{*2} = \lambda(\varphi^*). \tag{35}$$

In what follows, we will work under conditions (33). We omit the corresponding terms in the expression for the distribution function $\Phi(r, \varepsilon, M^2)$ and write Eq. (23) in the form

$$\frac{1}{r^2}\frac{d}{dr}\left(r^2 \frac{d\varphi}{dr}\right) = -\frac{n_p^0 e}{r^2}\sqrt{\frac{2\pi}{c^2 k^3 T^3 m_e^3}} \frac{\iint_{\Gamma_e(r)} e^{-\frac{\varepsilon}{kT}} d\varepsilon dM^2}{\sqrt{1 - \left(1 + \dfrac{e\varphi}{m_e c^2}\right)^{-2}}}. \tag{36}$$

We can easily show that the integral $\iint_{\Gamma_e(r)} e^{-\frac{\varepsilon}{kT}} d\varepsilon dM^2$ on the right-hand side of Eq. (36) is proportional to the current of the plasma electrons through a spherical surface with the radius $r = R^*$. First, note that, the plasma electrons that move in the radial direction under conditions (33) in the region $r < R^*$ and reach the surface $r = R^*$ are later observed at arbitrary distances r from the body surface in the region $R_0 < r < R^*$. Consequently, for any radius r from the radial interval $[R_0, R^*]$, the regions $\Gamma_e(r)$ of the permissible values of ε and M^2 at a distance r are equivalent to the regions $\Gamma_e(R^*)$ at the spherical surface $r = R^*$. The current of the plasma electrons through the spherical surface $r = R^*$ is described by the integral expression

$$I_e\big|_{R^*} = 4\pi R^{*2} \int_{\Gamma_e(R^*)} \left|v_r(\varepsilon, M^2)\right| \Phi_e(R^*, \varepsilon, M^2) d\varepsilon dM^2. \tag{37}$$

Using the energy and angular momentum integrals, we can readily express the radial velocity v_r of a particle in terms of the variables ε and M^2:

$$v_r = c\sqrt{1 - \frac{1}{\left[1 - \dfrac{\varepsilon + e\varphi(r)}{m_e c^2}\right]^2} - \frac{M^2}{m_e^2 c^2 r^2 \left[1 - \dfrac{\varepsilon + e\varphi(r)}{m_e c^2}\right]^2}}. \tag{38}$$

With formula (38) for v_r and formula (21) for $\Phi_e(r, \varepsilon, M^2)$, the integral expression (37) becomes

$$\begin{aligned} I_e\big|_{R^*} &= n_p^0 \sqrt{\frac{2\pi}{k^3 T^3 m_e^3}} \iint_{\Gamma_e(R^*)} e^{-\frac{\varepsilon}{kT}} d\varepsilon dM^2 \\ &= n_p^0 \sqrt{\frac{2\pi}{k^3 T^3 m_e^3}} \iint_{\Gamma_e(r)} e^{-\frac{\varepsilon}{kT}} d\varepsilon dM^2 \\ &\quad (\forall r < R^*). \end{aligned} \tag{39}$$

On the other hand, the current of the plasma electrons through the spherical surface $r = R^*$ is described by formula (31). Substituting this formula into the left-hand side of expression (39) yields the following expression for the integral $\iint_{\Gamma_e(r)} e^{-\varepsilon/kT} d\varepsilon dM^2$:

$$\int\int_{\Gamma_e(r)} e^{-\frac{\varepsilon}{kT}} d\varepsilon dM^2 = 2k^2T^2 m_e \lambda(\varphi^*) R^*. \quad (40)$$

We take into account expression (40) and introduce the dimensionless variables $\nu = e\varphi/m_e c^2$ and $\eta = r/R^*$ to write Eq. (36) in the form

$$\frac{d}{d\eta}\left(\eta^2 \frac{d\nu}{d\eta}\right) = \frac{\lambda(\varphi^*)}{\sqrt{2\pi}}\left(\frac{kT}{m_e c^2}\right)^{3/2}\left(\frac{R^*}{D}\right)^2 \frac{\nu + 1}{\sqrt{\nu(\nu + 2)}}, \quad (41)$$

where the radius R^* of the space charge region is related to the potential φ^* and the beam current by Eq. (35). Taking into account the asymptotic value $\lambda(\varphi^*) \approx 1.47$ in the limit $\varphi^* \gg 1$, we reduce Eq. (41) to

$$\frac{d}{d\eta}\left(\eta^2 \frac{d\nu}{d\eta}\right) = 0.59\left(\frac{kT}{m_e c^2}\right)^{3/2}\left(\frac{R^*}{D}\right)^2 \frac{\nu + 1}{\sqrt{\nu(\nu + 2)}}. \quad (42)$$

The dimensionless potential ν should satisfy the boundary conditions

$$\nu(1) = \nu^* = \frac{e\varphi^*}{m_e c^2}, \quad (43)$$

$$\nu'(1) = -1.29(\nu^*)^{1/2}\left(\frac{kT}{m_e c^2}\right)^{3/4}\frac{R^*}{D}. \quad (44)$$

Condition (43) corresponds to the boundary condition $\varphi(R^*) = \varphi^*$, and condition (44) corresponds to the boundary condition (30) for the electric field strength at the inner boundary of the double layer. One can readily see that, for nonrelativistic velocities of the neutralizing plasma flux ($\nu \ll 1$), Eq. (42) yields the familiar equation [5]

$$\frac{d}{d\eta}\left(\eta^2 \frac{d\tilde{\nu}}{d\eta}\right) = \frac{0.42}{\sqrt{\tilde{\nu}}}, \quad (45)$$

where $\tilde{\nu} = \left(\frac{m_e c^2}{kT}\right)\left(\frac{D}{R^*}\right)^{4/3}\nu = \frac{e\varphi}{kT}\left(\frac{D}{R^*}\right)^{4/3}$, in which case the boundary conditions (43) and (44) correspond, respectively, to the conditions

$$\tilde{\nu}(1) = \tilde{\nu}^* = \frac{e\varphi^*}{kT}\left(\frac{D}{R^*}\right)^{4/3}, \quad (46)$$

$$\tilde{\nu}'(1) = 1.29(\tilde{\nu}^*)^{1/4}. \quad (47)$$

Hence, we have reduced the problem of determining the electric field in the region $R_0 \le r \le R^*$ to that of constructing the solution to Eq. (42) across the radial interval $\eta_0 = R_0/R^* \le \eta \le 1$ under the boundary conditions (43) and (44) at $\eta = 1$. This problem is easy to solve by the corresponding methods for numerical integration of second-order ordinary differential equations, e.g., by one of the Runge–Kutta methods. However, it is necessary to keep in mind that the solution so obtained exactly describes the radial behavior of the electric potential in the space charge region only under the assumptions made in deriving Eq. (42), namely: the potential of the body at the surface $\eta = \eta_0$ should satisfy condition (24); the quantities φ^* and R^* should satisfy conditions (25), (26), and (28); and the local potential values should satisfy conditions (33).

4. SOME RESULTS OF NUMERICAL CALCULATIONS

In order to demonstrate a practical application of the method developed here, we calculate the electric field induced in the vicinity of the screen neutralizing system of a SV injecting a steady electron beam in the following particular case. Let the beam current be 10 A, and let the beam energy be high enough for the beam electrons to escape from the potential well that forms in the vicinity of the injector during its electrostatic charging. The screen neutralizing system is a spherical conducting shell with the given radius $R_0 = 20$ m, connected electrically to the SV by a set of conductors (the characteristic dimensions of the SV are assumed to be much smaller than the screen radius R_0). The background plasma parameters are set to be $T = 1$ eV and $n_p^0 = 10$ cm^{-3}.

According to the above analysis, the radial profile of the electric potential in the space charge region around the screen is determined by solving Eq. (41) with the boundary conditions (43) and (44) at $\eta = r/R^* = 1$. In order to specify the radius R^* of the space charge region in Eq. (41) and conditions (43) and (44), we set the electric potential φ^* at $r = R^*$ equal to 10 V (in which case we have $e\varphi^*/kT = 10$). The radius R^* corresponding to the chosen value for φ^* can be found from Eq. (35). Substituting the asymptotic value $\lambda(\varphi^*) \approx 1.47$ (in the limit $e\varphi^*/kT \gg 1$) and the above values of the beam current J_b, the density n_p^0 of an unperturbed plasma, and its temperature T into Eq. (35), we obtain $R^* = 1.42 \times 10^5$ cm = 1.42 km.

We numerically integrate Eq. (42) with conditions (43) and (44) at the outer boundary of the space charge region to obtain the dimensionless electric potential ν and its derivative at the screen surface: $\nu|_{\eta = \eta_0} = 3.11$ and $(d\nu/d\eta)|_{\eta = \eta_0} = -226$ (in the case at hand, we have $\eta_0 = R_0/R^* = 0.0141$). Using these values, we find that the dimensional electric potential of the screen is $\varphi_0 = 1.59$ MV and the electric field strength at the screen surface is $E_0 = 81.3$ kV/m. The radial profile of the electric potential across the space charge region is shown in Fig. 2. We can see that, in the case under consideration,

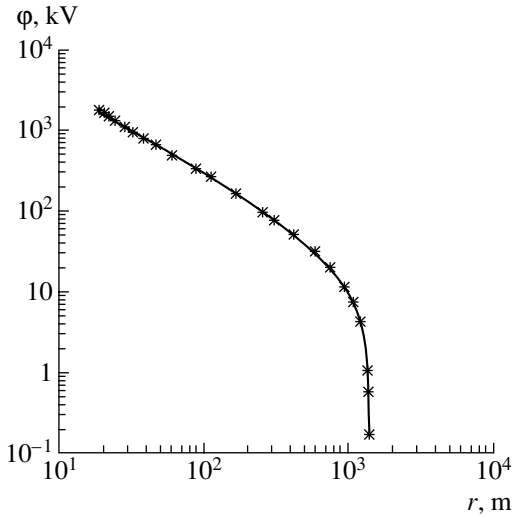

Fig. 2. Electric potential φ vs. radial coordinate *r* across the space charge region.

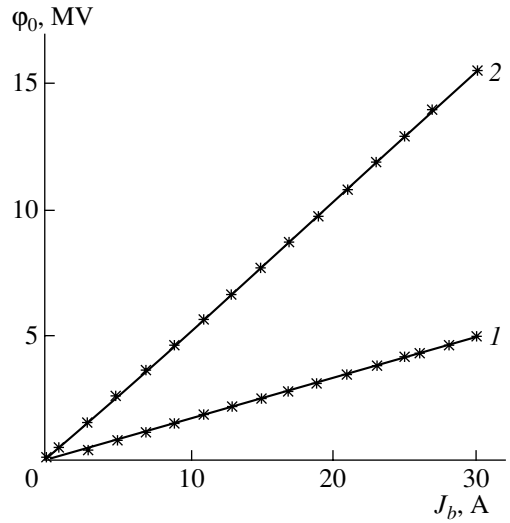

Fig. 3. Screen potential φ_0 vs. injected current J_b for the background plasma density n_p^0 = (*1*) 10 and (*2*) 1 cm^{-3}.

it is only at large distances from the screen (comparable to R^*) that the radial behavior of the potential of the electron space charge is significantly affected by the neutralizing plasma current. Consequently, across the main part of the space charge region, the potential of the induced electric field decreases with distance from the screen center according to the vacuum law $\varphi = \varphi_0(R_0/r)$.

In order to demonstrate the possible values of the screen potential at different currents of the injected beam, Fig. 3 shows the surface potential φ_0 calculated as a function of the current J_b for two background plasma densities: $n_p^0 = 10$ cm^{-3} (curve *1*) and $n_p^0 = 1$ cm^{-3} (curve *2*). In both cases, the plasma temperature was set equal to 1 eV. As may be seen, the screen potential increases essentially linearly with beam current. At the background plasma density $n_p^0 = 10$ cm^{-3}, the surface potential at which the relativistic motion of the electrons of the neutralizing plasma current becomes important ($e\varphi_0 \gtrsim 200$ keV) is reached at a beam current of about $J_b \gtrsim 1.3$ A. In the case $n_p^0 = 1$ cm^{-3}, relativistic effects should be taken into account at beam currents $J_b \gtrsim 0.4$ A.

5. CONCLUSION

The main results of the present work can be summarized as follows.

(i) A kinetic approach has been developed to solve the problem of determining the plasma particle distributions and the electric field induced in the vicinity of a conducting spherical body that is at rest in a collisionless plasma and at the surface of which there is a prescribed sink of negative charge. The formulation of the problem takes into account the possibility of charging the body to the potential at which the electron velocity in the neutralizing plasma current are comparable with the speed of light.

(ii) A general integrodifferential equation has been obtained that describes the radial behavior of the electric field potential in the vicinity of the injector.

(iii) A simplified method for determining the electric potential in the perturbed plasma region has been developed. The method implies that the problems of the potentials in a space charge region of radius R^* (at which the potential φ^* is prescribed) adjacent to the body and in the outer region $r > R^*$ are solved separately and then the solutions obtained are matched at the boundary between these regions. It is shown that, under certain restrictions on the parameters R^*, φ^*, R_0, and φ_0, the general integrodifferential equation for the electric potential in the space charge region can be significantly simplified; specifically, it can be reduced to a second-order ordinary differential equation that generalizes the corresponding familiar equation from [5] to the case of relativistic motion of the electrons of the neutralizing plasma current.

(iv) Results have been presented from numerical calculations of the electric field induced in the vicinity of a spherical screen system for neutralizing a SV injecting a steady relativistic electron beam. The calculated results show that, for background plasma densities of about $n_p^0 \sim 1$–10 cm^{-3}, which are characteristic of plasma conditions near high-altitude SVs, the

motion of the electrons of the neutralizing plasma current becomes relativistic at comparatively low beam currents, $J_b \gtrsim 0.1$–1 A.

REFERENCES

1. V. A. Fedorov, Fiz. Plazmy **26**, 287 (2000) [Plasma Phys. Rep. **26**, 266 (2000)].
2. E. K. Kolesnikov and A. B. Yakovlev, Kosm. Issled. **34**, 666 (1996).
3. E. K. Kolesnikov and A. P. Kuryshev, Available from VINITI No. 41-82 (Leningrad, 1982).
4. E. K. Kolesnikov, A. P. Kuryshev, and A. S. Manuĭlov, *X-ray Spectroscopic Analysis Methods* (Nauka, Novosibirsk, 1986), p. 85.
5. Ya. L. Al'pert, A. V. Gurevich, and L. P. Pitaevskiĭ, *Artificial Satellites in a Rarefied Plasma* (Nauka, Moscow, 1964).
6. V. A. Fedorov, Fiz. Plazmy **9**, 874 (1983) [Sov. J. Plasma Phys. **9**, 510 (1983)].
7. A. K. Berezin, V. A. Kiselev, and Ya. B. Faĭnberg, *Plasma Electronics* (Naukova Dumka, Kiev, 1989), p. 29.
8. S. A. Vavilov and E. K. Kolesnikov, in *Physical Mechanics*, Vol. 4: *Dynamic Processes in Gases and Solids* (Leningr. Gos. Univ., Leningrad, 1980), p. 168.

Translated by O. Khadin

Plasma Physics Reports, Vol. 28, No. 4, 2002, pp. 335–341. Translated from Fizika Plazmy, Vol. 28, No. 4, 2002, pp. 368–374.

OSCILLATIONS AND WAVES IN PLASMA

Propagation of MHD Waves in a Plasma in a Sheared Magnetic Field with Straight Field Lines

P. N. Mager and D. Yu. Klimushkin

Institute of Solar and Terrestrial Physics, Siberian Division, Russian Academy of Sciences, Irkutsk, 664033 Russia

Received May 29, 2001; in final form, November 15, 2001

Abstract—The propagation of MHD plasma waves in a sheared magnetic field is investigated. The problem is solved using a simplified model: a cold plasma is inhomogeneous in one direction, and the magnetic field lines are straight. The waves are assumed to travel in the plane perpendicular to the radial coordinate (i.e., the coordinate along which the plasma and magnetic field are inhomogeneous). It is shown that the character of the singularity at the resonance surface is the same as that in a homogeneous magnetic field. It is found that the shear gives rise to the transverse dispersion of Alfvén waves, i.e., the dependence of the radial component of the wave vector on the wave frequency. In the presence of shear, Alfvén waves are found to propagate across magnetic surfaces. In this case, the transparent region is bounded by two turning points, at one of which, the radial component of the wave vector approaches infinity and, at the other one, it vanishes. At the turning point for magnetosonic waves, the electric and magnetic fields are finite; however, the radial component of the wave vector approaches infinity, rather than vanishes as in the case with a homogeneous field. © *2002 MAIK "Nauka/Interperiodica".*

1. INTRODUCTION

In this paper, we study the resonant excitation of Alfvén waves in an inhomogeneous plasma. The phenomenon of Alfvén resonance is of fundamental importance in the physics of wave processes in the magnetosphere [1, 2]. At present, there are numerous observations indicating the resonance excitation of Alfvén modes by fast magnetosonic (FMS) waves arriving from the outer layers of the magnetosphere or from interplanetary space [3]. This involves the excitation of Alfvén waves in which the magnetic field lines execute azimuthal oscillations (these waves are usually referred to as toroidal). At the same time, there are Alfvén waves that are characterized by radial oscillations of the magnetic field lines (poloidal oscillations). The origin of these waves is still poorly understood [4]. When studying hydromagnetic waves in an inhomogeneous plasma, we will focus mainly on magnetospheric issues. We note, however, that Alfvén resonance is a more universal phenomenon. For example, it was invoked to explain solar corona heating [5] and to develop new methods for plasma heating in fusion devices [6–9]. The character of the models used in this study makes it possible to easily extend our results to Alfvén resonances in these and other branches of physics.

In the simplest model in which the plasma is assumed to be inhomogeneous in one direction and the magnetic field lines are straight and mutually parallel, the Alfvén resonance implies that FMS waves arriving from the outer layers of the magnetosphere excite an Alfvén mode near the surface at which the wave frequency ω is equal to the local Alfvén frequency $\Omega_A = k_\parallel A(x)$, where A is the Alfvén velocity [1, 2]. A large number of studies were devoted to the development of the theory of Alfvén resonance with the use of more complicated (but, at the same time, more realistic) models. Thus, it was shown that Alfvén resonance also occurs in a two-dimensional model that takes into account the curvature of the magnetic field lines and the inhomogeneity of the background plasma in the direction of the magnetic field [10–16]. Furthermore, the field line curvature gives rise to a specific transverse dispersion of Alfvén waves, i.e., the dependence of the radial component of the wave vector on the Alfvén wave frequency [16]. In this case, the waves propagate across the magnetic shells. Taking into account the finite plasma pressure and equilibrium current in a magnetic field with curved field lines leads to an even more drastic change of the transverse dispersion law for hydromagnetic waves [17].

When the problem is treated in a two-dimensional model, some of the factors related to inhomogeneity are often ignored. This naturally brings up the question as to whether these factors can significantly contribute to the overall picture of the process. In recent paper [18], attention was drawn to one of the factors that was previously disregarded—the magnetic field shear caused by the current flowing along the magnetic field. Since field-aligned currents are a rather common phenomenon in the magnetosphere [19], it is worthwhile to take magnetic shear into account in order to gain a comprehensive insight into the physics of MHD waves in the magnetosphere. Up to the present time, much attention has been given to the effect of shear on the plasma stability (see, e.g., [20]). In our study, the problem is for-

1063-780X/02/2804-0335$22.00

mulated in a different way: we investigate the structure of the wave field at a fixed wave frequency ω. Note that many authors treated the wave structure near the resonance surface without allowance for shear (see, e.g., [1, 2, 11]). In this paper, we investigate the wave structure not only in the vicinity of the resonance, but also in the entire plasma volume.

The paper is organized as follows. In Section 2, we introduce the coordinate system and specify the equilibrium plasma parameters. In Sections 3 and 4, we derive an equation describing the structure of a wave traveling in the plane parallel to the magnetic field lines and study the character of the wave field at the singular points. Section 5 is devoted to the study of the wave structure. The results obtained are summarized in Section 6.

2. EQUILIBRIUM STATE AND COORDINATE SYSTEM

To ascertain how shear can influence the structure of the wave field, we investigate a relatively simple model in which all the equilibrium parameters depend only on one coordinate x, imitating the radial coordinate in the magnetosphere. The magnetic field lines are straight and lie in the (y, z) plane. At a given coordinate x, the magnetic field lines are parallel to each other; however, the angle between the field lines and the z-axis depends on the x coordinate (the field lines rotate about the x-axis). One-dimensional models similar to that employed in this study are widely used to investigate MHD waves in the Earth's magnetosphere and the resonance heating of space and laboratory plasmas, whereas the plasma stability is usually examined in cylindrical or toroidal geometry. As a shear parameter, we will use the tangent of the angle between the field lines and the z-axis,

$$\tan\alpha = \frac{B_{0y}}{B_{0z}} = \tau(x),$$

where B_{0y} and B_{0z} are the components of the ambient magnetic field $\mathbf{B}_0$. The nonzero derivative $d\tau/dx$ implies the presence of magnetic shear.

The plasma is assumed to be cold; therefore, the equilibrium current with the density $\mathbf{J}_0 = \nabla \times \mathbf{B}_0$ can only flow along the magnetic field lines; i.e. $\mathbf{J}_0 \times \mathbf{B}_0 = 0$. It is easy to see that the current density and the shear parameter τ are related by

$$J_0 = B_0 \frac{\tau'}{1 + \tau^2}.$$

In this paper, we focus on the study of the wave processes in the magnetosphere. The x and y coordinates imitate, respectively, the radial and azimuthal coordinates in the magnetosphere. The parameter $\tau(x)$ and the Alfvén velocity $A(x)$ are assumed to be monotonic functions varying on the same scale length L, as is shown in Fig. 1. It is also assumed that, these functions tend to constant values as $x \longrightarrow \pm\infty$.

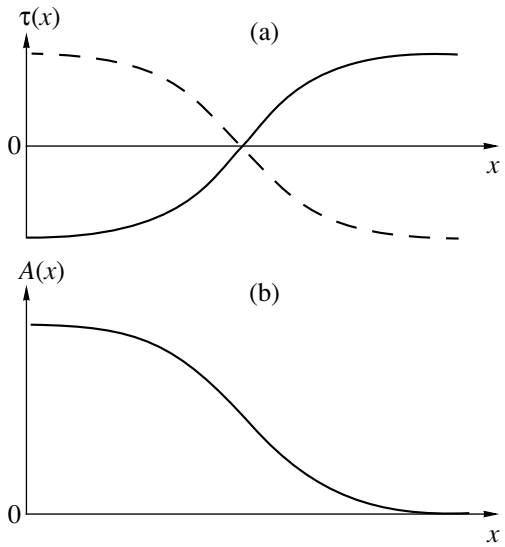

Fig. 1. (a) Profiles of $\tau(x)$ for $\tau' > 0$ (solid line) and $\tau' < 0$ (dashed line) and (b) the Alfvén velocity profile $A(x)$.

3. DERIVATION OF AN EQUATION DESCRIBING THE WAVE STRUCTURE ALONG THE x COORDINATE

A linear monochromatic MHD wave propagating through a cold plasma is described by the equation

$$-4\pi\rho_0\omega^2\boldsymbol{\xi} = \mathbf{J}_0 \times \delta\mathbf{B} + \delta\mathbf{J} \times \mathbf{B}_0, \quad (1)$$

where $\boldsymbol{\xi}(x, y, z)$ is the vector of the plasma displacement from the equilibrium position; ω is the wave frequency; ρ_0 is the plasma mass density; and $\delta\mathbf{B}$ and $\delta\mathbf{J}$ are small deviations of the magnetic field and current density from their equilibrium values $\mathbf{B}_0$ and $\mathbf{J}_0$, respectively. The magnetic field perturbation $\delta\mathbf{B}$ can be expressed in terms of the wave electric field $\mathbf{E}$:

$$\delta\mathbf{B} = -\frac{ic}{\omega}\nabla \times \mathbf{E}, \quad (2)$$

where c is the speed of light. The displacement $\boldsymbol{\xi}$ can be found from the frozen-in condition by assuming the plasma to be perfectly conducting:

$$\boldsymbol{\xi} = -\frac{ic}{\omega}B_0^{-2}\mathbf{B}_0 \times \mathbf{E}. \quad (3)$$

The infinite plasma conductivity also implies that the wave electric field is perpendicular to field lines,

$$E_y B_{0y} + E_z B_{0z} = 0. \quad (4)$$

Substituting expressions (2) and (3) into Eq. (1), we obtain:

$$-\frac{\omega^2}{A^2}\mathbf{B}_0\times\mathbf{E} = \mathbf{J}_0\times(\nabla\times\mathbf{E}) - \mathbf{B}_0\times(\nabla\times\nabla\times\mathbf{E}),$$

where $A = B_0/\sqrt{4\pi\rho_0}$ is the Alfvén velocity. We take the vector product of the above equation with $\mathbf{B}_0$ and, in view of Eq. (4), retain only the transverse components. As a result, we arrive at the equation

$$\frac{\omega^2}{A^2}\mathbf{E} = (\nabla\times\nabla\times\mathbf{E})_\perp - \kappa(\nabla\times\mathbf{E})_\perp, \qquad (5)$$

where $\kappa = \mathbf{J}_0\cdot\mathbf{B}_0/B_0^2 = \tau'/(1+\tau^2)$ is the shear-related quantity. Thus, we have obtained an equation describing an MHD wave in a cold plasma in a sheared magnetic field. A particular model of the medium described in the previous section has not yet been used; hence, Eq. (5) describes an MHD wave in a cold plasma with an arbitrary magnetic field configuration. Below, we will apply the above model to examine the propagation of MHD waves.

We seek the solution to Eq. (5) in the form

$$E_i(x, y, z, t) = E_i(x)\exp(-i\omega + ik_y y + ik_z z)$$

which implies that the wave is a traveling wave in the (y, z) plane. Then, after simple but laborious manipulations, we obtain from Eq. (5) the equation for the E_y component,

$$E_y'' + a(x)E_y' + b(x)E_y = 0, \qquad (6)$$

where the prime denotes differentiation with respect to x. Here, the following notation is introduced:

$$a(x) = \frac{K_A'}{K_A} - \frac{K_F'}{K_F} + 2\tau\kappa, \qquad (7)$$

$$b(x) = K_F + \kappa\tau\left(\frac{K_A'}{K_A} - \frac{K_F'}{K_F}\right) + \left(\frac{\tau\tau''}{1+\tau^2} + \kappa^2\right), \qquad (8)$$

where $K_A = \omega^2/A^2 - k_\parallel^2$, $K_F = \omega^2/A^2 - k_y^2 - k_z^2$, and $k_\perp = (k_y - \tau k_z)/\sqrt{1+\tau^2}$ and $k_\parallel = (k_z + \tau k_y)/\sqrt{1+\tau^2}$ are the transverse and longitudinal components of the wave vector, respectively. If $\tau' = 0$, Eq. (6) reduces to a one-dimensional equation describing the wave structure in a cold plasma in a magnetic field with straight parallel field lines:

$$E_y'' - k_\perp^2\left(\frac{\omega^2}{A^2}\right)'\frac{E_y'}{K_A K_F} + K_F E_y = 0, \qquad (9)$$

which was derived in [1, 2].

4. SINGULAR POINTS

Equation (6) involves singular points x_A and x_F, at which the functions $a(x)$ and $b(x)$ become infinite. It is seen from expressions (7) and (8) that these points satisfy the equations $K_A(x_A) = 0$ and $K_F(x_F) = 0$; i.e.,

$$\omega^2 = \Omega_A^2(x_A),$$

$$\omega^2 = \Omega_F^2(x_F),$$

where

$$\Omega_A^2(x) = A^2(x)k_\parallel^2(x),$$

$$\Omega_F^2(x) = A^2(x)(k_y^2 + k_z^2).$$

To analyze the solution to Eq. (6), we expand K_A and K_F in the vicinities of the points x_A and x_F:

$$K_A = K_A'(x - x_A), \qquad (10)$$

$$K_F = K_F'(x - x_F). \qquad (11)$$

In view of expansion (11), Eq. (6) in the limit $x \longrightarrow x_F$ reduces to the equation

$$E_y'' - \frac{E_y'}{x - x_F} + \gamma\frac{E_y}{x - x_F} = 0, \qquad (12)$$

where $\gamma = -\tau\kappa$ is a quantity related to shear. The solution to this equation is the function

$$E_y = C_1(x - x_F)J_2(Z) + C_2(x - x_F)Y_2(Z);$$

where $Y_2(Z)$ and $J_2(Z)$ are the linearly independent solutions to the Bessel equation and $Z = \sqrt{4\gamma(x - x_F)}$. This solution contains a singularity of the form $(x - x_F)^2\ln(x - x_F)$; i.e., x_F is a branch point. Nevertheless, the function $E_y(x)$ is finite near the point x_F. In this regard, the situation is similar to that in the absence of shear, when Eq. (9) near the point x_F takes the form

$$E_y'' - \frac{E_y'}{x - x_F} + K_F'(x - x_F)E_y = 0$$

(see, e.g., [1]). This equation has the same singular point x_F, but its solution has no singularity. In both cases (with and without shear), the electromagnetic field is finite near this point. An important difference between these cases arises when the WKB approximation is applied (see the next section).

In the vicinity of the point x_A, expansion (10) is valid and Eq. (6) reduces to

$$E_y'' + \frac{E_y'}{x - x_A} + \beta\frac{E_y}{x - x_A} = 0, \qquad (13)$$

where $\beta = \tau\kappa$. The solution to this equation is

$$E_y = C_1 J_0(Z) + C_2 Y_0(Z),$$

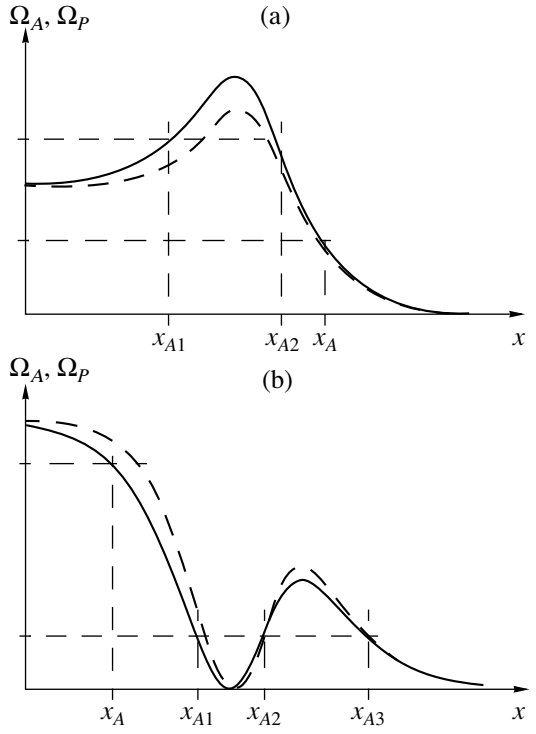

Fig. 2. Functions $\Omega_A^2(x)$ (solid line) and $\Omega_P^2(x)$ (dashed line) for (a) $k_z \gg k_y$ and (b) $k_y \gg k_z$. Indices 1, 2, and 3 stand for different Alfvén resonances at the same frequency ω.

where $J_0(Z)$ and $Y_0(Z)$ are the linearly independent solutions to the Bessel equation and $Z = \sqrt{4\beta(x - x_F)}$. As $x \approx x_A$, this solution has the following asymptotic representation:

$$E_y \approx C_1 \ln(x - x_F) + C_2,$$

i.e. the wave field has a singularity of the same type as in the absence of shear [1, 2]. Hence, at the point x_A, Alfvén resonance occurs. In view of this, the surface $x = x_A$ will be referred to as the resonance surface. The functions $\Omega_A(x)$ for $k_z \gg k_y$ and $k_y \gg k_z$ are plotted in Fig. 2. It is seen in the figure that, even with a monotonic $A(x)$ profile, there can be several Alfvén resonances, whose number depends on the $\tau(x)$ profile and the relation between the wave vector components k_y and k_z. Note that resonance exists even if $A(x) = \text{const}$. Hence, magnetic shear is an additional factor that, along with the plasma inhomogeneity, gives rise to Alfvén resonance. We note that the inequalities $E_x \gg E_y$ and $\delta B_x \ll \delta B_y$ hold near the point x_A; i.e., the field lines oscillate in the (y, z) plane. Such oscillations are often referred to as toroidal pulsations (especially, in publications on magnetosphere physics).

5. RADIAL STRUCTURE OF AN MHD WAVE IN THE WKB APPROXIMATION

When studying the excitation of Alfvén waves in the magnetosphere, the following scenario is usually considered: FMS waves arrive from the outer layers of the magnetosphere, reach the boundary of the transparent region, and are reflected back; however, their field partially penetrates deep into the magnetosphere and excites oscillations in the Alfvén resonance region. With this scenario in mind, we will use, as the boundary condition, the boundedness of the function E_y as $x \longrightarrow -\infty$. Furthermore, in the case of an inhomogeneous plasma, we should speak of a single MHD mode, because the separation of the solution into an Alfvén mode and an FMS wave is, strictly speaking, rather arbitrary. Nevertheless, by tradition, we will use these terms, trying to more strictly define them.

To solve Eq. (6) with the boundary condition $|E_y(x \longrightarrow -\infty)| < \infty$, we will use the WKB approach, assuming that the inequalities $k_y \gg L^{-1}$ and $k_z \gg L^{-1}$ are satisfied, where L is the typical scale length on which the equilibrium parameters of the medium vary. The main WKB order gives the radial component of the wave vector. In the case at hand, we have

$$k_x^2(x, \omega) = K_F + \kappa\tau\left(\frac{K_A'}{K_A} - \frac{K_F'}{K_F}\right). \qquad (14)$$

In the next WKB order, we can determine the wave amplitude as a function of the radial coordinate. In our analysis, the terms with the first derivative with respect to the radial coordinate refer just to this order because they contain a large parameter to the first power.

In the transparent region, we have $k_x^2 > 0$. One of the transparent regions exists even in the absence of shear: if $\tau' = 0$ and $\kappa = 0$, then, from Eq. (14), we obtain a well-known FMS dispersion relation, $k_x^2 = K_F$. In the presence of shear, the FMS transparent region consists of two separate (but close to each other) regions (Fig. 3b). One of these regions (to the left of the point x_F) is similar to the transparent region in the absence of shear (Fig. 3a). The second region is bounded by the point where $k_x^2 = 0$ and the point x_F, where $k_x^2 = \infty$; i.e., it resembles the Alfvén transparent region described below. Recall that the wave amplitude is finite near the point x_F.

The other transparent region is adjacent to the resonance surface $x_A(\omega)$. In this transparent region, the waves have, to a high degree of accuracy, the Alfvén mode polarization ($E_x/E_y = k_x/k_y$). Hence, this region will be referred to as the Alfvén transparent region. It is seen from relation (14) that, when $\omega = \Omega_A(x)$, we have $k_x^2 \longrightarrow \infty$. Let us introduce the poloidal frequency $\Omega_P(x)$, such that, when $\omega = \Omega_P(x)$, the equality $k_x = 0$ is

satisfied. Accordingly, the surface $x_P(\omega)$, on which the equality $\omega = \Omega_P(x)$ is satisfied, will be referred to as poloidal, because, near the point x_P, the inequality $k_x \ll k_y$ holds and, consequently, we have $E_x \ll E_y$ and $\delta B_x \gg \delta B_y$. The second of the last two inequalities suggests that the field lines oscillate in the radial direction; i.e., the oscillations are poloidal in character. At large values of k_y and k_z, it is easy to obtain from relation (14) the difference between the poloidal and resonance frequencies,

$$\Omega_P^2(x) - \Omega_A^2(x) = qA^2k^{-2},$$

where $k^2 = k_y^2 + k_z^2$ and $q = \tau\kappa K_A'$. The distance between the poloidal and resonance surfaces is determined by the expression

$$\Delta = x_P - x_A = \frac{q}{k^2 K_A'}.$$

The function $\Omega_P(x)$ is plotted in Fig. 2. It is seen in the figure that $\Delta \ll L$. In the vicinities of the resonance and poloidal surfaces, relation (14) takes a simpler form:

$$k_x^2 = k^2\frac{\Omega_P^2(x) - \omega^2}{\omega^2 - \Omega_A^2(x)}. \quad (15)$$

This formula can be regarded as a dispersion relation for Alfvén waves in the presence of magnetic shear in a plasma whose parameters vary along one coordinate. The dependence $k_x(\omega)$ indicates the emergence of the transverse dispersion of Alfvén waves. As is known, the dispersion relation for the Alfvén mode in a homogeneous plasma is $\omega^2 = k_\parallel^2 A^2$. The dependence of the transverse component of the wave vector on the frequency appears when nonideal MHD effects (such as the electron inertia and the effects related to the finite ion Larmor radius) are taken into account. We can see that, even in an ideal one-fluid magnetohydrodynamics, the transverse dispersion arises if magnetic shear is taken into account. It should be noted that the transverse dispersion similar to that described by Eq. (15) was found for waves in a two-dimensional plasma in a magnetic field with curved field lines [16], whereas, in our model, the magnetic field lines are straight and the plasma is inhomogeneous along one direction.

The profiles of $k_x^2(x)$ outside the FMS transparent region (i.e., at $x < x_F$) are plotted in Fig. 4. The plots illustrate the arrangement of the transparent regions for Alfvén waves under different assumptions about the ambient medium. It is seen in the figure that there are generally several such regions. Let us consider Fig. 4a in more detail, where only one Alfvén transparent

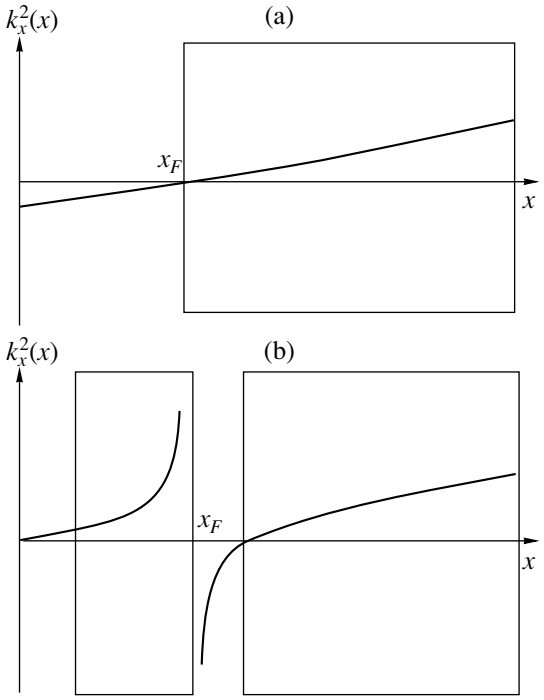

Fig. 3. Profiles of $k_x^2(x)$ near the x_F point (a) without and (b) with shear.

region is present. If $k_y, k_z \gg L^{-1}$, then, in this region and around it, Eq. (6) can be brought to the form

$$E_y'' + \frac{1}{x - x_A}E_y' + k^2\frac{x_P - x}{x - x_A}E_y = 0. \quad (16)$$

Near the Alfvén resonance, this equation can be even more simplified [see Eq. (13)]. Near the poloidal point, it reduces to the Airy equation. To solve Eq. (6), the WKB solutions must be matched with the solutions near the points x_A, x_P, and x_F. Omitting intermediate manipulations, we give the final solution. In accordance with the boundary condition, in the opaque region (at $x \ll x_A$), we have

$$E_y = c_1\exp(-kx)$$

(here and below, we will not give the expressions for the constants because they are rather unwieldy). In the Alfvén transparent region (i.e., at $x_A < x < x_P$), the wave is described by the expression

$$E_y = c_2[(x_P - x)(x - x_A)]^{-1/4}\exp ik\int_{x_P}^{x}\sqrt{\frac{x_P - x'}{x' - x_A}}dx';$$

i.e., it is a traveling wave propagating across magnetic shells. In this case, the wave phase velocity is directed along the x-axis ($v_{ph} > 0$) and the group velocity, as is seen from relation (15), is directed from the poloidal surface toward the resonance surface. Note that this is a

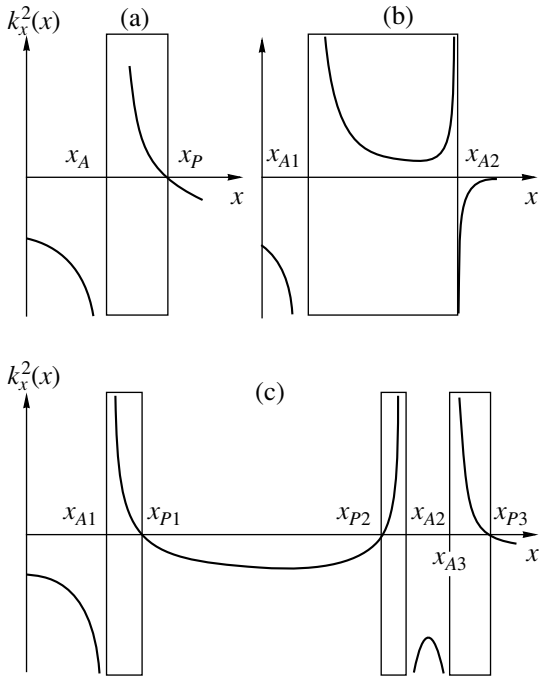

Fig. 4. Profiles of $k_x^2(x)$ at $x < x_F$ for the cases of (a) one, (b) two, and (c) three resonances. Indices 1, 2, and 3 stand for the Alfvén transparent regions adjacent to the different Alfvén resonances shown in Fig. 2.

general result, irrespective of the relative positions of x_P and x_A; i.e., we always have $v_{\rm ph} > 0$, and the group velocity is always directed toward x_A. As the wave propagates, its radial wavelength decreases and the character of the mode polarization also changes. At $x \approx x_P$, the wave is poloidally polarized ($E_y \gg E_x$ and $\delta B_y \ll \delta B_x$), whereas at $x \approx x_A$, it is toroidally polarized ($E_y \ll E_x$ and $\delta B_y \gg \delta B_x$). Near the points x_P and x_A, the applicability conditions of the WKB approximation fail to satisfy and the structure of the wave is described in terms of the functions obtained by solving Eq. (16) near these points:

$$E_y = \begin{cases} c_3 K_0(\sqrt{4k^2\Delta(x_A - x)}) & \text{for } x \le x_A \\ c_4 H_0^{(1)}(\sqrt{4k^2\Delta(x - x_A)}) & \text{for } x_A \le x \ll x_P \\ c_5 \mathrm{Ai}((k^2/\Delta)^{1/3}(x - x_p)) & \text{for } x \approx x_P, \end{cases}$$

where K_0 is the modified Bessel function, $H_0^{(1)}$ is the Hankel function, and Ai is the Airy function. The constants are obtained by matching these solutions with the WKB solutions. Finally, in the FMS transparent region, we have a standing wave; thus, at $x \gg x_F$, we obtain

$$E_y = c_6 \cos\left(kx - \frac{\pi}{4}\right).$$

Note that the penetration of an FMS wave beyond the transparent region slightly affects the structure of this mode (see also [21]).

Such a structure of an MHD wave generally corresponds to the conventional propagation scheme of low-frequency waves in the magnetosphere, as was described at the beginning of this section. However, the situation with the Alfvén transparent region differs radically from that in the absence of shear [1, 2] (in the latter case, the wave is a solitary resonance and there is no poloidal surface). On the other hand, it resembles a situation considered in [16, 17]. In that case, the waves also propagate across the magnetic shells; however, this is related to the curvature of magnetic field lines.

6. CONCLUSION

(i) An equation describing the electric field of a wave propagating in a cold plasma in a sheared magnetic field has been derived. The equation holds for any magnetic field configuration. A particular case of a wave traveling in the plane parallel to the magnetic field lines has been examined assuming that the plasma is inhomogeneous along one direction and the magnetic field lines are straight.

(ii) It has been shown that, on the magnetic surfaces where the condition $\omega^2 = A^2 k_\parallel^2$ is satisfied, there are logarithmic singularities similar to that in the absence of shear. Thus, we can state that the Alfvén resonances occur just on these surfaces. In a sheared magnetic field (unlike the case without magnetic shear), there can be several Alfvén resonances at a fixed frequency even if the Alfvén velocity $A(x)$ has no local extrema. The number of resonances depends on the $\tau = \tau(x)$ profile and the relation between the wave vector components k_y and k_z. It has been shown that the Alfvén resonance exists even if $A(x) = \text{const}$. This suggests that shear is one of the factors (along with the plasma inhomogeneity) that gives rise to Alfvén resonance.

(iii) It has been shown that, at the turning point for magnetosonic waves, the equation possesses a singularity. At this point, the solution is finite, but has a branching singularity.

(iv) It has been established that the presence of shear gives rise to the transverse dispersion of Alfvén waves, i.e., the dependence of the radial component of the wave vector on the wave frequency ω. This phenomenon has no analogue in the case of a magnetic field with straight parallel field lines and a plasma that is inhomogeneous along one direction. However, transverse dispersion can also arise due to the field line curvature [16] or the finite plasma pressure [17]. The presence of shear also slightly changes the FMS dispersion law; however, this change does not play an important role because this mode has a significant transverse dispersion ($k_x^2 = \omega^2/A^2(x) - k_y^2 - k_z^2$) even in the absence of shear.

(v) The wave structure has been studied in the model in question. It is shown that the MHD mode has two transparent regions. The first region, corresponding to small values of the Alfvén velocity, refers to FMS waves. In this region, the mode is a standing wave occurring between magnetic shells. The second transparent region is adjacent to the Alfvén resonance surface and, thus, can be called the Alfvén region. This region is bounded by the Alfvén resonance surface on the one side and the poloidal surface ($k_x = 0$) on the other side. Within this transparent region, the mode is a traveling wave and the energy of the wave is transported from the poloidal surface to the resonance surface. This situation differs radically from that with straight parallel field lines [1, 2], in which case an Alfvén wave is a solitary resonance and there is no poloidal surface. However, it resembles a situation in which a similar phenomenon is caused by the curvature of magnetic field lines [16, 17].

ACKNOWLEDGMENTS

We are grateful to A.S. Leonovich and V.A. Mazur for helpful discussions and to J. Tataronis for encouraging advice. We wish to express our gratitude to V.G. Mikhalkovsky for his assistance in preparing the English version of the manuscript. This study was supported in part by the Council of the Expert Competition of Young Scientists' Research Projects at the Siberian Division of the Russian Academy of Sciences.

REFERENCES

1. D. J. Southwood, Planet. Space Sci. **22**, 483 (1974).
2. L. Chen and A. Hasegawa, J. Geophys. Res. **79**, 1024 (1974).
3. A. S. Potapov and V. A. Mazur, in *Solar Wind Sources of Magnetospheric Ultra-Low-Frequency Waves*, Ed. by M. J. Engebretson, K. Takahashi, and M. Scholer (American Geophysical Union, Washington, 1994), Geophysical Monograph, Vol. 81, p. 135.
4. H. J. Singer, W. J. Hughes, and C. T. Russel, J. Geophys. Res. **87**, 3519 (1982).
5. J. A. Ionson, Astrophys. J. **226**, 650 (1978).
6. A. V. Timofeev and K. Yu. Kharitonov, Fiz. Plazmy **15**, 674 (1989) [Sov. J. Plasma Phys. **15**, 389 (1989)].
7. P. E. Moroz, Fiz. Plazmy **13**, 558 (1987) [Sov. J. Plasma Phys. **13**, 317 (1987)].
8. W. Grossmann and J. A. Tataronis, J. Phys. **261**, 217 (1973).
9. L. Chen and A. Hasegawa, Phys. Fluids **17**, 1399 (1974).
10. A. E. Lifshits and E. N. Fedorov, Dokl. Akad. Nauk SSSR **287**, 90 (1986).
11. A. S. Leonovich and V. A. Mazur, Fiz. Plazmy **15**, 660 (1989) [Sov. J. Plasma Phys. **15**, 381 (1989)].
12. E. N. Fedorov, N. G. Mazur, and V. A. Pilipenko, Fiz. Plazmy **21**, 333 (1995) [Plasma Phys. Rep. **21**, 311 (1995)].
13. A. L. Krylov and A. F. Lifshitz, Planet. Space Sci. **32**, 481 (1984).
14. A. N. Wright, J. Geophys. Res. **97**, 6429 (1992).
15. A. N. Wright and M. J. Thompson, Phys. Plasmas **1**, 691 (1994).
16. A. S. Leonovich and V. A. Mazur, Planet. Space Sci. **41**, 697 (1993).
17. D. Yu. Klimushkin, Fiz. Plazmy **23**, 931 (1997) [Plasma Phys. Rep. **23**, 858 (1997)].
18. A. Salat and J. A. Tataronis, J. Geophys. Res. **105**, 13055 (2000).
19. D. P. Stern, J. Geophys. Res. **99**, 17169 (1994).
20. G. Bateman, *MHD Instabilities* (MIT Press, Cambridge, 1978; Énergoatomizdat, Moscow, 1982).
21. A. S. Leonovich and V. A. Mazur, J. Geophys. Res. **106**, 3919 (2001).

Translated by V. Mikhalkovsky

Plasma Physics Reports, Vol. 28, No. 4, 2002, pp. 342–350. Translated from Fizika Plazmy, Vol. 28, No. 4, 2002, pp. 375–383.

PARTICLE MOTION

Boundary of the Adiabatic Motion of a Charged Particle in a Dipole Magnetic Field

S. N. Kuznetsov and B. Yu. Yushkov

Skobeltsyn Institute of Nuclear Physics, Moscow State University, Vorob'evy gory, Moscow, 119899 Russia

Received October 24, 2001; in final form, November 18, 2001

Abstract—The motion of a charged particle in a dipole magnetic field is considered using a quasi-adiabatic model in which the particle guiding center trajectory is approximated by the central trajectory, i.e., a trajectory that passes through the center of the dipole. A study is made of the breakdown of adiabaticity in the particle motion as the adiabaticity parameter χ (the ratio of the Larmor radius to the radius of the magnetic field line curvature in the equatorial plane) increases. Initially, for $\chi \gtrsim 0.01$, the magnetic moment μ of a charged particle undergoes reversible fluctuations, which can be eliminated by subtracting the particle drift velocity. For $\chi \gtrsim 0.1$, the magnetic moment μ undergoes irreversible fluctuations, which grow exponentially with χ. Numerical integration of the equations of motion shows that, during the motion of a particle from the equatorial plane to the mirror point and back to the equator in a coordinate system related to the central trajectory, the analogue of the magnetic moment μ is conserved. In the equatorial plane, this analogue undergoes a jump. The long-term particle dynamics is described in a discrete manner, by approximating the Poincaré mapping. The existence of the regions of steady and stochastic particle motion is established, and the boundary between these regions is determined. The position of this boundary depends not only on the adiabaticity parameter χ but also on the pitch angle. The calculated boundary is found to agree well with that obtained previously by using the model of a resonant interaction between particle oscillations associated with different degrees of freedom. © *2002 MAIK "Nauka/Interperiodica".*

1. INTRODUCTION

An effective, generally accepted method for investigating particle dynamics in magnetic fields is that provided by the adiabatic (drift) theory [1–3], which implies that, under certain circumstances, the complicated motion of a particle can be described as the superposition of two independent motions: the particle cyclotron gyration and the motion of the instantaneous center of this gyration, i.e., the particle guiding center (GC) motion. The guiding center moves along magnetic field lines and, in the case of a nonuniform magnetic field, drifts across the magnetic field. In a moving coordinate system (CS) related to the GC, the particle trajectory is almost circular, in which case the first adiabatic invariant (the magnetic moment) is conserved,

$$\mu = \frac{mV^2\sin^2\alpha}{2B}, \qquad (1)$$

where m is the mass of a particle, V is its velocity, the pitch angle α is the angle between the vectors **V** and **B** (the magnetic field strength at the GC). The conventional applicability conditions for the validity of the adiabatic theory are

$$\frac{\rho|\nabla B|}{B} \ll 1, \quad \frac{dB}{dt} \ll \omega B, \qquad (2)$$

where $\rho = V/\omega$ is the gyroradius, $\omega = eB/mc$ is the gyrofrequency, e is the charge of a particle, and c is the speed of light. According to [4], it is more correct to rewrite the first of conditions (2) in terms of the adiabaticity parameter $\chi = \chi/R_c$ (where R_c is the radius of curvature of a magnetic field line in the region where the field strength is minimum), specifically, $\chi \ll 1$. In fact, this condition indicates that a particle makes each Larmor revolution in a uniform field. However, as the particle energy increases, this condition is inevitably violated (e.g., due to the increase in ρ). It therefore seems worthwhile to analyze the limit of applicability of the adiabatic theory and the methods for describing particle motions near this limit. This will be done below for particle motion in a dipole magnetic field by using the quasi-adiabatic model that has been developed by the authors in recent years [5–7].

2. FORMULATION OF THE PROBLEM

The magnetic field of a dipole that is placed at the origin of a Cartesian CS and whose magnetic moment M is oriented antiparallel to the z-axis has the components

$$B_x = -3xz\frac{M}{R^5}, \quad B_y = -3yz\frac{M}{R^5},$$

$$B_z = (R^2 - 3z^2)\frac{M}{R^5}, \quad R^2 = x^2 + y^2 + z^2.$$

1063-780X/02/2804-0342$22.00 © 2002 MAIK "Nauka/Interperiodica"

The steady-state problem of the motion of a charged particle in such a field was first formulated and solved in a general form by Stormer [8], who obtained the second integral of motion (the generalized angular momentum) and showed the existence of allowed and forbidden regions of motion. Under certain conditions, there exists an internal allowed region, namely, a dipole trap, in which a particle executes finite motion [9]. In this region, the relationship that is usually called the Stormer integral and corresponds to the second integral of motion can be written in the following form [5–7]:

$$\frac{r}{S} = \frac{\cos^2\lambda}{\gamma + \sqrt{\gamma^2 - \sin\alpha\sin\varphi\cos^3\lambda}}, \quad (3)$$

where r is the position vector of the particle, $S = \left(\frac{eM}{mVc}\right)^{1/2}$ is the Stormer length unit, and $\lambda = \arcsin(z/r)$ is the latitude measured from the equatorial plane of the dipole. The dimensionless Stormer constant γ, which is directly proportional to the angular momentum and is larger than unity for finite motion ($\gamma > 1$), is calculated from the particle parameters in accordance with relationship (3). The angles α and φ are defined in an orthogonal local coordinate system (LCS) with origin at the instantaneous position of the particle. The unit vector $\mathbf{e}_3$ is defined by the vector $\mathbf{B}$ [6, 7]:

$$\mathbf{e}_1 = \frac{[\mathbf{r}\times\mathbf{B}]}{|[\mathbf{r}\times\mathbf{B}]|}, \quad \mathbf{e}_2 = [\mathbf{e}_3\times\mathbf{e}_1].$$

The phase φ is determined by the projection of the vector $\mathbf{V}$ onto the plane ($\mathbf{e}_1$, $\mathbf{e}_2$) and is measured from $\mathbf{e}_2$, in which case the value $\varphi = \pi/2$ corresponds to the direction of the azimuthal drift of a positively charged particle. In the LCS, the particle velocity $\mathbf{V}$ is equal to

$$\mathbf{V} = V(\mathbf{e}_1\sin\alpha\sin\varphi + \mathbf{e}_2\sin\alpha\cos\varphi + \mathbf{e}_3\cos\alpha).$$

Note that, by virtue of the axial symmetry of the problem, Eq. (3) completely (correct to a rotation about the z-axis) determines the phase trajectory of a particle, and the components of the velocity vector (as well as of any other vector) are determined by its absolute value and by the angles α and φ.

In a dipole magnetic field, the adiabaticity parameter χ can be defined [10] as the ratio of the gyroradius ρ to the radius $R_c = r_e/3$ of the magnetic field line curvature in the equatorial plane (here, r_e is the distance from the field line in this plane). Setting $\lambda = 0$ and $\sin\alpha = 0$ (or $\sin\varphi = 0$) in Eq. (3), we can show that $\chi\gamma^2 = 0.75$; i.e., the value of χ is calculated from the integral of motion and, consequently, is constant along the entire particle trajectory.

In the absence of an electric field, the motion of a charged particle in a magnetic field is described by the Lorentz equation

$$\frac{d^2\mathbf{r}}{dt^2} = \frac{e}{mc}[\mathbf{V}\times\mathbf{B}]. \quad (4)$$

Note that, in the case at hand, the total particle energy and, accordingly, the relativistic particle mass remain unchanged, so that there is no need to consider relativistic effects.

We investigated the particle dynamics by integrating Eq. (4) numerically using a fourth-order Runge–Kutta method supplemented with the standard techniques for controlling the accuracy of calculations and the conservation of the integrals of motion—the energy and the Stormer constant γ. An analysis of the computational results shows that, even for $\chi \gtrsim 0.01$, the pitch angle should be calculated with allowance for the azimuthal drift of the GC, whose velocity in the equatorial plane is equal to

$$V_d = \frac{\chi V}{2}(2 - \sin^2\alpha). \quad (5)$$

For $\chi \gtrsim 0.1$, the deviation of the GC trajectory from the magnetic field line cannot be explained exclusively in terms of the azimuthal drift [7]. Retaining next-order terms in the expansion of the adiabatic invariant in powers of χ leads to fairly lengthy expressions [6], but even these expressions do not ensure that the invariant is conserved as χ increases.

Figure 1 shows the magnetic moment μ calculated from expression (1) for two different values of χ. Significant fluctuations of μ are associated primarily with the particle gyration. This conclusion is confirmed by the circumstance that fluctuations are synchronous with the change in the phase φ. Note that the fluctuations of μ are most intense in the region of the weakest magnetic field. This seemingly paradoxical result is explained as being due to the fact that the breakdown of adiabaticity in the particle motion is associated with the ratio ρ/R_c rather than with the quantities B and grad$B$. The local value of this ratio is maximum precisely near the equatorial plane and decreases substantially with distance from the equator, as does the drift velocity, whose dependence on the latitude has the form

$$f(\lambda) = \frac{\cos^5\lambda(1 + \sin^2\lambda)}{(1 + 3\sin^2\lambda)^2}. \quad (6)$$

For $\chi = 0.12$, the fluctuations are almost completely reversible and the magnetic moment μ takes on the same values at the mirror points. For $\chi = 0.30$, the magnetic moment μ undergoes not only reversible but also irreversible fluctuations, which change the magnetic field strength at the mirror points.

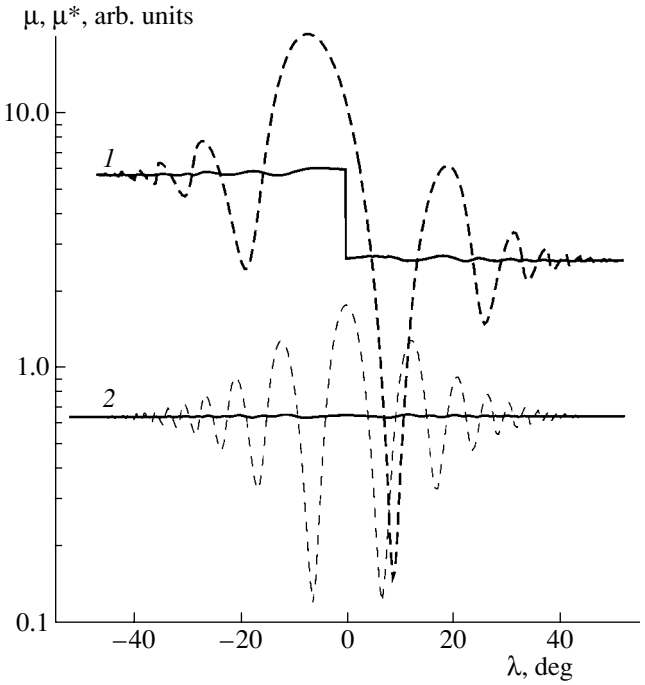

Fig. 1. Change in the magnetic moment μ (dashed curves) and in the quasi-magnetic moment μ* (solid curves) over one-half of the bounce period for χ = (*1*) 0.3 and (*2*) 0.1.

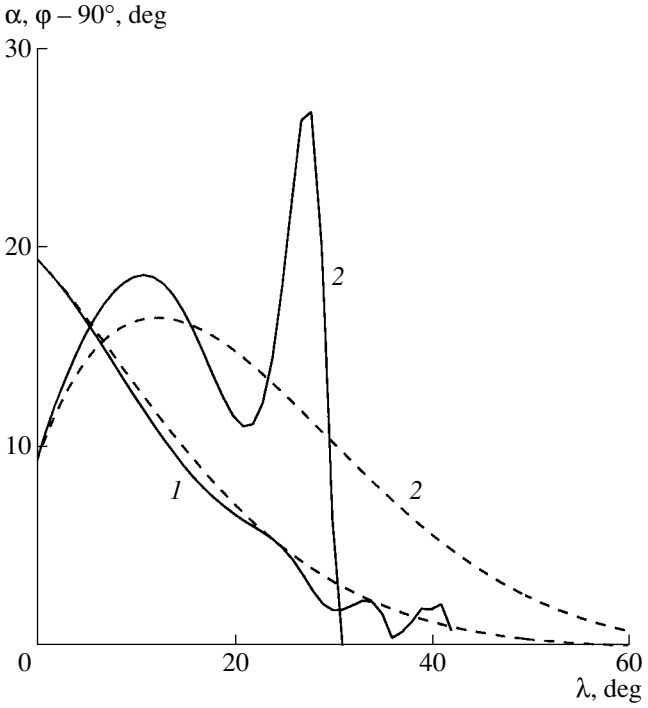

Fig. 2. Latitude dependence of (*1*) the pitch angle α and (*2*) the phase φ along the direct CT (dashed curves) and along the GC trajectory (solid curves) for χ = 0.30.

3. QUASI-ADIABATIC MODEL

Based on the analysis of the results of our numerical simulations, we developed a quasi-adiabatic model of particle motion, which adequately describes particle dynamics in the range $0.1 < \chi < 0.75$, i.e., over the entire region of finite motion. The basic assumptions of the model can be formulated as follows.

(i) In a dipole trap, the character of particle motion is governed primarily by the adiabaticity parameter χ.

(ii) The best model of the particle GC trajectory is the *central trajectory* (CT)—a part of the particle trajectory that is between the dipole and the equatorial plane and passes through the dipole center along the magnetic field line $r = r_e\cos^2\lambda$, in which case we have $2\gamma r_e = S$. When moving along the CT, a particle undergoes no obvious cyclotron gyration, because its velocity component in the direction of the unit vector $\mathbf{e}_1$ of the LCS is essentially equal to the velocity of its drift motion around the dipole. Figure 2 shows how the pitch angle and phase of a particle change along the CT. The phase of the particle deviates from π/2 because its radial velocity is nonzero. It is necessary to distinguish between the CT toward the dipole (the direct CT) and the CT outward from the dipole (the reverse CT): along the direct CT, we have $\varphi_1 > \pi/2$ (the CT approaches the magnetic field line), while, along the reverse CT, we have $\varphi_2 < \pi/2$ (the CT departs increasingly from it). For the above χ value, the direct and reverse CTs are, in particular, symmetric at an arbitrary latitude such that $\varphi_1 + \varphi_2 = \pi$. The particle trajectory that passes through the dipole center has peculiar properties only in the region between the dipole and the equatorial plane; in the opposite hemisphere, the trajectory becomes twisted and does not reach the dipole (see Fig. 1 from [7]). The departure of the CT from the magnetic field line is maximum in the equatorial plane and tends to zero as the dipole is approached [7]:

$$r(\lambda) = r_e\cos^2\lambda \times\left(1 + \frac{1}{3}\chi^2 f(\lambda)\cos^3\lambda + \frac{1}{9}\chi^4 f^2(\lambda)\cos^6\lambda\right), \quad (7)$$

where $r(\lambda)$ is the instantaneous distance from the CT, r_e corresponds to the field line along which the CT passes when approaching the dipole, and the function $f(\lambda)$ is given by formula (6). In numerical simulations, the role of the CT was played by the trajectory of a particle injected from the region near the dipole center along the field line, i.e., at the pitch angle $\alpha = 0$.

The values of the parameters α_0 and φ_0 of the CT in the equatorial plane (Fig. 3) depend only on χ. For $0.08 < \chi < 0.75$, these values are approximated by the expressions

$$\sin\alpha_0 = 0.983\chi^{0.753}\exp(-0.0538/\chi), \quad (8)$$

$$\cos\varphi_0 = \pm 1.45\chi^{-0.743}\exp(-0.908/\chi). \quad (9)$$

For $\chi > 0.1$, the CT is such that $\left.\frac{dr}{d\lambda}\right|_{\lambda = 0} \neq 0$, which results in the inequality $\varphi_0 \neq \pi/2$. Consequently, the function describing the matching of the direct and reverse CTs in the equatorial plane has a discontinuous (rather than continuous) derivative in this plane. The angle δ (given in degrees) between the tangents to the direct and reverse CTs is equal to

$$\delta = 2\arcsin(\sin\alpha_0\cos\varphi_0) = 2.761\chi^{0.07}\exp\left(-\frac{0.962}{\chi}\right). \quad (10)$$

(iii) Along the particle trajectory from the equatorial plane to the mirror point and back to the equator, the analogue of the magnetic moment,

$$\mu^* = \frac{mV^2\sin^2\alpha^*}{2B}, \quad (11)$$

is conserved to a high degree of accuracy. In what follows, we will call this analogue the "quasi-magnetic moment." We will also use the term "quasi-pitch angle" for the angle α^* between the vector $\mathbf{V}$ and the straight line that is tangent to the CT with the same χ value at the same latitude and whose direction corresponds to particle motion along the direct or reverse CT. The quasi-pitch angle is calculated from the relationship

$$\cos\alpha^* = \cos\alpha\cos\alpha_0 + \sin\alpha\sin\alpha_0\cos(\varphi + \varphi_0), \quad (12)$$

where the subscript zero stands for the values of the quantities at the CT and B is the magnetic field strength at the position of the particle. Figure 1 shows the behavior of the quasi-magnetic moment calculated from expression (11) for the same particles for which the conventional magnetic moment μ was previously determined from expression (1). We can see that, between the equatorial plane and the mirror point, the quasi-magnetic moment μ^* remains essentially constant.

Figure 4 shows how the parameters of the particle with $\chi = 0.30$ at the equator change over the period of longitudinal bounces. In simulations, the particles injected from the equatorial plane were divided into two ensembles. The particles in the first ensemble are injected at the same pitch angle, $\alpha = 12°$, and are distributed uniformly over the phase φ (curve *1*). At the mirror points, the magnetic field strength B_m for the particles from this ensemble differs by more than one order of magnitude. In the equatorial plane, the reflected particles are randomly distributed over a wide range of α and φ values (Fig. 4 presents only a part of the particles from the first ensemble, namely, those in the ranges $0 < \alpha < 40°$ and $0 < \varphi < 180°$).

The particles in the second ensemble are injected at the constant quasi-pitch angle $\alpha^* = 12°$ (measured from the direct CT with the same χ value) and are uniformly

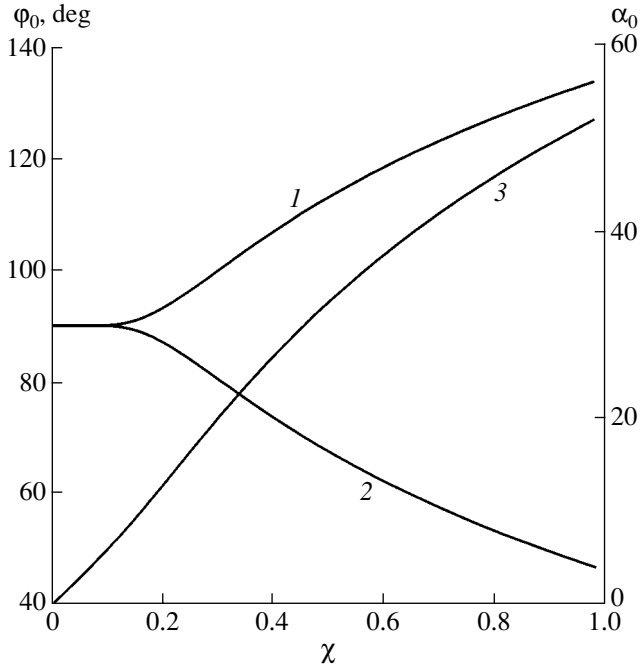

Fig. 3. Parameters of the CT in the equatorial plane: (*1*) the phase φ for the direct CT, (*2*) the phase φ for the reverse CT, and (*3*) the pitch angle α for the direct and reverse CTs.

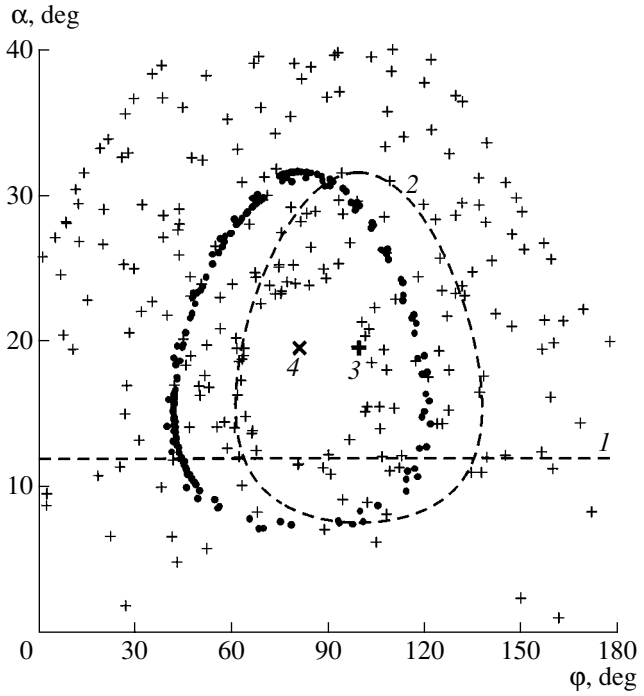

Fig. 4. Change in the parameters of the particle with $\chi = 0.30$ during its motion from the equatorial plane to the mirror point and back. Dashed curve *1* indicates the initial positions of the particles with $\alpha = 12°$, and the crosses show their final positions. The initial positions of the particles with $\alpha^* = 12°$ are represented by curve *2*, and their final positions are shown by closed circles. Points *3* and *4* indicate the positions of the direct and reverse CTs, respectively.

distributed over the initial gyrophase angle ϕ_i (where i is the number of the particle), which is related to φ by

$$\sin\phi_i = \frac{\sin(\varphi_i - \varphi_0)\sin\alpha_0}{\sin\alpha_i^*}. \quad (13)$$

The injection points so defined are represented by curve *2* in Fig. 4. At the mirror point for the particles from the second ensemble, the magnetic field strengths B_m differ by no more than fractions of a percent. In the equatorial plane, the reflected particles form a nearly perfect circle with the same value of the quasi-pitch angle α^*, which now is measured from the reverse CT (corresponding to particle motion outward from the dipole).

When moving either toward or away from the dipole, the particles injected at the same α^* (and, accordingly, μ^*) values describe perfect circles not only in the equatorial plane but also at any latitude up to the mirror point. This circumstance makes it possible to determine from relationship (12) such values of α_0 and φ_0 for the centers of these circles at which the dispersion of the α^* values about their ensemble average is minimum. The full set of these centers at different latitudes can be legitimately regarded as the GC trajectory for the particle ensemble under investigation. The GC trajectory that refers to Fig. 2 and is associated with an ensemble of the particles whose initial positions are shown in Fig. 4 deviates considerably from a magnetic field line. For a given χ value, the pitch angle along the GC trajectory and along the CT with the corresponding direction obeys essentially the same latitude dependence; for the phase, this is true only on the average. The fluctuations of φ, and, in particular, their growth with λ, stem from the fact that φ was calculated from formula (12), which produces large errors in the limit $\alpha_0 \longrightarrow 0$. In the first approximation, the GC trajectories with different α^* values in the equatorial plane coincide at a given χ value.

Hence, it is the CT that defines the desired moving coordinate system, in which the magnetic moment (or, more precisely, the quasi-magnetic moment) of a gyrating charged particle is conserved. In particular, the drift-induced parts of the deviations of the GC trajectory and the CT from a magnetic field line cancel one another (in which case the CT itself is not a plane curve because of the particle drift).

Note that, in the presence of an absorbing sphere around a dipole (as is the case in, e.g., a geomagnetic trap), there is a loss cone for a group of particles that are reflected at magnetic field strengths B_m larger than a certain value. The axis of the loss cone is not a magnetic field line but rather a tangent to the CT. In turn, the CT itself can be regarded as a limiting (at $\alpha^* \longrightarrow 0$) trajectory for an ensemble of particles reflected at the same magnetic field strength B_m.

(iv) When the particle crosses the equatorial plane, the quasi-magnetic moment μ^* undergoes a jump (Fig. 1) because the GC trajectory has a break related to the transition from the CS associated with the reverse CT to that associated with the direct CT. It is for this reason that the quasi-pitch angle α^* and, consequently, the quasi-magnetic moment μ^* change in a jumplike manner as a particle crosses the equatorial plane. The mean jump $\Delta\mu^*$ is determined by the angle δ [see formula (10)] between the tangents to the direct and reverse CTs and increases exponentially with χ. For each individual particle, the jump $\Delta\mu^*$ depends on the relative position of the particle with respect to the direct CT [11], i.e., on the phase of the particle in the equatorial plane. In fact, Fig. 4 shows that particles with the same value of α^* measured from the reverse CT have a significant spread in the values of α^* measured from the direct CT. That is why this ensemble of particles subsequently spreads out over a wide range of α and φ values.

(v) The jump in the magnetic moment obtained analytically by Il'in and Il'ina [12] for a particle moving between the mirror points depends not only on χ but also on α:

$$\frac{\Delta\mu}{\mu} \sim \exp\left(-\frac{\psi(\alpha)}{\chi}\right),$$

where

$$\psi(\alpha) = \frac{1}{\sqrt{2}\sin^2\alpha}\left(\frac{1+\sin^2\alpha}{\sin\alpha}\ln\frac{1+\sin\alpha}{\cos\alpha} - 1\right). \quad (14)$$

Numerical experiments yield an analogous result: the reversible fluctuations of μ^* are minimum if the trajectory of the GC of a particle with the quasi-pitch angle α^* is modeled by a CT corresponding to the effective value

$$\chi_{\text{eff}}(\alpha^*) = \chi\psi(0)/\psi(\alpha^*) = 0.75\gamma^{-2}\psi(0)/\psi(\alpha^*) \approx 0.75\gamma^{-2}\cos\alpha^*, \quad (15)$$

in terms of the χ_{eff} value in the equatorial plane. The dependence of χ_{eff} on α stems from the fact that, according to expression (5), the drift velocity, in turn, depends on α, or, more precisely, on α^*.

(vi) The phase accumulation $\Delta\phi$ during the motion of a particle from the equatorial plane to the mirror point and back to the equator depends not only on χ and α^* but also on the initial phase ϕ of cyclotron gyration. For $\chi = 0.1$–0.3 and for pitch angles of about 10°, the particle makes several tens of Larmor revolutions over one-half of the bounce period, in which case the mean phase accumulation in terms of α^* and χ is equal to [7]

$$\Delta\phi = 6F(\alpha^*)/\chi, \quad F(\alpha^*) = \sin^{-1.348}\alpha^* - 0.255. \quad (16)$$

In addition, the mean phase accumulation undergoes variations with an amplitude of at most a few percent, which depend on the initial value of the phase ϕ measured in the CS associated with the direct CT. The numerically calculated value of $\Delta\phi(\phi)$ is shown in Fig. 5, where $\Delta\phi$ is measured from the phase of the par-

ticle that was injected with the phase $\phi = 0$. The functions α_i^* and $\Delta\phi_i$ are seen to be in antiphase. Curve *3* is the plot of the function $\alpha^*(\phi) = \tilde{\alpha} + k\Delta\phi(\phi)$, where the quantities $\tilde{\alpha}$ and k were determined from the computed values of α_i^* by the least squares method. The amplitude of $\Delta\phi$ increases with increasing χ and decreasing α^*.

(vii) The residual fluctuations of μ^*, as well as the ϕ-dependent variations of the phase accumulation $\Delta\phi$, can be described by the following approximate expression for the fluctuations of α^*:

$$\Delta\alpha^* = 1.25\chi^{0.753}\exp(-0.524/\chi)\sin^{1.09}\alpha^* \times (1 - \sin^{1.258}\alpha^*)\sin 2\phi/\cos\alpha^*. \quad (17)$$

Of course, this representation simplifies the corresponding dependence shown in Fig. 5, but, on the other hand, it significantly reduces the number of adjustable parameters.

Note that the above model is adequate at quasi-pitch angles ranging to approximately 30°. In our opinion, at larger quasi-pitch angles, it is necessary to take into account the difference between the drift velocities of the particles moving along the CT and those moving along other trajectories. In fact, the drift velocity (5) of a particle on the CT in the equatorial plane is approximately equal to $V_d \approx \chi V$, which is also true for particles with small α^* values. However, for $\alpha^* \longrightarrow \pi/2$, we have $V_d \approx 0.5\chi V$, which restricts the applicability region of the CT approach when modeling the GC trajectory.

For $\chi \longrightarrow 0$, the quasi-adiabatic model gradually passes over to the traditional adiabatic model, in which case the CT asymptotically approaches the magnetic field line [see formula (7)].

4. MAPPING WITH THE CT

In the quasi-adiabatic model, reversible fluctuations of the quasi-magnetic moment μ^* can be reduced to nearly zero and irreversible fluctuations can be reduced to the jump $\Delta\mu^*$ in the equatorial plane of a dipole trap. Such a piecewise constant behavior of the conserved quantity μ^* makes it possible to pass over in a natural way to a discrete model of particle motion, specifically, a model based on the mappings that approximate the Poincaré mapping. The approximating mapping is constructed in the equatorial plane using the pitch angle α–phase φ variables in the LCS. In addition, we use the quasi-pitch angle α^*–gyrophase ϕ variables in the coordinate system associated with the direct CT ($CSCT_1$) and in the coordinate system associated with the reverse CT ($CSCT_2$).

The successive steps in the iterative procedure for constructing the mapping are as follows.

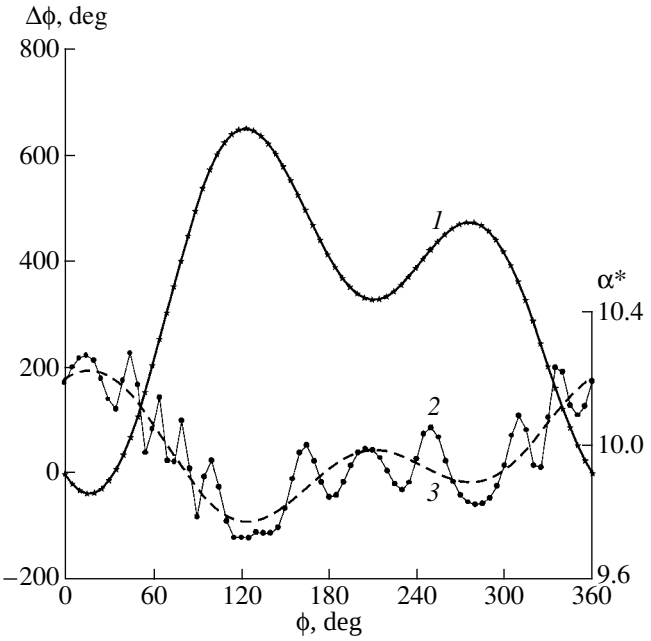

Fig. 5. Dependence of (*1*) the phase accumulation $\Delta\phi$ and (*2*) the quasi-pitch angle α^* on the initial phase ϕ over one-half of the bounce period for $\chi = 0.273$ and $\alpha^* = 10°$.

(i) Let the particle coordinates be specified in the LCS: α_i and φ_i (where $i = 1, \ldots, N$ is the number of the iteration step).

(ii) The coordinates $(\alpha_0)_1$ and $(\varphi_0)_1$ of the origin of the $CSCT_1$ in the LCS and the quasi-pitch angle α_i^* are determined from the solution to Eqs. (8), (9), (12), and (15).

(iii) The coordinates ϕ_i in the $CSCT_1$ are calculated from relationship (13).

(iv) According to the quasi-adiabatic model, the particle that starts from the equatorial plane at the angles α_i^* and ϕ_i in the $CSCT_1$ will be reflected and will reach the equator at the angles α_{i+1}^* and ϕ_{i+1} in the $CSCT_2$:

$$\alpha_{i+1}^* = \alpha_i^* + \Delta\alpha_i^*, \quad \phi_{i+1} = \phi_i + \Delta\phi_i,$$

where $\Delta\alpha_i^*$ and $\Delta\phi_i$ are determined from expressions (17) and (16), respectively.

(v) The coordinates of the origin of the $CSCT_2$ are determined from α_{i+1}^* using Eqs. (8), (9), and (15), in which case $(\varphi_0)_2 = \pi - (\varphi_0(\chi_{\text{eff}}(\alpha_{i+1}^*)))$.

(vi) Finally, the coordinates α_{i+1} and φ_{i+1} in the LCS are calculated from relationships (12) and (13). Then, the procedure may be repeated starting with step (i).

This iterative procedure, although fairly involved, provides single-valued mappings and can be implemented as a computer algorithm. Simulations of particle dynamics with the help of computer programs implementing this algorithm showed that the particles

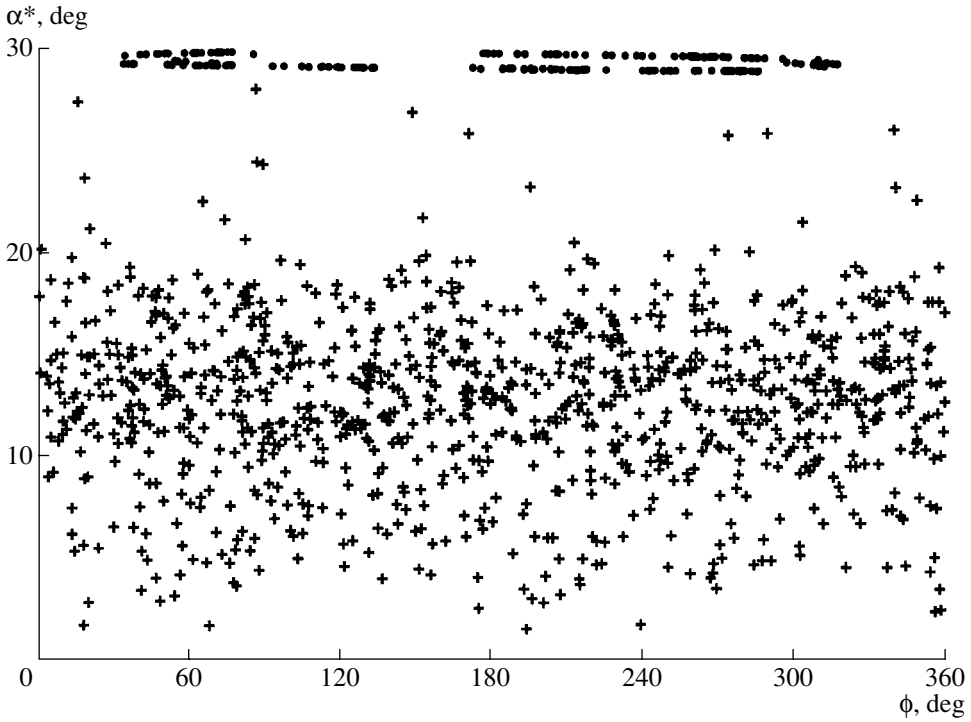

Fig. 6. Phase diagrams of the particles for $\chi = 0.18$. The circles and crosses are for the particles in the states of stable and stochastic motions, respectively.

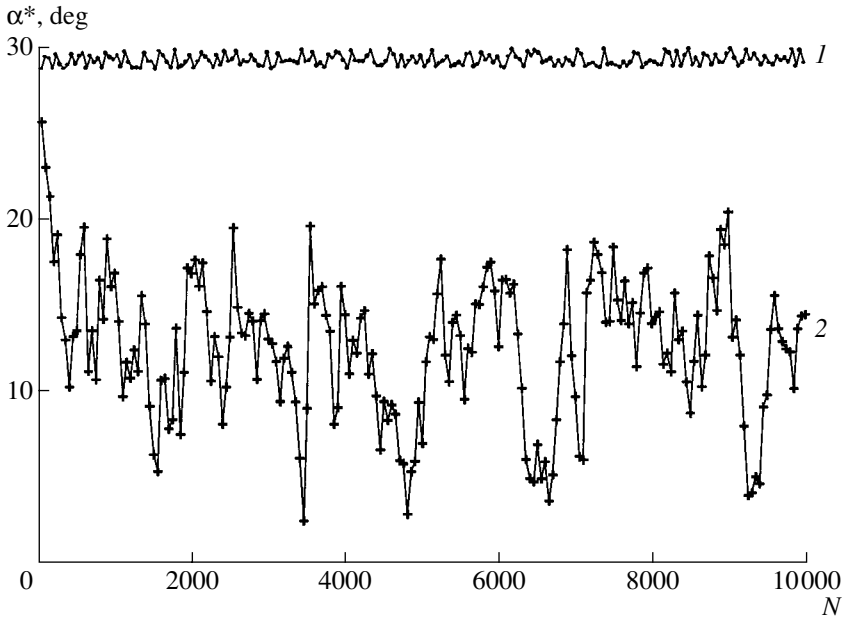

Fig. 7. Dependence of the quasi-pitch angle α* on the number *N* of the iteration step. Curves *1* and *2* are for the states of stable and stochastic motions, respectively.

keep their state of motion even after 10^6 iterations. There are two states of particle motion: the stochastic state, in which the quasi-pitch angle α* and, accordingly, the quasi-magnetic moment μ* change in a jumplike manner from one iteration step to another, and the stable state, in which the quasi-pitch angle α* is conserved. Figure 6 shows the phase diagrams of two particles with $\chi = 0.18$ in these two states of motion. Figure 7 shows the time dependence of the quasi-pitch angle for these particles, specifically, the dependence of

α^* on the number N of the iteration step, i.e., on time (shown are the points obtained after every 50 iterations).

In the range $0.1 < \chi < 0.3$, the boundary between these states of motion is described by the approximate expression

$$\alpha^* = \arcsin[0.486\chi^{-2}\exp(-0.615/\chi)]. \quad (18)$$

The width of this boundary is determined by the spread in the initial ϕ values and does not exceed 1°.

The mapping constructed is not canonical because its Jacobian is $\frac{\partial(\alpha^*_{i+1}, \phi^*_{i+1})}{\partial(\alpha^*_i, \phi^*_i)} \neq 1$. In our opinion, this stems from the approximate character of the mapping. On the other hand, an analysis of the long-term dynamics of the parameters α^* and ϕ shows that the phase volume occupied by the particle is essentially conserved.

We emphasize that it is precisely by using the effective value χ_{eff} of the adiabaticity parameter and by taking into account the modulation of $\alpha^*(\phi)$ [see expression (17)] that we were able to construct a stable mapping, i.e., to achieve the situation in which the particles keep their state of motion for a long time.

5. RESONANT PROCESSES

That the magnetic moment μ in a magnetic trap is not conserved is explained, according to [4], by the resonant interaction between particle oscillations associated with different degrees of freedom, primarily, between cyclotron gyration and longitudinal bounces of the particles. These resonant processes were considered in [13] for a dipole trap under the assumption of particle gyration about the magnetic field lines. According to the quasi-adiabatic model, the cyclotron gyration should be described using the quasi-pitch angle α^*. Near the boundary of the region of stochastic motion, the most important resonant processes are those for which $\bar{\omega}_1 - 2n\omega_2 = 0$, where $\bar{\omega}_1$ is the gyrofrequency averaged over the period $T_2 = 2\pi/\omega_2$ of longitudinal bounces and n is the order of the resonance. Note that the frequency ω_2 depends on the α^* value in the equatorial plane. In accordance with [13], we have

$$n = \frac{3F(\alpha^*)}{\pi\chi}, \quad (19)$$

where $F(\alpha^*)$ is determined from expression (16). From formula (19), we can calculate the angular distance $\Delta\alpha^*(n)$ between the neighboring resonance lines. On the other hand, the mean amplitude of the fluctuations of the quasi-pitch angle α^* that are associated with the nonadiabatic character of particle motion is equal to

$$\Delta\alpha^* = 0.185(14 - \sin^2\alpha^*)/\cos^2\alpha^* \exp(-\psi(\alpha^*)/\chi).$$

When $\Delta\alpha^*(n)$ is larger than $\Delta\alpha^*$, the phase oscillations of the particles in the vicinity of the resonance are stable. Otherwise, the resonances overlap and the particles are in the state of stochastic motion. Figure 8 illustrates the results calculated from formula (19), specifically, the resonance curves and the boundary that separates the regions of steady and stochastic particle motions and is governed by the overlapping of resonances. Also shown in Fig. 8 is the relevant boundary calculated from expression (18). Note that, for $\chi < 0.07$, the resonances do not overlap regardless of the value of the pitch angle, indicating that the particle motion is absolutely stable.

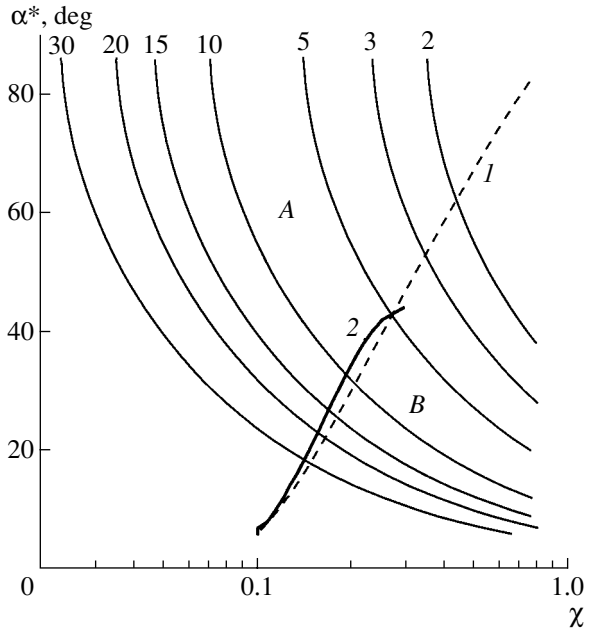

Fig. 8. Resonance curves and boundaries of the region of stochastic motion. Numerals above the curves refer to the order n of the resonance. Curve *1* is the boundary determined by the overlapping of resonances and curve *2* is calculated from expression (18). Regions *A* and *B* correspond to stable and stochastic particle motions, respectively.

In our opinion, a good coincidence of these boundaries indicates that the quasi-adiabatic model and the corresponding mapping provide an adequate description of particle dynamics in a dipole magnetic trap.

The boundary between the regions of stable and stochastic motions depends not only on the adiabaticity parameter χ but also on the quasi-pitch angle α^*. The dependence on the quasi-pitch angle determines, in particular, the maximum energy of the deeply trapped, anomalous cosmic ray ions (primarily, oxygen ions) that are accelerated in the heliosphere in the charge state $Q = 1(2)$, penetrate into the Earth's magnetosphere, and are completely stripped of their electrons in the outer atmospheric layers [14]. An analysis of the experimental data on the fluxes of oxygen ions in the Earth's radiation belts show that the boundary of the region of stable ion motion corresponds to the range of χ values from 1/9 to 1/7 [15]. This conclusion agrees well with our results, especially if we take into account

the fact that the geomagnetic field near the Earth, being as a whole nearly dipolar, at the same time has nondipole components and varies in time.

The quasi-adiabatic model can also be efficiently utilized to describe another magnetic configurations. In particular, the quasi-adiabatic approach was applied to study particle dynamics in a geomagnetic trap whose magnetic field was described with allowance for the contribution from external current systems. In the zone of the quasi-dipolar field, the experimentally obtained boundary of the region where the particle motion is adiabatic corresponds to the boundary determined from the break in the CT in the equatorial plane [16].

6. CONCLUSION

The quasi-adiabatic model of particle motion in a dipole magnetic field has been developed based exclusively on the analysis of the results of numerical integration of the equations of motion. Approximating the GC trajectory by the CT made it possible to automatically take into account the effects associated with both particle drift around the dipole and the deviation of the GC trajectory from a magnetic field line. This approach allowed us to construct a mapping that approximates the Poincaré mapping and to model the long-term dynamics of a particle. The calculated boundary of the region of stable particle motion, on the one hand, coincides with the boundary determined from the model of the resonant interaction between cyclotron gyration and longitudinal bounces of a particle and, on the other hand, correlates reasonably well with the experimental data on charged particles in the Earth's radiation belts.

ACKNOWLEDGMENTS

The present paper is dedicated to the memory of Vladislav Dmitrievich Il'in (1932–1996), who contributed importantly to the development of the quasi-adiabatic model. This work was supported in part by the Russian Foundation for Basic Research, project no. 00-02-16404.

REFERENCES

1. H. Alfven and C.-G. Falthammar, *Cosmical Electrodynamics* (Clarendon, Oxford, 1963; Mir, Moscow, 1967).
2. T. Northrop, *The Adiabatic Motion of Charged Particles* (Interscience, New York, 1963; Atomizdat, Moscow, 1967).
3. D. V. Sivukhin, in *Reviews of Plasma Physics*, Ed. by M. A. Leontovich (Gosatomizdat, Moscow, 1963; Consultants Bureau, New York, 1963), Vol. 1.
4. B. V. Chirikov, in *Reviews of Plasma Physics*, Ed. by B. B. Kadomtsev (Énergoatomizdat, Moscow, 1984; Consultants Bureau, New York, 1987), Vol. 13.
5. I. V. Amirkhanov, E. P. Zhidkov, A. N. Il'ina, V. D. Il'in, S. N. Kuznetsov, and B. Yu. Yushkov, Izv. Akad. Nauk SSSR, Ser. Fiz. **52**, 2422 (1988) [Bull. Acad. Sci. USSR, Phys. Ser. **52**, 129 (1988)].
6. I. V. Amirkhanov, A. N. Il'ina, V. D. Il'in, and B. Yu. Yushkov, Kosm. Issled. **29**, 282 (1991).
7. I. V. Amirkhanov, A. N. Il'ina, V. D. Il'in, I. V. Il'in, S. N. Kuznetsov, and B. Yu. Yushkov, Zh. Éksp. Teor. Fiz. **104**, 2721 (1993) [JETP **77**, 246 (1993)].
8. C. Stormer, *The Polar Aurora* (Clarendon, Oxford, 1955).
9. A. J. Dragt, Rev. Geophys. **3**, 255 (1965).
10. S. F. Singer, Phys. Rev. Lett. **3**, 188 (1959).
11. V. D. Il'in, A. N. Il'ina, and B. Yu. Yushkov, Fiz. Plazmy **23**, 397 (1997) [Plasma Phys. Rep. **23**, 367 (1997)].
12. V. D. Il'in and A. N. Il'ina, Zh. Éksp. Teor. Fiz. **75**, 518 (1978) [Sov. Phys. JETP **48**, 259 (1978)].
13. V. D. Il'in, I. V. Il'in, and S. N. Kuznetsov, Kosm. Issled. **24**, 88 (1986) [Cosmic Res. **24**, 75 (1986)].
14. S. N. Kuznetsov and B. Yu. Yushkov, Adv. Space Res. **27**, 631 (2001).
15. A. J. Tylka, P. R. Boberg, and J. H. Adams, Jr., Adv. Space Res. **17**, 42 (1996).
16. S. N. Kuznetsov and A. Yu. Rybakov, Vestn. Mosk. Univ., Ser. 3: Fiz., Astron., No. 5, 47 (2000).

Translated by I. Kalabalyk

Plasma Physics Reports, Vol. 28, No. 4, 2002, pp. 351–358. Translated from Fizika Plazmy, Vol. 28, No. 4, 2002, pp. 384–391.

BEAMS IN PLASMA

Nonlinear Interaction of an Annular Electron Beam with Azimuthal Surface Waves

V. O. Girka and S. Yu. Puzyr'kov

Karazin National University, pl. Svobody 4, Kharkov, 61077 Ukraine

e-mail: girka@pem.kharkov.ua

Received April 24, 2001

Abstract—A nonlinear theory is developed that describes the interaction between an annular electron beam and an electromagnetic surface wave propagating strictly transverse to a constant external axial magnetic field in a cylindrical metal waveguide partially filled with a cold plasma. It is shown theoretically that surface waves with positive azimuthal mode numbers can be efficiently excited by an electron beam moving in the gap between the plasma column and the metal waveguide wall. Numerical simulations prove that, by applying a constant external electric field oriented along the waveguide radius, it is possible to increase the amplitude at which the surface waves saturate during the beam instability. The full set of equations consisting of the wave-envelope equation, the equation for the wave phase, and the equations of motion for the beam electrons is solved numerically in order to construct the phase diagrams of the beam electrons in momentum space and to determine their positions in coordinate space (in the radial variable–azimuthal angle plane). © *2002 MAIK "Nauka/Interperiodica".*

1. INTRODUCTION

Active research on hybrid waveguide structures during the last 15 years has been motivated by the demand for continuously tunable (over a broad frequency range) and relatively small-scale microwave oscillators and amplifiers in modern-day radio engineering and electronics. The term "hybrid waveguide structures" refers to plasma-filled metal waveguides, in which the plasma serves to neutralize the space charge of the transported beams. The plasma also affects the dispersion properties of such waveguide structures. The waveguide walls may be protected by dielectric coatings, and the waveguide itself may have a certain slow-wave system. Thus, the waveguide walls may be corrugated, which makes it possible to lower the phase velocity of the eigenmodes of the waveguide and, accordingly, to enhance their interaction with charged particle beams. Various aspects of the problem of the interaction between electron beams and the eigenmodes of hybrid waveguides were investigated in [1–3].

Interest in studying the beam–plasma interaction stems primarily from the potential importance of the results obtained in this field, because they are expected to have a broad range of applications: from the beam heating of plasmas in controlled fusion devices [4] and geophysical experiments in space [5, 6] to solving the problems in plasma electronics. Our theoretical paper is devoted to investigating one of the problems of plasma electronics [7, 8], namely, the problem of the interaction between charged particle beams and the eigenwaves of the plasma waveguide. Here, we develop a nonlinear model of a fairly small-scale hybrid waveguide capable of generating continuously tunable radiation over a broad frequency range.

Among the issues that have been studied in considerable detail are the conditions for the onset of beam instabilities and the nonlinear interaction of charged particle beams with plasmas in an infinitely strong external magnetic field (a one-dimensional model) and in a magnetic field of finite strength. The effect of the spectra of the generated waves on the nature of the beam–plasma interaction has also been analyzed quite thoroughly, but without allowance for the effect of plasma boundaries [9, 10]. However, the finite plasma dimensions not only change the excitation dynamics of bulk waves but also provide conditions favorable for the onset of surface waves (SWs) [11].

This study is focused on the above characteristic features of the beam–plasma interaction in hybrid waveguides. Our purpose here is to investigate how an electron beam resonantly excites a surface wave with the extraordinary polarization, which is an eigenmode of a cylindrical metal waveguide partially filled with a cold plasma. The wave under consideration propagates across a constant external axial magnetic field (and, accordingly, along the minor azimuthal angle) and is called an azimuthal SW (ASW) [12]. In the plasma region, the ASW field is described in terms of a superposition of the modified Bessel functions and their derivatives. In the vacuum region, where a low-density electron beam propagates, it is expressed in terms of the first- and second-order Bessel functions [13]. The linear theory of the excitation of an ASW by a beam was constructed in [14]. In that paper, it was shown that the growth rate of the resonant beam-driven instability of

1063-780X/02/2804-0351$22.00

an ASW increases with the azimuthal wavenumber m and there exists an optimum value of m/R_1 (where R_1 is the radius of the plasma column) at which the growth rate of the instability of an ASW is maximum. The dissipative instability of an ASW was studied in [15], where it was found that its growth rate is lower than that of the resonant beam-driven instability of an ASW. The nonlinear theory of the excitation of ASWs by an annular electron beam propagating in the vacuum region surrounding the plasma column in an axial magnetic field under the resonant instability conditions was developed in [16]. Here, we investigate the nonlinear interaction of an ASW with an electron flow in a class of radio engineering devices called magnetrons, which operate with both a constant axial magnetic field and a constant radial electric field.

2. FORMULATION OF THE PROBLEM

It is proposed to excite ASWs in a cylindrical metal waveguide of radius R_2 with a coaxial plasma column of radius R_1. The waveguide is supposed to operate with a gaseous plasma in a thin-walled dielectric vessel or with a semiconductor plasma. The gap between the plasma and the metal waveguide wall is assumed to be small, $R_2 - R_1 \ll R_2$. The density n_b of an annular electron beam rotating in the region $R_1 < r < R_2$ around the plasma column is much lower than the plasma density n_p. The beam rotates in constant crossed magnetic and electric fields. The constant external magnetic field $\mathbf{B}_0$ is oriented along the cylinder axis (the z-axis), and the electric field is directed along the cylinder radius. Such an electric field in the waveguide can be created by auxiliary electrodes, e.g., in the form of thin axial conductors that are built at equal distances into the dielectric vessel filled with a gaseous plasma.

The electrical conductivity of the metal waveguide wall is assumed to be high enough for the tangential component of the electric field of an ASW to satisfy the boundary condition $E_\tau(R_2) = 0$ at the metal surface. In the z direction, the system is assumed to be uniform, so that the electromagnetic perturbations under consideration are independent of the z coordinate.

The desired set of differential equations describing the nonlinear stage of the excitation of an ASW by an electron beam can be obtained from the hydrodynamic equations for the plasma, Maxwell's equations, and the equation of motion for the beam electrons in the region $R_2 > r > R_1$. Since the beam and plasma densities are such that $n_b \ll n_p$, we can neglect both the effect of the beam on the dispersion properties of an ASW and the effect of the self-field of the beam on the electromagnetic field in which the beam propagates.

3. DERIVATION OF THE MODEL EQUATIONS

In the cold plasma approximation, Maxwell's equations can be split into two independent subsets of equations by representing the dependence of the wave field on the time t and the azimuthal angle φ in the form $E, H \propto \exp(im\varphi - i\omega t)$ and assuming that the system at hand is uniform along the z-axis. One of the subsets describes the field of an ASW with the extraordinary polarization. For the magnetic component H_z of the ASW field, it is possible to obtain a second-order differential equation, in which case the components of the wave electric field in a plasma cylinder $r < R_1$ are related to H_z by

$$\frac{\partial^2 H_z}{\partial \xi^2} + \frac{1}{\xi}\frac{\partial H_z}{\partial \xi} - \left(1 + \frac{m^2}{\xi^2}\right)H_z = 0,$$

$$E_r = \frac{\varepsilon_2}{k\varepsilon_1 \psi^2}\frac{\partial H_z}{\partial r} + \frac{mH_z}{kr\psi^2}, \qquad (1)$$

$$E_\varphi = \frac{im\varepsilon_2 H_z}{kr\varepsilon_1 \psi^2} + \frac{i}{k\psi^2}\frac{\partial H_z}{\partial r},$$

where $\xi = kr\psi$, $k = \omega c^{-1}$, c is the speed of light, $\psi^2 = (\varepsilon_2^2 - \varepsilon_1^2)\varepsilon_1^{-1}$, and ε_1 and ε_2 are the components of the dielectric tensor of a cold magnetized plasma (see, e.g., [11]).

In the plasma region, the solution to Eqs. (1) for the H_z component of the ASW field is expressed in terms of the modified Bessel functions $I_m(\xi)$ and the solutions for the E_r and E_φ field components are represented as linear combinations of the functions $I_m(\xi)$ and their derivatives $I_m'(\xi)$ with respect to the argument. The corresponding boundary condition on these solutions implies that the ASW field is finite at the waveguide axis ($r = 0$).

In the beam region, the ASW field is described by the following set of differential equations, which differ from Eqs. (1):

$$\frac{\partial^2 H_z}{\partial \zeta^2} + \frac{1}{\zeta}\frac{\partial H_z}{\partial \zeta} - \left(1 - \frac{m^2}{\zeta^2}\right)H_z = F_b,$$

$$E_r = \frac{4\pi}{i\omega}j_r - \frac{mH_z}{\zeta}, \qquad (2)$$

$$E_\varphi = \frac{4\pi}{i\omega}j_\varphi - i\frac{\partial H_z}{\partial \zeta},$$

where

$$F_b = -\frac{4\pi}{\omega\zeta}\left[\frac{\partial}{\partial \zeta}(j_\varphi \zeta) - imj_r\right], \quad \zeta = kr,$$

$$j_r = -|e|\sum_{i=1}^{N}\delta(r-r_i)\delta(\varphi-\varphi_i)\frac{\partial r}{\partial t},$$

$$j_\varphi = -|e|\sum_{i=1}^{N} r\delta(r-r_i)\delta(\varphi-\varphi_i)\frac{\partial \varphi}{\partial t},$$

and δ is the delta function.

Equations (2) were solved by the method of variation of a constant. The components of the ASW field in the region $R_1 < r < R_2$ are expressed in terms of the Bessel functions of the first kind $J_m(\zeta)$, the Neumann functions $N_m(\zeta)$, their derivatives with respect to the argument, and the components j_r and j_φ of the beam current density.

In order to derive the wave-envelope equation and the equation for the wave phase, we turn to the following boundary conditions: (i) the tangential electric field of an ASW vanishes at the metal surface of the waveguide wall, $E_\varphi(R_2) = 0$; (ii) the field component E_φ is continuous at the plasma boundary $r = R_1$, $\{E_\varphi(R_1)\} = 0$; and (iii) there are no currents at the metal surface of the waveguide wall and at the plasma–vacuum interface, $j_\varphi(R_1) = j_\varphi(R_2) = 0$.

Neglecting the dissipative processes in the plasma and using the standard procedures for averaging and singling out the slow time (see, e.g., [2, 7]), we arrive at the following equations for the envelope and phase of the natural waves excited in the waveguide:

$$\frac{\partial A}{\partial t} = -\frac{\alpha D_p}{NzPL}\sum_{i=1}^{N}\left[\frac{m}{w}\frac{\partial R_i}{\partial t}L_1(\zeta_i)\sin(m\varphi_i+\Theta-\omega t)\right.$$
$$\left. + R_i^2\frac{\partial \varphi_i}{\partial t}L_2(\zeta_i)\cos(m\varphi_i+\Theta-\omega t)\right],$$
$$\frac{\partial \Theta}{\partial t} = -\frac{\alpha D_p}{NzPLA}\sum_{i=1}^{N}\left[R_i^2\frac{\partial \varphi_i}{\partial t}L_2(\zeta_i)\sin(m\varphi_i+\Theta-\omega t)\right. \quad (3)$$
$$\left. - \frac{m}{w}\frac{\partial R_i}{\partial t}L_1(\zeta_i)\sin(m\varphi_i+\Theta-\omega t)\right],$$

where $A = E_y B_0^{-1}$ is the dimensionless amplitude of the wave envelope, Θ is the wave phase, $\alpha = n_b n_p^{-1}$, $z = |\omega_e|\Omega_e^{-1}$, $w = \omega\Omega_e^{-1}$, $R_i = r_i\Omega_e c^{-1}$, ω_e is the electron cyclotron frequency, Ω_e is the electron Langmuir frequency, $L = J_m(\zeta_1)N_m'(\zeta_2) - J_m'(\zeta_2)N_m(\zeta_1)$, $\zeta_1 = kR_1$, $\zeta_2 = kR_2$, $L_1(\zeta_i) = J_m(\zeta_i)N_m'(\zeta_2) - J_m'(\zeta_2)N_m(\zeta_i)$, $L_2(\zeta_i) = J_m'(\zeta_i)N_m'(\zeta_2) - J_m'(\zeta_2)N_m'(\zeta_i)$, $D_p = \frac{I_m'(\psi\zeta_1)}{\psi I_m(\psi\zeta_1)} + \frac{m\varepsilon_2}{\varepsilon_1\psi^2\zeta_1}$, and $P = \frac{d}{dw}\left[D_p + \frac{L_2(\zeta_1)}{L}\right]$.

The equation of motion for the beam electrons can be conveniently written in terms of the electron momentum $\mathbf{p} = \gamma m_e\mathbf{V}$ (where γ is the relativistic factor):

$$\frac{d\mathbf{p}}{dt} = e\mathbf{E} + e\mathbf{E}_0 + \frac{e}{c}[\mathbf{V}\times(\mathbf{H}+\mathbf{B}_0)]. \quad (4)$$

Substituting the ASW field components calculated in the region $R_1 < r < R_2$ yields the following set of equations for the ith electron:

$$\frac{\partial R}{\partial t} = |\omega_e|\frac{v_i}{z\gamma_i}, \quad \frac{\partial \varphi_i}{\partial t} = |\omega_e|\frac{u_i}{z\gamma_i R_i} + |\omega_e|\frac{\varepsilon}{zR_i},$$
$$\frac{\partial v_i}{\partial t} = -|\omega_e|\frac{u_i}{\gamma_i}\left(1-\frac{u_i}{zR_i}\right) + |\omega_e|\varepsilon$$
$$+ AR_1\left(\frac{m}{R_1} - w\frac{u_i}{\gamma_i}\right)\left(\frac{1}{\zeta_1 D_p} - R_\alpha\right)\sin(m\varphi_i+\Theta-\omega t),$$
$$\frac{\partial u_i}{\partial t} = |\omega_e|\frac{v_i}{\gamma_i}\left(1-\frac{u_i}{zR_i}\right) \quad (5)$$
$$+ \frac{AwR_1}{\zeta_1}\left[R_\alpha - 1 + \frac{R_\alpha}{D_p}\left(\frac{m^2}{\zeta_1}-\zeta_1\right)\right]\cos(m\varphi_1+\Theta-\omega t)$$
$$+ \frac{AwR_1 v_i}{\gamma_i}\left(\frac{1}{\zeta_1 D_p} - R_\alpha\right)\sin(m\varphi_1+\Theta-\omega t).$$

Here, $R_\alpha = r_i R_1^{-1} - 1$, $v = p_r m_e^{-1} c^{-1}$, $u = p_\varphi m_e^{-1} c^{-1}$, and $\varepsilon = E_0/B_0$, where v and u are, respectively, the dimensionless radial and azimuthal momenta of the beam electrons.

Equations (3) and the last two equations in set (5) were derived under the basic assumption that the region where the beam propagates is relatively narrow, $R_2 - R_1 \ll R_1$. This assumption made it possible to significantly simplify these equations by using the asymptotic expansions of the cylindrical Bessel functions and their Wronskians (see, e.g., [13]) and, thus, to substantially reduce a large amount of computer time required for the direct calculation of all cylindrical functions in Eqs. (3) and (5). The nonlinear interaction of an ASW with an annular electron flow was investigated by solving Eqs. (3) and (5) numerically.

4. RESULTS OF NUMERICAL SIMULATIONS OF THE ASW–ELECTRON BEAM INTERACTION

The model set of equations was solved using a fourth-order Runge–Kutta method, which is one of the

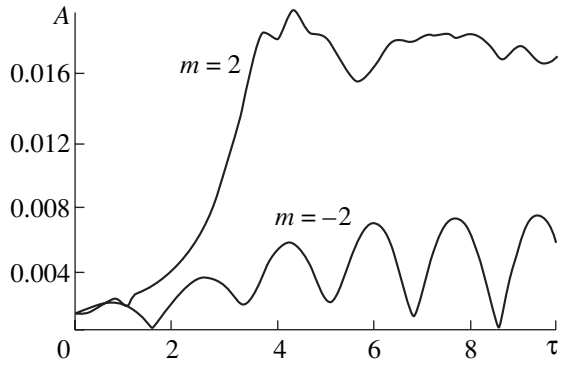

Fig. 1. Dependence of the dimensionless amplitude A of the envelope of two oppositely propagating ASWs (with the azimuthal wavenumbers $m = 2$ and $m = -2$) on the dimensionless time τ.

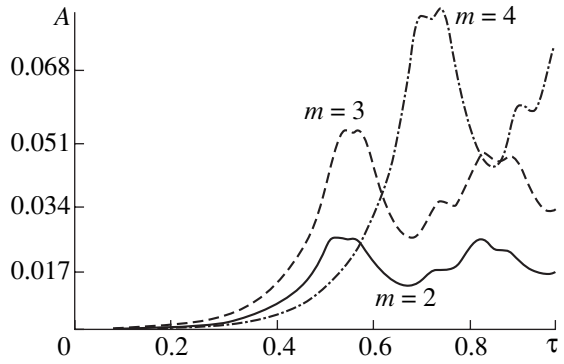

Fig. 2. Dependence of the dimensionless amplitude A of the envelope of three ASWs on the dimensionless time τ. The time evolutions $A = A(\tau)$ for the waves with $m = 2$, $m = 3$, and $m = 4$ are shown by the solid, dashed, the dashed-and-dotted curves, respectively.

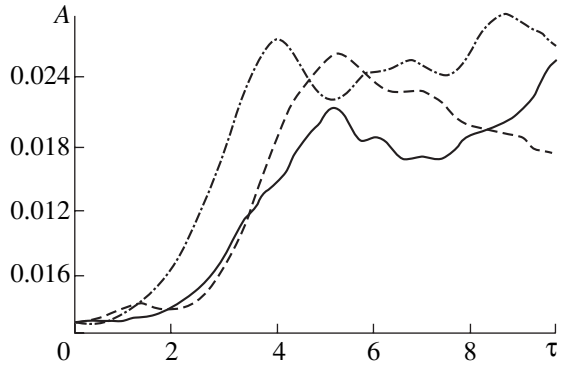

Fig. 3. Effect of the external radial electric field on the development of the beam-driven instability of ASWs. The dimensionless amplitude A of the envelope of ASWs was calculated as a function of the dimensionless time τ for three different values of the parameter $\varepsilon = E_0/B_0$. The solid, dashed, the dashed-and-dotted curves show the time evolutions $A = A(\tau)$ for $\varepsilon = 0$, –0.08, and –0.1, respectively.

best standard methods for numerical integration of differential equations and which makes it possible to reduce the number of computational operations required to calculate their right-hand sides. This circumstance is especially important for the solution of equations whose right-hand sides are very complicated. Fourth-order methods provide high accuracy of the numerical integration of differential equations and are traditionally used to solve the problems of the beam–plasma interaction. The time integration step was varied depending on the rate at which the functions changed during the process of numerical integration.

The number of macroparticles used to model an electron beam was $N = 500$. The interaction of the beam electrons with the plasma boundary and metal waveguide wall was simulated using the mirror reflection model, which implies that the electrons do not disappear in interactions, but rather their radial momenta are reversed by mirror reflection and they are reflected back into the region $R_1 < r < R_2$. This model is frequently used to investigate the interaction of charged particle beams with finite-size plasmas and is best suited for the description of a beam–solid body boundary [11].

The results of numerical simulations of the development of the resonant beam-driven instability of an ASW are illustrated in Figs. 1–8. The simulations were carried out for the following starting values of the waveguide and beam parameters: the wave amplitude was $A = 10^{-3}$, the waves phase was $\Theta = 0$, and the radial momentum of the beam electrons was $v_i = 0$. The geometric parameters of the waveguide were chosen to satisfy the condition $R_2 - R_1 = 0.1R_1$. The initial distribution of the beam electrons over the angle φ was approximately uniform, the random deviation being small, $\Delta\varphi = \pm 1\%$. Over the radius, the beam electrons were initially distributed in a random manner in the spatial region $R_1 + \frac{1}{3}(R_2 - R_1) < r < R_1 + \frac{2}{3}(R_2 - R_1)$. In most of the simulations, the initial angular momentum u_i of the beam electrons was set equal to zR_i, the random deviation being $\pm 2\%$.

As was shown in [14], there is an effective wavenumber $k_{\text{eff}} = mcR_1^{-1}\Omega_e$ for which the growth rate of the beam-driven instability of an ASW is maximum. In the case at hand, the effective wavenumber is approximately equal to $k_{\text{eff}}^* \approx 0.4$. That is why, for simulations, we chose the corresponding values of R_1 for different azimuthal wavenumbers. Our investigation of the question of how the choice of the value of k_{eff} affects the development of the beam instability confirmed the results obtained in [14]. In fact, we found that, if the value of k_{eff} was chosen to differ from k_{eff}^*, the ASW amplitude increased at a slower rate.

From Fig. 1, we can see that the only waves that are excited resonantly are ASWs with positive values of the azimuthal wavenumber m, propagating in the direction in which the beam electrons gyrate in the external axial magnetic field. The waves with $m < 0$ are not excited. The excitation of ASWs is highly sensitive to the beam electron density. A decrease in the beam density by a factor of 2 to 2.5 reduces the wave amplitude in the saturation stage of the instability by a factor of approximately 2, in which case the time required for the instability to saturate becomes longer by about 50%. A decrease in the ratio $|\omega_e|\Omega_e^{-1}$ and an increase in the parameter α shorten the time scale on which the ASW amplitude increases from the initial to the maximum value. The curves in Fig. 1 were obtained for $|\omega_e| = 0.1\Omega_e$ and $n_b = 0.01n_p$.

In the saturation stage of the beam instability, the ASW amplitude increases significantly with increasing azimuthal wavenumber m. Figure 2 illustrates the results of studying the dependence of the ASW amplitude on the m value for $|\omega_e| = 0.01\Omega_e$ and $n_b = 0.01n_p$. It can be seen that, as the azimuthal wavenumber increases from 2 to 3, the amplitude of the ASW increases by a factor of about 2, and an increase in the azimuthal wavenumber from $m = 2$ to $m = 4$ results in an increase in the ASW amplitude by a factor of more than 3.

Figure 3 shows the results of simulations of the nonlinear stage of the beam-driven instability of an ASW in external radial electric fields of different strengths. The values of α and z were chosen to be the same as those in Fig. 1. One can see that applying an external electric field makes it possible to enlarge the fraction of the energy of an annular electron beam that is expended on the excitation of an ASW. Of course, this series of computations was carried out for higher initial momenta of the beam electrons. In the presence of a constant external electric field $\mathbf{E}_0$ directed opposite to $\mathbf{e}_r$, the ASW amplitude in the saturation stage of the resonant beam instability is larger than that in the absence of $\mathbf{E}_0$. Reversing the field $\mathbf{E}_0$ reverses the drift velocity of the beam electrons, thereby significantly affecting the development of the instability of an ASW. The stronger the external electric field so directed, the smaller is the saturating ASW amplitude and the lower is the instability growth rate. Applying a sufficiently strong electric field suppresses the instability.

An increase in the width of the gap between the plasma column and the metal waveguide wall, $R_1 \gg R_2 - R_1 > 0.1R_1$, also unfavorably affects the development of the resonant beam instability. The reasons for this are twofold: the spatial distribution of the ASW field changes and the beam electrons move at a larger distance from the plasma surface, at which the SW amplitude is known to be maximum (see, e.g., [11]).

In order to confirm that the ASW amplitude increases as a result of energy transfer from the beam to the wave, we calculated the time evolution of the sum of the squared momenta of all the beam electrons (this sum determines the beam kinetic energy). According to Fig. 4, the ASW amplitude and the beam kinetic energy change in antiphase: as the wave amplitude increases, the beam electron energy decreases synchronously. Using these data, we can estimate the electron efficiency of the waveguide structure under discussion. For $R_2 - R_1 = 0.1R_1$, the maximum efficiency is about 10%. The curves in Fig. 4 were calculated for $|\omega_e| = 0.01\Omega_e$, $n_b = 0.05n_p$, and $m = 2$.

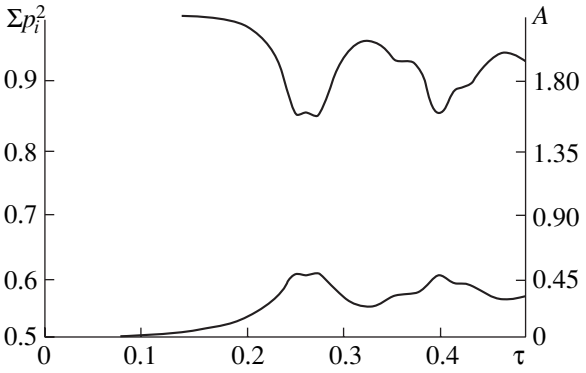

Fig. 4. Illustration of the energy conservation in the wave–beam system. The upper curve shows the time evolution of the dimensionless squared momentum of the beam electrons (left coordinate axis) and the lower curve shows the time evolution of the dimensionless amplitude A of the envelope of ASWs (right coordinate axis).

It is also of interest to investigate the time evolution of the phase diagram of the beam electrons and their spatial distribution. Figure 5 shows the initial distribution of the beam electrons in coordinate space. The electrons are distributed nearly uniformly in the azimuthal angle around the plasma in the middle of the gap between the metal waveguide wall and the plasma cylinder. The distribution to which the initial electron beam evolves over the time interval $\tau = 0.2$ under the action of the growing ASW field is shown in Fig. 6. In the field of an ASW with the azimuthal wavenumber $m = 2$, the spatial distribution of the electrons acquires an elliptical shape. At the same time, we can see the formation of two groups of electrons: under the action of the ASW field, one group is forced to move closer to the inner boundary of the beam ($r = R_1$) and another, to the outer boundary ($r = R_2$).

Figures 7 and 8 depict phase diagrams of the beam electrons in the form of the dependence of the azimuthal momenta of the electrons on their angular coordinates at different times during the development of the beam-driven instability of an ASW. The phase diagram in Fig. 7 was obtained at the time $\tau = 0.2$, at which the ASW amplitude approaches its first maximum (but have not yet reached it). The phase diagram in Fig. 8 refers to the time when the ASW amplitude has already passed its minimum and when the dense bunches

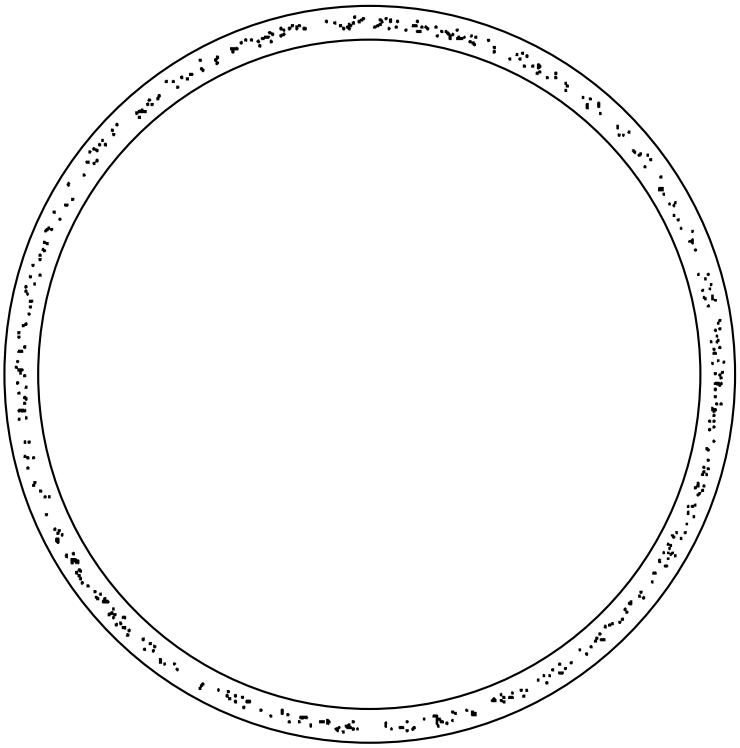

Fig. 5. Distribution of the beam electrons in coordinate space (in the radial variable–azimuthal angle plane) at the initial time $\tau = 0$.

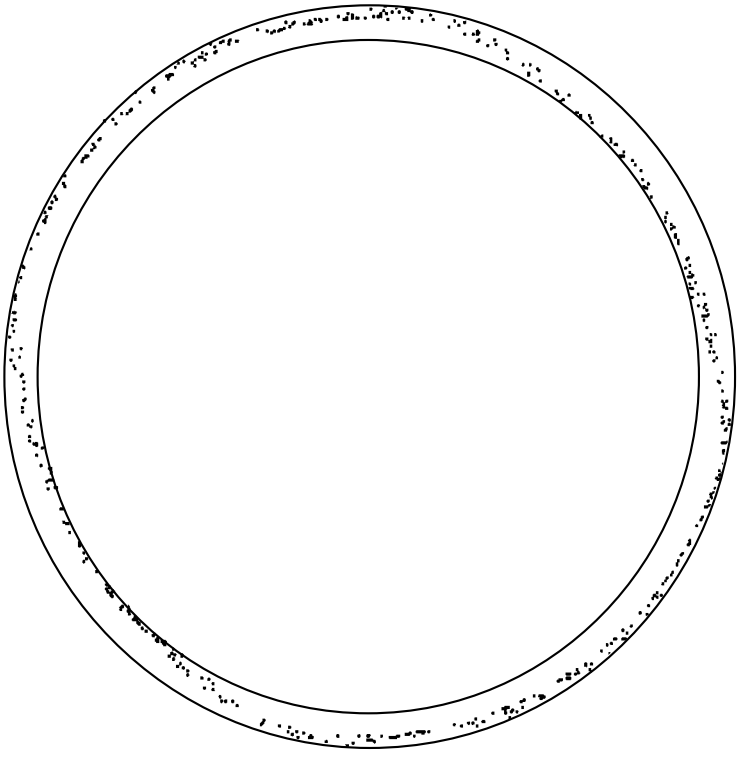

Fig. 6. Distribution of the beam electrons in coordinate space (in the radial variable–azimuthal angle plane) at the time $\tau = 0.555$.

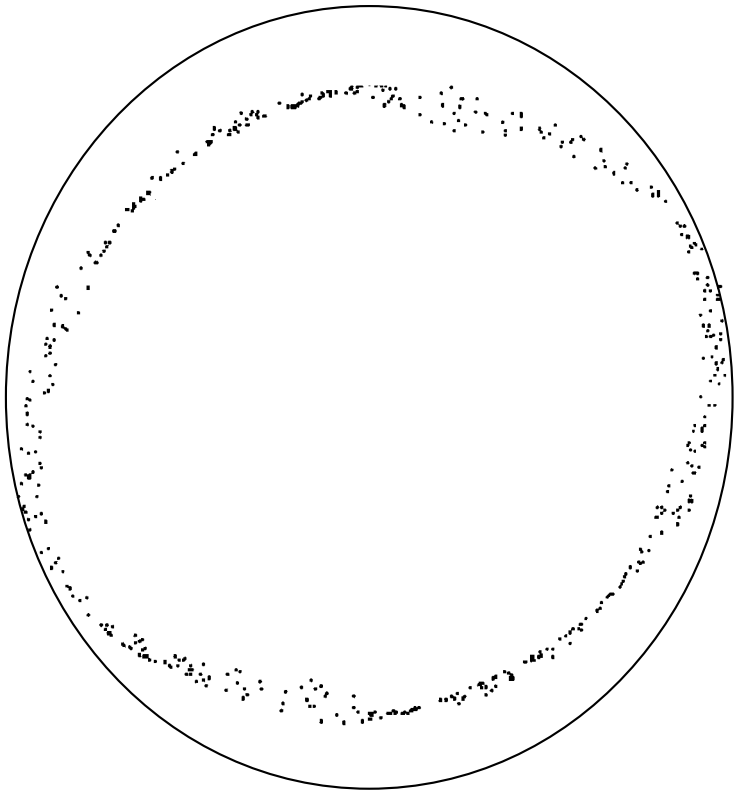

Fig. 7. Distribution of the beam electrons in phase space (in the radial momentum–azimuthal momentum plane) at the time $\tau = 0.555$, at which the ASW amplitude is maximum.

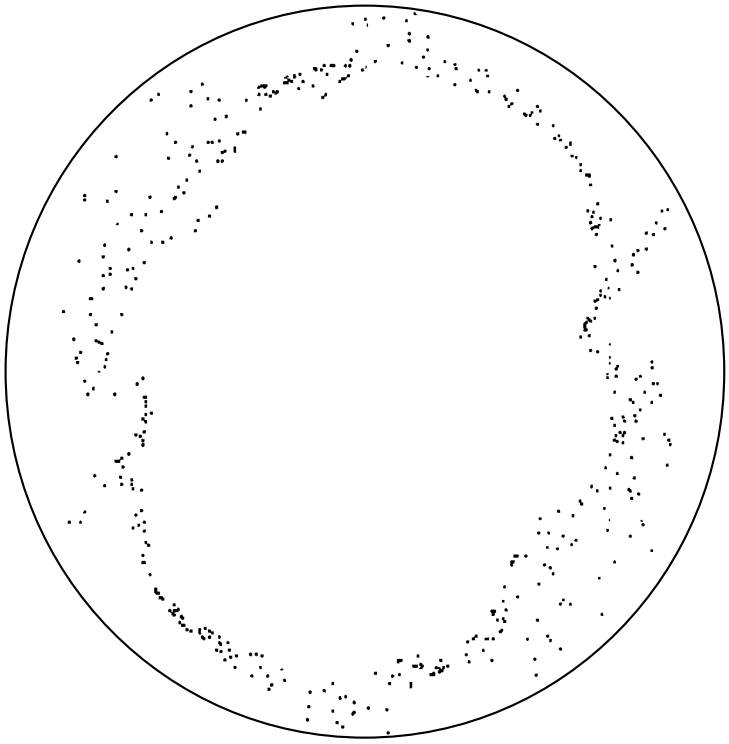

Fig. 8. Distribution of the beam electrons in phase space (in the radial momentum–azimuthal momentum plane) at the time $\tau = 0.624$, at which the beam electrons have already transferred a portion of their energy to the excited wave and have lost their phase synchronism with the wave.

formed by the beam electrons in the regions in which the ASW field is minimum are destroyed. We can see that, at a fixed angular coordinate, the beam electrons have a large spread in the momentum component p_φ. In contrast, in Fig. 7, the spread in the angular momenta at each angular coordinate is very small. The computational results presented in Figs. 5–8 were obtained for $|\omega_e| = 0.01\Omega_e$, $n_b = 0.05n_p$, and $m = 2$.

5. CONCLUSION

We have studied the excitation of ASWs with frequencies in the range $|\omega_e| < \omega < \sqrt{\Omega_e^2 + \omega_e^2/4} - |\omega_e|/2$ by an annular electron beam rotating around the plasma column that partially fills a cylindrical metal waveguide operating with steady-state crossed magnetic (axial) and electric (radial) fields. The resonant beam-driven instability of an ASW has been investigated in the single-mode approximation.

We have derived a two-dimensional model set of equations describing the evolution of the envelope of the wave field, the phases of ASWs, and the coordinates and momenta of the electrons of a low-density beam. We have numerically analyzed the effect of the waveguide and beam parameters on the development of the resonant beam instability. We have shown that changing the sign of the azimuthal wavenumber (or, equivalently, reversing the propagation direction of the ASW) leads to the suppression of the instability. The rate at which ASWs with large azimuthal wavenumbers are excited is high, so that large wave amplitudes are achievable in the saturation stage of the instability. Applying an external radial electric field makes it possible to increase the fraction of the kinetic energy of beam electrons that is transferred to the ASW, provided that the condition for phase synchronization of the ASW with an annular electron beam are satisfied.

The results obtained can be used to develop small-scale devices for radio engineering and electronics and to explain the results obtained from experiments on the excitation of SWs. Finally, we point out the following two characteristic features of the above model of a hybrid waveguide structure excited by an electron beam: first, the eigenfrequency of the structure can be continuously tuned by varying the plasma density and, second, the axial dimensions of the structure are small because the beam interacts with the wave propagating in the azimuthal direction.

REFERENCES

1. A. A. Rukhadze, L. S. Bogdankevich, S. E. Rosinskiĭ, and V. G. Rukhlin, *Physics of High-Current Relativistic Electron Beams* (Atomizdat, Moscow, 1980).
2. M. V. Kuzelev and A. A. Rukhadze, *Electrodynamics of Dense Electron Beams in a Plasma* (Nauka, Moscow, 1990).
3. I. N. Onischenko, V. A. Balakirev, A. M. Korostelev, *et al.*, in *Proceedings of the 11th International Conference on High Power Particle Beams, Prague, 1996*, Vol. 1, p. 426.
4. M. Fujiwara, O. Komeko, A. Komori, *et al.*, Plasma Phys. Controlled Fusion **41** (12B), 157 (1999).
5. É. P. Kontar', V. I. Lapshin, and V. N. Mel'nik, Fiz. Plazmy **24**, 832 (1998) [Plasma Phys. Rep. **24**, 772 (1998)].
6. C. Krafft and A. S. Volokitin, Plasma Phys. Controlled Fusion **41** (12B), 305 (1999).
7. A. N. Kondratenko and V. M. Kuklin, *Foundations of Plasma Electronics* (Énergoatomizdat, Moscow, 1988).
8. R. Ando, V. A. Balakirev, K. Kamada, *et al.*, Fiz. Plazmy **23**, 1042 (1997) [Plasma Phys. Rep. **23**, 964 (1997)].
9. R. C. Davidson and K. I. Tsang, Laser Part. Beams **6**, 661 (1988).
10. R. B. Miller, *Introduction to the Physics of Intense Charged Particle Beams* (Plenum, New York, 1982; Mir, Moscow, 1984).
11. A. N. Kondratenko, *Surface and Bulk Waves in Bounded Plasma* (Énergoatomizdat, Moscow, 1985).
12. V. A. Girka, I. A. Girka, A. N. Kondratenko, and V. I. Tkachenko, Radiotekh. Élektron. (Moscow) **33**, 1031 (1988).
13. D. S. Kuznetsov, *Special Functions* (Vysshaya Shkola, Moscow, 1968).
14. V. A. Girka, I. A. Girka, V. P. Olefir, and V. I. Tkachenko, Pis'ma Zh. Tekh. Fiz. **17** (1), 81 (1991) [Sov. Tech. Phys. Lett. **17**, 35 (1991)].
15. V. A. Girka, I. A. Girka, and V. I. Tkachenko, Zh. Tekh. Fiz. **66** (4), 114 (1996) [Tech. Phys. **41**, 357 (1996)].
16. V. A. Girka, A. M. Kondratenko, and A. E. Sporov, Zh. Tekh. Fiz. **69** (7), 84 (1999) [Tech. Phys. **44**, 814 (1999)].

Translated by I. Kalabalyk

Plasma Physics Reports, Vol. 28, No. 4, 2002, pp. 359–366. Translated from Fizika Plazmy, Vol. 28, No. 4, 2002, pp. 392–400.

LOW-TEMPERATURE PLASMA

Scanning Calorimetry Measurements of the Energy Parameters of a Plasmochemical Polymer Oxidation Reaction

A. N. Magunov

Institute of General Physics, Russian Academy of Sciences, ul. Vavilova 38, Moscow, 117942 Russia

Received September 10, 2001; in final form, October 10, 2001

Abstract—The contributions of heat fluxes of different nature to the total heat flux from a weakly ionized oxygen plasma of a low-pressure (20–120 Pa) RF discharge onto the calorimeter surface, on which a chemical reaction between atomic oxygen and a polymer proceeds, are distinguished. The activation energy ($\Delta E \approx 0.37$ eV), the reaction heat ($H \approx 27$ kJ/g), and the rate constant for heat release in a surface plasmochemical reaction are determined.© *2002 MAIK "Nauka/Interperiodica".*

1. INTRODUCTION

Indirect methods based on analyzing the plasma chemical composition with the help of optical spectroscopy or mass spectrometry [1] are widely used to investigate surface plasmochemical reactions. Studying the plasmochemical processes directly on the surface is a rather difficult problem because of the low thickness of the surface layer (~10 nm) in which the reaction goes on.

It is known that chemical reactions are related not only to the particle conversion, but also to the energy transformation, whose rate is proportional to the reaction rate. Macrokinetics of a surface plasmochemical process can be studied by measuring the rate dT/dt at which the sample temperature varies, i.e., the heat power released or absorbed in the reaction zone [2]. A preliminary task is to distinguish the contributions from different heat sources: the heat power fraction related to the surface plasmochemical reaction is to be resolved against the background of heat transfer from the discharge.

In this study, differential scanning calorimetry [3] is used to quantitatively investigate the kinetics of plasmochemical polymer etching in a plasma of a low-pressure RF discharge in oxygen. The contributions of heat fluxes from the sources of different nature on the plasma–surface interface are distinguished. The main energy characteristics of the reaction are determined.

2. TEMPERATURE SCANNING

Differential scanning calorimetry in a discharge (SCD) consists in permanently measuring heat power transferred to a calorimeter, provided that its temperature varies in time in a known manner determined by the heat flux from the discharge. The measurement of the non-steady-state temperature $T(t)$ is simultaneously the measurement of the power $P = cm(dT/dt)$, where c and m are the specific heat capacity and mass of the calorimeter. Continuously changing the calorimeter temperature in the discharge can be regarded as scanning over the temperature, in the course of which the powers of heat fluxes transferred to the surface via different heat exchange mechanisms change.

At pressures of ≥10 Pa and low degrees of ionization (≤10^{-5}–10^{-6}), the main heat transfer mechanism ensuring temperature scanning is gas heat conduction and the energy relaxation of the particle translational (and, possibly, rotational) degrees of freedom in collisions with a surface [4]. The dependence $T(t)$ is nonlinear. For a plane inert calorimeter with the thickness h, in the absence of radiative heat exchange, this dependence takes the form

$$T(t) = T_g - (T_g - T_0)\exp(-2\alpha t/c\rho h), \qquad (1)$$

where T_g is the gas temperature in the discharge (beyond the thermal boundary layer), T_0 is the calorimeter initial temperature, α is the heat transfer coefficient (proportional to the heat conductivity), and ρ is the material density. According to formula (1), the temperature dependence of the power density $D = P/S$ (where S is the area of the calorimeter surface) is linear,

$$D(T) = 2\alpha(T_g - T), \qquad (2)$$

where α is independent of T (as was experimentally established in [4], this is valid at gas pressures on the order of 1 torr). The catalytic inertia of the calorimeter is ensured by depositing thin films made of materials for which the relaxation probability of the particle excited states in collisions with the surface is very low (no higher than 10^{-4}). In particular, water vapor adsorbed on the surface significantly reduces its catalytic activity; even in a discharge, the removal of water vapor from the surface takes a long time (in our experiments, this time exceeded 100 s [5]). It is also necessary that the surface be chemically inert with respect to any particles generated in the discharge. When deriving formulas (1) and (2), it was assumed that heat transfer

1063-780X/02/2804-0359$22.00

by charged particles can be ignored, because, at low degrees of ionization, the contribution of charged particles to the heat flux is negligible.

The quantity α depends on neither the surface material nor the presence/absence of the adsorbed surface layers, provided that the condition of continual heat exchange, $\mathrm{Kn} \cdot \mathrm{Nu} \ll \gamma$, is satisfied (here, $\mathrm{Kn} = \lambda_p / L$ is the Knudsen number, λ_p is the gas particle mean free path, L is the calorimeter characteristic size, $\mathrm{Nu} = \alpha L/\lambda$ is the Nusselt number, λ is the gas thermal conductivity, and γ is the coefficient of thermal accommodation of the particle kinetic energy in collisions with the surface) [6]. At a calorimeter size of about 1 cm, this condition is satisfied at a gas pressure of $p \geq 10$ Pa. Both parameters (α and T_g) in formula (2) are determined from the heating kinetics of the inert calorimeter. The limiting stage of this heat exchange mechanism is energy transfer through the thermal boundary layer.

In the case of a chemically and catalytically inert calorimeter, the linear behavior of the $D(T)$ dependence allows one to consider it as a base line, with respect to which the onset of additional heat sources or sinks related to plasmochemical reactions on the surface can be recorded. The calorimeter heat capacity must be sufficiently high for its heating time to be significantly longer than the relaxation time of the discharge parameters.

3. HEAT RELEASE IN A PLASMOCHEMICAL REACTION

We suppose that, on one of the surfaces of a plane calorimeter, an exothermic plasmochemical reaction proceeds, whose rate is determined by an Arrhenius temperature dependence. Since the reaction rate is directly related to the heat release rate, the temperature dependence of the specific power released in the reaction is also described by the Arrhenius dependence:

$$D_r = HZ\exp(-\Delta E/kT), \tag{3}$$

where H [J/g] is the reaction heat (at $H > 0$, the reaction is exothermic, whereas, at $H < 0$, it is endothermic); Z [g/(cm^2 s)] is the preexponential factor, having the dimension of the reaction rate; and ΔE is the activation energy. In the simplest case, the non-steady-state equation of the heat balance of an active calorimeter is

$$D_1 = c\rho h(dT_1/dt) = D_g + D_r - D_e, \tag{4}$$

where D_1 is the total power density spent on the calorimeter heating, D_g is determined by formula (2), D_r is determined by formula (3), and D_e is the power density of the radiative cooling of the calorimeter.

The heat balance equation of an inert calorimeter is

$$D_2 = c\rho h(dT_2/dt) = D_g - D_e. \tag{5}$$

Let us assume the total thermal flux toward the calorimeter to be the sum of independent fluxes related to different heat exchange mechanisms. Apparently, ion bombardment (which causes the sputtering of adsorbed layers and the creation of active sites on the surface) can violate the additivity and lead to the synergism of the heat fluxes. However, at low degrees of ionization, at the floating potential of the surface (approximately equal to –10 V), and in the drift mode of ion motion in the near-surface layer, such an influence is unlikely to occur and, thus, is not taken into account in Eq. (4).

The left-hand side of Eq. (4) is determined by differentiating the measured non-steady-state temperature of the calorimeter. To determine $D_r(T)$, we need to determine the $D_g(T)$ and $D_e(T)$ dependences. Under the condition $D_g(T)$, the $D_e(T) \ll D_g(T)$ dependence can be determined based on the heating kinetics of an inert calorimeter using Eq. (5). For a silicon calorimeter, this condition is satisfied at $T \leq 200$–250°C. The power of radiative heat removal is determined from the calorimeter cooling kinetics after switching off the discharge.

To determine the reaction heat it is necessary to integrate D_r over a time period during which the chemical reaction on the active calorimeter surface goes on. In the experiment, only the δH (where $0 \leq \delta \leq 1$) fraction of the total reaction heat transferred to the calorimeter is determined. The rest of the energy (equal to $(1 - \delta)H$) is carried away with the reaction products. To find δH, the mass of the substance involved in the reaction must be determined. For this purpose, it is enough to weigh the calorimeter before and after the discharge, because the reaction products go away from the surface to the gas phase. Then, we can determine the reaction heat fraction transferred to the calorimeter:

$$\delta H = \frac{\int_0^{t_e} [c_{Si}\rho_{Si}h_{Si}(dT_1/dt) - 2\alpha(T_g - T_1) + (D_e)_1]dt}{\rho_f \int_0^{t_e} (dh_f/dt)dt}, \tag{6}$$

where the *Si* index denotes the calorimeter, the *f* index indicates the film of the reacting material, and the integration limit t_e is equal to the time required for the complete removal of the film from the surface.

The geometry of the experiment with a finite-size plane calorimeter in a plasma is not one-dimensional; hence, it is necessary to control the reaction rate homogeneity over the calorimeter surface. The inhomogeneity of the reaction rate may be related to the inhomogeneity of the flux density of chemically active particles arriving at the calorimeter surface from the discharge (the flux density near the calorimeter edge is higher than in the geometrical center of the calorimeter). The second probable reason for the reaction rate inhomogeneity is in the temperature inhomogeneity over the calorimeter surface. If a small-sized semiconductor single

crystal is used as a calorimeter, the temperature inhomogeneity is unimportant because of the high thermal conductivity of the crystal.

4. EXPERIMENT

We studied the plasmochemical etching of a 1- to 2-μm polymer film deposited on the surface of a silicon calorimeter (a square single crystal with an area of 6 cm^2 and a thickness of ~0.5 mm). The polymers used—phenolformaldehyde resin (PFR) and polyimide (PI)—are widely employed in microtechnology as protective masks in producing integrated microcircuits. The polymer film was deposited on the crystal surface from the solution with the help of a centrifuge with a subsequent drying and thermal treatment. The film thickness was determined using a Linnik microinterferometer and also by transmission spectrum interferograms in the wavelength range 2–25 μm (the spectrum was recorded using a Bruker IFS-88 IR Fourier-transform spectrometer). The methods for the film deposition and controlling the film thickness are standard in microtechnology [7]. The PFR vitrification temperature lies in the range $T \le 120$°C; in the temperature range 150–300°C, the polymer undergoes thermal destruction, whose activation energy is ~1.5 eV. PI is more thermostable; the loss of mass due to thermal destruction begins at $T \ge 400$–450°C.

Etching was performed in a cylindrical 45-cm-long quartz reactor 20 cm in diameter. A capacitive RF discharge was driven at a frequency of 13.56 MHz using external electrodes. The discharge was ignited in oxygen at a pressure of 50 Pa. When the matching conditions between the oscillator and reactor are satisfied, the discharge runs in the α-form, which is characterized by a higher temperature and higher gas chemical activity at the reactor axis. The oxygen flow rate through the reactor is ≈100 cm^3/min, the degree of gas ionization is ~10^{-6}, and the degree of molecular oxygen dissociation is (1–3) × 10^{-2}. The calorimeter is placed at the discharge axis using a holder made of two thin (1.5 mm in diameter) quartz rods. In more detail, the experimental setup is described in [3, 4].

The etching reaction is the breaking of the polymer chains under the action of atomic oxygen and discharge radiation with the formation of volatile products going away to the gas phase (in the case of complete PFR transformation, these products are H_2O and CO_2). The reaction is exothermic, and its rate increases with the surface temperature according to the Arrhenius law. The calorimeter size and the film thickness were chosen such that, at the highest temperature, the flux of the reaction products from the surface did not exceed the flux of impurities present in oxygen passing through the reactor (approximately 0.3 vol %). The etching rate in the sample geometrical center was monitored using reflected light interferometry at a He–Ne laser wavelength of λ = 0.63 μm (the laser beam diameter being 1 mm, and the angle of incidence onto the sample surface being 5°).

The crystal non-steady-state temperature $T(t)$ was measured by laser interferometric thermometry at a He–Ne laser wavelength of λ = 1.15 μm (the laser beam diameter on the crystal surface being 0.5 mm, and the angle of incidence being 5°) [8]. The plane-parallel crystal acts as a Fabry–Perot interferometer for the probing radiation in the crystal transparency region. After the polymer film is completely removed from the surface, the discharge is switched off. Then, for the purpose of comparison, the same crystal, used as an inert calorimeter, is heated in the discharge under the same conditions and the $T(t)$ dependence is measured.

On the silicon crystal surface, there is a native oxide film with a thickness of ~10 nm. At relatively low temperatures characteristic of this study, no further silicon oxidation occurs (as is proved by the ellipsometry measurements of the oxide film thickness after 30-min-long stay of the crystal in the discharge).

5. RESULTS AND DISCUSSION

5.1. Interferograms

Figure 1 shows the time evolution of the light reflection coefficients (interferograms) measured when probing the silicon–polymer structure starting from the instant of discharge ignition in oxygen. Oscillations of the reflection coefficient at a wavelength of λ = 633 nm stem from the decrease in the film thickness h_f. The shift of the interferogram by one fringe corresponds to the decrease in the thickness by $\Delta h_f = \lambda/2n_f \approx 0.2$ μm (for the polymers under study, the refractive index is

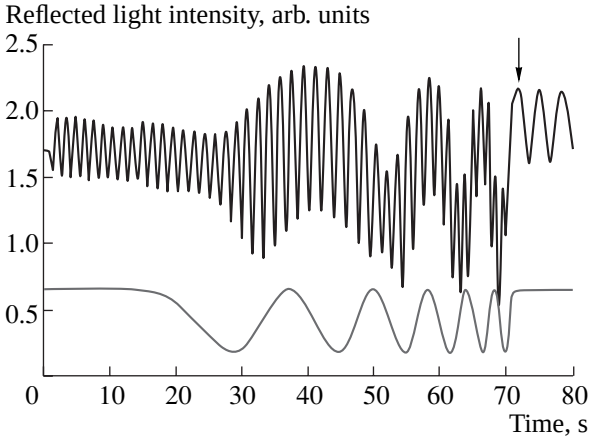

Fig. 1. Coefficient of light reflection from an 0.5-mm-thick silicon single crystal covered with a transparent 1.2-μm polymer film after discharge ignition in oxygen at a pressure of 50 Pa and an input power of 180 W. The He–Ne laser wavelength is 1.15 (upper curve) and 0.633 μm (lower curve).

$n_f \approx 1.6$). The initial film thickness is $h_0 \approx 1.2$ μm. After the complete removal of the film from the surface (at $t \geq 72$ s), the reflection coefficient becomes constant. Silicon is opaque for radiation with $\lambda = 633$ nm (the absorption coefficient is $\approx 4 \times 10^3$ cm^{-1}).

The structure of interferograms in reflected light at a wavelength of $\lambda = 1.15$ μm can be explained as follows. The high-frequency oscillations are related to the increase in the crystal temperature; the shift of the interferogram by one fringe corresponds to the increase in temperature by

$$\Delta T = (\lambda/2nh)[n^{-1}(\partial n/\partial T) + h^{-1}(\partial h/\partial T)]^{-1}.$$

For $T \approx 300$ K and 0.5-mm-thick silicon single crystal, $\Delta T \approx 5$ K; at higher temperatures, ΔT is somewhat lower. The low-frequency modulation is caused by a decrease in the film thickness h_f, and the shift by one fringe corresponds to the decrease in the thickness by $\Delta h_f = \lambda/2n_f \approx 0.34$ μm (the number of periods is almost two times smaller than that for $\lambda = 0.63$ μm). After the film removal, only oscillations related to the change in the crystal temperature are present in the interferogram. It is seen in both interferograms that the rate at which the film thickness changes increases with time.

5.2. Calorimeter Temperatures

Figure 2 shows the time evolution $T(t)$ of the temperature of crystals covered with a 2.1-μm polymer film after the discharge ignition in oxygen for two values of the RF input power. For comparison, the $T(t)$ dependences for crystals without a film are also presented. The $T(t)$ curve for an inert calorimeter is described by expression (1), whereas that for an active calorimeter has two inflection points. At the instant corresponding to the complete removal of the film from the crystal surface, the heating rate substantially decreases.

5.3. Heating Kinetics

At temperatures of ≤200–250°C, radiative losses from a silicon single crystal are negligibly small as compared to those from a polymer film. For this reason, in the initial stage, the inert calorimeter is heated faster than a crystal covered with a film. The rate of the chemical reaction and the related heat release power increase with the temperature. For the calorimeter covered with a film, the first inflection point in the $T(t)$ curve indicates the beginning of a significant heat release in the plasmochemical reaction. The positive feedback between the crystal temperature and the reaction rate results in the exponential growth of the temperature, lasting until the film is completely removed from the crystal surface. Time dependences of the calorimeter heating rate after the discharge ignition are shown in Fig. 3.

Temperature dependences of the calorimeter heating rate are shown in Fig. 4. The existence of two segments in the plot that can be fitted by straight lines implies that the heat exchange kinetics within these segments can be described by the first-order linear differential equations [2]

$$dT/dt = k_1(T_g - T), \quad (7)$$

$$dT/dt = (-k_1 + k_2)T + (k_1 - k_3)T_g, \quad (8)$$

where Eq. (7) corresponds to heating lasting from the instant of discharge ignition to the inflection point, Eq. (8) corresponds to heating lasting from the inflection point to the end of the reaction, $k_1 = 2\alpha/c\rho h$ is the rate constant for the plasma–surface heat exchange pro-

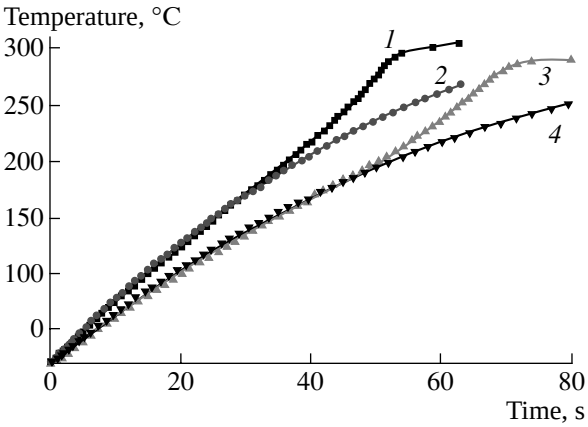

Fig. 2. Time evolution of the temperature of a silicon single crystal (*1*, *3*) with and (*2*, *4*) without a surface polymer film after discharge ignition in oxygen at a pressure of 50 Pa and an input power of (*1*, *2*) 300 and (*3*, *4*) 200 W. The initial film thickness is 2.1 μm, the crystal size is 2.5×2.5 cm, and the crystal thickness is 0.5 mm.

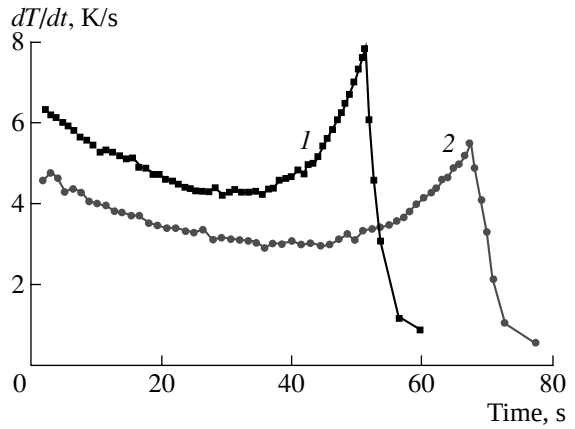

Fig. 3. Heating rate of a silicon single crystal covered with a polymer film in an oxygen plasma for an input power of (*1*) 300 and (*2*) 200 W. After the film has been completely removed from the surface, the endothermic reaction terminates, which corresponds to a sharp decrease in the heating rate.

ceeding via molecular heat conduction, $k_2 = HZ\Delta E/c\rho hkT_0^2$ is the rate constant for heat release related to the chemical reaction, $k_3 = HZ(c\rho T_g)^{-1}\exp(\Delta E/kT_0)(\Delta E - kT_0)/kT_0$ is the auxiliary parameter with a dimension of s^{-1}, k is the Boltzmann constant, and T_0 is the temperature in the vicinity of which the exponential dependence was linearized (in the theory of thermal explosion [9], this temperature is called the temperature of self-ignition).

Designating the heating rates of the inert and active calorimeters as V_1 and V_2 and differentiating them over the temperature, we obtain

$$dV_1/dT = k_1, \quad (9)$$

$$dV_2/dT = -k_1 + k_2. \quad (10)$$

From here, we can determine the rate constant k_2 for the reaction heat release. For tens of PI and PFR samples of different thicknesses exposed to an oxygen plasma in the pressure range 20–120 Pa and at the discharge input powers in the range 140–340 W, it was found that $k_2 > k_1$, which implies the development of a thermochemical instability. Using empirical approximations of the plot segments in Fig. 3, we obtain that, at an input power of $P = 200$ W, the rate constants are $k_1 \approx 1.52 \times 10^{-2}$ s^{-1} and $k_2 \approx 4.14 \times 10^{-2}$ s^{-1}. The corresponding scanning and plasmochemical reaction time constants are $\tau_1 \approx 66$ s and $\tau_2 = (k_2)^{-1} \approx 24$ s, respectively. At $P = 300$ W, we have $k_1 \approx 1.57 \times 10^{-2}$ s^{-1}, $k_2 \approx 5.04 \times 10^{-2}$ s^{-1}, $\tau_1 \approx 64$ s, and $\tau_2 \approx 20$ s. Generally, the rate constants are related to each other as $k_2 \approx (2–3)k_1$ for PFR and $k_2 \approx (1.5–2)k_1$ for PI.

5.4. Mechanisms for Crystal Heating

Any particle species in the discharge can be associated with a certain heat exchange mechanism involving the creation of an energy reservoir (gas heating, ionization, excitation of the metastable states, etc.), the transportation of this energy toward the surface, and the energy relaxation accompanied by the heating of a solid. These mechanisms are relatively independent because the energy relaxation rates in different subsystems of a low-pressure nonequilibrium plasma are rather low (except for the fast rotational–translational relaxation).

The contribution of charged particles to the heat flux onto the surface is negligible because of the low degree of gas ionization. Earlier, it was shown that the contributions of the discharge optical radiation and the RF power absorption by a silicon single crystal are also negligible [4].

Estimates show that, at a degree of gas ionization of ≤10%, the power density transferred to the crystal surface covered with a silicon oxide or polymer film due to the recombination of atoms does not exceed 5×10^{-3} W/cm^2. The contribution from quenching the metastable levels of oxygen molecule ($^1\Sigma_g^+$ and $^1\Delta_g$ states with energies of 1.6 and 1 eV, respectively) is even lower. These estimates were confirmed by experiments. The relaxation probabilities for the excited levels increase with the surface temperature [10]; hence, the slope of the $D(T)$ dependence must decrease with the temperature if this mechanism plays an important role in the heating of the inert calorimeter. Curves *3* and *4* in Fig. 4 do not show a tendency to the slope lowering. This means that heterogeneous relaxation does not play a significant role in the calorimeter heat balance. However, provided the surface is cleaned in a discharge or is covered by a thin film with catalytic properties (platinum, etc.), this mechanism explicitly manifests itself by an increase in the power transferred to the calorimeter. Thus, on a silicon surface cleaned of water vapor with the help of a surface active Langmuir–Blodgett film, which is quickly removed in the discharge, an extra power of ~40 mW/cm^2 is released [5]. For a crystal surface covered with a platinum film (whose catalytic properties are the strongest), the extra power transferred to the calorimeter is ~0.1 W/cm^2 [11]. On the crystal surface covered with a polymer film, whose catalytic properties are significantly weaker than those of a platinum film, the extra heat release related to the deactivation of the excited states should be much less than 0.1 W/cm^2. Hence, extra heat release with a power of up to 0.5–0.7 W/cm^2, which is observed in the experiment, results from chemical reactions.

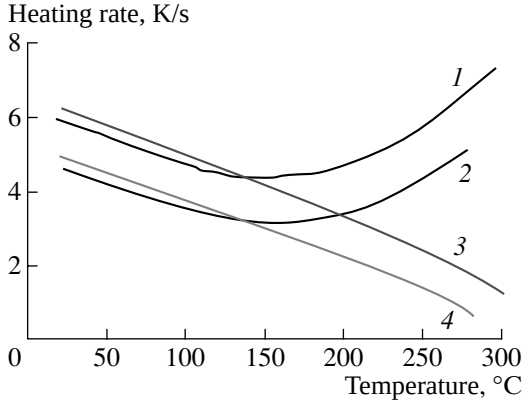

Fig. 4. Temperature dependence of the heating rate of a silicon single crystal (*1*, *2*) with and (*3*, *4*) without a 2.1-μm polymer film in an oxygen plasma for an input power of (*1*, *3*) 300 and (*2*, *4*) 200 W.

The neutral gas temperature beyond the calorimeter thermal boundary layer was determined from the inert calorimeter heating kinetics. For $P = 300$ and 200 W, this temperature is 420 and 350°C, respectively. Within the boundary layer, whose thickness is comparable with the calorimeter size, the energy density in the subsystem of translational degrees of freedom of the neutral particles decreases as approaching the surface.

The origin of the boundary layer is related to (i) the high relaxation rate of the energy of translational degrees of freedom in collisions of the particles with the surface (the accommodation coefficient is approximately 0.3–1) and (ii) the limited rate of energy transfer from the discharge to the surface. For subsystems of vibrational and electronic levels, in which the probability of energy transfer to a solid is low, the energy density does not depend on the coordinate, so that the boundary layer is absent. In this case, heat transfer is limited by the low rate of energy relaxation on the surface.

5.5. Radiative Heat Losses

Radiative properties of a silicon single crystal and a silicon–polymer structure are very different. Polymer films are characterized by a set of strong absorption bands in the mid-infrared range. In the range $\lambda \approx 5$–20 μm, about ten absorption bands with bandwidths of $\Delta\nu \approx 20$–40 cm^{-1} and absorption coefficients of $\alpha \sim 10^{-4}$ cm^{-1} are observed in the PI transmission spectrum. For films with a thickness of 1–2 μm, the absorption factor in these bands is as high as $A \approx 0.5$–0.8. According to Kirchhoff's law, thermal emission is also localized in these spectral bands.

At temperatures of $T \le 200$–250°C, a weakly doped silicon single crystal with a free carrier (electrons or holes) concentration of $n \le (0.1\text{–}1) \times 10^{16}$ cm^{-3} is almost transparent in the mid- and far-infrared spectral regions. At $400 \le T \le 700$ K, the temperature dependence of the power radiated by a single crystal is of the Arrhenius type with an activation energy close to the one-half of the band gap energy [12].

The presence of a film on the surface substantially modifies the calorimeter radiative properties. Figure 5 presents the time dependences of the temperature of calorimeters covered with PI films of different thickness (in the range 0–2.5 μm) after the discharge is switched on and off. It is seen that, in the discharge, the crystal covered with a film is heated more slowly than without a film. The larger the film thickness, the lower the calorimeter heating rate (this fact proves the radiative loss mechanism: if the film somehow influenced the particle–surface heat exchange, then the film thickness would not reduce the heating rate because the properties of the film surface are independent of the film thickness). After the discharge is switched off, a crystal covered with a film is cooled faster than that without a film.

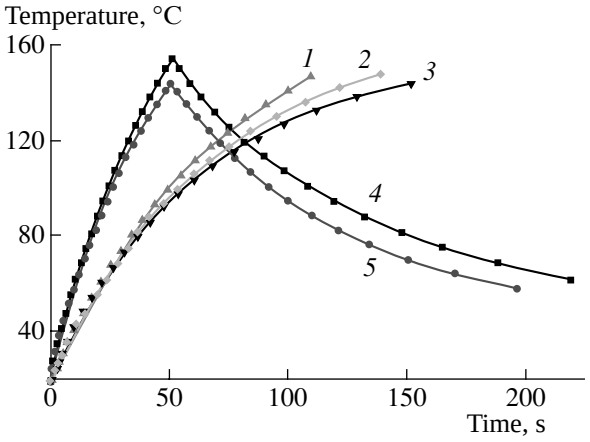

Fig. 5. Heating kinetics of a 0.5-mm-thick silicon single crystal (2.5 × 2.5 cm in size) covered with a polymer film in a discharge and the cooling kinetics after the discharge is switched off. The film thickness is (*1*) 0, (*2*) 1.5, (*3*, *5*) 2.5, and (*4*) 0.2 μm; the input power is (*1*–*3*) 110 and (*4*, *5*) 160 W.

To properly take into account radiative losses from a calorimeter covered with a film is not a simple matter because the film thickness decreases with time (or with increasing temperature). For this reason, precise measurements of the temperature dependence of $(D_e)_1$ are rather difficult and require the determination of thermal losses for crystals covered with films of different thickness at specific temperatures depending on the thickness itself. The temperature dependences of the intensity of radiative heat removal were measured for calorimeters covered with films of three different thicknesses. When calculating the integrals in formula (6), the results obtained with films of the largest, intermediate, and the smallest thickness were used in the temperature ranges 20–180, 180–260, and $T > 260$°C, respectively.

5.6. Reaction Heat and Activation Energy

By taking the integrating in the numerator of expression (6), we find an extra heat energy received by the calorimeter in the process of plasmochemical oxidation of a PFR polymer film: $\Delta Q_{\text{chem}} = 6.76$ J/cm^2 for the input power $P = 300$ W and $\Delta Q_{\text{chem}} = 6.79$ J/cm^2 for $P = 200$ W. The heat released in the chemical reaction amounts to higher than 30% of the energy (≈20 J/cm^2) transferred to the inert calorimeter from the discharge over a time required for the complete oxidation of the film on the active calorimeter.

The heat of the plasmochemical oxidation of PFR, determined by expression (6), is $\delta H = 2.68 \times 10^4$ J/g for $P = 300$ W and $\delta H = 2.69 \times 10^4$ J/g for $P = 200$ W. The mean value obtained by averaging over five samples is $\delta H = (27 \pm 1)$ kJ/g. The measurements carried with a calorimetric bomb showed that the enthalpy of the complete combustion of PFR in molecular oxygen is $\approx 2.8 \times 10^4$ J/g [7, 13]. In this case, the work of expansion is negligible because the number of atoms involved in the reaction is close to the number of molecules produced in the reaction. The value of δH obtained when oxidizing the film in the plasma and the heat of complete combustion in hot oxygen are close to each other, which, however, does not mean that $\delta \approx 1$. The point is that, in a nonequilibrium plasma, atomic oxygen is produced

from an O_2 molecule via an electron impact in the discharge volume, rather than via thermal dissociation on the calorimeter surface. Hence, the heat of polymer oxidation by atomic oxygen must be $\sim 6.5 \times 10^4$ J/g. It follows from here that $\delta \geq 0.4$. The energy fraction not intercepted by the calorimeter can be taken away by the electronically and vibrationally excited reaction products. The desorption of incompletely oxidized macromolecule fragments (monomeric links, molecular hydrogen, etc.) is also possible. Per every removed C_7H_6O fragment of a $(C_7H_6O)_n$ PFR macromolecule (where $n > 100$), an energy of ~30 eV is transferred to the calorimeter. For complete oxidation, it is necessary that 9.4×10^{22} oxygen atoms react with 1 g of polymer. On each oxygen atom involved in the reaction, an energy of ≈ 2 eV is released in the calorimeter. This is an estimate from below because polymer oxidation is usually not completed and a lesser amount of oxygen atoms is required to remove the film. The study of the issues related to both the degree of the substance transformation in plasmochemical reactions and the energy distribution among the calorimeter and reaction products is also of interest.

The slope of the temperature dependence of the power released in the chemical reaction is constant in Arrhenius coordinates ($\log D_r - T^{-1}$), which enables the determination of the activation energy of the exothermic process: $\Delta E = 0.38$ eV for $P = 300$ W and $\Delta E = 0.36$ eV for $P = 200$ W. The average over five samples is $\Delta E = (0.37 \pm 0.02)$ eV. The same quantity also characterizes the temperature dependence of the chemical reaction rate. The preexponential factor Z increases from 4 to 9 mg/cm^2 s with increasing discharge input power. The constant slope of the $D_r(T)$ dependence allows us to conclude that, in this case, the rates of the surface processes are the reaction limiting factor. When the transportation of chemically active particles from the discharge to the surface is the limiting factor, the temperature dependence in Arrhenius coordinates is a curve whose slope decreases with the temperature (i.e., the temperature dependence of the reaction rate becomes saturated).

5.7. Film Oxidation Rate

The interferometric oscillations of the intensity of the reflected light with a wavelength of 633 nm allow one to plot the time dependence of the film thickness after the discharge ignition. This method is based on the assumption on the layer-by-layer removal of the film from the surface. This assumption is confirmed by analyzing the film transmission spectra after removing one-half and three-quarters of the initial film thickness. The refractive index holds constant in the mid-infrared spectral region, which indicates that the composition and structure of the remaining film remain unchanged.

Let us consider another method, which is more universal and may be applied, for example, to the plasmo-

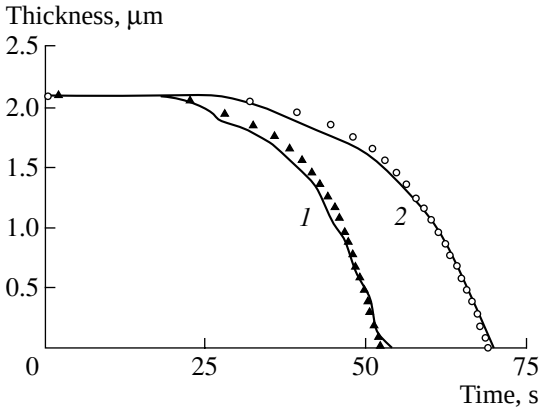

Fig. 6. Decrease in the polymer film thickness in an oxygen plasma for an input power of (*1*) 300 and (*2*) 200 W. The thickness is determined from an interferogram at a wavelength of 0.633 μm (symbols) and from the released thermal energy (solid lines).

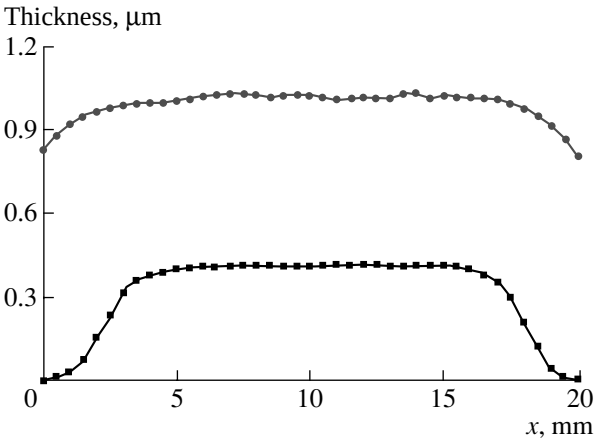

Fig.7. Profiles of the film thickness along the 2×2-cm sample 55 (circles) and 65 (squares) s after discharge ignition in oxygen for an input power of 185 W. The initial film thickness is 2 μm; the film is completely removed over ≈70 s.

chemical etching of opaque (e.g., metal) films. The heat energy $\delta(\Delta H)$ released in a chemical reaction by the instant t is proportional to the decrease in the film thickness; i.e., $h(t) = h_0[1 - \Delta(\delta H)/\delta H]$. The instant $\Delta(\delta H)$ can be found by performing integration in expression (6) to the instant t. Figure 6 shows the $h(t)$ dependences obtained by two different methods. The difference between them stems from the fact that the interferometry method of the thickness determination is local, whereas the thermal method is integral because of the high thermal conductivity of the silicon single crystal. The film thickness at the edge of the sample decreases faster than in the center (Fig. 7).

The fact that the film etching rates obtained by the two different methods are close to each other allows us to conclude that the power of extra heat release and the

film etching rate increase with temperature in the same way. This is indirect evidence that the source of extra heat release, which leads to the heating of the calorimeter covered with a film, is related to a surface chemical reaction. If there were several surface heat sources with comparable powers and different activation energies, then the $h(t)$ dependences obtained by these two methods would differ from each other.

6. CONCLUSION

Monitoring the rate of heat release in a surface plasmochemical reaction allows one to determine such reaction parameters as the reaction heat, the activation energy, and the rate constant of heat release. The activation energy measured when oxidizing a polymer in an oxygen plasma is about three times lower than that during polymer heating in oxygen. Varying the power deposited in the discharge does not considerably change the activation energy. Reactions with the participation of radicals, discharge initiation by UV radiation, etc., can lead to a decrease in ΔE in the plasma.

The heat released in a plasmochemical reaction is lower than the heat of the complete combustion of a polymer film in atomic oxygen. One of the possible reasons is the desorption of deficiently oxidized products from the film surface. To verify this assumption, it is necessary to analyze the reaction products.

With a scanning calorimetry, the number of mechanisms governing heat release on the calorimeter surface can be determined from the number of the nearly linear segments in the temperature dependence of the power transferred to the calorimeter. The problem of resolving contributions from different heat sources by the method concerned is similar to resolving overlapped spectral lines: if the maxima of heat release are localized in different temperature ranges, resolving is an easy task. If some sources with approximately equal powers act simultaneously and their powers have similar temperature dependences (e.g., several sources with Arrhenius temperature dependences), then the problem becomes more complicated but not insolvable, because each source has its own characteristic activation energy; i.e., on the temperature–power plane, its contribution is marked off by a linear segment with its own slope.

ACKNOWLEDGMENTS

This study was supported by the Russian Foundation for Basic Research, project no. 01-02-17209.

REFERENCES

1. I. P. Herman, *Optical Diagnostics for Thin Film Processing* (Academic, San Diego, 1996).
2. A. N. Magunov, Pis'ma Zh. Tekh. Fiz. **21** (5), 44 (1995) [Tech. Phys. Lett. **21**, 185 (1995)].
3. A. N. Magunov, Prib. Tekh. Éksp., No. 5, 131 (1995).
4. A. N. Magunov, Fiz. Plazmy **23**, 1018 (1997) [Plasma Phys. Rep. **23**, 940 (1997)].
5. A. N. Magunov, Prib. Tekh. Éksp., No. 1, 92 (1999).
6. A. N. Magunov, A. Yu. Gasilov, and O. V. Lukin, Teplofiz. Vys. Temp. **37**, 202 (1999).
7. W. M. Moreau, *Semiconductor Lithography* (Plenum, New York, 1988; Mir, Moscow, 1990).
8. A. N. Magunov and E. V. Mudrov, Teplofiz. Vys. Temp. **30**, 372 (1992).
9. N. N. Semenov, *Chain Reactions* (Nauka, Moscow, 1986).
10. V. D. Berkut, V. M. Doroshenko, V. V. Kovtun, and N. N. Kudryavtsev, *Nonequilibrium Physicochemical Processes in Hypersonic Aerodynamics* (Énergoatomizdat, Moscow, 1994).
11. A. N. Magunov, Fiz. Plazmy **27**, 378 (2001) [Plasma Phys. Rep. **27**, 355 (2001)].
12. A. N. Magunov, Pis'ma Zh. Tekh. Fiz. **20** (7), 65 (1994) [Tech. Phys. Lett. **20**, 289 (1994)].
13. *Concise Handbook of Physicochemical Quantities*, Ed. by A. A. Ravdel' and A. M. Ponomareva (Khimiya, Leningrad, 1983).

Translated by N. Ustinovskiĭ